



# **Phase II SBIR Final Report: An Ultra-Sensitive Optical Biosensor for Food Safety**

**Contract # DAAD16-01-C-0001**

**Prepared for**

**US Army Soldier & Biological Chemical Command  
Soldiers System Command  
Performance Enhancement & Nutritional Quality  
Combat Feeding Team  
Kansas Street  
Natick, MA 01760-5019**

**Prepared by**

**SatCon Applied Technology  
161 First Street  
Cambridge, MA 02142**

**August 23, 2002**

## Report Documentation Page

<b>Report Date</b> 23 Aug 2002	<b>Report Type</b> N/A	<b>Dates Covered (from... to)</b> -
<b>Title and Subtitle</b> Phase 2 SBIR Final Report: An Ultra-Sensitive Optical Biosensor for Flood Safety		<b>Contract Number</b>
		<b>Grant Number</b>
		<b>Program Element Number</b>
<b>Author(s)</b>		<b>Project Number</b>
		<b>Task Number</b>
		<b>Work Unit Number</b>
<b>Performing Organization Name(s) and Address(es)</b> SatCon Applied Technology 161 First Street Cambridge, MA 02142		<b>Performing Organization Report Number</b>
<b>Sponsoring/Monitoring Agency Name(s) and Address(es)</b> US Army Soldier & Biological Chemical Command, Soldiers System Command Performance Enhancement & Nutritional Quality Combat Feeding Team Kansas Street Natick, MA 01760-5019		<b>Sponsor/Monitor's Acronym(s)</b>
		<b>Sponsor/Monitor's Report Number(s)</b>
<b>Distribution/Availability Statement</b> Approved for public release, distribution unlimited		
<b>Supplementary Notes</b> The original document contains color images.		
<b>Abstract</b>		
<b>Subject Terms</b>		
<b>Report Classification</b> unclassified	<b>Classification of this page</b> unclassified	
<b>Classification of Abstract</b> unclassified	<b>Limitation of Abstract</b> UU	
<b>Number of Pages</b> 247		

## **Phase II SBIR Final Report: An Ultra-Sensitive Optical Biosensor for Food Safety (Contract DAAD16-01-C-0001)**

**Executive Summary.** The further development of a unique interferometric based optical biosensor platform for the rapid unlabelled detection and identification of foodborne pathogens was carried out under Phase II SBIR contract DAAD16-01-C-0001 entitled: An Ultra-Sensitive Optical Biosensor for Food Safety. The potential in combining optical methods with biomolecular recognition techniques is the high signal gain derived from photonic amplification and thus high sensitivity, specificity, and rapid response time.

This Phase II effort was focused on the development of the following innovations:

- Microfluidic diffusional filtering of bacterial cells for high-throughput ‘on-chip’ purification of real-world samples prior to detection,
- Biomolecular immobilization based on the application of thin self-assembled polyethylene oxide derived molecular films with for highly controlled positioning of receptor sites and the suppression of non-specific binding events,
- Uigh resolution interferometric evanescent wave detection based on the modulation of polarization and the subsequent differencing of TE and TM modes for highly stable and self-compensated operation, and
- The spatial manipulation of the cells within a microfluidic environment to steer the sample stream nearer to the receptors for increased probability of capture.

The goal of the effort was the eventual development of a portable biosensing platform for the detection and identification of viable pathogenic microbes in foods at the level of 1 CFU/mL within a 30-minute period.

The usual 24-month Phase II SBIR program was accelerated to hasten the commercialization of the technology, however the program was terminated at 18 months after both contract funding and SatCon cost-share had been expended, and no follow-on funding was attainable. The original proposal, written only four months into the Phase I effort, was modified to perform a bench-top level effort and not the fully miniaturized development originally proposed. Cost-sharing equivalent to the indirect program costs was borne by SatCon.

*Laboratory Development.* The different sub-systems were developed, tested, and integrated to the extent possible. A summary of these efforts are provided below:

- A ‘doubly differential’ interferometer, relying on the difference in evanescence response between modulating polarizations, was built. The transducer monitored changes in the speed of light caused by surface binding propagating through a single-mode waveguide. A first generation grating coupled waveguide was fabricated but was unusable due to poor light throughput. The design of the next generation waveguide was improved with the incorporation of 1<sup>st</sup> order diffraction gratings. A commercial fabrication facility capable of doing the work was identified and contracted. The fabrication setup of these devices was completed, photolithographic masks were purchased, wafers were delivered,

and the process was ready for thin film deposition and feature etching, however, the step to manufacturing was not taken due to delays and to inconsistencies in modeling results which have confused the selection of the final design specifications. The development of the interferometer and the biosensor overall was eventually hampered by the unavailability of working waveguides needed to prove the feasibility of the doubly-differential technique and make measurements of microbiological targets.

- The waveguide surface was derivatized with a self-assembled monolayer (SAM) of polyethylene oxide (PEO) to which protein-A was covalently attached by the Laibinis group at MIT. This provided a 'Teflon' like surface for the suppression of non-specific binding and the carefully controlled positioning of receptors. The development of the initial chemistry was completed, however, its optimization and patterning could not be completed before the end of the program.
- A receptor system based on a protein-A linker for the general attachment of IgG immuno-receptors was successfully developed. A model *E. coli* system was developed as a laboratory standard and immuno-receptor attachment and regeneration was demonstrated.
- Non-specific binding (NSB) of proteins was addressed by the application of a PEO SAM mentioned above. A novel optical technique proposed by the Boston University group for the controlled desensitization of the waveguide surface and the microfluidic based filtering to diffuse small molecules from large cells as a means of mass extraction was also explored as an additional approach to NSB and for 'on-chip' sample preparation, respectively. No data were able to be produced from the former optical experiments. Stand-alone gravity driven disposable cartridges were designed by Micronics, Inc for SatCon and tested. Cell recovery was typically measured at 60-70% while removal of BSA protein was slightly higher. Although not optimized, these results suggest that this technique alone will not be adequate for 'on-chip' sample preparation.
- A novel flow cell based on the dynamics of flow at low Reynolds number to spatially direct cells nearer to the receptors for enhanced capture efficiency was conceived. A device was designed and tested. The experimental data were in excellent agreement with theoretical predictions and eventually limited by the stability of the pump station. Although hydrodynamic focusing is an important contribution for increasing the capture probability its practical use comes at the price of longer processing times.
- Preliminary integration and laboratory characterization was carried out with grating coupled waveguide devices obtained from Dr. Daniel Campbell at the Georgia Tech Research Institute. Refractive index data on bulk fluidics, non-specific protein adsorption, and specific capture of proteins was collected; however, experiments with bacterial cells were not able to be completed because of the unavailability of quality waveguides. Experiments were originally planned using prism-coupled waveguides produced by the Boston University group to obtain intermediate data. No data were able to be produced due to a fatal design flaw in the production of the waveguides.
- Finally, an in-depth food-testing program was planned to characterize the platform's ability to recovery *E.coli* 0157 and *S.aureus* pathogenic cells from different food systems. Experiments establishing model systems were begun but not fully executed before all resources were expended.

Overall, the lack of availability of working grating-coupled waveguides has delayed the demonstration of the effectiveness of this approach and further work described herein is required before the value of this technique can be fairly accessed.

# Table of Contents

<b><u>Section</u></b>	<b><u>Page</u></b>
<b>Executive Summary</b>	i
<b>Chapter 1: Overview</b>	
Introduction	1-1
Phase II Objectives	1-1
Rapid Methods for Food Safety	1-3
Portable Biosensing Platform	1-4
Optical Detection	1-5
Evanescent Wave Surface Detection	1-6
Interferometer Design	1-6
Work by Others	1-7
<b>Chapter 2: Programmatics</b>	
Original Program Plan	2-1
Modifications to the Plan	2-1
Schedule	2-3
Description of the Team: Roles and Responsibilities	2-5
<b>Chapter 3: Optical Design</b>	
Phase II Transducer Design	3-1
Phase Detector and Data Acquisition	3-1
Optical Signal Processing Test Results	3-3
Prototype Transducer Optical Design	3-5
Preliminary Double Differential Measurements	3-6
Summary	3-7
<b>Chapter 4: Waveguide Development</b>	
Overview	4-1
Completion of Silicon-on-Insulator (SOI) Measurements	4-1
Design of Single Mode Waveguides	4-1
Intermediate Data: Prism Coupling	4-4
Wafer Processing at Boston University	4-5
Summary	4-6
Appendix 4-A: Modeling for Sarnoff PECVD Fabrication	
Appendix 4-B: Boston University Report on Prism Coupling Work October 14, 2001	
Appendix 4-C: Design Report for Grating Coupled Waveguides	
Appendix 4-D: Mechanical Layout of Grating Coupled Waveguides	
Appendix 4-E: Original Waveguide Specification	
<b>Chapter 5: Surface Derivatization</b>	
Overview	5-1
Chemical Synthesis	5-1
Protein-A Attachment	5-4
Summary	5-5

<b>Chapter 6: Model Systems and Receptor Platform Development</b>	
Model Systems	6-1
Model System Verification	6-1
Verify Activity of Protein-A on Solid Support	6-6
Binding of Cells onto Solid Supports	6-7
Regeneration	6-9
Summary	6-11
<b>Chapter 7: Non-Specific Binding</b>	
Introduction	7-1
Optical Suppression of Non-Specific Binding	7-1
Microfluidic Extraction	7-3
H-Filter Development	7-4
Summary	7-10
Appendix 7-A: Surface Desensitization of Polarimetric Waveguide Interferometers	
Appendix 7-B: Experimental Plan for Optical Surface Desensitization	
<b>Chapter 8: Microfluidic Primer</b>	
Introduction	8-1
Overview of Microfluidics	8-1
Analytical Modeling Tools for Microfluidic Devices	8-3
<b>Chapter 9: Microfluidic Flow Cell for Enhanced Capture Efficiency</b>	
Introduction	9-1
SatCon Concept	9-1
Analysis of the Flow Cell	9-2
Flow Cell Fabrication	9-9
Technical Challenges	9-9
Background	9-9
Survey of Micro-Fabrication Techniques	9-10
Materials	9-13
Fabrication of the Flow Cell	9-15
Laboratory Characterization	9-16
Experiment #1: Unfocused Flow Cell Results	9-18
Experiment #2: Hydrodynamic Focusing	9-19
Summary	9-22
Appendix 9-A: Mechanical Drawings for Microfluidic Flow Cell	
<b>Chapter 10: Laboratory Characterization</b>	
Experiment Setup	10-1
Waveguides and Flow Cells	10-1
Gaskets	10-5
Integration effort	10-5
System Integration	10-5
Automated Pump Station	10-5
Laboratory Results	10-7
Bulk Index Changes	10-7
Surface Detection: Protein Adsorption	10-8
Specific Binding	10-10
Suppression of Non-Specific Binding	10-11

Cell Detection effort	10-12
Summary	10-12
Appendix 10-A: Mechanical Drawings for Waveguide-Flow Cell Mounting Fixture	
Appendix 10-B: Flow Cell Mechanical Drawings	

## **Chapter 11: Application to Food System Testing**

Food System Testing	11-1
Description of Experiments	11-2
Capture from Spiked Food Matrices	11-4
Non-Specific Binding of food Samples	11-5
Summary	11-7

<b>Summary and Conclusions</b>	12-1
--------------------------------	------

## Chapter 1 : Program Overview

**Introduction** The further development of a unique interferometric based optical biosensor platform for the rapid unlabeled detection and identification of food-borne pathogens was carried out under Phase II SBIR contract DAAD16-01-C-0001 entitled: An Ultra-Sensitive Optical Biosensor for Food Safety. The utility in combining optical methods with biomolecular recognition techniques is the high signal gain derived from photonic amplification and thus high sensitivity, specificity, and rapid response time.

Recently published results by Demarco et al.<sup>1</sup> on the detection of *E.coli* 0157:H7 in ground beef samples using fluorescent tagging clearly demonstrate the ability of optical biosensors to detect and identify foodborne pathogens at population levels of great interest to the food safety community. The goal of this project is to advance the state-of-the-art by demonstrating unlabelled detection with commensurate sensitivities in a simplified implementation.

The overall thrust behind this work is that the potential of interferometric based biosensors, while universally recognized, has not yet been appreciably realized. The major obstacles limiting interferometric evanescent and most biosensors overall have been:

- Interference resulting from non-specific surface binding, and
- System stability and sensitivity of the detection method.

These technical barriers have generally slowed the commercial development of many optical biosensing technologies in this country<sup>2</sup>. This Phase II effort addressed these obstacles through the development of:

- Microfluidic diffusional filtering of bacterial cells for high-throughput ‘on-chip’ purification of real-world samples prior to detection,
- Biomolecular immobilization based on the application of thin self-assembled polyethylene oxide derived molecular films for highly controlled positioning of receptor sites and the suppression of non-specific binding events, and
- Uigh resolution interferometric evanescent wave detection based on the modulation of polarization and the subsequent differencing of TE and TM modes for highly stable and self-compensated operation.

A problem unique to the detection of cells using biosensors is the efficient capture of the organisms prior to detection. SatCon has addressed this challenge by

- The spatial manipulation of the cells within a microfluidic environment to steer the sample stream nearer to the receptors for increased probability of capture.

**Phase II Objectives.** The focus of this Phase II effort was the development of a portable biosensing platform with the ultimate goal of the detection and identification of viable pathogenic microbes in foods at the level of 1 CFU/mL within a 30-minute period. The combination of the sensitive optical transducer with a novel microfluidic ‘membraneless’ diffusional filter lends itself naturally to the separate delivery of both whole cells as well as small

molecules such as toxins for detection of both targets. After integration of all hardware a laboratory test program was conducted to characterize the ability of the platform to sense pathogenic microbes in food substances.

Phase II technical objectives were:

1. Platform Advancement - Development of the optical transducer with miniaturization of optical components and the incorporation of a microfluidic transport system,
2. Laboratory Integration - Portable platform integration and testing. The basic testing will be accompanied by any required refinements to the platform and will characterize its operation under ideal conditions.
3. Food Testing - An in-depth food-testing program will be conducted to characterize the platform's ability to detect *E.coli* 0157 and *S.aureus* pathogenic cells in food substances.

The following text describes the successes and present status of experiments designed and conducted to achieve these objectives. Overall, the ability to complete these objectives was impeded by the lack of functional waveguides. The programmatics are described in Chapter 2. The development of the overall optical design is found in Chapter 3 while optical waveguide development is described in Chapter 4. Surface derivatization, receptor development, and non-specific binding are found in Chapters 5, 6, and 7, respectively. The primer for microfluidic flow is found in Chapter 8 followed by a description of the flow cell in Chapter 9. A description of the laboratory characterization experiments carried out is described in Chapter 10. Finally, work carried out for the application of the biosensor system to the detection of Foodborne pathogens is described in Chapter 11.

## Background

**Rapid Methods for Food Safety.** Food testing places very stringent criteria on assay technology. In contrast to clinical samples, food is neither sterile nor highly contaminated. Pathogen testing requires detection at a level of a single organism per 25g of foodstuff, challenged by the presence of deliberately cultured benign bacteria. The matrices assayed by the food industry are complex and come in a staggering array of compositions, containing bacterial growth inhibitors such as egg white, or substances that interfere with the assay itself, such as fats.

At this time no commercial sensors exist that are capable of real or near real time detection of food microbes at the levels mandated by current regulations without first resorting to culture enrichment for amplifying the population of the pathogens<sup>3</sup>. This was the topic of the NSF jointly sponsored Workshop on Enhancing Food Safety through the Use of Sensors, September 24, 1997.

Current Methodology. Currently accepted methods for detection of bacterial pathogens rely on culturing the organisms and require at least 48 hours to obtain conclusive results. Since the organisms are grown and characterized by using selective media and biochemical tests these procedures can detect 1 CFU/ 25 gm of food sample. However, the limitation of these procedures is the time required for the analysis. Improvements in the time were provided by the use of immunoassays because these tests are specific for the organism and can be completed in 2 to 4 hours. Currently accepted tests using commercial test kits based on immunochemical techniques offer results in 22 to 24 hours from time of sampling to obtaining final results. There are several commercially available test kits for *E. coli* O157:H7. There is one commercial test kit for the detection of *S. aureus* available from TECRA but it requires a 24-hour pre-enrichment phase to increase the number of bacterial cells. Although immunochemical tests may be completed in a few hours these assays often require at least  $10^5$  or  $10^6$  CFU/ml and thus are not sensitive enough for direct, real time detection of the pathogens.

Su and Wong have reviewed several commercially available immunoassays developed to check for Staphylococcal enterotoxins with sensitivities ranging from 0.2 ng/ml to 1.0 ng/ml and a total assay time of 1.5 to 24 hours<sup>4</sup>. Some of the more rapid enterotoxin kits require special equipment or involve several handling steps common to most immunoassays.

Biosensors. Recent developments in biotechnology are quickly giving rise to rapid techniques.<sup>5</sup> Adenosine triphosphate (ATP) assays are a promising technique because of their fast response time ( $10^4$  cells in 10 minutes). However, since ATP is present in all bacteria, specificity is lacking to differentiate pathogenic from normal bacteria. ELISA tests have response times of 10 minutes up to 2 hours, but poor sensitivities of  $10^4$  cell/g requires prior enrichment. DNA based assays using PCR such as those under development by bioMerieux, while still having theoretical promise, have not yet been successful in avoiding culture enrichment steps.

Significant progress has been made recently using optical fluorescence-based systems such as the Analyte 2000, a portable fiber optic evanescent wave probe. Demarco et al.<sup>6</sup> report the detection of 3 to 30 CFU/ml of *E.coli* O157:H7 from spiked ground beef samples demonstrating the

feasibility of using optical biosensing devices to detect small numbers of cells. The unit utilizes a portable fiber optic spectrometer to detect a sandwich immunoassay performed on tapered fiber tips. The system total analysis time was 38 minutes with a sensitivity that has the potential to permit near real time analysis. However, the system still relies on a sandwich immunoassay for labeling and detection of the organisms and some of the subsequent rinsing steps involved with this format.

Ye, et al, 1999, have developed a membrane-based fiber optic biosensor with the capability of detecting  $3.8 \times 10^4$  colony forming units/ml (CFU/ml) of *S. aureus*<sup>7</sup>. Pivarnik, et al, 1999 have developed an immunomagnetic sensor for detection of *Salmonella* with a detection limit of  $1 \times 10^5$  cfu/ml<sup>8</sup>.

Staphylococcal enterotoxin A has been detected with a commercially available biosensor. The IAsys evanescent wave biosensor was used in a single antibody capture -direct detection procedure with a sensitivity in the range of 10 - 100 ng/g of sample signal<sup>9</sup>. When used as a single antibody capture and measurement the assay could be completed in as little as 4 minutes. To improve sensitivity the system was used with a secondary antibody and a sandwich assay. Although the signal obtained in the sandwich format was greater it required more time and extra handling steps. In the single capture and measurement procedure the instrument was faster than the currently available immunoassay kits but less sensitive by at least a factor of 10.

**Portable Biosensing Platform.** The technology is based around the concept of a small, integrated disposable cartridge containing all fluidic circuitry as well as the active sensing element. The cartridge is interchangeable for eventual testing of different microbial pathogens and sealed to eliminate contamination. A conceptual design of the platform is shown in Figure 1-1 below along with the integrated disposable cartridge. Sample is injected into a port located on the surface of the cartridge and pumped into the optical sensing chamber via microfluidic circuitry. The entire instrument can be packaged smaller than a laptop computer weighing less than 5 lbs; dimensions of the disposable cartridge are anticipated to be within a volume defined by 3" long x 2" wide x 0.5" high.

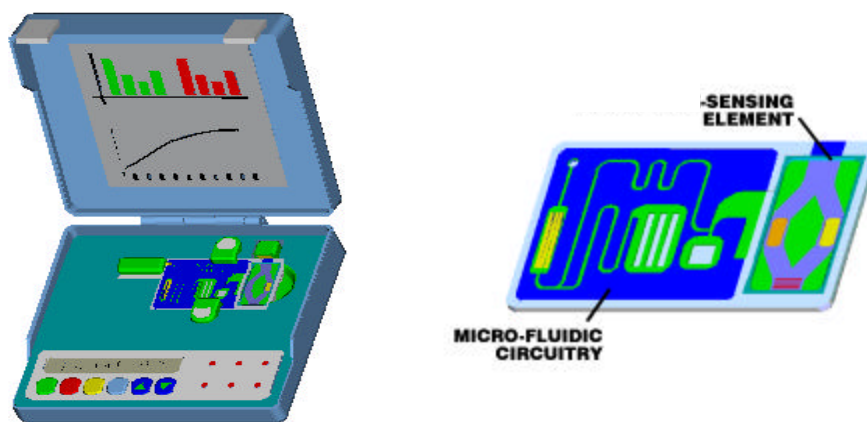


**Figure 1-1:** Conceptual drawing of the biosensing platform (left) and a detail of the integrated cartridge containing both fluidics and the optical sensing element (right).

**Optical Detection.** The United States needs robust portable detectors of biological and chemical samples, which work with great accuracy and at high speeds. Optical biosensing has particular promise due to the combined advances in molecular biology and the development of inexpensive lasers and optics. The utility in combining optical methods with biomolecular recognition techniques is the high signal gain derived from photonic amplification and thus high sensitivity, specificity, and rapid response time. This promise has not yet been fulfilled. As a result of these barriers, the commercialization of optical biosensing technologies has remained slow in this country.<sup>10</sup>

Evanescent wave detection is a popular optical technique because of its capability to sense surface binding. An evanescent wave field is an electromagnetic field at the outside surface of an optic generated by light totally internally reflected within that optic. The evanescent field intensity falls off exponentially with distance ( $E = \exp(-\alpha z)$ , where  $\alpha$  is on the order of one over the wavelength of the light) and is therefore ideal for the detection of localized phenomena such as pathogen binding onto a surface.

One class of evanescent sensors relies on fluorescent markers to monitor pathogen binding. In these devices the excitation and emission light are delivered and collected, respectively, via evanescent wave coupling using multi-mode waveguides for optical transport and the primary detection mode is through the sample's fluorescence.<sup>11,12,13,14,15</sup> Similar techniques have used optical fibers and various concentration schemes<sup>16</sup> and are occasionally referred to as Total Internal Reflection Fluorescence (TIRF).<sup>17,18</sup> These methods have become popular because of their optical simplicity. The difficulties are that amplification methods are still required for highly sensitive biological detection, and intensity detection is unstable to source noise and optical scattering, as well as being inherently limited by the statistics of the detected number of emission photons. Most importantly, these methods are not differential and the process of fluorescent tagging is imperfect, leading to a background of non-specific surface and molecular binding limiting the signal.

The use of a reporter fluorochrome can be avoided entirely by measuring changes in the optical fields from the direct binding of the target onto the surface. The two most commercially successful optical biosensors developed by the Swedish Pharmacia Biotech and the British Affinity Biosensors (recently acquired by ThermoElectron, Inc), respectively, are based on non-labeled evanescent wave.

An important example of non-labeled detection is surface plasmon resonance (SPR)<sup>19</sup> where the incident optical field resonantly transfers energy to a surface plasmon (i.e. the allowed surface mode). The surface is coated with a thin layer of metal, and the binding of the target changes the effective index of refraction of the combined layers. The in-plane wave vector of the optical field is then scanned, and an intensity minimum is observed at the momentum and energy matching condition. Differential techniques<sup>20</sup> for SPR are quickly becoming standard; novel metal films for amplification<sup>21</sup> are also under development to increase sensitivity. SPR has not been readily applied to low concentration microbial populations to date, and its marketability is likely limited by its high user cost.

The technique investigated by SatCon under this program substantially increases sensitivity through the use of single-mode planar waveguides and precision interferometry to detect changes

in the effective index of refraction resulting from surface binding. This approach differs from other evanescent techniques (e.g. conventional SPR) through the detection of optical phase instead of intensity distributions. This approach is particularly attractive because of its potential for extremely high sensitivity from large photonic amplification, its inherently differential nature, simplicity in implementation (i.e. integrated optics), and high volume/low cost manufacturing. However, interferometry has tended to be less popular because of the optical sophistication required for its development.

### Evanescent Wave Surface Detection.

The basic working principle behind single-mode interferometric surface detection as applied to biosensing is shown in Figure 1-2. Light is guided through a thin-film optic having highly specific receptors immobilized to the surface. The optic is designed to support a single spatial mode so that the intensity distribution of the light remains constant. When a target pathogen binds to a receptor, its physical presence causes a change in the local index of refraction. The evanescent field of the guided light wave senses this change modifying the effective refractive index of the optic causing a shift in the optical phase.

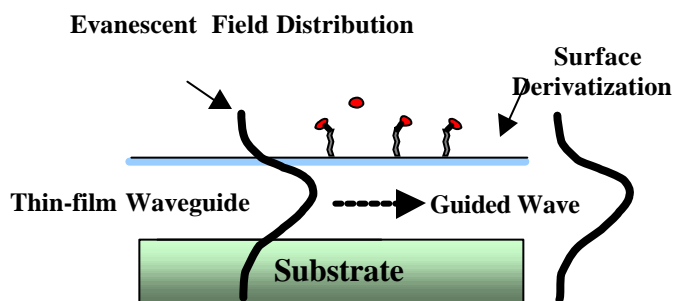


**Figure 1-2:** Schematic diagram of evanescent wave detection. Coherent light is constrained to propagate via a single spatial mode when guided through a thin-film. Interaction of the light with surface binding events results in a well-defined shift in the phase of the light wave.

Innovations. The area we have identified as a major obstacle to the application of sensitive waveguide detection systems is the transducer stability and optical phase detection. Our significant design advance comes from a doubly differential interferometric waveguide design implemented in combination with high-speed, high-sensitivity optical phase detection to solve the problem of time-dependent ambient fluctuations. Optical phase will be recovered at the level of  $\delta\phi \sim 10^{-7}$  cycles/ $\sqrt{\text{Hz}}$  – a factor of up to 1000 times better than competing optical biosensor detectors.

**Interferometer Design.** The SatCon approach exploits the difference in response of the effective refractive index to surface binding from two orthogonal polarization modes propagating simultaneously combining it with a two-arm Mach-Zehnder configuration to form a doubly differential interferometer.

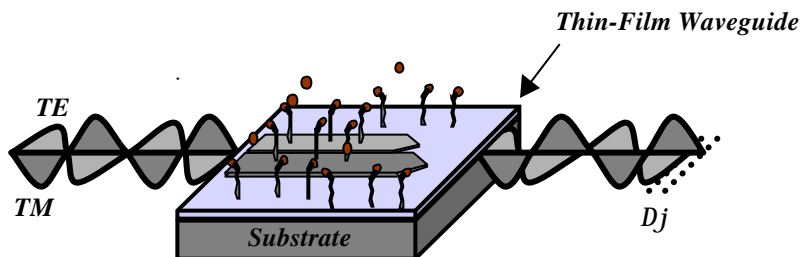


**Figure 1-3:** Illustration of phase shift between TE (light gray) and TM (dark gray) components of guided wave induced by surface binding events for one arm of the interferometer.

Since the length of the evanescent tails above the surface of the two modes differ considerably, their respective phase shifts form the basis for a differential measure of the change in the

effective index. Figure 1-3, expanding on the basic phenomena described by Figure 2, illustrates the consequential shift in relative phase between the two polarization modes caused by surface binding for a single interferometric arm.

Although a coaxial single arm (differential polarization) design, as first demonstrated by Lukosz<sup>2</sup>, very effectively provides immunity to inherent thermal and mechanical perturbations, the differing evanescent tails of TM<sub>0</sub> and TE<sub>0</sub> are affected by other surface effects such as the temperature dependence on the refractive index of the contact solution.

These shortcomings are addressed by the introduction of a second optical branch, itself also coaxial, used as an environmental and biological reference to subtract optically, extraneous temperature effects and non-specific binding.

The interferometer is implemented on a planar waveguide and thus the two arms are not only constructed from identical material but are also located in extremely close proximity (hundreds of microns) to each other ensuring highly effective differential performance. A schematic diagram of the doubly differential interferometer design is shown in Figure 1-4.

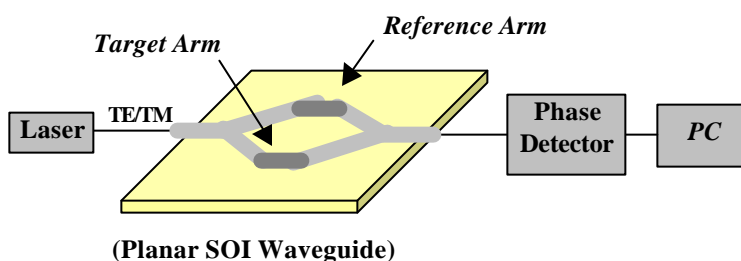


**Figure 1-4.** Doubly Differential Interferometer with Crystalline Silicon (SOI) Waveguides and a Precision Phasemeter for the detection of microbial pathogens.

**Work by Others.** Several earlier and on-going efforts to develop an interferometric detector for biosensing have resulted in integrated optical (IO) devices. Coaxial polarization interferometers (interference of the two orthogonal polarization states) have been developed by the Swiss group headed by Lukosz<sup>2,22</sup> and subsequently configured for Zeeman interferometry at Los Alamos with the University of Arizona.<sup>23,24</sup> Mach-Zehnder IO interferometers have been developed by Hartman<sup>1</sup> at the Georgia Tech Research Center with Photonic Sensor Systems (their commercial spin-off) and by Helmers et al.<sup>25</sup> A large ongoing international research effort at the Optoelectronics Research Centre, University of Southampton, England<sup>26,27</sup> is presently developing a novel IO multi-branch Mach-Zehnder interferometer design for unambiguous fringe counting. Unfortunately, all of these efforts are compromised by phase noise from thermal, mechanical, or environmental instabilities and lossy optical materials at a typical detection level of 10<sup>-3</sup> cycles or worse. Thus, the SatCon approach promises significant advancement over current state-of-the-art transducer technology.

<sup>1</sup> DeMarco, D.R., E.W. Saaski, D.A. McRae, and D.V. Lim, 'Rapid Detection of Escherichia coli 0157:H7 in Ground Beef Using a Fiber-Optic Biosensor', *Journal of Food Protection*, **62** (7), 1999, 711-716.

<sup>2</sup> Weetall, H.H., "Chemical sensors and biosensors, update, what, where, when, and how", *Biosensors & Bioelectronics*, **14**, 237-242, 1999.

<sup>3</sup> Feng, P., "Current Technologies Used in Rapid Methods for Detecting Foodborne Pathogens and Their Toxins", presented at the FDA/NSF/USDA jointly sponsored *Workshop on Enhancing Food Safety through the Use of Sensors*, September 24, 1997.

- <sup>4</sup> Su, Y.-C. and Wong, A.C.L. 1997. Current perspectives on detection of Staphylococcal enterotoxins. *J. Food Prot.*, 60 (2):195-202.
- <sup>5</sup> Feng, P., "Emergence of Rapid Methods for Identifying Microbial Pathogens in Foods", *J. AOAC Int.*, **79**: 809-812, 1996.
- <sup>6</sup> DeMarco, D.R., E.W. Saaski, D.A. McRae, and D.V. Lim, 'Rapid Detection of Escherichia coli 0157:H7 in Ground Beef Using a Fiber-Optic Biosensor', *Journal of Food Protection*, **62** (7), 1999, 711-716.
- <sup>7</sup> Ye, J., Pivarnik, P.E., Senecal, A.G., and Rand, A.G. 1999. Rapid detection of *Staphylococcus aureus* using a membrane fiber optic biosensor, , in "Pathogen Detection and Remediation for Safe Eating", Yud-Ren Chen, Editor. *Proceedings of SPIE*, 3544: 2-9.
- <sup>8</sup> Pivarnik, P.E., Cao, H., Letcher, S., Pierson, A. and Rand, A.G. 1999. Magnetic focusing immunosensor for the detection of Salmonella typhimurium in foods, in "Pathogen Detection and Remediation for Safe Eating", Yud-Ren Chen, Editor. *Proceedings of SPIE*, 3544: 41-49.
- <sup>9</sup> Rasooly, L. and Rasooly, A. 1999. Real time biosensor analysis of Staphylococcal enterotoxin A in food. *Int. J. Food Microbiol.*, 49:119-127.
- <sup>10</sup> Weetall, H.H., "Chemical sensors and biosensors, update, what, where, when, and how", *Biosensors & Bioelectronics*, **14**, 237-242, 1999.
- <sup>11</sup> Abel, P.A., M. G. Weller, G.L. Duveneck, M. Ehrat, and H. M. Widmer, "Fiber-Optic Evanescent Wave Biosensor for the Detection of Oligonucleotides", *Anal. Chem.*, **68**, 2905-2912, 1996.
- <sup>12</sup> James, E.A., K. Schmelter, and F.S. Ligler, "Detection of Endotoxin Using an Evanescent Wave Biosensor", *Applied Biochemistry and Biotechnology*, 60, 189-202, 1996.
- <sup>13</sup> White, J. J.S. Kauer, T.A. Dickenson, and D.R. Walt, "Rapid Analyte Recognition in a Device Based on Optical Sensors and the Olfactory System", *Anal. Chem.*, **68**, 2191-2202, 1996.
- <sup>14</sup> Walt, D.R., V. Agayn, K. Bronk, S. Barnard, "Fluorescent Optical Sensors", *Applied Biochemistry and Biotechnology*, **41**, 129-139, 1993.
- <sup>15</sup> Bluestien, B.I., I.M. Walczak, and S. Chen, "Fiber-Optic Evanscent Wave Immunosensors for Medical Diagnostics", *Tibtech*, **8**, 161-168, 1990.
- <sup>16</sup> Zhou, C., P. Pivarnik, S. Anjou, A. Rand, and S. Letcher, "A Compact Fiber-Optic Immunosensor for Salmonella Based on Evanescent Wave Excitation", *Sensors and Actuators B (Chemical)*, 1997.
- <sup>17</sup> Rockhold, , S.A., R.D. Quinn, R.A. Van Wegenen, J.D. Andrade, M. Reichert, "Total Internal Reflection Fluorescence (TIRF) as a quantitative probe of protein adsorption." *J. Elect. Chem.* Vol. 150, pp 261-275; 1983.
- <sup>18</sup> Axelrod, D., T.P. Barghardt, N.L. Thompson, "Total Internal Reflection Fluorescence," *Ann. Rev. Biophys. Bioeng.*, Vol. 13 pp. 747-768; 1984.
- <sup>19</sup> Hutchinson, , A.M., "Evanescent Wave Biosensors", *Molecular Biotechnology*, **3**, 47-54, 1995.
- <sup>20</sup> O'Brien, , M.J., S.R.J. Brueck, V.H. Perez-Luna, L.M. Tender, G.P. Lopez, " SPR biosensors: simultaneously removing thermal and bulk-composition effects", *Biosensors & Bioelectronics*, **14**, 145-154, 1999.
- <sup>21</sup> Lyon, L. A., Musick, M. D., Natan, M. J., "Colloidal Au-Enhanced Surface Plasmon Resonance Immunosensing", *Anal. Chem.*, **70**, (24); 5177-5183, 1998
- <sup>22</sup> Lukosz, W., *Sensors and Actuators B*, **29**, 37-50, 1995
- <sup>23</sup> Ayras, P. et al., "Thin Film Chemical Sensors with Waveguide Zeeman Interferometry", *Pure and Applied Optics (to be published)*, 1998.
- <sup>24</sup> Grace, K.M., K. Shrouf, S. Honkanen, P. Ayras, P. Katila, M. Leppihalme, R.G. Johnston, X. Yang, B. Swanson, and N. Peyghambarian, "Waveguide Zeeman Interferometry for Thin Film Chemical Sensors", *Electronics Let.*, **33**, No 19, 1651-1653, 11 Sept. 1997.
- <sup>25</sup> Helmers, et al., *Applied Optics*, **35**, No. 4, 676, 1996.
- <sup>26</sup> Luff, B.J., S. Wilkinson, J. Piehler, U. Hollenbach, J. Ingenhoff, and N. Fabricus, "Integrated Optical Mach-Zehnder Biosensor", *J. Lightwave Technol.*, **16**, No. 4, 563-592, April 1998
- <sup>27</sup> Drapp, B., J. Piehler, A. Brecht, G. Gauglitz, B.J. Luff, J.S. Wilkinson, and J. Ingenhoff, "Integrated Optical Mach-Zehnder Interferometers as Simazine Immunoprobes", *Sensors and Actuators B*, **38-39**, 277-282, 1997.

## Chapter 2 : Programmatics

**Original Program Plan.** The original work plan to accomplish the objectives set forth in the previous section naturally decomposed into five basic tasks: 1.) optical development, 2.) fluidics development, 3.) surface derivatization, 4.) laboratory characterization, and 5.) food testing. The majority of the hardware development was proposed to be completed by the end of month 12 while months 13-24 were devoted to characterizing the platform in a wide range of microbiological environments and refining the platform as needed. At the end of year 2 the feasibility of the integrated platform to detect and identify viable food-borne pathogens was to be demonstrated in a food testing program.

Months 1-12 consisted of the laboratory development of each of the component subsystems. The development of a preliminary disposable microfluidic cartridge demonstrating all of the specified fluidic operations was planned. The fabrication and evaluation of several different waveguide designs incorporating grating coupling was planned. An optical design was to be specified and constructed, and a miniature optical phasemeter was to be produced. Protocol for patterned receptor immobilization was to be demonstrated and waveguides coated with receptors were to be produced. At the end of year one all hardware was to be integrated into a portable system that can be easily transported to outside laboratories for testing and demonstration.

Months 13-24 were devoted primarily to the biological characterization of the hardware first at SatCon, then at URI. During the last six months of the program an in-depth food testing program would be conducted to evaluate the platform's ability to detect both *E. coli* and *S. aureus* in various food substances.

**Modifications to the Plan.** The original Phase II proposal was submitted four months into the Phase I effort. After completion of the Phase I and Phase I Option efforts, new insights were gained into the program goals. Three major insights were realized:

- 1.) Cell capture was a key problem for biosensors and significant resources should be put into this unanticipated effort,
- 2.) The development of the individual components would require more time and resources than originally envisioned. Therefore the Phase II plan was modified after discussions with Natick to consist exclusively of a breadboard setup with discrete stand-alone subsystems because its miniaturization into a functional disposable coupon was beyond the resources available for this Phase II effort.
- 3.) The development of pure silicon waveguides at 1.3  $\mu\text{m}$ , as originally proposed, was riskier than anticipated, and it was therefore determined that the highest probability of success was to pursue the development of  $\text{Si}_3\text{N}_4$  waveguides using visible light. This was because of the ease of working with visible light in contrast to the NIR spectrum and risks associated with the development of pure silicon waveguides during the Phase I Option at Boston University.

These planning changes were discussed with Dr. Andre Senecal, technical monitor at Natick, and considered reasonable.

Program Acceleration. In the spirit of the Small Business Innovative Research Program, SatCon Technology Corporation made the following changes to its biosensing program as a commitment to bringing this technology to the marketplace.

- Laboratory Facilities. SatCon invested in the construction of a new dedicated biosensing laboratory providing microbiology, chemistry, and optic capabilities. The newly furnished 300 square foot laboratory space is divided into two separate rooms: i.) a laboratory area dedicated to microbiological work and ii.) an optics laboratory for working in a darkened environment.

The microbiological laboratory contains over 20 feet of working bench space and has all of the standard equipment and reagents for culturing and quantifying microbial populations. Laboratory equipment includes an autoclave, incubator, an orbital shaker incubator, refrigerator, precision balance, and UV/Visible spectrophotometer for quantification. The laboratory is also equipped with a fume hood and has a proper arrangement for the disposal of bio-hazardous and chemical wastes.

The optical laboratory facilities include a 3' x 6' vibration isolated optical table and various high- performance optical breadboards for mounting experiments. Laboratory equipment available for experiments includes an ultra-stabilized HeNe laser and a 1.3  $\mu\text{m}$  TEC diode laser, InGaAs and Si detectors, broadband power meter, and standard components including lens sets, ND filters, mounts, translation stages, mirrors, and beamsplitters.

- Accelerated Technology Demonstration. In order to speed up its commercial development a technology Proof-of-Principle" demonstration was planned for a 9-month time frame. A time line for this plan is shown in Figure 2-1.

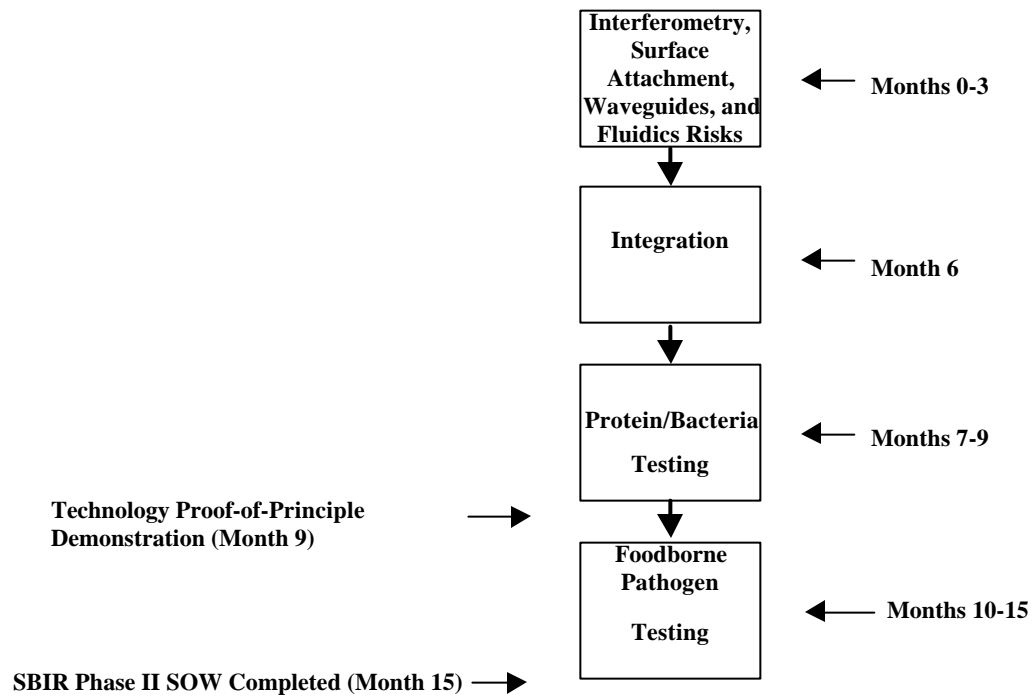


**Figure 2-1.** Timeline for 9-month technology demonstration.

- **Cost Sharing.** Significant funding well in excess of the Phase II award was required to accomplish this effort. In recognition of this SatCon Technology Corporation cost-shared this effort. Specifically, the Phase II award was used 100% for direct labor and materials. All other expenses were covered by SatCon for an estimated amount of \$588,436 increasing the total value of the program from \$719,082 to an equivalent SBIR award equal to \$1,307,518, not including the expense of the laboratory.

**Schedule.** The original schedule included in the Phase II proposal is shown with black text and with gray shading in Figure 2-2. The actual schedule progress is overlaid on top of the original proposal in blue to illuminate any variations from and additions to the original schedule. The yellow vertical strip indicates the point at which the program funding (both SatCon and Army funding) was exhausted and the program was ended.

## Integrated Schedule based on Phase II Proposal

Tasks	Months	1-2	3-4	5-6	7-8	9-10	11-12	13-14	15-16	17-18	19-20	21-22	23-24
<b>Optical Development</b>													
Completion of SOI													
Optical System Development													
Phasemeter Development													
Interferometer Development													
Grating Coupled Waveguide Fabrication													
Design													
Fabrication (Sarnoff)													
Optical Switch													
Intermediate Data (Prism Coupled Waveguides)													
<b>Fluidic Development</b>													
Automated Flow System													
Disposable Cartridge/Flow Cell Design													
Design Microfluidic Flow Cell													
Fabrication													
Laboratory Characterization													
<b>Non Specific Binding</b>													
High Pass Filter Design and Fabrication													
High Pass Filter Lab Characterization													
Optical Desensitization													
Microfluidic embedded subsystem													
<b>Biomolecule Immobilization</b>													
Protein A covalent attachment chemistry													
Optimization													
Patterning													
<b>Receptor Platform Development</b>													
Integration													
Laboratory Characterization													
Delivery to URI													
<b>Food Testing</b>													
Non-Specific Binding													
Model Systems													
Sampling Procedures													
E. coli Testing													
Salmonella Testing													

**Description of the Team: Roles and Responsibilities.** The interdisciplinary nature of biosensing requires an unusually broad set of expertise for successful development. A major strength of the SatCon effort is the assemblage of a world-class team having the depth and experience to innovate and develop the needed technology all located within a few miles radius. The proximity of all collaborators with the exception of Micronics allowed for bi-weekly group meetings promoting easy communication and visitation.

*Original Team.* The overall program and technical management of the program was performed by Dr. Ronald Rieder. Dr. Rieder was also responsible for the development of the interferometer and all associated optics and detectors. The Laibinis group in the Dept. of Chemical Engineering at MIT was tasked with the surface engineering for the immobilization of receptors. Dr. Hitesh Jindal was hired by SatCon as fulltime senior microbiologist/biochemist in support of this program. Micronics, Inc of Redmond, WA was tasked with the development of disposable microfluidic cartridges for diffusion-based filtering. Dr. Jianming Ye in the Department of Food Science and Nutrition at the University of Rhode Island was responsible for the characterization of the SatCon biosensor with different food and pathogen system. Drs. Goldberg and Unlu of the Photonics Center at Boston University were responsible for the development of the waveguides essential to the success of this program. A graphic showing the organization of the team is shown in Figure 2-4.

As the program developed, additional subcontractors were used. VTECH Engineering (Andover, MA) was used to assist with the electrical engineering of the phase detector. Standard MEMS (Burlington, MA), Sarnoff Corporation (Princeton, NJ), and Optical Switch (Bedford, MA) were all involved in the fabrication of the waveguide devices. Finally, Drs. Andre Senecal and Phillip Pivarnic at the U.S. Army Soldier and Biological Chemical Command, Soldier System Command, Natick, MA agreed to complete the work intended for the URI group after their default because of the dissolution of the URI research group.

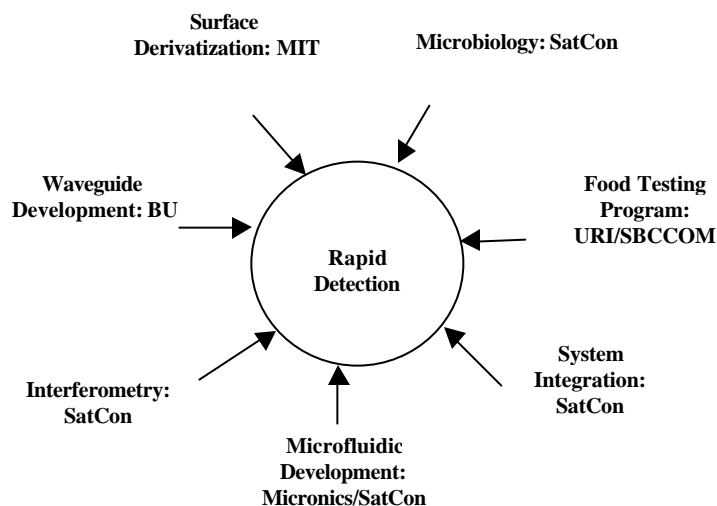


**Figure 2-4.** Organization Chart

A summary of the principals conducting the work performed during this Phase II effort:

- Ron Rieder, Ph.D., SatCon Technology Corp. (*Precision Interferometry/Phase Detection*)
- Prof. Paul Laibinis, Dept. Chemical Engineering, M.I.T. (*Surface Derivatization*)
- Hitesh Jindal, Ph.D., SatCon (*Microbiology*)
- Bernhard Weigl, Ph.D., Micronics, Inc, Redmond, WA (*Microfluidics*)
- Andre Senecal, Ph.D. and Phillip Pivarnic, Ph.D., U.S. Army Soldier and Biological Chemical Command, Soldier System Command, Natick, MA (*Food Testing*).
- Prof. Bennett Goldberg, Physics Dept., Boston University (*Waveguide and Optical Design*)
- Prof. Selim Unlu, Dept of Elec. and Comp. Eng., Boston University (*Waveguide Design and Fabrication*)

## Chapter 3 : Optical Design

**Phase II Transducer Design.** The objective of the optical setup is to couple light of both polarizations in (and out) of a single-mode waveguide and image it onto a detector array. The current waveguide design relies on a single uniformly spaced grating for coupling both polarizations. The coupling angle depends on the grating period and the effective indices for each polarization. Thus, the coupling angles for each polarization are different and the supporting optics must be spatially separated into two beams<sup>1</sup>. This is accomplished by introducing the birefringent material calcite into the beam. A schematic of the optical setup is shown below in Figure 3-1.

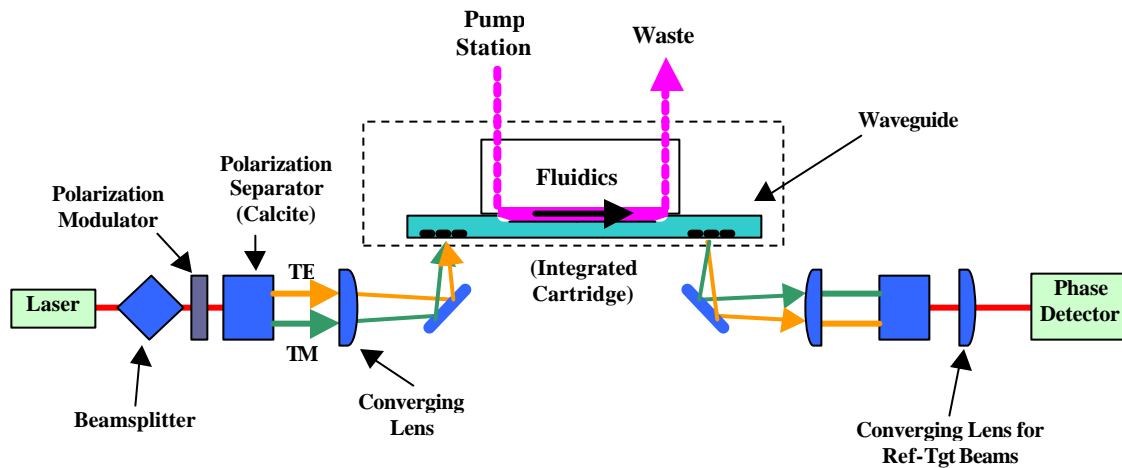


**Figure 3-1.** Schematic of experimental setup used for Doubly Differential Interferometer testing with GTRI waveguide. The side view is shown only to illustrate the paths of the different polarizations. The laser is split into two lateral beams prior to the polarization modulator to form the reference and target channels. Thus, four optical paths (2 polarizations x two channels) were aligned for this optical demonstration.

**Design Details.** A HeNe (633 nm) laser beam was passed through a cube beamsplitter to divide the light into two beams for the reference and target arms (not shown) followed by a polarization modulator (Displaytech Inc.) that switches between polarizations sequentially exciting the TE and TM guided modes within the waveguide. It was necessary to modulate the polarizations after the beamsplitter because the coating properties of the beamsplitter were optimized for a single polarization. Each beam then passed through a calcite optic that separated the light according to polarization. The beams were then focused independently to their respective incident grating coupling angles and launched into the waveguide. The output optics were similar with the exception of the combination of a converging and diverging lens to combine the reference and the target beams onto the detector forming a fringe pattern matched to the pitch of the pixel array of the phase detector.

**Phase Detector and Data Acquisition** The new phasemeter and data acquisition system was designed and constructed based around a cooled integrating linear imaging device manufactured

<sup>1</sup> This complication will be overcome in future designs by designing more complicated gratings that will couple light of both polarizations at the same angle. This will simplify the supporting optics significantly by requiring only a single beam containing both polarization and make for a more compact system.

by Hamamatsu (Model C5964-0800). This detector has 256 pixels each  $50\mu\text{m} \times 2500\mu\text{m}$  in size and is cooled to  $0^\circ\text{C}$  by a built-in thermo-electric cooler for stability. The detector signals are converted to a digital signal by a National Instruments (Model 6502E) 16-bit data acquisition card. The data are now processed entirely by a high-speed PC containing a 733 MHz processor. The program is user friendly and includes provisions for data analysis and system diagnostic testing in addition to acquiring measurement data.

A small subcontract was let to VTech Engineering (Andover, MA) to assist with the connection of the detector to the National Instrument data acquisition board. The completion of the phasemeter was originally scheduled for month 2 and was delayed until month 6 because of shipping problems with the detector during transit from Japan, ultimately requiring the delivery of a second detector.

The data acquisition program is highly versatile containing a full set of statistical and Fourier transform tools for a full analysis of the data. A picture of the user interface is shown in Figure 3-2.

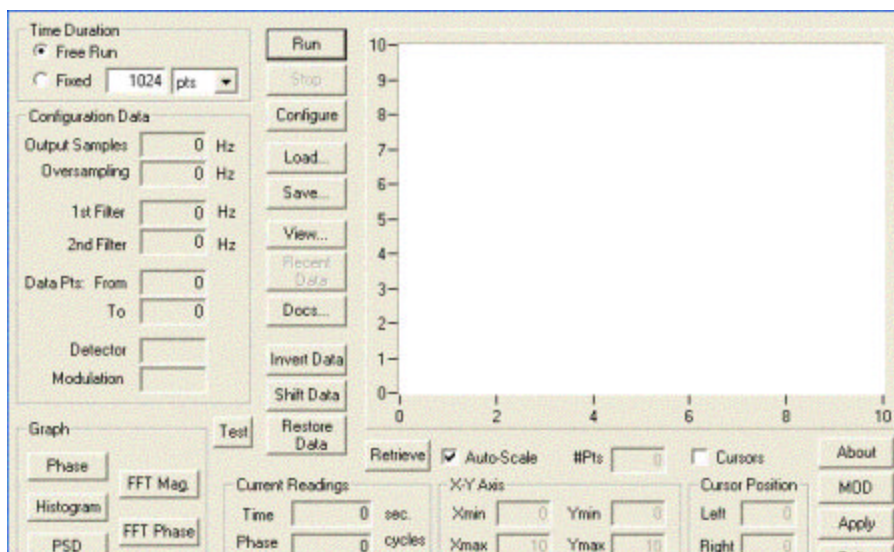


**Figure 3-2.** User interface for optical phase detector (OPD) data acquisition program.

The phase detection system used during Phase I results was limited but very useful in obtaining preliminary results. It was constructed from available in-house components consisting of a dedicated processor board performing both data acquisition and analysis combined with a linear photodiode array detector. However, the precision of the data resulting from this phasemeter was limited by the sampling rate of the processor board thus processing only a fraction of the light incident on the detector. The new system sports the following improvements:

- The integrating detector continuously stores all charge generated by the incident light signal (except during readout) utilizing the majority of the available information and is a cooled detector for low noise detection.

- Each detector pixel is now individually recorded providing additional diagnostic information for alignment and allowing for flexible algorithm development if needed.
- The data analysis is now performed exclusively in software allowing for a more accommodating development platform.

**Optical Signal Processing Test Results.** As a first test of the optical signal processing and data acquisition system, a simple optical system was set up to measure intensity. The results of this test demonstrated the effectiveness of the optical signal processing technique showing an increase in S/N by over two orders of magnitude. This test was performed by constructing a light shutter from two crossed polarizers and switching the polarization of a single light beam between the two states using the Displaytech polarization modulator. A schematic of the experimental setup is shown in Figure 3-3.

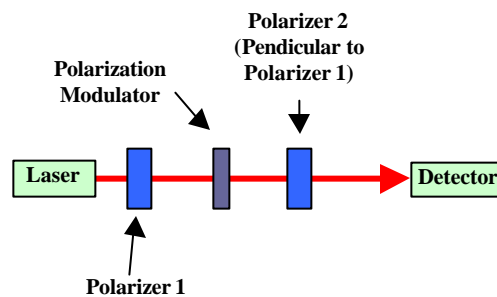


**Figure 3-3.** Schematic of the optical shutter for producing intensity modulations

Two data sets were obtained where the polarization modulator was turned off and on, respectively, for comparison. Both data sets were analyzed with the same low pass filter (0.5 Hz) but the latter data set employs the common-mode rejection technique. The results of these experiments are shown below as histograms of the time series data. Figure 3-4 (top) shows a symmetric distribution using conventional filtering techniques only and having a standard deviation of  $\sigma = 69.1$  mV. The plot on the bottom shows data with the same setup using common-mode rejection; its associated noise is  $\sigma = 0.64$  mV – a factor of 110 reduction in noise. (Please note that the x-axis scales for these two plots differ by a factor of 100.)

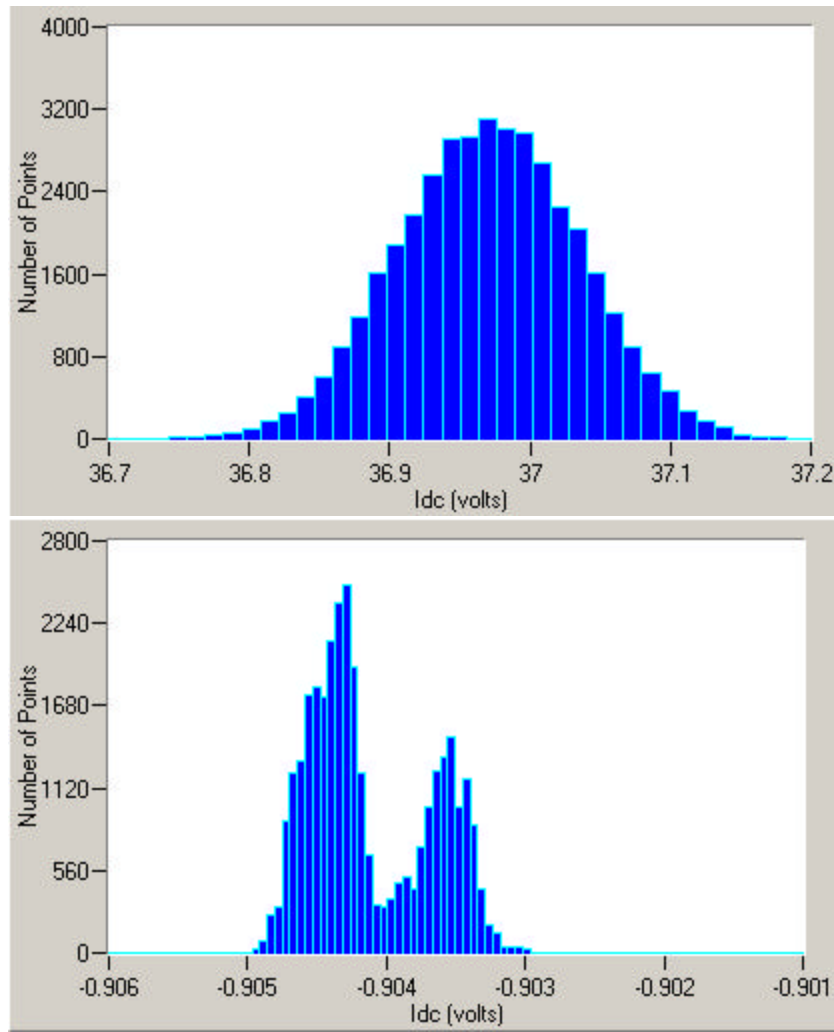


**Figure 3-4: Top:** Histogram of time series data for a conventionally filtered signal. A 0.5 Hz low pass filter was applied leading to a noise threshold of  $\sigma = 69.1$  mV. **Bottom:** Same experimental setup but employing common-mode rejection technique. The signal noise is now reduced by a factor of  $\sim 110$  to  $\sigma = 0.64$  mV. The double peak is the result of an unexplained discrete jump in laser intensity.

*Phase Measurements.* An experiment was then setup to demonstrate the optical signal processing with interferometric data. A Young’s interferometer was configured as shown in Figure 3-5 and the polarization modulator was inserted into the beam to switch between the two polarizations. The two beams were mixed to produce a fringe pattern onto the phase detector that was analyzed with the new data acquisition program described in the previous section.

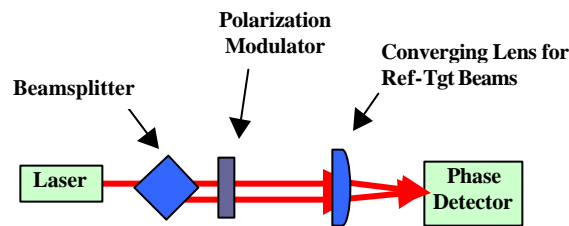


**Figure 3-5.** Schematic of a simple Young’s interferometer for modulated polarization measurement using Doubly Differential optical signal processing technique.

Figure 3-6 shows 650 seconds of baseline data collected to establish the stability of the free space interferometer. The standard deviation for these data is  $\sigma = 1.7 \times 10^{-5}$  cycles of phase. These measurements were made with free space optics containing several open paths making it unnecessarily susceptible to thermal and mechanical perturbations. Nevertheless, the result was less than a factor of 6 from the design goal of  $10^{-6}$  cycles which would correspond to an index change of  $\Delta n = 10^{-9}$ . While this result demonstrates promise, please note that the addition of a waveguide has the potential to degrade the result because of the additional degrees of freedom.

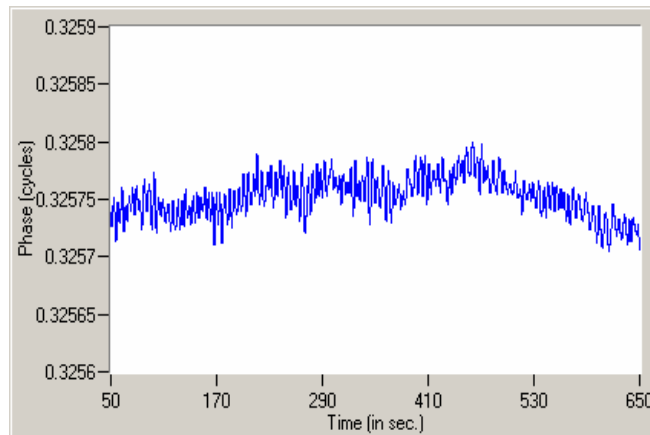


**Figure 3-6.** Doubly differential interferometric data collected with a simple Young's interferometer and a polarization modulator.

**Prototype Transducer Optical Design.** The SatCon Doubly Differential Interferometer (DDI) is based on the coupling of both light polarizations into a single-mode planar waveguide (and their subsequent response difference). For a fixed grating period each polarization couples into the guiding layer at a different angle requiring a more complicated optical configuration to accommodate the separated optical paths shown previously in Figure 3-1.

The configuration shown in Figure 3-1 is fine for initial testing however a better design that is cheaper, more compact, and more sensitive is possible. The transducer configuration can be simplified from a total of 12 to 7 components by collapsing the two polarized beams into a single beam as shown below. This configuration is identical to that of a simple Mach-Zehnder interferometer with the addition of a polarization switch.

This simplification is accomplished at the expense of a more complicated I/O grating coupler design for the waveguide. One possibility is a matrix of two gratings with different periods, one for TE and one for TM.

*Conceptual Design.* A concept for the transducer portion is pictured below in Figure 3-7. It is desirable to keep the thermal and mechanical mass no larger than necessary to minimize the effects from temperature and vibration. It is desirable that all components be formed into an integrated monolithic component. This could be made out of plastic depending on the sensitivity requirements.

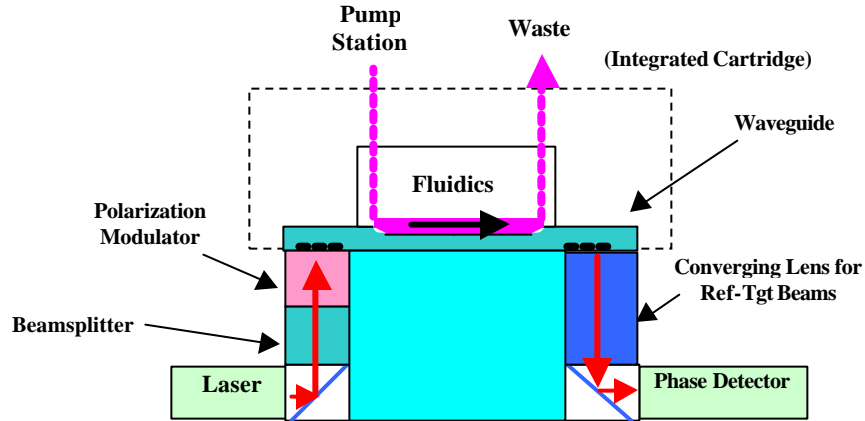


**Figure 3-7.** Schematic of concept prototype for optical transducer. Polarizations are contained in a single beam reducing the total number of components from 13 to 8.

**Preliminary Double Differential Measurements.** Shortly after receiving sample waveguides from GTRI (Chapter 10, Waveguides and Flow Cells) an attempt was made to use these devices in the doubly differential configuration. A polarization modulator was inserted into the beam path after the beamsplitter to switch between the two polarizations, and the respective polarizations were spatially separated and independently coupled into the waveguide as described by Figure 3-1.

The objective of these experiments was to determine the utility of the GTRI waveguides for use in ‘Doubly Differential’ measurements. The GTRI waveguides were optimized for only a single polarization - the TM mode, however adequate throughput was obtained for TE mode excitation. More importantly the grating and cuvette structures were confined to a 1 mm width and scattering off the edges of these structures significantly distorted the fringe pattern degrading the results. This problem was further aggravated by alignment errors from the large number of optical components used in the demonstration. Please note that the results presented in Figure 3-8 demonstrate the waveguide’s operation in air.

Approximately one hour of data were collected. Thermal equilibration occurred during the initial 25 minutes followed by stabilization. This is not surprising because of the large number of opto-mechanical fixtures involved in these initial experiments. An expanded view of the last 1000 seconds of data are shown in Figure 3-8 right. The calculated standard deviation for these data is  $\sigma_{\phi} \sim 9.8 \times 10^{-5}$  cycles – a factor of 60 enhancement compared with the ‘singly differential’ data shown in Figure 10-7.

While these data are very encouraging in meeting the ultimate goal of  $10^{-6}$  cycles, care must be taken in interpreting these data because of the marginal S/N of the actual fringe pattern from which these data are obtained. It is the expectation that the SatCon waveguide geometry, once fabricated, will provide significantly improved fringe patterns from the reduction in scattering, ease in alignment and thus experiment execution, and high confidence measurements.

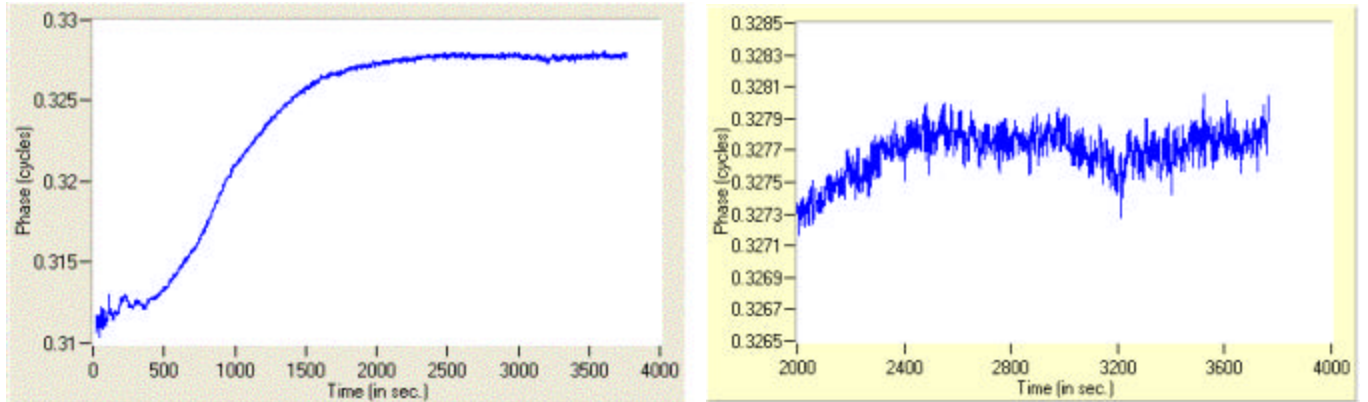


**Figure 3-8.** Preliminary Double Differential Interferometer Measurements. Doubly differential interferometer measurements were obtained using a waveguide provided by GTRI. In this experiment the waveguide was exposed to air and no flow cell was introduced into the setup. The S/N of the interference pattern on which these data rely was compromised by the significant scattering of the propagating guided TM and TE light. A baseline of  $\sigma_\phi \sim 9.8 \times 10^{-5}$  cycles was established after thermal settling.

**Summary.** The optical setup supporting the doubly differential interferometer was constructed. A phasemeter using a cooled detector was built along with a data acquisition system having analysis capabilities. The polarization based common-mode rejection technique was tested confirming the enhanced sensitivity of the optical signal processing technique. The initial use of the same I/O grating for both polarization modes required the independent alignment of the two polarizations. This optical setup can be collapsed into a simple configuration using a single coaxial beam with the development of multiplexed gratings. Finally, waveguide provided by GTRI were used to obtain doubly differential. These measurements were compromised by severe light scattering off of the edges of the narrow grating and cuvette structures. We anticipate that this problem should be minimized by the larger structures in the SatCon waveguide design.

## Chapter 4 : Waveguide Development

**Overview** A key task in the development of this biosensor remains the design and fabrication of the single-mode  $\text{Si}_3\text{N}_4$  waveguides that support both TE and TM excitation modes. The Boston University group, under the direction of Professors Bennett Goldberg and Selim Unlu, were tasked with the design and general development of these waveguides. Three design cycles and two fabrication cycles for these waveguides were undertaken. As with prior attempts, the last fabrication cycle, subcontracted to Optical Switch, Corp, was discontinued due to delays, and consequently the SatCon waveguide design has not been successfully fabricated to date. Intermediate laboratory experiments were also planned using prism-coupled waveguides fabricated by the BU group. As is described below, this task was abandoned after no visible success was reported. However, waveguides were eventually provided by Dr. Daniel. P. Campbell at GTRI and were used to provide the first laboratory results in a single differential mode.

In addition to the  $\text{Si}_3\text{N}_4$  work, the Silicon-on Insulator work remaining from the Phase I program was continued as part of the Phase II effort, but again had to be abandoned because of no visible results reported by the BU group.

**Completion of Silicon-on-Insulator (SOI) Measurements.** Refraction measurements on the SOI waveguides produced during the Phase I effort were continued using the earlier setup at Boston University. These waveguides were designed by the BU group, however, they were unable to implement a working device by the end of the Phase I effort. Although the thrust of the optical design was changed from SOI to  $\text{Si}_3\text{N}_4$ , it was the intent of SatCon to complete the characterization of the SOI waveguides with the assistance of the BU group. To this end:

1. The BU setup was adapted to accommodate the introduction of the fiber optics needed for these experiments.
2. Two of three polished SOI waveguides were attached to glass mounting blocks designed to support the waveguide. Unfortunately, both waveguides fractured during removal from the gluing jig due to inadequately cleaned gluing surfaces that prohibited the uniform adhesion of the silicon surface to the glass. The third and final polished SOI waveguide was successfully glued to the mounting block and prepared for final measurements.

Regrettably, Boston University reported significant difficulties guiding light through the SOI waveguide. No explanation for the difficulty was found. Because this experiment tied up key equipment that was needed for other optics development tasks and for testing with prism-coupled waveguides, SatCon was forced to abandon this task to focus on obtaining intermediate data with prism-coupled waveguides.

**Design of Single-Mode Waveguides.** The design report submitted by the BU group is attached at the end of this chapter as Appendix 4-C along with the original design specifications. Numerous simulations were performed, as described in detail within the report, examining the sensitivity of the evanescent field distributions and the coupling of the grating. In short, a design was created that permitted the coupling of light in and out of the waveguide exclusively with a

1<sup>st</sup> order diffraction grating. This is desirable because all of the guided light is coupled into a single order instead of distributing it among many orders providing for good throughput. However, this requires the use of gratings having sub-micron dimensioned periods.

The final dimensions of the design provided to Optical Switch are also found in Appendix 4-D. The most important modification besides changes to the overall size is the extension of the grating to cover the entire lateral dimension to add more flexibility in aligning the incident laser beam and to avoid scattering.

Waveguide Fabrication. A significant challenge for this effort was the fabrication of the grating-coupled waveguides.  $\text{Si}_3\text{N}_4$  and  $\text{SiO}_2$  are common materials for deposition available at every fabrication house, however, sub-micron spatial features such as the 411 nm grating period required for 1<sup>st</sup> order diffraction coupling and good throughput, are atypical. Standard commercial fabrication houses are limited in capability to critical dimensions of 1-2  $\mu\text{m}$  relying exclusively on the exposure of photolithographic masks. Additionally, many vendors contacted during 2001 were unwilling to accept any work outside of the telecommunications industry.

Eventually, a contract to fabricate the grating coupled waveguides was negotiated and let to Standard MEMS Inc. (Burlington, MA), a large and well established MEMS fabrication house. SMEMS would be responsible for all deposition tasks, gratings would be made at Cornell University using deep-UV exposure, and the overall coordination would be handled by SMEMS. Other grating fabrication methods were examined in addition to UV exposure and rejected: Direct e-beam writing (available at Penn State University) was prohibitively expensive and time consuming; Holographic exposure was proposed by the BU group but rejected because of lack of experience.

After much discussion, the group at SMEMS was instructed by their management to default on the SatCon contract and on other development work to focus on projects involving higher short-term income, to address their apparent financial crisis. Recognizing the predicament they had created for SatCon, SMEMS arranged for the contract to be transferred to the Sarnoff Corp (Princeton, NJ). Sarnoff does not have a relationship with Cornell and therefore gratings were to be fabricated in-house. Only a 1  $\mu\text{m}$  period was possible at Sarnoff and 2<sup>nd</sup> order diffraction had to be considered. The details of a new contract were negotiated and Sarnoff began work after a delay of many months.

Sarnoff Effort. Sarnoff was given the BU specification and began working it immediately. After solving compatibility issues between the quartz wafers and the Sarnoff equipment designed for silicon wafers, a fundamental problem was encountered. The waveguide specification (Table 4-1) called for LPCVD nitride and oxide deposition on quartz. However, the LPCVD process is not thermally compatible with the quartz, and cracking of the films was persistent caused by the difference in thermal expansion coefficients.

After further examination, the nitride deposition process was changed to PECVD and a lower index of refraction. It is noted that while LPCVD is compatible with pure silicon substrates, PECVD is the standard process used with quartz to ensure thermal compatibility. Additional modeling was performed by the BU group and their report is attached as Appendix 4-A at the end of this chapter. In summary, changes in sensitivity from the lower refractive index were expected to be insignificant, however, related decreases in throughput resulting from different grating coupling angles were expected to be as high as a factor of two. Coupling efficiencies

were eventually calculated to be 0.2 % and 0.06% for TE and TM respectively, for the 2<sup>nd</sup> order grating.

Waveguides were delivered by Sarnoff in early February that met the SatCon revised specification. A photograph of these devices is shown in Figure 4-1. These devices were evaluated in both BU's and SatCon laboratories and the values predicted by the BU model were confirmed. It was ultimately found that the low throughput of guided light was too difficult to conduct experiments with and a new design iteration was needed.



**Figure 4-1.** Photograph of Sarnoff Waveguide Devices.

*GTRI.* As an intermediate solution Dr. Daniel P. Campbell at GTRI was contacted and provided several working waveguides optimized for TM mode excitation. These waveguides were fabricated with PECVD nitride ( $n=1.85$ ,  $d=166\text{nm}$ ) on BK7 glass substrate. The grating was etched directly onto the substrate and had a period of 720 nm and a depth of 70 nm. These waveguides had I/O coupling efficiencies of approximately 3 percent, respectively, and were used to obtain the laboratory characterization data described in Chapter 10: Laboratory Characterization.

*Optical Switch Effort.* The fabrication of the SatCon-design grating-coupled waveguide was recently contracted to Optical Switch Corporation of Bedford, MA. These waveguides were designed to fit SatCon's flow cell form factor as shown in Figure 4-5 and to employ sub-micron dimensioned 1<sup>st</sup> order diffraction gratings relying on the design parameters of the demonstrated GTRI waveguides. The needed sub-micron structures for this design were to be created by directly exposing the photoresist using near-field holography. Optical Switch's processing capabilities are unique, as standard commercial fabrication houses are typically limited to critical dimensions of 1-2  $\mu\text{m}$  relying exclusively on the exposure of photolithographic masks. Under contract, Optical Switch performed supporting modeling calculations, designed and produced peripheral fabrication photomasks, and initiated in-house testing of their deposition process to determine if they could produce the target refractive index of the nitrite.

Based upon this work, several risks associated with the fabrication process were identified:

1. Optical Switch can manufacture  $\text{Si}_3\text{N}_4$  at indices from 1.90 - 1.95; but  $n = 1.85$  is not easily obtained,
2. Special techniques are required to obtain critical dimensions as small as 411 nm, and
3. The modeling results for the grating efficiency using GSOLVER do not support the strong coupling seen for the GTRI parameters suggesting that i.) the model is not reliable or ii.) the GTRI parameters are not reliable.

Additional modeling confirming the earlier results of the BU group was performed as well. Based upon this work two potential designs were possible:

- i.) Use the same design parameters claimed by Campbell<sup>1</sup> at GTRI to replicate already proven waveguides (in spite of the incompatibility of the GTRI parameters and the modeling results), or
- ii.) Implement the BU design parameters for a larger index nitride layer and smaller grating period.

A summary of these key parameters is given in Table 4-1.

Design Parameters	$\text{Si}_3\text{N}_4$ Refractive Index	DEPOSITION LAYER THICKNESS (nm)	GRATING PERIOD (nm)
GTRI	1.85	166	720
BU	1.95	177	411

**Table 4-1. Summary of Waveguide Design Parameters**

The inconsistencies and uncertainties mentioned above, the associated risk of once again fabricating unusable waveguides, and the fact that the efforts were over a month behind schedule all contributed to a decision to discontinue the Optical Switch contract rather than repeat the history of the prior contracts.

**Intermediate Data: Prism-Coupling.** The original schedule planned for intermediate data to be obtained while the more time-intensive development of the optical grating coupling waveguides was being pursued. This would allow integration of the different biological, optical, and fluidic components to gain experience and assess the performance of the biosensor. An excellent method for obtaining preliminary system refraction data is to couple the light into the waveguide using a prism. While the coupling method is very efficient, it requires the careful alignment of additional optical components that clutter the surface interfering with the placement of a flow cell.

*Prism Coupling Effort.* The Boston University group was tasked with the design and fabrication of prism-coupled waveguides for this intermediate data. In summary, a prototype waveguide accommodating both input and output prism coupling was designed and fabricated. The optical

---

<sup>1</sup> Daniel P. Campbell, Georgia Tech Research Institute, *Private Communication*, March 2002.

setup for obtaining intermediate biosensing data was designed, components purchased, and constructed at SatCon. However, after significant effort, the Boston University group reported continued difficulties with their fabrication process and ultimately severe difficulty guiding light through the  $\text{Si}_3\text{N}_4$  prism-coupled waveguides; Consequently, the experiments were unable to be conducted.

After a thorough review, SatCon requested that Boston University abandon this task to focus on their final task Optical Surface Desensitization in a timely manner and within budget (see Chapter 9). A detailed report of the BU effort is attached as Appendix B: Report on Prism Coupling Work October 14, 2001.

**Wafer Processing at Boston University.**  $\text{Si}_3\text{N}_4$  wafers were obtained by the Boston University group for additional processing at BU to support the essential laboratory effort, prism coupling to collect intermediate data, as well as the feasibility demonstration of the optical surface desensitization for the ‘optical’ suppression non-specific binding.

An order for the fabrication of several  $\text{Si}_3\text{N}_4$  wafers was placed to the Microfabrication Technology Laboratory (MTL) at MIT by the Boston University group. The guiding layer geometry and the corresponding thicknesses and refractive indices specified by BU were identical to those used in waveguides produced to obtain the Phase I data taken by SatCon. Specifically, the  $\text{Si}_3\text{N}_4$  guiding thickness was 166 nm with an index of 2.05. However, the one crucial difference was the  $\text{Si}_3\text{N}_4$  was fabricated by LPCVD deposition in the earlier wafers whereas the newly requested wafers were to be deposited by PECVD.

Figure 4-2 is a plot (courtesy of Sarnoff Corporation) of the optical loss per unit distance propagated from PECVD  $\text{Si}_3\text{N}_4$  layers having different refractive indices. For example, after propagating 7 mm the optical transmission is 96% ( $n=1.9$ ), 12.9% ( $n=2.0$ ), and 0.1% ( $n=2.1$ ). This is because the larger indices are obtained by an increase in the amount of silicon that absorbs light in the visible wavelength region. Thus, for a total propagation length of 1.2 cm or greater, as is the case for the SatCon experiments, nitride with an index of 2.05 would result in unusable waveguide devices having transmission less than 1%. This is consistent with the results from BU.

It is the opinion of SatCon that the failure of the prism coupling and optical desensitization experiments is the result of improperly specified  $\text{Si}_3\text{N}_4$  wafers rendering them opaque to visible light. This claim remains still unconfirmed by the BU group.

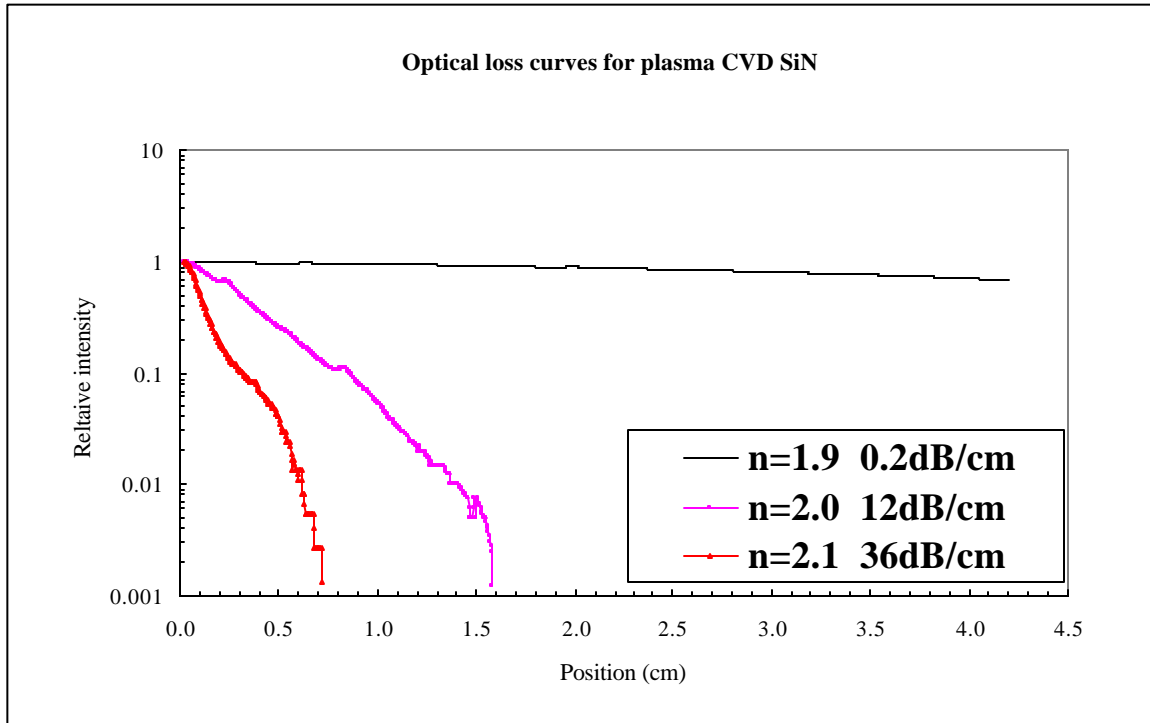


**Figure 4-2.** Optical Corporation)

**Su  
m  
ma  
ry.**  
A  
des  
ign  
for  
a  
gra  
tin  
g  
cou  
ple

d  $\text{Si}_3\text{N}_4$  optical waveguide capable of supporting TE and TM single-mode excitation was created. The sub-micron grating period required for 1<sup>st</sup> order coupling and high throughput put stringent specifications on the fabrication process limiting the number of possible vendors. Second-order gratings were successfully produced by Sarnoff Corp but had poor light throughput. A subcontract to fabricate the SatCon design was let to Optical Switch Corp., a leader in holographic lithography for sub-micron features, but it was ultimately discontinued due to delays and unresolved risks. To date, no usable waveguides of the SatCon design have been fabricated, thus preventing the integrated demonstration of the double-differential approach.

Intermediate ‘doubly differential’ data were planned using prism-coupled waveguides, however, these experiments were not able to be conducted because prism-coupled waveguide devices weren’t able to be successfully fabricated by the BU group. It is believed that this is the result of improperly specified test wafers by the BU group.

Grating coupled waveguides optimized for only TM propagation were provided by the Georgia Tech Research Institute to obtain intermediate data.

# **Appendix 4-A: Modeling for Sarnoff PECVD Fabrication**

## **Waveguide Sensitivity and Grating Coupling Angle Determination for Different Values of the Refractive Index of Silicon Nitride**

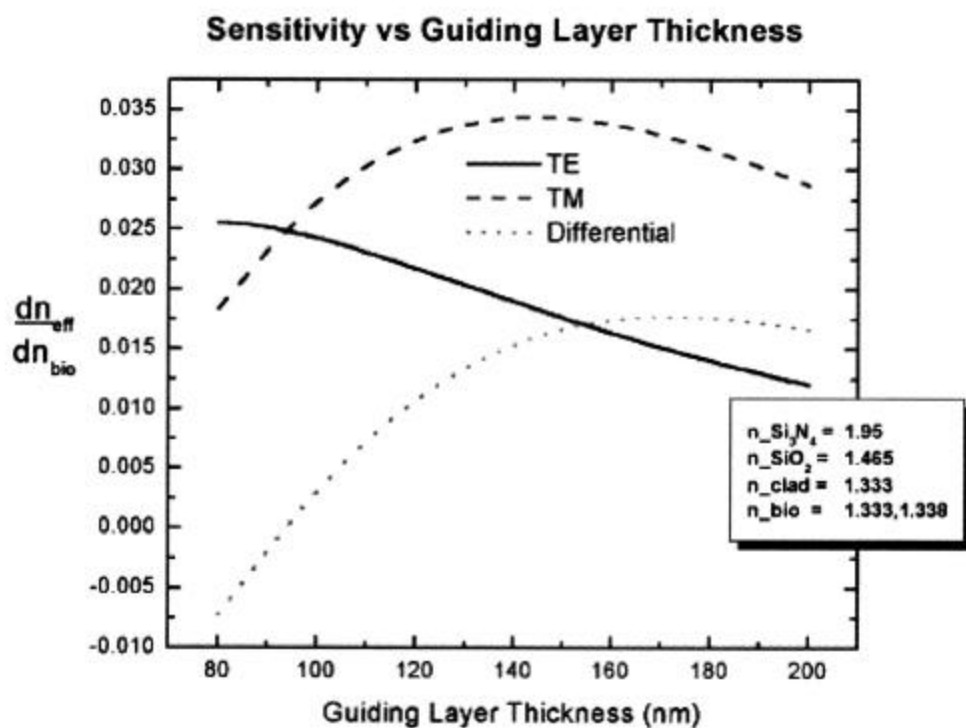
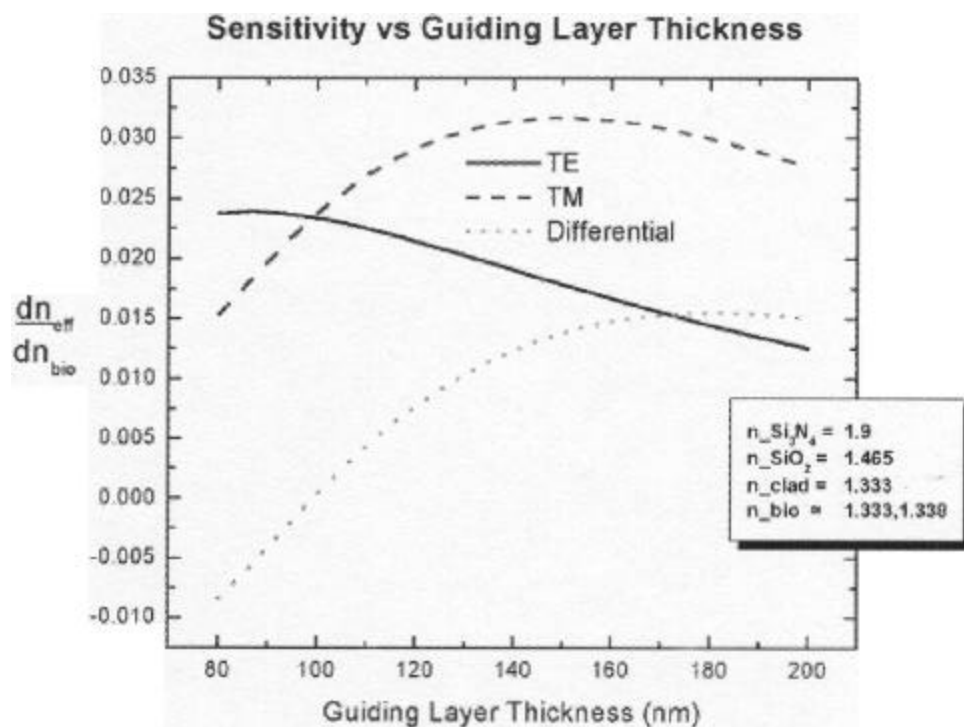
11/14/01

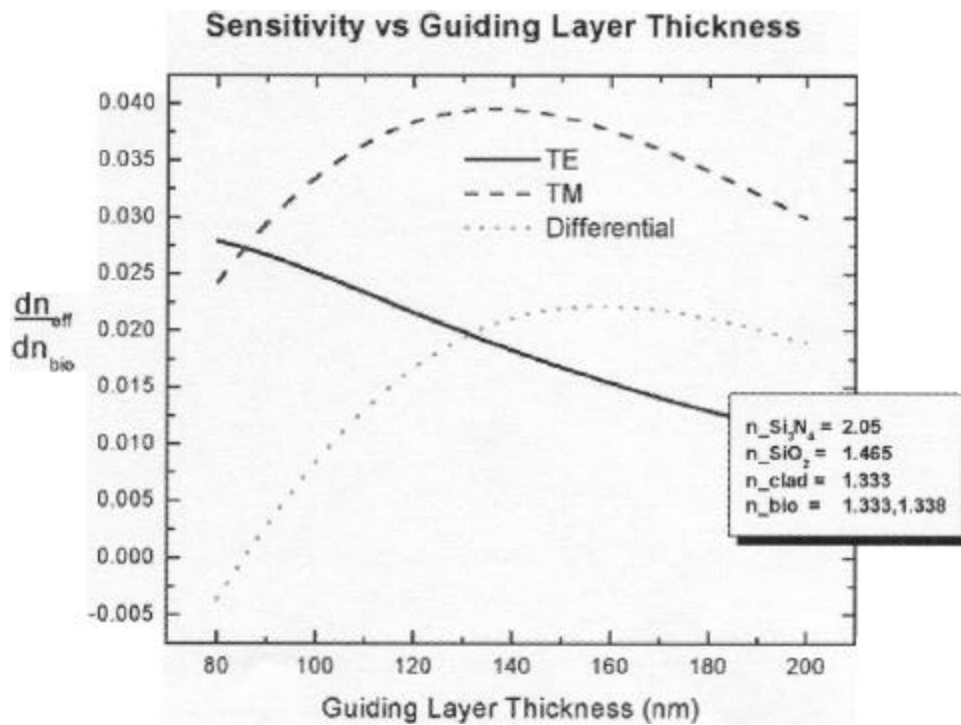
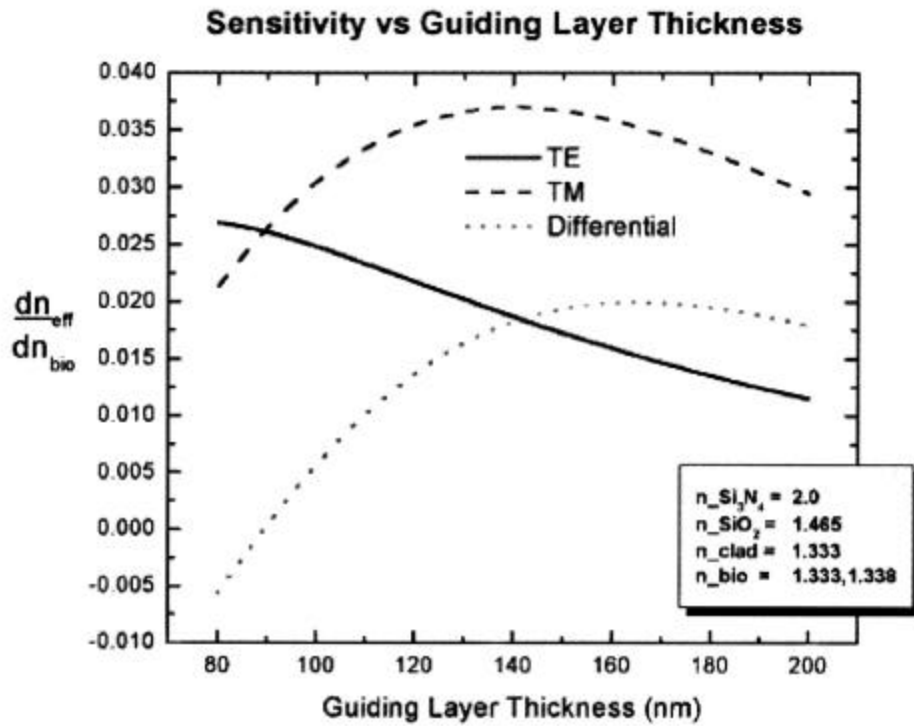
These simulations predict the effective indices, the sensitivities, and the grating coupling angles for a  $\text{SiO}_2\text{-Si}_3\text{N}_4\text{-SiO}_2$  waveguide and grating with period 1.0 microns. Results for the four different SiN index values listed below are compared.

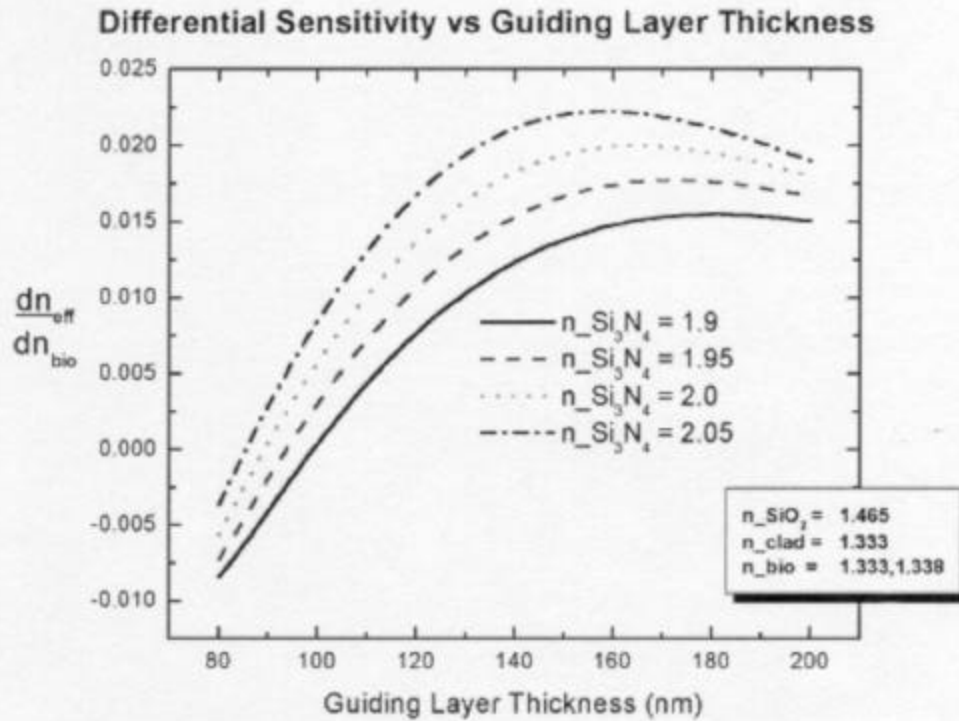
Layer:	Index:
$\text{SiO}_2$	1.465
$\text{Si}_3\text{N}_4$	1.9, 1.95, 2.0, 2.05
$\text{H}_2\text{O}$	1.333
Biolayer	1.333, 1.338 for sensitivity calculations

### ***Sensitivity Calculations***

Effective indices were determined using BeamProp, from RSoft, Inc. for a waveguide with a 10 nm uniform biolayer and water cladding. The indices were used to compute the TE0 and TM0 mode sensitivities, defined as the change in the effective index of the mode due to a change in biolayer index (1.333  $\rightarrow$  1.338), divided by the change in the biolayer index. The plots on the following pages show TE, TM, and differential sensitivity as a function of guiding layer thickness, for four possible SiN indices. The last plot compares the differential sensitivities from the first four plots.







Figures 1-5. The plots show the mode and differential sensitivities as a function of guiding layer thickness. The index of SiN used is displayed on the plots. In general, the sensitivity decreases as the index decreases and the optimal guiding layer thickness shifts to the right.

The following table compares the differential sensitivity at the optimal waveguide thickness to the sensitivity at 166 nm thickness (the latter corresponds to our current waveguides). The table indicates that the sensitivity loss is less than 2.2% for the lowest index SiN.

Refractive Index of SiN	Optimal Guiding Lyr Thickness (nm)	Sensitivity at Optimal Thickness	Sensitivity at Thickness = 166 nm	Sensitivity Ratio (%)
1.9	182	0.01550	0.01516	97.806
1.95	173	0.01771	0.01767	99.774
2	164	0.01998	0.01997	99.950
2.05	160	0.02224	0.02208	99.281

Table 1. Optimal guiding layer thickness, differential sensitivity at the optimal thickness, and comparison with sensitivity at thickness = 166 nm.

### Grating Coupling Angles

The grating coupling angles were calculated from the values of the waveguide mode effective indices. The latter were obtained by simulation for a three layer  $\text{SiO}_2\text{-Si}_3\text{N}_4\text{-SiO}_2$  waveguide structure (this differs from the sensitivity waveguide model because in the grating region, the guiding layer is surrounded by thick layers of silicon dioxide) for a guiding layer thickness of 166 nm and grating depth of 20 nm, and 25 nm and a grating period 1 micron, for light at wavelength 632.8 nm. The index of silicon nitride was varied from 1.9 to 2.05.

Coupling Angles for 25 nm grating depth			Coupling Angles for 20 nm grating depth		
Nitride Index	Coupling Angles (degrees)		Nitride Index	Coupling Angles (degrees)	
	TE	TM		TE	TM
1.9	23.28	19.06	1.9	23.47	19.26
1.95	25.63	20.45	1.95	25.85	20.69
2	28.13	21.94	2	28.38	22.21
2.05	30.79	23.52	2.05	31.07	23.84

**Table 2: Coupling angles in air for grating coupling into the TE<sub>0</sub> and TM<sub>0</sub> waveguide modes for two different grating depths, and grating period,  $\Lambda = 1 \mu\text{m}$ .**

11/28/01

These simulations predict the coupling angles and input coupling efficiencies for the waveguide/grating system described in the first section by simulating the behavior of a Gaussian beam (beam diameter 6 microns) incident on a waveguide/grating structure. The simulations are done with Fullwave, from Rsoft, which iteratively solves Maxwell's Equations to determine the electric and magnetic field strengths, as a function of time, within a given spatial area. The index of refraction of the simulation space can be specified arbitrarily as a function of position.

### ***Simulation Setup***

The simulation space consists of a 15 micron x 15 micron area in the x-y plane. The features in the space are assumed to have infinite extent in the third (z) direction. The waveguide is aligned along the x-axis in the center of the simulation space. The layer profile lies along the y-axis, and consists of (with increasing y), the BOX layer, the guiding layer, the grating/guiding layer, and an oxide cladding. The grating/guiding layer is a 25 micron thick layer with alternating oxide and SiN segments along the x-direction. The length of each segment is 0.5 microns, so that the grating period is 1 micron. A Gaussian light beam (diameter 6 microns) is incident from the negative y limit of the space, directed towards the waveguide at some angle,  $\theta$ , to the y axis ( $\theta = 0$  corresponds to normal incidence on the waveguide / grating). The initial x-position of the beam is adjusted according to the angle of the light so that light striking the waveguide is centered on the grating. Light coupled into the waveguide in the grating region propagates along the waveguide in the +x direction. The amount of light power reaching the +x end of the waveguide is recorded throughout the simulation until a steady state is reached.

### ***Simulation Results***

Simulation results for different input angles, guiding layer refractive index values, and polarization are shown in Fig. 6. Fig. 6 is explained here and in the figure caption. Each curved line corresponds to one guiding layer index value and one polarization (either TE or TM). The line indicates the strength of the light detected at the +x end of the waveguide, as a function of the angle of the incident coupling beam, once a (quasi-)steady state is reached.<sup>1</sup> The four higher, brightly colored lines correspond to TE coupling for each different guiding layer index, as indicated. The four lower lines are the same for TM coupling. The number of data points is limited due to time constraints; each data point requires one half-hour of simulation time.

Following Fig.6 is Table 3 listing the angle and amplitude of maximum coupling for each guiding layer index / polarization. In general, TE coupling is a factor of three to five greater than TM coupling, and also in general, the amount of coupling increases with

---

<sup>1</sup> In fact, the 'steady' state oscillates slightly around a constant value, due to resonance effects within the waveguide. The data points represent the average over several periods of the oscillation once the quasi-steady state is reached.

increasing guiding layer index. For both TE and TM, the coupling magnitude is a factor of  $\sim 2.1$  greater for  $n_{\text{SiN}}=2.05$  as compared to  $n_{\text{SiN}}=1.9$ . However, this must be weighed against the loss due to scattering in waveguides with high index SiN. The table also lists analytically calculated angles for maximum coupling, in the 'Previously Calculated Angles' column, since there is some discrepancy between the analytic and the simulation results.<sup>2</sup> (this necessitated a second round of simulations, because the angular ranges in the first round were dictated by the calculated, analytic values) I believe the analytic results for the angle to be the real coupling angles. More simulations could be done to try to improve the agreement. The coupling amplitude results are discussed further in the Table 3 caption.

---

<sup>2</sup> This is unexpected, because the analytic and simulated angles in earlier work involving first-order coupling through small grating periods were in close agreement. The discrepancy may be due to the fact that for a 1 micron grating, the input beam (beam diameter 6 microns) does not refract from as many periods of the grating, as it would for a smaller grating, and therefore does not approach the behavior of a plain wave as closely as in previous simulations.

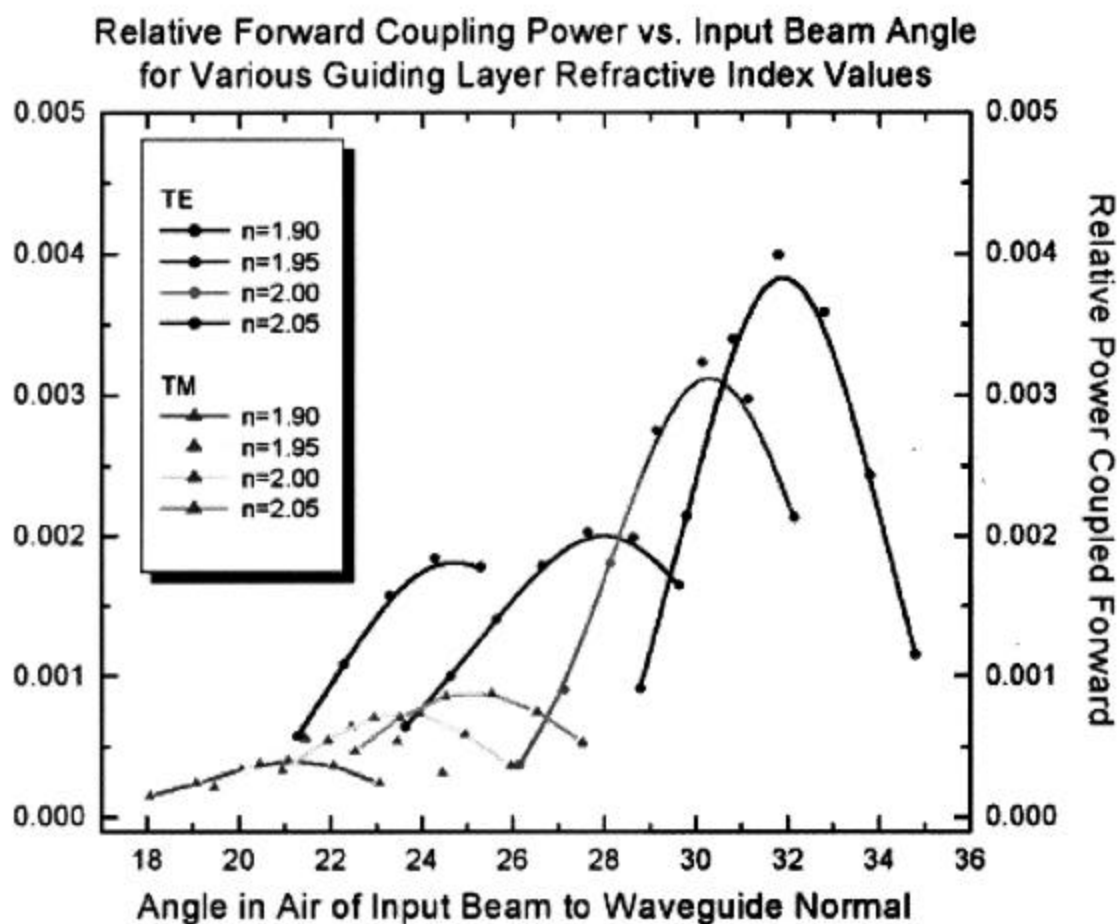


Figure 6. Each curved line corresponds to a single guiding layer index value and one polarization (either TE or TM). The data represents the amount of light detected at the +x end of the waveguide, as a function of the angle of the incident beam. The four higher, brightly colored lines correspond to TE coupling for  $n=1.9$ , 1.95, 2.0 and 2.05, from left to right, respectively. The four lower lines correspond to the same for TM coupling.

Angle (calculated and simulated) and Amplitude of Maximum Input Coupling								
Index	Previously Calculated Angle		Simulation-Angle Result		Power Detected In Waveguide		Power Relative to n=2.05	
	TE	TM	TE	TM	TE	TM	TE	TM
1.9	23.3	19.1	24.3	21.1	0.00184	0.000406	0.46	0.46
1.95	25.6	20.5	27.6	22.5	0.00203	0.000646	0.51	0.74
2	28.1	21.9	30.1	23.9	0.00324	0.000737	0.81	0.84
2.05	30.8	23.5	31.8	25.5	0.00399	0.000875	1	1

Table 3. Angle and amplitude of maximum coupling for each guiding layer index / polarization. In general, TE coupling is a factor of three to five greater than TM coupling, and also in general, the amount of coupling increases with increasing guiding layer index. For both TE and TM, the coupling magnitude is a factor of ~2.1 greater for  $n_{\text{SiN}}=2.05$  as compared to  $n_{\text{SiN}}=1.9$ . 'Previously Calculated Angle' refers to the analytically calculated result. The values for power indicate results for a total incident beam flux normalized to 1. Due to the limited scale of the simulations, the limit on the diameter of the input beam, and outcoupling from the grating, this number should not be interpreted as the coupling efficiency. For maximum coupling efficiency, the beam must strike the grating at an optimal position near the grating edge (in the +x direction) to avoid outcoupling. The simulation results obtained are nonetheless useful for *comparing* coupling strengths for different SiN indices and polarizations.

## **Appendix 4-B: Boston University Report on Prism Coupling Work October 14, 2001**

Boston University Group  
Prof. Bennett Goldberg  
Prof. M. Selim Ünlü  
Colin Worth

Report on Prism Coupling Work  
October 14, 2001

Table of Contents:

<b>1</b>	<b>INTRODUCTION .....</b>	<b>3</b>
<b>2</b>	<b>PRISM COUPLING OF SOI WAVEGUIDES .....</b>	<b>3</b>
2.1	REVIEW OF PRISM COUPLING SETUP .....	3
2.2	ADDITIONS TO SETUP FOR SOI WORK: .....	4
2.3	SUMMARY OF PRISM COUPLING DATA: .....	4
2.4	COUPLING EFFICIENCY MEASUREMENTS OF SOI: .....	5
2.5	COUPLING AS A FUNCTION OF POSITION: .....	6
2.6	COUPLING AS A FUNCTION OF ANGLE: .....	6
2.7	CONCLUSION .....	7
<b>3</b>	<b>PRISM COUPLING OF SILICON NITRIDE WAVEGUIDES .....</b>	<b>8</b>
3.1	WAVEGUIDE FABRICATION FOR PRISM COUPLING EXPERIMENTS .....	8
3.1.1	<i>Mask Fabrication</i> .....	9
3.1.2	<i>Lithography</i> .....	9
3.2	PRISM COUPLING WITH NEW WAVEGUIDES .....	10
3.2.1	<i>Experiment 1: End-coupling input, prism coupling output on near facet (see text)</i> .....	10
3.2.2	<i>Experiment 2: Prism coupling input, end-coupling output</i> .....	11
3.2.3	<i>Experiment 3: Prism coupling input, end coupling output at opposite facet (see below)</i> .....	12
3.2.4	<i>Experiment 4: End coupling input, end coupling output</i> .....	12
3.2.5	<i>Experiment 5: Etch waveguide-sized piece to prism area height</i> .....	12
3.3	CONCLUSION .....	12
<b>4</b>	<b>THEORETICAL WORK AND SIMULATIONS .....</b>	<b>13</b>
4.1	GUIDING LAYER THICKNESS AND COUPLING ANGLES .....	13
4.2	GAP HEIGHT DETERMINATION .....	15
<b>5</b>	<b>CONCLUSION .....</b>	<b>17</b>
<b>6</b>	<b>APPENDIX A. EXPERIMENTAL SETUP FOR PRISM INPUT COUPLING .....</b>	<b>18</b>
<b>7</b>	<b>APPENDIX B. DERIVATION OF GAP HEIGHT EQUATION .....</b>	<b>21</b>
<b>8</b>	<b>APPENDIX C. PLANS FOR PRISM CLAMPING DEVICE .....</b>	<b>23</b>
<b>9</b>	<b>APPENDIX D. MASK IMAGES FOR NITRIDE PRISM-COUPLED WAVEGUIDES .....</b>	<b>25</b>

## 1 Introduction

This report describes the BU prism coupling effort, beginning with our work on SOI waveguides in Section 2. Section 3.1 describes the fabrication of silicon nitride waveguides, including mask design, wafer fabrication, and waveguide processing, and the obstacles encountered with each. Section 3.2 describes experiments and other work to improve and characterize prism input and output coupling, and to establish through-coupling using two prisms. Section 4 describes the modeling and theoretical work done to implement prism coupling, including the determination of the coupling angles, and the optimum spacing between prism and waveguide. The appendices contain supplemental information, including diagrams of the experimental setup and mechanical prism mount.

## 2 Prism Coupling of SOI Waveguides

### 2.1 Review of Prism Coupling Setup

Light from a 1.3 micron fiber coupled (FC) laser passes through a polarization-sensitive beam splitting prism. The transmitted and reflected beams, with polarizations corresponding to the TM and TE waveguide modes, respectively, strike the top surface a silicon prism, at such an angle that the internal beams couple via their evanescent fields to the two guided waveguide modes. The optical setup is shown in Appendix A. In outcoupling, the process is reversed. Figure 1 shows a diagram of the prism and incident or outgoing light. The lines labeled with a polarization (TE and TM), represent the center of the beams described. The lines labeled TE 2 and TM 2, were each observed in separate *outcoupling* experiments as the result of multiple internal reflections within the prism, as depicted in Figure 1. In outcoupling, the TM beam reflects off of the upper prism surface as shown by the dashed line and exits the prism at angle almost parallel to the TE beam. The unexpected result of this geometry was that we were able to use a single (mixed polarization) input beam striking the prism at approximately the angle for TM coupling to simultaneously couple TE and TM light into the waveguide. This technique could be used in future work to eliminate noise in an interferometric measurement caused by using two different optical paths for incoupling.

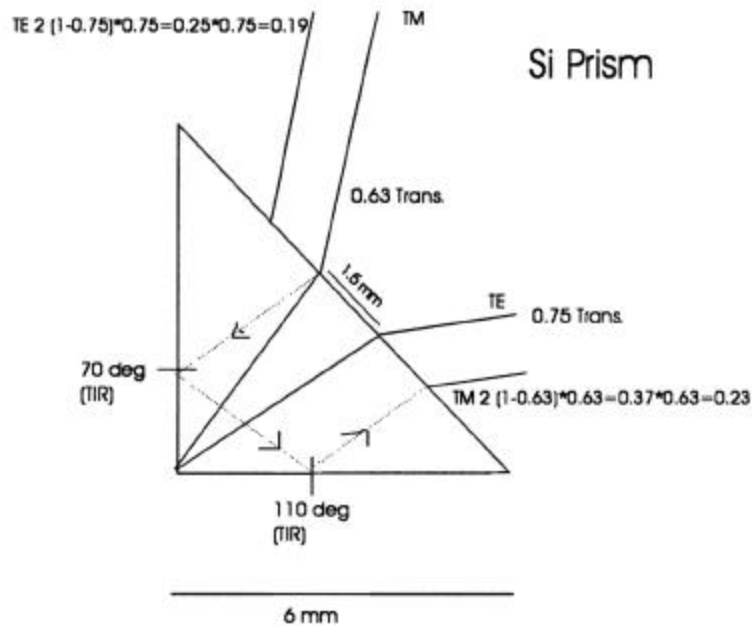


**Figure 1.** Diagram of prism output coupling in SOI experiments. The beams labeled TE and TM are the primary coupling beams for the two waveguide modes. The lines labeled TE2 and TM2 are the result of multiple reflections within the prism of the primary beams, as depicted for the TM polarization. The numbers stand for the fraction of power transmitted through the upper surface.

## 2.2 Additions to setup for SOI work:

The SOI waveguides used differed from silicon nitride waveguides in that the substrate and guiding layer were both made of a transparent material (silicon). Thus, light measured at the output facet was a combination of the guided light in the waveguide mode and light passing through the substrate. In order to distinguish the two, and maximize the guided light, we imaged the output facet of the waveguide with an IR camera attached to a video monitor.

## 2.3 Summary of Prism Coupling Data:

We took three sets of data to characterize prism coupling. The first was the maximum overall coupling efficiency for TE and TM, respectively. These measurements were made by placing a light meter at the output facet of the waveguide, shining beams on the prism at the correct angle for coupling, and collecting the transmitted light. A negligible amount of light was transmitted through the substrate for optimal coupling. The amount of light at the output facet was compared to the amount of light in the corresponding (TE or TM) input beam. The second type of data recorded was coupling strength as a function of input angle. Prism coupling efficiency drops sharply on either side of the optimum coupling angle. From the measured angle of maximum coupling, we calculated the effective indices of the TE and TM waveguide modes, and thus the width of the silicon-guiding layer. Since each mode provides an independent measure for the guiding layer width, we were able to compare the results to confirm the consistency of our theoretical model. The third type of data was coupling strength as a function of beam position. The input beams must be positioned so that inside the prism they strike close to the back (vertical) prism wall, to avoid subsequent out-coupling of the light as it travels through the waveguide. Translational motion of each beam was decoupled from angular variations by

moving the mirror parallel to the initial beam direction (horizontally for TM, vertically for TE; see Appendix A).

## 2.4 Coupling efficiency measurements of SOI:

Coupling was maximized by optimizing the angle of incidence of the two polarized input beams, and the height at which they struck the prism. The input beam diameter was adjusted by fiber launching the input laser through various objective lenses of different focal lengths. We also varied the beam divergence by varying the separation of the fiber facet with respect to the effective focal length of the objective. Using our lens system, these two parameters are not completely decoupled, and losses occurred due to components of the beam which were no longer directed at the critical angle for prism coupling.

Maximum coupling was achieved with a slightly focused beam and a 40X Objective. The coupling efficiencies were 1% for the TE polarization, and 0.1 % for the TM polarization. Coupling efficiency was measured by comparing the total light output at the waveguide facet with the intensity of the (TE or TM) beam before striking the prism.

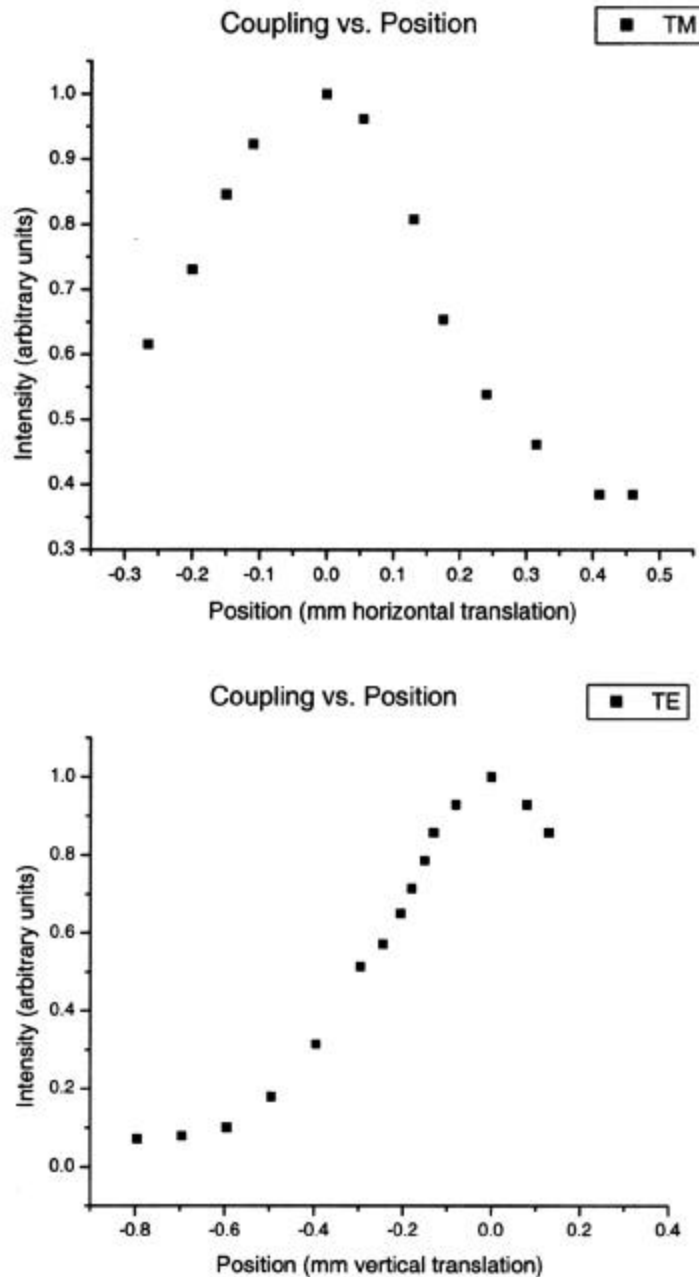
We believe the low efficiency of the TM coupling is due to a non-optimal air gap width between the prism and waveguide guiding layer. TM light couples between the prism and waveguide much more rapidly than TE light, and therefore, unless the input beam is very intense over a short distance (i.e. tightly focused), the rate of TM light coupled back out of the waveguide is comparable to the light in-coupled from the beam. A larger air gap slows the coupling and allows more light to build up in the guiding layer. This idea is supported by the fact that focusing the input beam to a more intense spot increased TM efficiency. In addition, an error was made by the group who provided the SOI wafer and prism coupling area. This error resulted in incorrect gap spacing, much less than we had calculated and requested.

We attempted to compensate for this error in several ways: (1) by changing the input beam diameter, and (2) by modifying the prism setup. For (2), we placed the back of the prism on a silicon dioxide 'step' that we etched out of the wall of the prism cuvette. In this configuration, the prism gap varied from zero at the front of the prism to about 500 nm at the back (a wedged shape). However, attempts to increase TM coupling by varying the position of the input beam with respect to the front and back of the prism were unsuccessful. The probable reason for this is that prism coupling relies on the coupling region (i.e. the prism) having a sharp cutoff when the maximum amount of light has been coupled into the waveguide. This is why the input beam is normally positioned to intersect the *very back edge* of the prism at the point of maximum beam intensity. This prevents light from coupling back out of the waveguide after maximum coupling has been achieved. We had hoped that the slope of the lower facet of the prism in the wedged configuration would be enough height variation to prevent out-coupling after the termination of the input beam. This appears not to be the case and the additional coupling gained by reducing the gap height was not maintained by light in the guiding layer. As a result, and in the interest of completing the experiment, we decided to proceed with fiber end-coupling. The results and technique are described below after further discussion of prism coupling.

## 2.5 Coupling as a function of position:

Relative coupling strength was measured as a function of position. The TM beam passed through a beam splitter and traveled horizontally towards a high-reflectivity mirror (see Figure 7,

Appendix A). By translating the mirror horizontally along the beam, the position of the TM beam on the prism surface was adjusted. The TE beam was reflected vertically from the beamsplitter to another mirror. The TE mirror was translated vertically to change the position of the beam on the prism surface. The data from these two experiments is displayed in Figure 2 to the left.



## 2.6 Coupling as a function of Angle:

Relative coupling strength was also measured as a function of angle. Fine adjust micrometers on the mirrors were used to adjust the angle. The TM graph shows some asymmetry due to the secondary reflections inside the prism of the TE input beam. The optimum angle for secondary TE coupling (after three reflections inside the prism) is slightly larger than the optimum angle for TM coupling. If we shine a beam of mixed polarization at the angle for TM, we get coupling of both

**Figure 2. TE and TM coupling as a function of position along the y and x axis, respectively.**

polarizations simultaneously. This effect can be seen in the TM plot in Figure 2. Although the light in the TM input beam passed through a polarizer, trace amounts of TE, which couples with a higher

efficiency, remained. The points to the left of the maximum are artificially raised as a result of stronger TE coupling at these positions; the optimum position for secondary TE coupling is higher on the prism facet than the optimum position for TM coupling, due to the birefringence of the prism material. When the beam strikes the facet slightly above the middle of the prism, a TM

maximum is observed. If the beam is translated towards the top of the prism, a TE maximum is observed. TE and TM light are distinguished by mounting a polarizer in front of the IR camera.

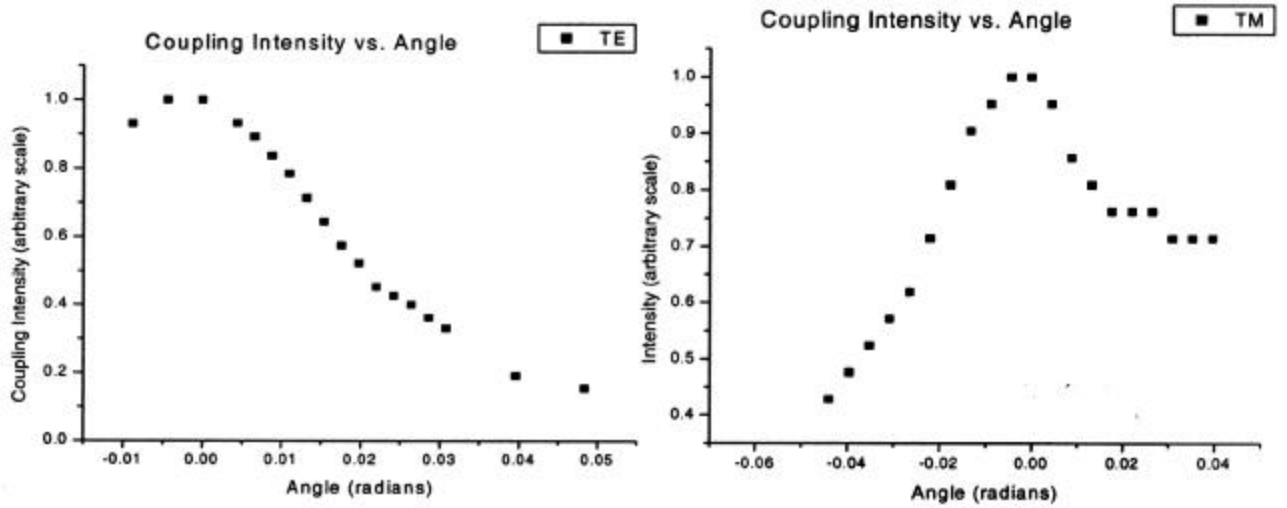


**Figure 3. Coupling efficiency as a function of input beam angle. See text for details. For both TE and TM, the half width of the coupling curve is ~ 20 mrad. It is likely that with further optimization of the air gap width between the prism and waveguide, the peak would become sharper and the coupling efficiency much greater**

## 2.7 Conclusion

SOI prism coupling was hampered by low coupling efficiencies, particularly for the TM polarization, as described in section 2.4. Due to an error in wafer fabrication at MIT, the gap spacing in the prism region was less than expected, and attempts to compensate for this were not successful. Because of this, we chose to focus on fiber endcoupling instead of prism coupling for SOI.

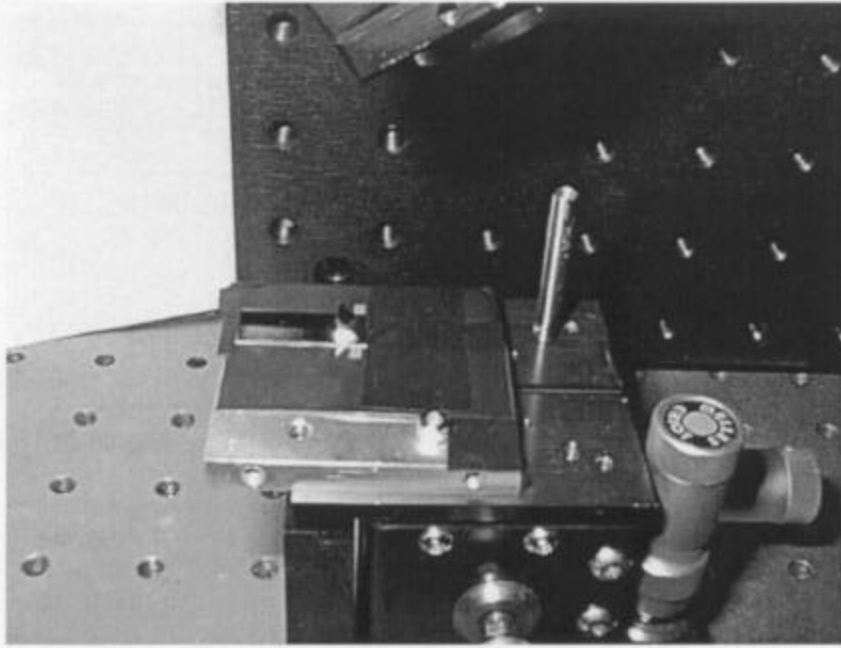


Figure 4. Prism coupling experimental setup. An SOI waveguide and right-angle prism are mounted on the adjustable stage.

Coupling Angle in Prism (degrees)			
Measured		Theoretical	
TE	TM	TE	TM
35 +/- 5	55 +/- 5	34	53

Overall Coupling Efficiency:			
Measured		Ideal	
TE	TM	TE	TM
~20%	< 0.1%	60%	40%

Table 1. Ideal and Measured coupling angles and coupling efficiencies for SOI.

### 3 Prism Coupling of Silicon Nitride Waveguides

Prism coupling in nitride waveguides required a high index material that does not absorb visible light (as silicon does). We used rutile glass prisms and the same experimental setup, minus the 1.33  $\mu\text{m}$  fiber-coupled laser, and adding a low power HeNe laser (wavelength = 632.8 nm) to produce a collimated visible Gaussian beam. We also fabricated new  $\text{SiO}_2\text{-Si}_3\text{N}_4\text{-SiO}_2$  waveguides with the same shape and features as the SOI waveguides, as described below.

#### 3.1 Waveguide fabrication for prism coupling experiments

We fabricated silicon dioxide – silicon nitride – silicon dioxide layers on doped silicon wafers at MIT according to our design specifications. These include wafers with standard guiding layer thickness (166 nm), as well as thinner guiding layers (103 nm, 97 nm) for testing surface desensitization (not covered in this report) of thin waveguides. Two runs of wafers were fabricated. Several from the first batch were scratched and were replaced by MIT.

Surface patterning of the top oxide layer of the waveguides was done at BU in the Optical Processing Facility (OPF) in the Photonics center by a two-stage lithographic process that included:

### **3.1.1 Mask Fabrication**

New masks were created which included two 7 mm x 7 mm x 1.4 microns deep wells on each waveguide to seat the coupling prisms. The 6" square chrome on soda-lime glass masks were designed at BU using the LASI mask design program and fabricated by Advanced Reproductions Inc. in North Andover, MA. A picture of each mask is shown in Appendix D.

### **3.1.2 Lithography**

#### **3.1.2.1 Process**

The fabrication process used was a two-step lithographic process.

In the first step, the first mask is used to define and isolate the cuvette regions on the waveguide surface. The top silicon dioxide layer of the wafer is then etched to completion in these areas using 7:1 Buffered Oxide Etching (BOE) solution. The silicon nitride layer is resistant to etching with BOE, and provides an effective stop for the etch.

In the second step, the second mask is used to define 7 x 7 mm square areas on either end of each waveguide for prism coupling. In this stage, the oxide layer is partially etched. This is necessary for efficient prism coupling. The tolerances for this step are rather stringent, flatness of 25-50 nm over 8mm region, or 1 part in  $10^5$  flatness, and an accuracy of the etch depth of 25-50nm over a distance of 1.5 microns. In this step we encountered some difficulties and tried different techniques.

#### **3.1.2.2 Etching Difficulty**

There were a number of issues involved with the etching of the prism areas. Different localized etch rates made it difficult to obtain uniformity. We tried two different approaches, wet and dry etching:

##### **3.1.2.2.1 Wet etching**

Partial etching of the oxide layer had been tried previously on another set of wafers. The resulting oxide surface was uniform to within 50 nm and the surface roughness was less than 10 nm. In this case, it was possible to seal prisms to the surface by applying a drop of water below the prism and allowing it to evaporate. Reasonable coupling efficiencies ~10-15% were achieved for prism input coupling at that time. However, etching of the new batch of wafers from MIT with BOE did not produce uniform results. In tests performed to determine the etch rate for the oxide, the first 50 nm of oxide etched very slowly at a rate of approximately 10 nm/minute. The remainder etched at various rates, up to 300 nm/minute. The etch rates were measured using a stepper with a height resolution of about 10 nm. The variation in oxide etch rates limited uniformity to 100-200 nm over the prism area, with surface roughness up to 50 nm. As a result, it was not possible to seal the prisms to the waveguide using the previous technique. In addition, we could not obtain optimal prism-guiding layer spacing. Etch tests were performed on samples from previous wafer sets which showed that the oxide etch rate was much more uniform and fixed at ~220 nm/minute in 7:1 BOE.

### 3.1.2.2.2 Dry etching

To obtain more uniform results, we performed a number of tests using reactive ion etching (RIE) and a plasma of  $\text{CF}_4$  and  $\text{O}_2$  gas. First a large sample was etched to check the uniformity. Non-uniform circular rings were observed beginning at a radius of about 30 mm from the center of the sample positioned at the middle of the RIE chamber. Rings were also observed around the edges of a smaller sample. But, by surrounding the smaller sample with other pieces of the same height, it was possible to etch the small, central sample uniformly. Using this technique, we fabricated a waveguide with 550 nm of oxide remaining in the prism regions. The uniformity improved to ~75 nm across the prism area. The RMS surface roughness was measured at BU using Atomic Force Microscopy (AFM) to be 5-10 nm. With the improved etch, it was possible to seal the prisms to the waveguides using the water evaporation technique.

## 3.2 Prism coupling with new waveguides

Purchased and received two 45-45-90 6x6 mm base Rutile prisms from OFR, Inc.

Despite an apparently good water seal between prisms and waveguide, no through coupling of a visible collimated Gaussian beam was detected. In addition, the water seal method of mounting the prisms was not always creating strong seals. Therefore we designed and fabricated an aluminum and delrin prism clamp device for making contact between prisms and waveguide at the BU machine shop. See copy of the specifications in the Appendix C. Even using new the new clamping device, however, no through coupling was seen. In parallel with fabrication of the new clamp, we attempted a number of coupling experiments using the water seal method, described below to measure different aspects of the coupling. The water seal method was usually successful in creating temporary seals between prisms and waveguides (due to more uniform prism areas, improved lithography).

### 3.2.1 *Experiment 1: End-coupling input, prism coupling output on near facet (see text)*

The purpose of this experiment was to check for prism output coupling, using end coupling to couple light into the waveguide. In addition, it would allow us to verify the prism coupling angles if output coupling was successful. One facet of the waveguide was polished and used for end coupling of light. A prism was mounted on the waveguide, in the prism area closest to the facet used for incoupling. We found that light was coupled into the waveguide, traveled about 2 mm to the prism and was outcoupled by the prism. We measured the intensity of the two outcoupled light beams (one for each polarization) and we measured their angles with respect to the waveguide surface. The results of the experiment are shown in Table 2.

In addition to the first two outcoupled beams, we found two secondary beams created by light from the brighter beams reflected back into the prism and (due to total internal reflection within the prism) were reflected back out in approximately the same vertical plane as the first two. The columns labeled TE2 and TM2 show the intensity and angles of the secondary beams. Because the internal angle of the right-angle prism is 45 degrees, the angle of a secondary reflected beam with respect to the waveguide surface must be the complement of the angle of the initial beam (because the prism, viewed in profile, is symmetric about a line starting at the right-angle vertex and bisecting the opposite face). The angles of the secondary beams are also measured and compared to the primary beam angles.

**Coupling in through facet out through nearside prism:**

Wavelength	632.8 nm
<b>Laser power (uW)</b>	<b>648; TE or TM</b>
Transmission Efficiencies (fractional):	
lens	0.8
rutile-air interface	0.83
Estimated end-coupling efficiency	0.01
effective power supplied ( $\mu$ W)	4.30272

**Measurements and analysis:**

Polarization	TM1	TE1	TE2	TM2	TE1+TM1	TE2+TM2
Intensity(uW)		8.100	0.140 n/m	n/m		
Angle(degrees)		62.26	52.19	36.81	26.43	88.69
						89.00

**Table 2. Data analysis from experiment one.** The upper part shows the initial intensity of the input beam and losses due to lenses, etc. in the beampath. In the bottom section, the intensity of the light output at the facet is shown, as well as the angle of the beams. The last two columns show that the angles of the two TE and two TM beams are approximately complementary.

**3.2.2 Experiment 2: Prism coupling input, end-coupling output**

To confirm that the beams in Experiment 1 came from the guiding layer of the waveguide and not from another source, and to measure the efficiency of prism input coupling, we reversed the first experiment (without changing the prism-waveguide setup), and directed a Gaussian beam of light into the prism at the measured angles of the output beams. The light now outcoupled through the adjacent waveguide facet. We placed a detector close to the facet and measured the output light. As expected, light of either polarization was found only for particular incoupling angles. For a polarized beam of light, we measured the following throughput.

Input laser power: **1270  $\mu$ W, TE or TM**

Light coupled out facet: TE: **1.9  $\mu$ W**, TM: **0.01  $\mu$ W**

Thus, we found that light was indeed incoupled by the prism. Estimating an 80% outcoupling efficiency and 20% loss at the prism facet, and assuming all the light from the prism reached the near facet, the prism coupling efficiency was 2.3% TE, and 0.12% TM.

Although the prism coupling efficiency measured in Experiment 2 was a factor of 10 less than expected for TE, and a factor of 100 less for TM, the amount of output light from the near facet for the TE polarization of the waveguide was significantly brighter than the intensity of light used for past biosensing experiments by Satcon and BU using end-coupling. Therefore it did not make sense that prism through-coupling (ie incoupling and outcoupling using two prisms) did not yield any detectable outcoupled light. This is further discussed in experiments 3,4 and 5.

### **3.2.3 *Experiment 3: Prism coupling input, end coupling output at opposite facet (see below)***

For this experiment, we incoupled light through the prism (now facing the opposite direction) such that it would be guided towards the farther facet of the waveguide. We expected to find the same output intensities as we found in experiment three, because of the optical guiding properties of the waveguide. However there was no detectable light at the far facet. This indicated that although experiment 2 indicated that light was prism coupled into the waveguide, no light was output after traveling through the waveguide.

### **3.2.4 *Experiment 4: End coupling input, end coupling output***

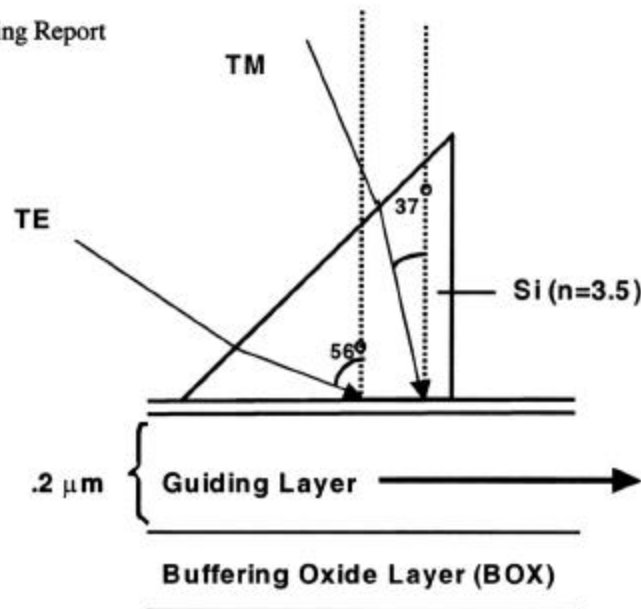
Finally, we polished both facets of a waveguide, and tried to use endcoupling for both incoupling and outcoupling. We found the same result as in Experiment 4, no light coupled out. To try to explain the behavior, we characterized the waveguide layer structure using Atomic Force Microscopy (AFM) by scanning along the facet of a polished, and then slightly etched waveguide. The etching allowed us see 15 nm deep depressions in the facet where oxide layers had been etched. We were also able to see the guiding layer, although variations in the etch depth around the nitride layer made it difficult to measure its thickness precisely. Measurements along the guiding layer cross-section determined that the guiding layer was present and between 100 and 180 nm thick.

### **3.2.5 *Experiment 5: Etch waveguide-sized piece to prism area height***

Using end coupling for input coupling, use prism coupling to output couple at several distances from the input face to look for an intensity decrease as the prism is moved farther away from the input facet. Experiment six was not carried out due to time constraints.

## **3.3 Conclusion**

Problems encountered during etching of the prism-coupled waveguides slowed this project considerably. Experiments performed on the longer, prism-coupled waveguides indicated that prism coupling and endcoupling were possible, so long as the light did not have to travel through the body of the waveguide. If, in fact, the light was lost during travel from one side of the waveguide to the other, this effect might have been caused by non-uniformity in the deposited silicon nitride guiding layer, or due to scattering due to features on the waveguide surface---either the recessed prism areas, or the cuvettes. Since end coupling in Experiment 4 was tried for beampaths that avoided the cuvette regions, it was likely not the cuvette regions that scattered the light. Further experiments could test these two hypotheses, by outcoupling after shorter travel paths, and/or fabricating pieces without surface features and using endcoupling, as described in Experiment 5.



## 4 Theoretical Work and Simulations

In preparation for prism coupling, simulations were performed to determine the angles needed for TE and TM coupling. In addition, research and analytic work were done to try to maximize the coupling efficiency by adjusting parameters of the experiment (see below).

Two methods were used for determining prism and waveguide parameters related to prism coupling. The first method determines the angle at which light will pass through the bottom of the prism into the waveguide mode. It uses the index of refraction of the prism and the effective index of the guided mode to determine the beam angle in the prism, and then calculates the angle at which a beam should be incident on the upper prism surface for prism coupling. The TE and TM modes couple at different angles because of the difference in effective index of the two waveguide modes and the birefringence of the prism material. It is convenient to have the two angles as close to each other as possible to minimize interferometric noise caused by using a different beam path for each polarization, and this can be adjusted by varying the guiding layer thickness. The second method was used to determine the spacing between the prism and guiding layer.

### 4.1 Guiding layer thickness and coupling angles

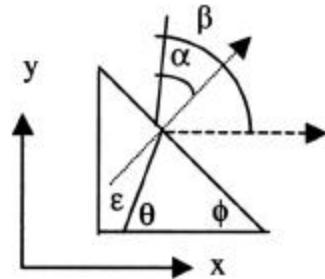
Coupling angles were determined from the effective indices of the waveguide modes, the index of refraction of the prism, and the shape of the prism, as shown in Table 3:

Prism	Length-x (mm)	Height-y (mm)	$n_{\text{prism}}$ (TE)	$n_{\text{prism}}$ (TM)	y/x	Prism Angle $\phi$ (deg)
Rutile right angle prism	6	6	2.584	2.865	1	45

Waveguide Model (nm)	$n_{\text{eff}}$ TE	$n_{\text{eff}}$ TM	Guiding Layer (nm)	$n_{\text{SiO}_2}$	$n_{\text{Si}_3\text{N}_4}$
SiO <sub>2</sub> -Si <sub>3</sub> N <sub>4</sub> -SiO <sub>2</sub>	1.85297	1.767693	166	1.465	2.02

Wavelength (nm)  
632.8



Results: Coupling angles  $\beta_{TE}$  &  $\beta_{TM}$

Angles:	TE	TM
$\theta$ (radians)	0.77	0.90
$\phi$ (rad)	0.78	0.78
$\epsilon$ (rad)	0.014	-0.12
$\alpha$ (rad)	0.036	-0.35
$\beta$ (degrees)	<b>42.89</b>	<b>65.14</b>

**Table 3. Angles necessary for coupling into an  $\text{SiO}_2\text{-Si}_3\text{N}_4\text{-SiO}_2$  waveguide with guiding layer thickness 166 nm. The angle's  $\beta$  are the angles of the input light beams with the horizontal (waveguide surface).  $\beta$  is calculated from the indices of the materials, the angle of the prism face, and simulation results for the  $n_{\text{eff}}$ 's of each waveguide mode.**

The coupling angles,  $\beta$ , are shown in the last row for the parameters specified. We performed simulations to determine if we could modify the height of the guiding layer to reduce the difference between the two coupling angles without sacrificing sensitivity. Our results are shown in Figure 5, which shows the difference (TM-TE) in the two coupling angles superimposed on a plot of the waveguide sensitivity vs. guiding layer height for an SOI waveguide/silicon prism setup.

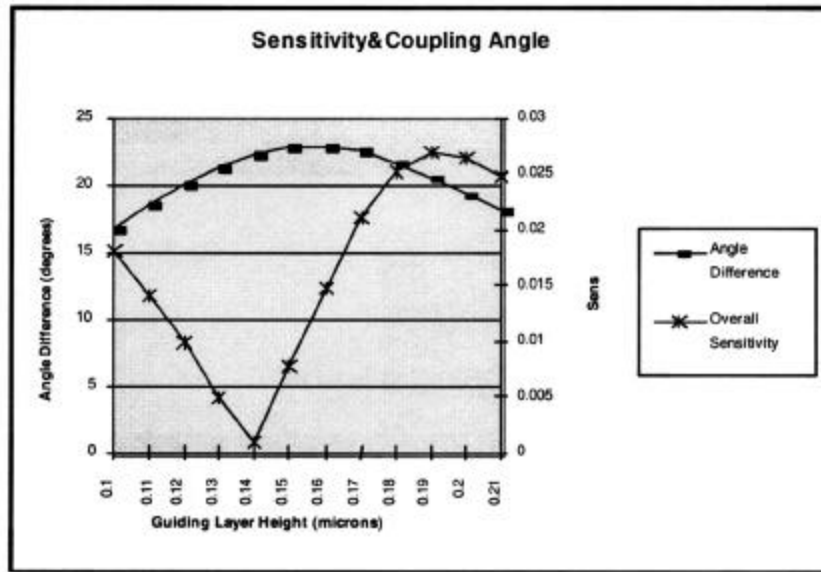


Figure 5. Difference in coupling angle compared to waveguide sensitivity. For maximum waveguide sensitivity, the difference in coupling angles is approximately 21 degrees. By increasing the guiding layer thickness to 0.2 microns we can reduce the coupling angles with little effect on the sensitivity.

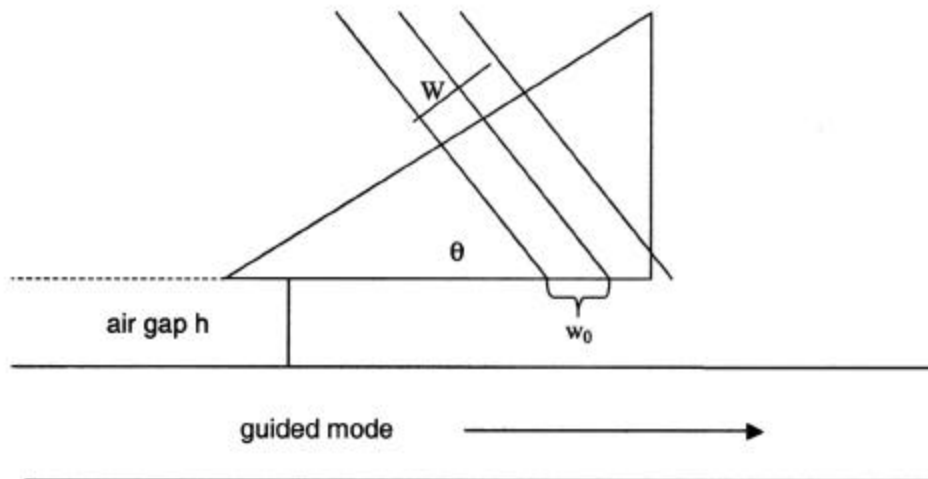


Figure 6. Diagram of beam and prism positioning for prism coupling into a waveguide guiding layer.

## 4.2 Gap height determination

The second model is used to calculate the desired 'gap' spacing between the prism and the guiding layer for maximum transfer of power into the guided modes. The idea, as described in previous reports, is to regulate the rate that light couples into and out of the waveguide guiding

layer through the prism, by changing the height of the gap. The rate that light couples out of or into the waveguide, in turn, determines the optimum beam width to use for maximum coupling efficiency.

The condition for optimal coupling of a Gaussian beam is a relation between the beam width ( $w_0$ ) and the coupling rate,  $\alpha$ , for the waveguide-prism system:

$$\alpha w_0 = 1.36.$$

Actually  $w_0$  is the length of the projection of the beam radius on the waveguide surface (see Figure 6). Assuming we have a fixed full beam width,  $W$ , we can solve for the optimum value for the coupling rate,  $\alpha$ .

$$w_0 = W/(2 \cos \theta) \Rightarrow$$

$$\alpha = \frac{1.36(2) \cos \theta}{W}$$

When this relation is satisfied, the maximum possible transfer of light from the incident beam to the guiding layer takes place.  $\alpha$  depends on the gap spacing between the prism and guiding layer as well as the index of refraction of the prism, gap, and the effective index of the waveguide mode. We use this relation to find the optimal gap height  $h$  for our system, taking into account the incident beam size:

$$h = -\frac{\ln\left(\frac{1.36(2)n_{eff}}{nAW}\right)}{2k_0\sqrt{n_{eff}^2 - n^2}}$$

where all the variables stand for system parameters;  $n_{eff}$  is the effective index of the coupled mode,  $n$  is the index of the prism, and  $n'$  is the index of the material in the gap.  $k_0$  is the free space wavevector of the light,  $W$  is the width of the beam, and  $A$  is a constant. We use this to determine the gap height for our prism coupling experiments. See Appendix B for a discussion of the height equation. Results for the gap spacing for our nitride system are shown in Table 4.

#### INPUT DATA:

$\lambda$	$W$	$n_{eff}$ TE	$n_{eff}$ TM	$n_{prism}$ TE	$n_{prism}$ TM	$n'$ (gap)	$A$
0.6328	2000	1.85297	1.767693	2.584	2.865	1.5	1

#### OUTPUT DATA:

$k_0$	Sqrt() TE	Sqrt() TM	Ln() TE	Ln() TM	Gap height $h$ TE ( $\mu m$ )	Gap Height $h$ TM ( $\mu m$ )	Average ( $\mu m$ )
9.9292	1.087887	0.935275	0.000975	0.000839	0.320909	0.381368	0.351139

**Table 4.** This table calculates  $h$  for a silicon nitride, rutile prism system. Values for the variables in the height equation are shown as input data. The final three columns of the output data show optimal gap heights for TE coupling, TM coupling, and the average of the two, respectively, for a silicon nitride waveguide system.

## **5 Conclusion**

Although input and output prism coupling was achieved for both SOI and silicon nitride waveguide setups, at angles in agreement with our theoretical predictions, through coupling—ie. prism input and output coupling simultaneously—was not. This was in part due to issues related to waveguide fabrication, at MIT and at BU, which slowed the process, and in part due to an inability to achieve high coupling efficiencies for both polarizations of light. Although efforts were made to solve these problems, they were not successful in the time frame allowed by the biosensing project. As a result, prism coupling was abandoned, and we proceeded with other aspects of the project, such as simulations and analysis of grating coupling, and preparations for surface desensitization experiments.

## 6 Appendix A. Experimental Setup for Prism Input Coupling

Figure 7 shows a schematic diagram of the setup BU designed as a light delivery system for prism input and output coupling. Before the light enters the diagram from the right, it passes through a collimator and the polarization is rotated so that light hitting the beam splitting cube has both TE and TM components. By adjusting the polarization angle, the relative amount of TE and TM light can be controlled. The light source is a fiber coupled, 1.3 micron wavelength, polarized FC-coupled laser for SOI waveguides and a 632.8 nm HeNe laser for nitride waveguides. After the light is split into TE and TM components, two mirrors adjust the angle at which the light hits the prism surface. The angle must be controlled very precisely to obtain a high coupling efficiency. The correct angle defined relative to the waveguide surface for each polarization is determined by the effective index of the corresponding waveguide mode, as described in section 4.1. Rotating one of the mirrors by an angle,  $\Delta$ , causes a change,  $2\Delta$ , of the angle at which the light hits the prism surface. Due to Snell's law, and the high index of refraction of the prism, the angular change in beam direction is smaller inside the prism. The input coupling efficiency as a function of the error in the angle of the mirror (relative to the position for maximum coupling) is listed in a table beside Figure 7. This does not include the loss at the upper prism face.

The mirrors in our setup are mounted on kinematic mirror mounts, which have a maximum angular accuracy of 0.1 mrad. The mirror holders are mounted on one-axis translation stages, so that the light can be directed towards the prism when the mirror is rotated. In addition, the position of the beam relative to the back of the prism can be controlled. The translation accuracy needed is about half a millimeter. The mirrors and beamsplitter are mounted on a 12" x 12" breadboard. We are investigating whether vibrations in the light delivery setup will be large enough to cause a significant reduction in the angular accuracy of the mirrors. In addition, since we are splitting the TE and the TM beams, we must control vibrations to maintain the high signal to noise ratio we have obtained in tests of the biosensor using end-coupling instead of prism-coupling. Vibration of the apparatus could introduce a time-dependent relative phase-shift between the TE and TM beams.

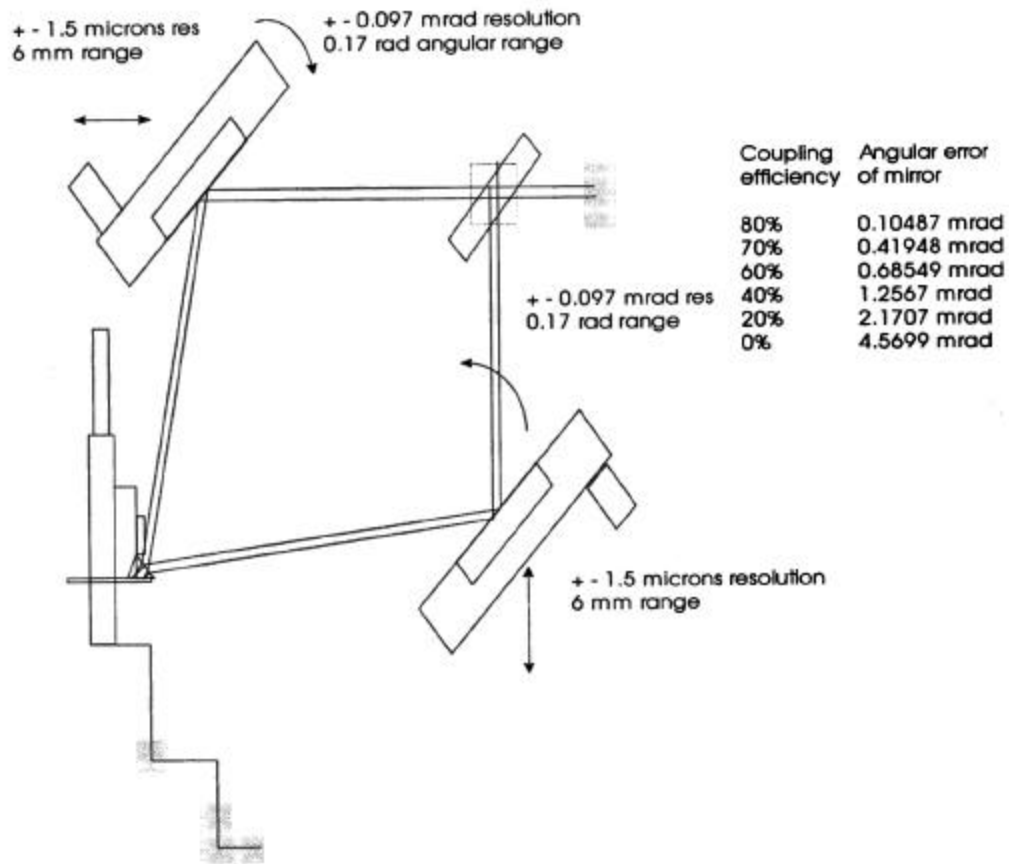


Figure 7. Light delivery system for prism input coupling.

The translation stages for the mirrors and beamsplitter fit inside an 8" x 8" area of the mounting board as shown in Figure 8. The stages are mounted on adjustable interface blocks attached with screws to the standard grid of 1/4-20 holes on the breadboard for the initial alignment of the components. Figure 9 shows a top view of our setup.

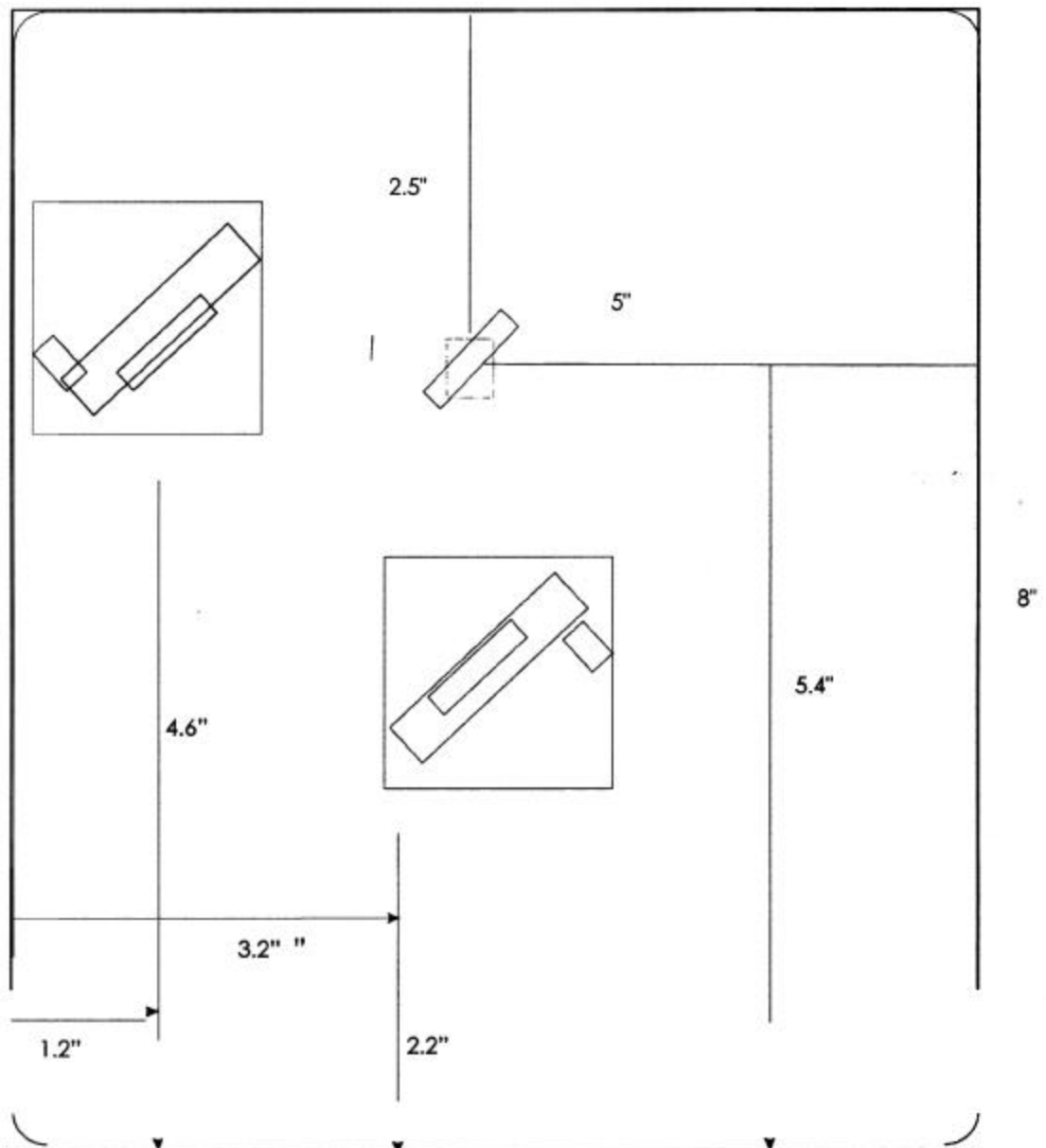


Figure 8. Placement of mirrors and beam splitter on breadboard.

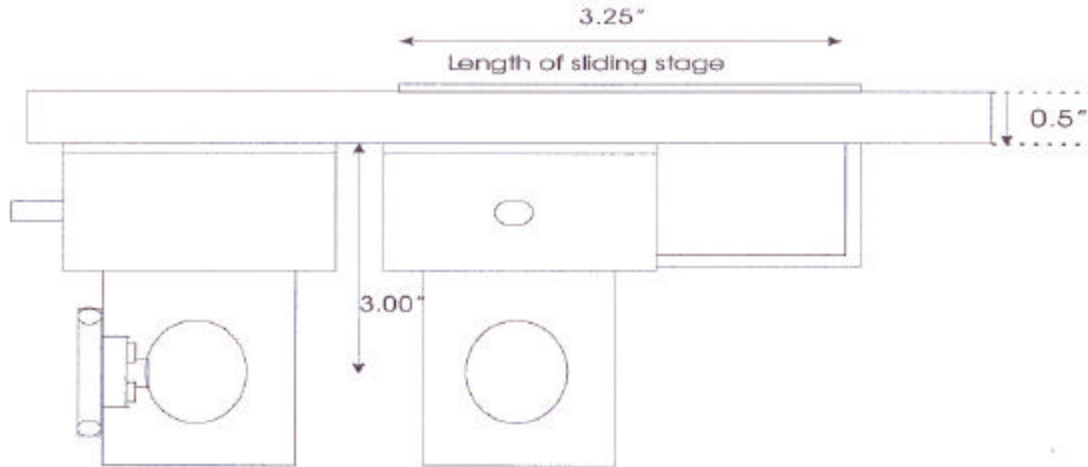


Figure 9. Top view of light delivery setup.

## 7 Appendix B. Derivation of Gap Height Equation

Determine the gap distance ( $h$ ) between the prism and guiding layer necessary to achieve a particular coupling rate. The coupling rate depends exponentially on the prism gap height:

$$\alpha = Ae^{-2|a|h}$$

The angle,  $\theta$ , in Figure 6, is determined by the  $n_{eff}$  of the waveguide mode and the index of refraction of the prism. The constant,  $a$ , is determined by the  $n_{eff}$  of the waveguide mode and the index of refraction of the material in the gap between the prism and waveguide surface. Putting in these dependencies, and solving for  $h$ :

$$\cos \theta = n_{eff} / n_p$$

$$\ln \alpha = -2hAk_0\sqrt{n_{eff}^2 - n^2} + \ln A$$

$$h = -\frac{\ln(\alpha / A)}{2k_0\sqrt{n_{eff}^2 - n^2}}$$

$$h = -\frac{\ln\left(\frac{1.36(2)\cos\theta}{AW}\right)}{2k_0\sqrt{n_{eff}^2 - n^2}}$$

$$h = -\frac{\ln\left(\frac{1.36(2)n_{eff}}{nAW}\right)}{2k_0\sqrt{n_{eff}^2 - n'^2}}$$

The above is an expression for the gap height to use for optimum coupling of a beam of width W. n and n' are the indices of refraction of the gap region and the prism region, respectively.  $k_0$  is the free space wavevector for the coupling light.

# 8 Appendix C. Plans for Prism Clamping Device

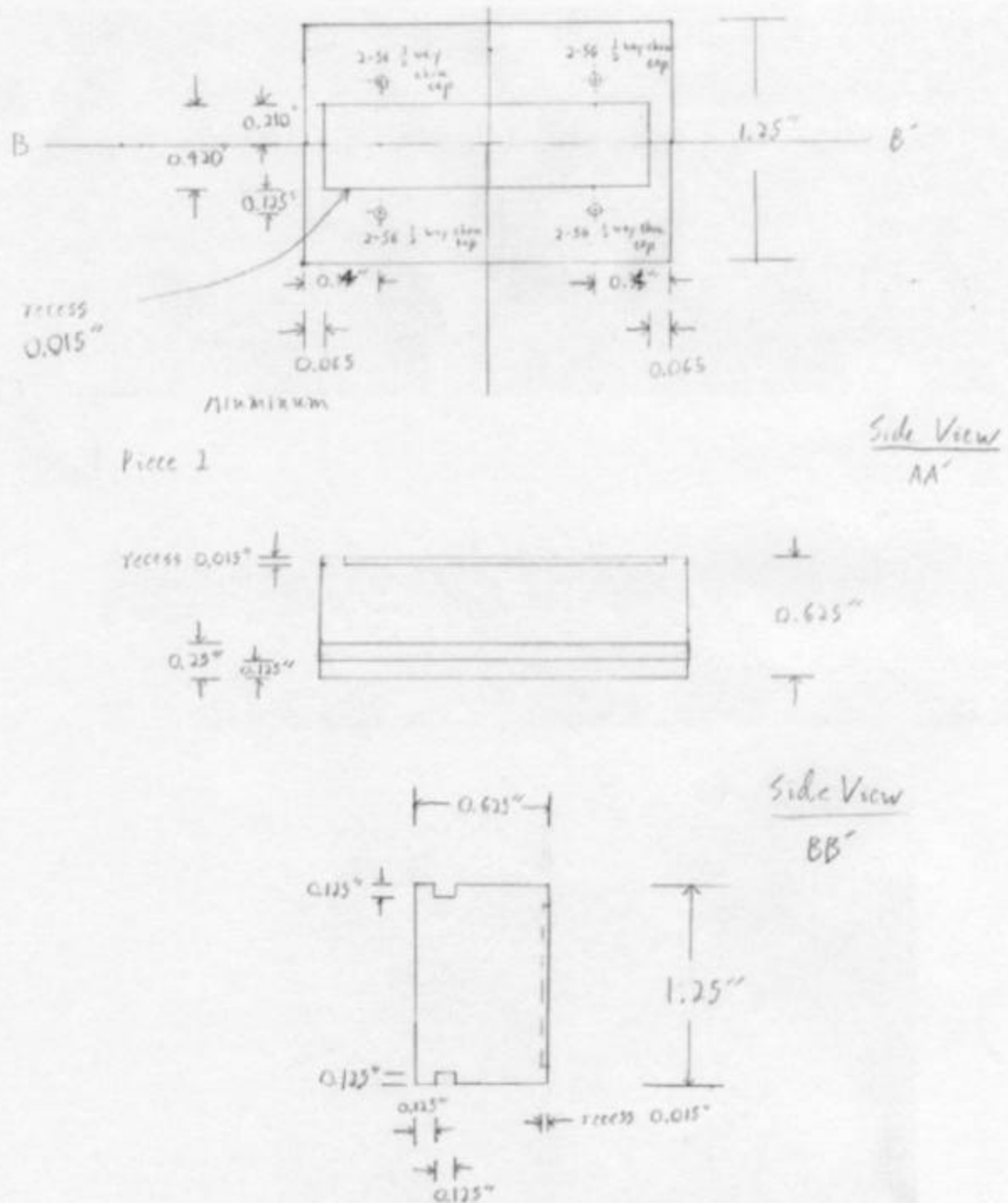


Figure 10. Plans for the aluminum base for the waveguide, prisms, and delrin clamps. The waveguide sits in the recessed areas. Screws hold the two delrin pieces in place above the prisms.

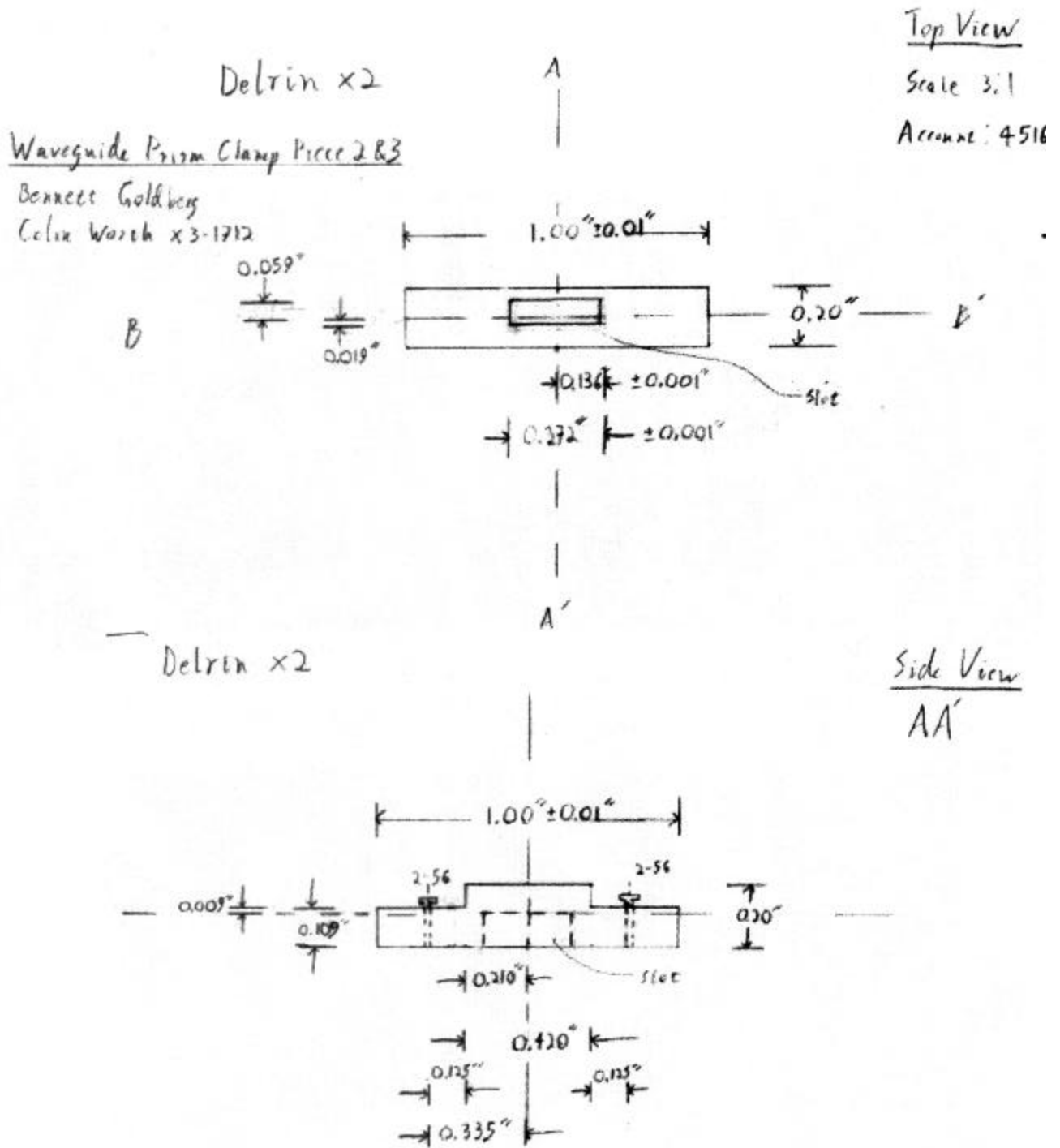
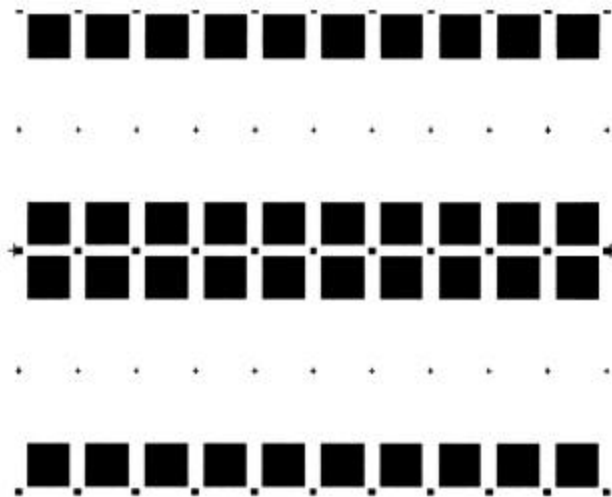


Figure 11. Plan for two delrin, rod shaped, slotted prism clamps. The upper prism corner fits inside the slot, and the clamp makes contact with the slanted face and back face of the prism. Downward pressure is applied to the prism by tightening the two 2-56 screws holding the delrin rods in place.

## 9 Appendix D. Mask Images for Nitride Prism-Coupled Waveguides



**Figure 12.** Layer one of Nitride-Mask-040401 for prism coupled, silicon nitride waveguides. This mask layer contains the cuvette regions and fiduciary marks for alignment with the second mask.



**Figure 13.** Layer two of Nitride-Mask-040401. This layer contains the rectangular prism areas on either end of each waveguide. Square fiduciary marks allow the mask to be aligned with the first layer mask.

# **Appendix 4-C: Design Report for Grating Coupled Waveguides**

Boston University Group  
Prof. Bennett Goldberg  
Prof. M. Selim Ünlü  
Colin Worth

Progress Report  
March 29, 2001

Progress report covers the following areas:

1. Numerical simulations and analytic analysis of gratings for waveguide coupling
2. Waveguide specifications for fabrication
3. Waveguide fabrication for prism coupling
4. Waveguide fabrication for MIT surface chemistry

## 1.0 Numerical Simulations and Analytic Analysis of Grating Coupling

### 1.1 Introduction

The next generation of evanescent wave phase biosensors requires a compact footprint and an integrated approach to the input and output optics. The optical path for the two polarization modes that interfere to generate signal from the surface bound moieties are planned to be underneath the waveguide while the microfluidic flow is above. To couple light in from underneath, waveguide grating coupling is the preferred method. This is simply because gratings can be buried within the structure and fabricated during the waveguide fabrication process. The competing approaches of end-fire coupling and prism coupling both pose much more substantial problems. Prism coupling is very difficult, since one must develop access to the guiding layer from below. In principle, this could be accomplished by etching through the substrate with vias, and then creating a supporting structure from above. However, this approach will have difficulties since the guiding layer will be exposed to the elements, especially those of the surface chemists. Also, such an approach would have strain fields that would compromise the coupling efficiencies. The final approach, endfire coupling, requires precise alignment and polished end facets, the latter which would again be exposed to the elements, especially those of the surface chemists. Thus, we have decided upon grating coupling.

To develop the correct approach and design the optimal structure we have done both analytic and numerical simulations of grating coupling. The problem consists of solving, either analytically or numerically, the angles, efficiencies, and tolerances of light incident on a periodic input grating etched into the guiding layer of a single-mode waveguide and the light extracted from a periodic output grating etched into the guiding layer of a single mode waveguide. The parameters include the period, duty cycle, depth, and length.

The software package we are using for numerical simulations is called FullWave, and distributed by RSoft, Inc. Fullwave works by solving Maxwell's equations for a given initial (harmonic) electromagnetic field and refractive index distribution in the 2D plane perpendicular to the layer, and updating the electro-magnetic field amplitude(s) based on the solutions over a short, adjustable time interval. It then solves Maxwell's equations for the new field, updates them again, etc., to simulate the behavior of light over time. This method is called FDTD, or finite difference time domain and is a different approach than the beam-propagation method (BPM) as it does not use para-axial approximations. The latter are not accurate unless the majority of the light travels in a certain numerical aperture in a particular direction. Since we plan to grating couple with light beam angles almost normal to the direction of light propagation in the waveguide, BPM methods (which we used for mode-solving and determination of waveguide biological sensitivity) are not sufficient for grating simulations. Thus FullWave simulations provide more freedom and information than BPM simulations.

In addition, we have performed our own first and second order analytic analysis to determine approximate coupling angles into the waveguide modes (TE and TM). The analytic approach allows us to confirm the numerical simulations, and determine the input parameters for the numerical simulations.

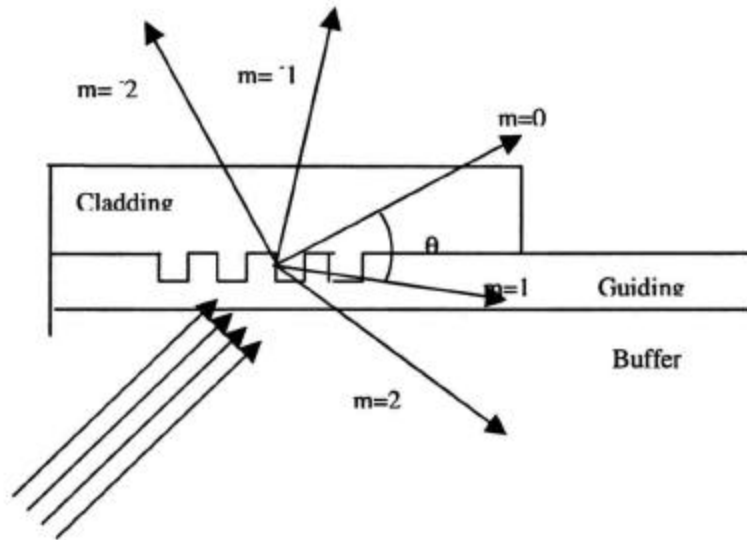


Figure 1. Grating in coupler for a slab waveguide. Guided light travels to the right (+z).  $\theta_{+1}$  indicates the angle between the zero<sup>th</sup> and first diffraction orders of the grating. This purpose of this figure is to illustrate the definition of the grating modes. The angles do not reflect the angles necessary

## 1.2 Basic Grating Coupling Parameters

The parameters to be determined for grating coupling are:

1. Grating period
2. Angle of incidence for incoming/outgoing light
3. Depth of grating
4. Length of grating (determined from coupling rate of external field to the waveguide modes)
5. Efficiency

## 1.3 Analytical Modeling

The analytic method is to solve for the wavefunction in the grating layer analytically and determine the characteristic leaky (input and output) and guided modes in the waveguide-grating structure. These are called leaky, since they couple light into or out of the guided mode. Several articles have been written on this topic<sup>1,2</sup>, and solutions have been obtained for rectangular, sinusoidal, and blazed gratings. These are the structure of the gratings in the plane perpendicular to the grating period. Like the software simulation, analytical methods can also provide the necessary grating parameters and calculate the coupling efficiency. In a recent article<sup>3</sup>, a group used a blazed grating with variable tooth depth to obtain slightly less than 50% input coupling efficiency, and 95% output coupling efficiency in a Polymer (PMMA) waveguide at 633 nm wavelength. (Note: the waveguides they used had different indices of refraction of the film and substrate layers than our silicon nitride/silicon dioxide waveguides. They may have varied the waveguide parameters to achieve such high coupling efficiencies.) We are working on a numerical mode-solving method based on a technique described in Peng, et. al. in parallel with the software simulations.

<sup>1</sup> S.T. Peng, Theodor Tamir, Henry L. Bertoni, "Theory of Periodic Dielectric Waveguides," IEEE Transactions on Microwave Theory and Techniques, MTT-23, 123-133 (1975)

<sup>2</sup> L. R. Lewis, A. Hessel, "Propagation Characteristics of Periodic Arrays of Dielectric Slabs," IEEE Transactions on Microwave Theory and Techniques, MTT-19, 276-286 (1971)

<sup>3</sup> R. Waldhausl et. al, "Efficient Coupling Into Polymer Waveguides by Gratings," Applied Optics 36, 9383-9390 (1997)

First, we present first order results determined analytically from the propagation factors of the guided mode, as well as an introduction to the operation of grating-waveguide couplers.

Grating couplers in monomoded and bimoded waveguides operate (to first order in accuracy) by diffracting light from an incident beam (see Fig. 1) at an angle that matches the characteristic angle associated with one of the propagating waveguide modes. A waveguide mode can be characterized by the z-component of its wavevector,  $k_z$ , or by the ratio,

$$n_z = n_{\text{eff}} = \frac{k_z}{k_0}, \quad k_0 = \frac{2\pi}{\lambda}$$

In the typical model of grating operation, light is scattered from each grating 'tooth' in all directions, and interferes constructively at several discrete angles to form new beams (cf. Fig. 1). The refracted beam that obeys Snell's law for the dielectric boundary (without grating) is the zero<sup>th</sup> order grating mode. Beams diffracted forward with respect to the zero<sup>th</sup> order mode ( $\theta > 0$ , cf. Fig. 1) have positive, integral mode numbers, and waves diffracted backwards ( $\theta < 0$ ) have negative, integral mode numbers. It is only necessary for one of these modes to match the  $n_z$  of the waveguide mode for coupling of power into the waveguide. It is important to note that for a guided (confined) waveguide mode,  $n_z > n_{\text{buffer}}$ , and therefore incoupling via the zero<sup>th</sup> order mode is impossible.<sup>4</sup> Therefore, depending on the grating period, coupling is accomplished through the  $m = -1$  or  $m = -2$  two grating mode. This is illustrated in Figure 2, below:

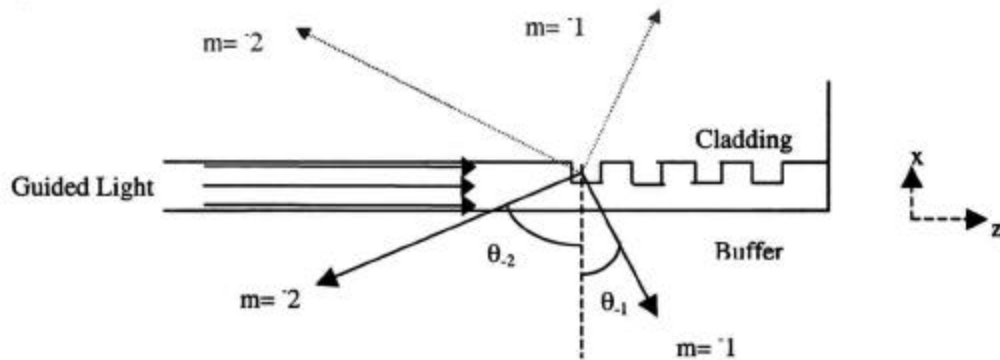


Figure 2. Grating outcoupling for a slab waveguide. This time the guided light is incident on the grating. It is diffracted into several output coupling orders.

In Figure 2, instead of fixing an external incident beam, we allow the guided mode field to impinge on the grating, creating diffracted beams. The diffracted beams are coupled to the waveguide mode, and carry energy away from the waveguide. The angles of the diffracted beams depend on the grating period. For the indices of refraction of silicon nitride ( $\text{Si}_3\text{N}_4$ ) and silicon dioxide ( $\text{SiO}_2$ ) the zero<sup>th</sup> mode is totally internally reflected, so we use the normal to the waveguide profile boundaries as a reference direction for defining the angles of the minus one and minus two diffraction beams. Since the behavior of light under time reversal can be depicted by reversing each arrow direction in Figure 2, this diagram also depicts the angles needed for input coupling.

The angles,  $\theta_1$  and  $\theta_2$ , are functions of the grating period. To select a convenient angle for coupling, we can vary the grating period. As the grating period increases (decreases), the two beams depicted above rotate in the counterclockwise (clockwise) direction. This behavior is illustrated for the minus one mode in Figure 3, below, for a guiding layer height of 166 nm. (Important note about

<sup>4</sup> Guided modes propagate at a shallow angle (with respect to z). The  $n_{\text{eff}} \propto k_z$  of the propagating mode meets the requirements for total internal reflection (TIR) inside the guiding layer boundaries. Therefore, there is no possible external incident beam that could couple to the guided mode at the dielectric interface.

polarizations: the  $n_{\text{eff}}$  values for the first TE and the first TM waveguide modes are slightly different and therefore produce slightly different coupling angles. The TE mode is indicated in blue, and the TM mode is indicated in red. The line marked 'Diff' is the difference (in degrees) between the two. The first two lines both represent a  $m=-1$  order grating)

Figure 4 shows a broader range of possible grating periods. At a grating period of about 0.72 times the wavelength, the minus two mode appears in addition to the minus one mode. It's angle is always lower than the angle for the  $m=-1$  mode. To connect this to Figure 2, if one scans across Figure 3 from left to right, the coupling angles rotate counterclockwise in Figure 2 (above). The first angle assumed by the  $m=-2$  mode is  $-90^\circ$ .

Below the cutoff at around 0.7 times the wavelength, only one coupling order exists. There are advantages and disadvantages to working in this regime. One advantage is that we do not have to deal with substrate modes excited by higher order grating modes, and thus the output coupling is simpler and not complicated by interference with higher order modes. Another advantage is that the efficiency of input coupling is increased due to the absence of higher order modes. On the other hand, gratings with smaller periods, of order 410 nm, are more difficult to fabricate. Expensive direct-write techniques (using e-beam writing) may be necessary if cheaper lithographic techniques do not provide high enough resolution.

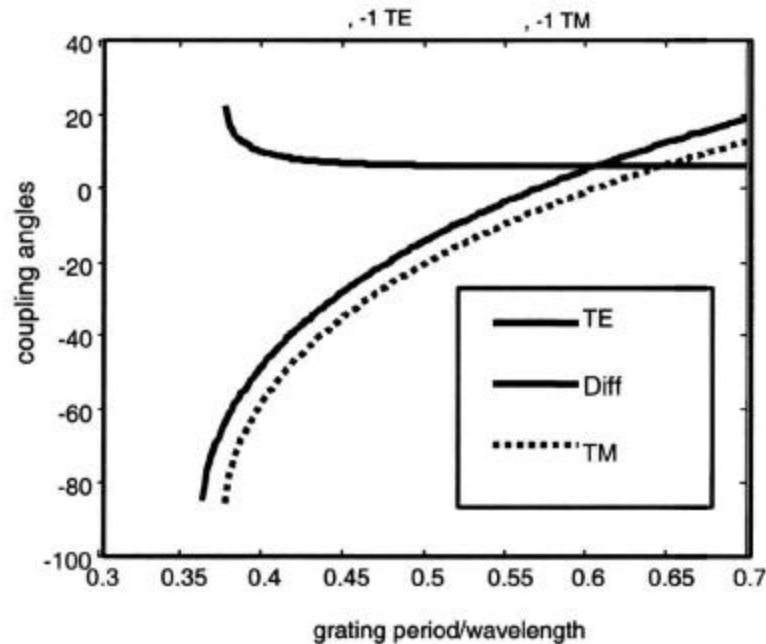


Figure 3: First order grating coupling angles for the TE and TM modes of our waveguide, as a function of grating period. The guiding layer is silicon nitride. The buffer and cladding are silicon dioxide.

#### Calculation of First and Second Order Grating Modes:

In summary of the analytic calculations, we have shown the coupling angles as a function of grating period for a silicon nitride waveguide of the 166nm thickness guiding layer. Note that the depth of the grating is not a parameter of the analytic calculation.

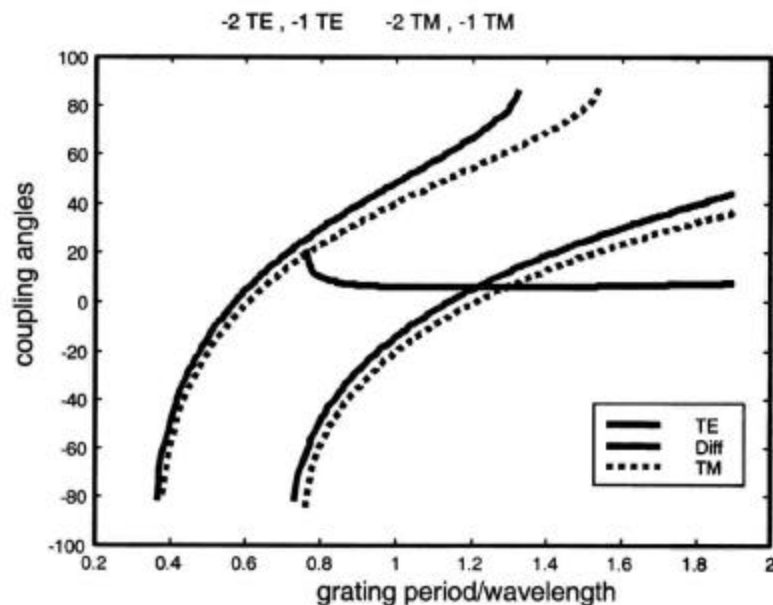


Figure 4: First and second order grating coupling angles. The left section of the plot is identical to Figure 3. As the grating period increases beyond  $0.7 \lambda$  (wavelength), the second order mode appears for TE and TM. In agreement with Figure 2, the angle of the  $m=-2$  mode is always more negative than that of the  $m=-1$  mode (as a function of grating period). The difference line in black is the difference between TE and TM coupling angles for the second order mode only.

## 1.4 Numerical Modeling

The previous analytic calculations incorporate the fact that the waveguide mode (i.e. electromagnetic field distribution in the waveguide) is affected by the presence of the grating by averaging the  $n_{\text{eff}}$  values for the guided modes with and without grating. However, the change in the guided light is due to a more complex interaction with the grating structure. This is the reason that we believe the numerical simulations differ from the analytic results shown in figure 10. We will return to this point later. First, however, we will describe the numerical simulations.

The waveguide with grating forms an (almost) periodic structure in the (z) direction of propagation. Therefore the solution for the guided wave has additional Fourier components that conform to the period of the grating. The additional components are analogous to the solutions for the wavefunctions of electrons in a periodic crystal lattice. The amplitude of each additional component is affected by the width(z-dir) and depth(x-dir) of the grating teeth, and by other aspects of the grating shape if it is not rectangular. To test our calculations, we therefore performed extensive numerical simulations using FullWave software described in the introduction.

## 1.5 FullWave Simulations

Numerical solutions were obtained with the Fullwave package provided by RSoft, Inc. The first step in our simulations was to experiment with simulation parameters such as the overall size of the simulation space and the size of the discretization grid. Currently we are using a simulation space 6 microns wide (x-direction, transverse to the waveguiding direction) and 12 microns long (z-direction, in the direction of wave propagation), with a mesh size of 10 nm along x, and 20 nm along z. We found that using larger mesh sizes induced artificial changes in results such as coupling angles. These distances can be compared to the approximate grating period of 370 nm, and grating depth (x-direction) of 25 to 40 nm. Although, ideally, we would like to expand our overall simulation space, the time necessary for a larger simulation, (due to the amount of numerical processing and not to memory size limitations) becomes

impractical. In addition, it is not difficult to determine the behavior of the light over long path lengths once the behavior over short path lengths is known.



Figure 5: Portion of waveguide with grating shown in profile. Red represents Silicon Nitride. Blue represents silicon dioxide. The grating material is also silicon dioxide and are illustrated with the small black cut-out portions. The green rectangles are power monitors, used for determining the rate of power coupling to radiation modes (outcoupling). The power monitors are thus used to determine the correct length and depth of the grating for the fabrication specifications.

A diagram of our simulation model is shown in Figure 5. One feature of FullWave is the ability to insert one dimensional or two dimensional power monitors (for two and three dimensional simulations, respectively), which measure instantaneous or average power flux through a particular area of the simulation space. By placing multiple power monitors which span the guiding layer, along the length of the grating region, we can determine the rate of outcoupling of the light. These are illustrated by the green power monitors in figure 5.

After establishing basic simulation parameters, we did multiple simulations for TE and TM light, varying the grating period and the grating depth. Varying the grating period changes the angle of the outcoupled beam in accordance with first order calculations (cf. Figs 3 and 4). Differences in angle were also observed for different grating depths, an effect which is not explained by first order arguments, but is related to a change in the effective index of the TE or TM mode due to the presence of deeper or shallower grating in the material. Aside from the slight change in outcoupling angle, varying the grating depth varies the rate of power transfer from the guided mode to the input or output beam.

The angles and power transfer rates determined for output coupling can be used to determine optimum parameters for input coupling, in particular the length of the grating, in a way similar to the technique we used for prism coupling in earlier work. Figure 6 shows a simulation demonstrating output coupling for a grating period of 0.65 wavelengths ( $0.411 \mu\text{m}$ ) and TE and TM polarization, respectively. Figure 7 shows an input coupling simulation. Note that the axes are rotated forty-five degrees from the Figure 6.

We have used such modeling to accurately determine the optimum grating parameters for the design of the initial waveguides. Figure 8 shows a summary of the outcoupling simulations, where the outcoupling angles as a function of the polarization, the grating depth and the grating period for first order coupling have been determined. From data, note that the depth has only a minor correction to the coupling angles as expected.

The way we determined the final period for the fabrication specifications was by examining the data in figure 8, where the coupling angles as a function period and depth are summarized. It is necessary to work at coupling angles which are positive, that is greater than zero, since at zero the left and right coupling is symmetric, leading to an equal amount of a backward propagating wave. We also wanted to work close to normal for several reasons. First, working at close to normal causes as few substrate losses as possible and second, working close to normal eases the construction requirements. Thus we have chosen 7 degrees and 12 degrees for TE and TM respectively. There is no particular reason why it is 7 and 12, it could have easily been different by a degree or two without changing fabrication tolerances. Thus we have determined the coupling angles.

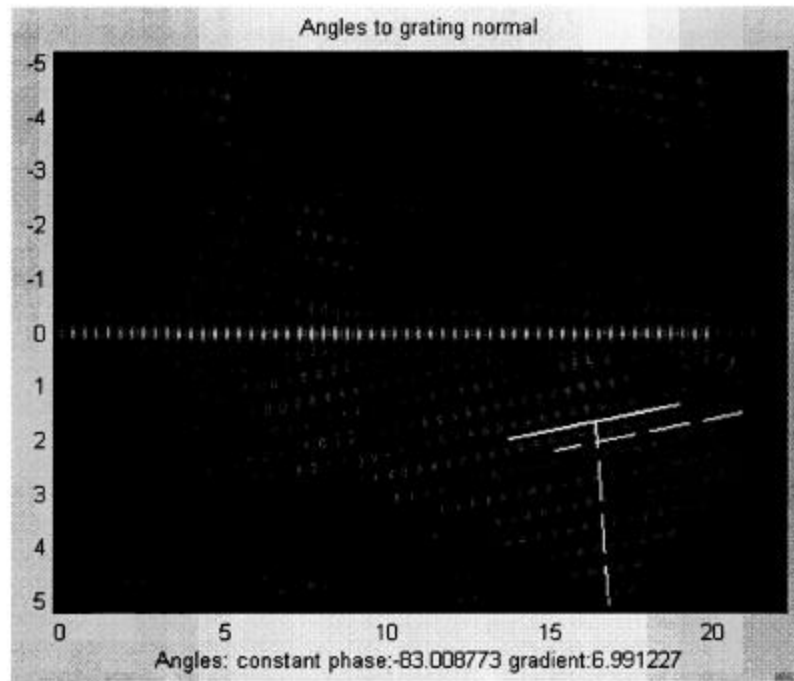
With the coupling angles determined as described above, we also did separate incoupling simulations to find the peak in coupling power as a function of the angle of the incident beam. This information is shown in figure 9, and represents a further check on the coupling as a function of angle. To perform these simulations, power monitors were used to find the dependence of the coupling as a function of angle. Note that we can also determine the amount of power coupled into the backward propagating mode with this technique.

Finally, to fully confirm the analytic and numerical simulations, we compared both the outcoupling and incoupling simulations and found them to be in close agreement, as displayed in figure 10. Figure 10 displays both the analytic and numerical simulations. The analytic solutions and the series of outcoupling simulations are shown as the solid lines and described in the figure caption. The solid dots represent several simulation runs of incoupling as in figure 9 and described above. There is good overall agreement, though the outcoupling simulations are slightly different than both the incoupling simulation and analytic calculations. We currently do not understand this difference.

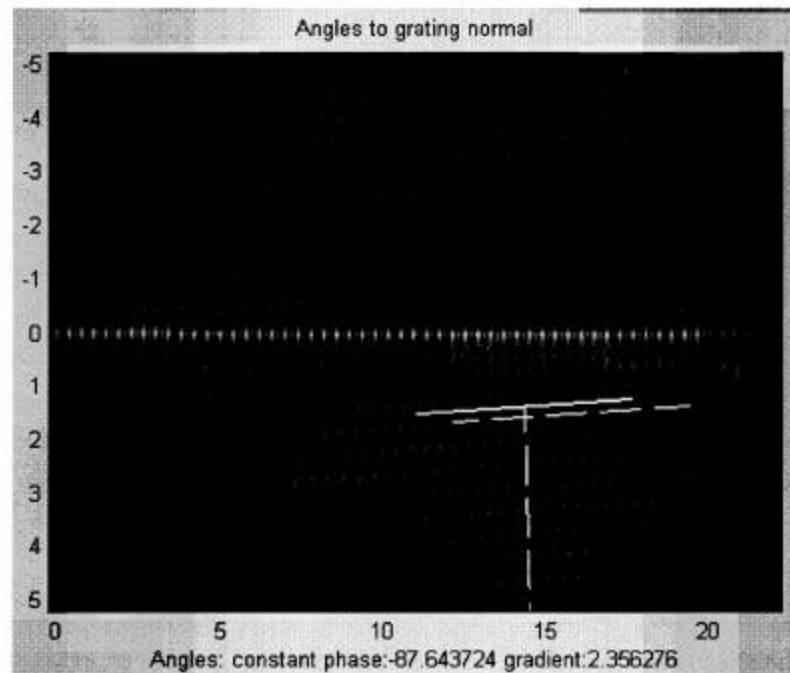
We also did calculations to determine the angular change that would result from the allowed fabrication tolerances for the width of the guiding waveguide layer and indices of refraction of the guiding and cladding materials. Simulations were performed to test the tolerance of the input angle to inaccuracies, or variances in the height of the guiding layer (due to the nature of the fabrication process). Deviations within the material tolerances specified in Section 2 result in a  $\pm 1$  degree or less change in the TE and TM coupling angles.

Having determined the grating period, we needed to find the optimal grating depth. To find the appropriate depth and length of the grating, that is the optimum beam size, one needs to determine the coupling rate of the light into and out of the grating as a function of its length and depth. This was determined by monitoring the power loss to outcoupling as a function of distance along the grating in the direction of wave propagation. The power loss is a decaying exponential function of distance. The data points in the plot of figure 11 are the inverse of the coupling or decay coefficient as a function of grating depth and period. They are arrived at by fitting the power loss as a function of distance for a given grating depth and period to a decaying exponential. The plots show an increase in outcoupling for deeper grating depths, but as expected there is not much change in the outcoupling rate as a function of the grating period (although the angle of the outcoupled light changes (see previous outcoupling plots). A major result of this plot is the significant difference in coupling rate of TE versus TM as a function of grating depth. For large grating depths, for example the 75 nm data set, the TM is 20-50 times smaller coupling, or larger effective beam size than TE. Thus, we choose a smaller grating depth to allow for coupling of similar size beams. A grating depth of 25 nm yields  $1/e$  points of 150 microns for TE and 400 microns for TM. Thus a grating length of several  $1/e$  lengths will couple most of the light into or out of the guiding layer.

In conclusion for the first order results, the grating period of  $0.65 \times$  wavelength was determined by choosing a small positive angle for coupling. The depth was determined by requiring similar beam sizes for TE and TM. The length was then determined by the coupling rate for that depth.



### Outcoupling\_TE



### Outcoupling\_TM

Figure 6: Numerical Simulations of outcoupling for a 0.65 wavelength grating period and a grating depth of 25 nm. Simulations were used to compare the angle of the diffracted mode with analytical calculations, and to monitor the rate of coupling.

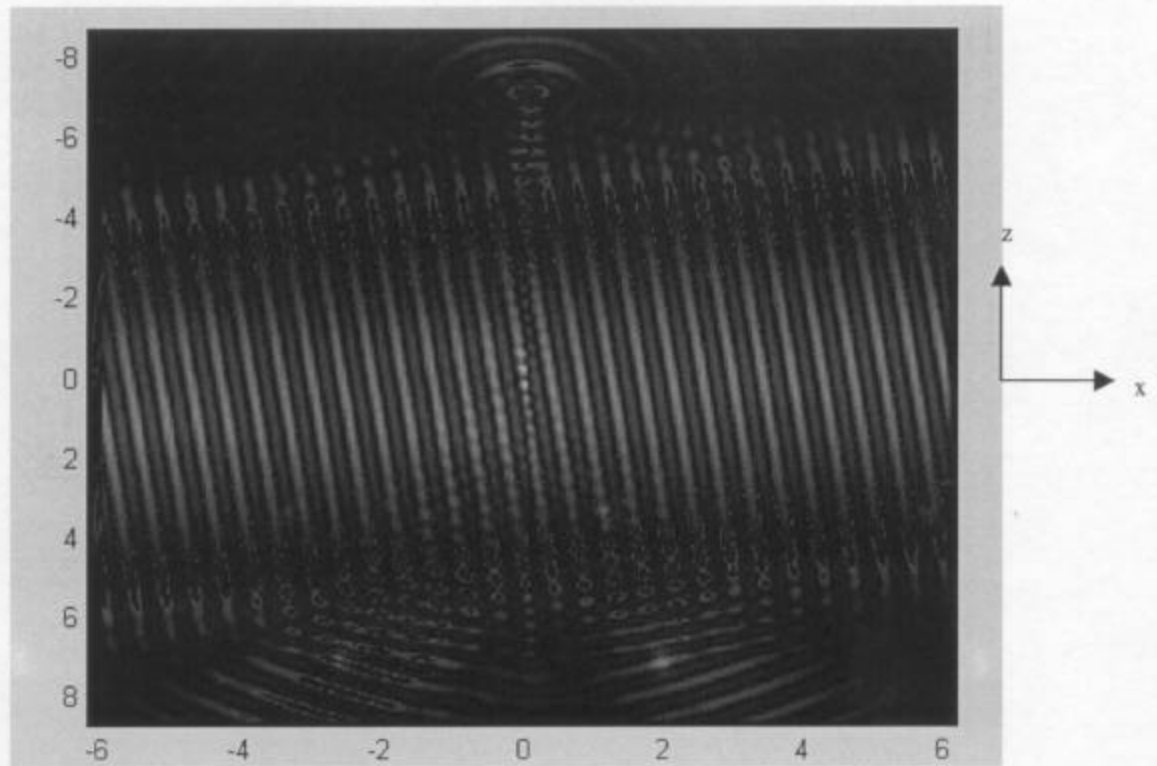


Figure 7: Incoupling. A large (8 micron) beam impinges on a waveguide, causing significant coupling in the positive z direction (light at top of figure). The waveguide direction of propagation is oriented upwards and the beam comes in at an angle of eight degrees below horizontal from the left. The beating behavior in the center of the picture is due to light interacting with the periodic grating.

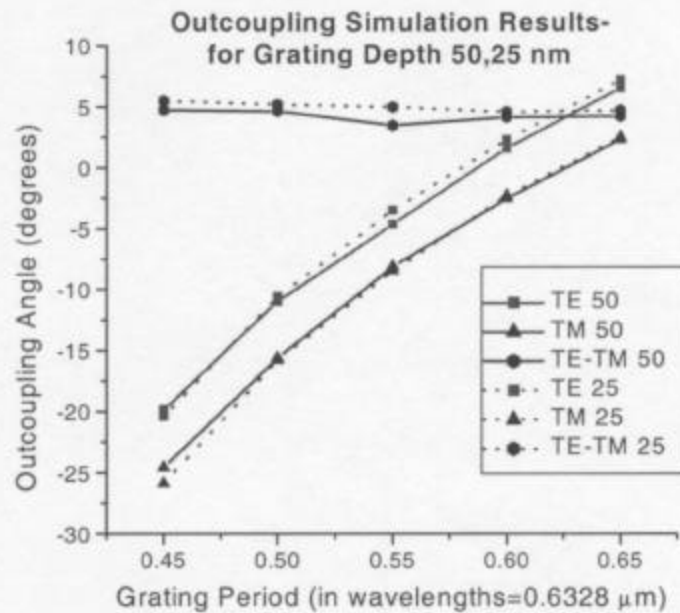


Figure 8: Summary of outcoupling results. Output angles were measured as a function of grating period. The solid and dashed lines correspond to grating depths of 50 and 25 nm, respectively

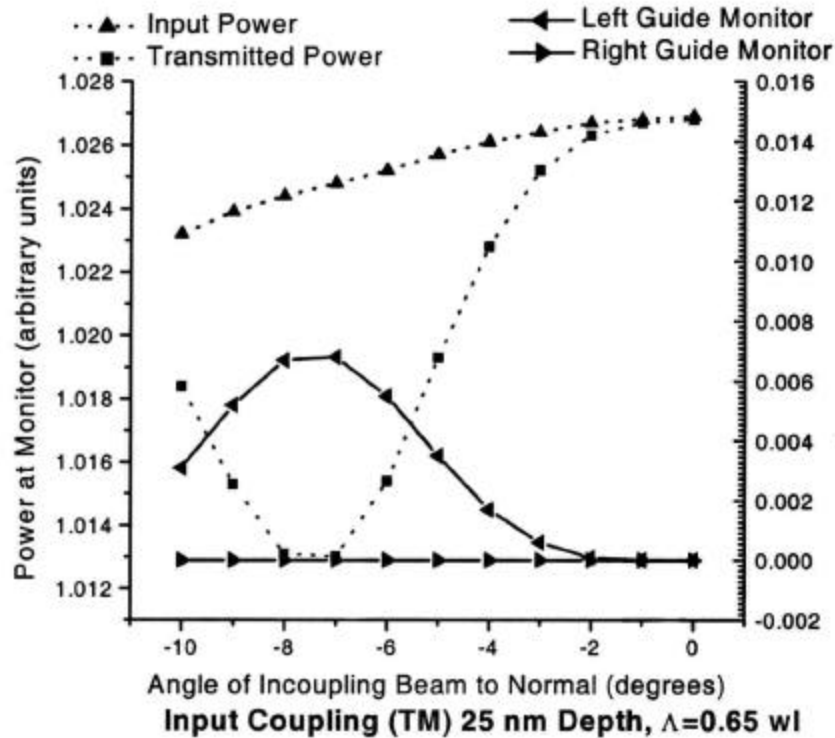


Figure 9: Sample input coupling result. This plot shows the amount of power coupled into the waveguide in the +z (blue) and -z (black) directions, as a function of the angle of the incident beam to the waveguide surface normal. The peak in input coupling is slightly above seven degrees for the TM polarization, in the buffer ( $\text{SiO}_2$ ) layer. This corresponds to an angle of 10.5 degrees in air. The black and blue lines are monitors of the total power at the source of the Gaussian (incident) beam, and at the exit point (light not coupled into the waveguide). Note the different scales for the former and latter type of power monitors. Using several plots like this for different grating periods, optimum input angles were determined and compared with the results of outcoupling and analytical methods. The results of these different runs are shown in figure 10 as the round dots referred to as the maximum forward incoupling.

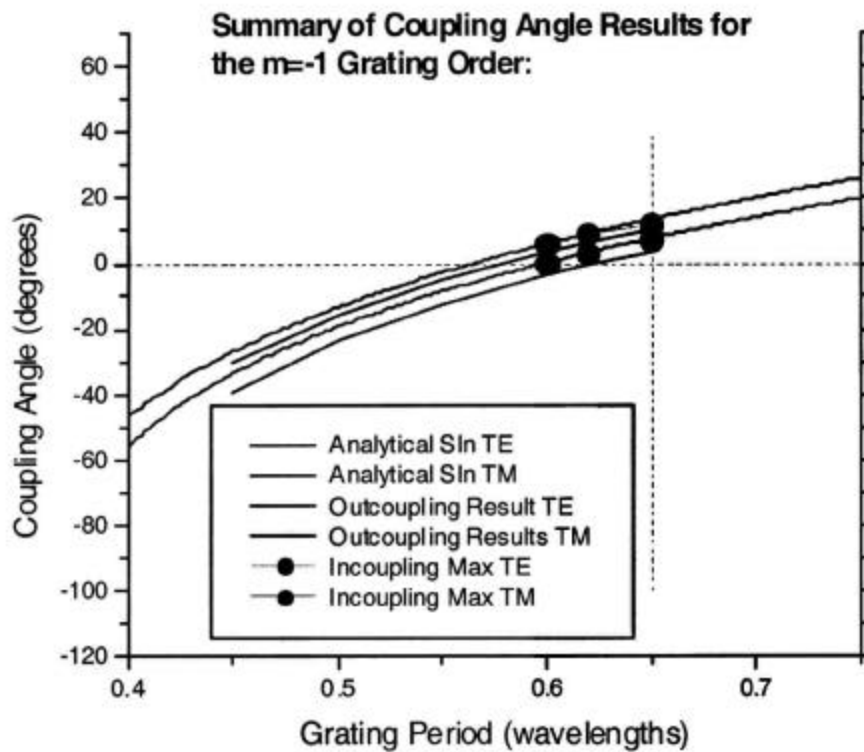


Figure 10: Results for the coupling angles determined both analytically, and with outcoupling and incoupling simulations. The agreement between the analytical solution and results obtained from incoupling agree quite closely. The results from output coupling are shifted by about three degrees towards lower angles.

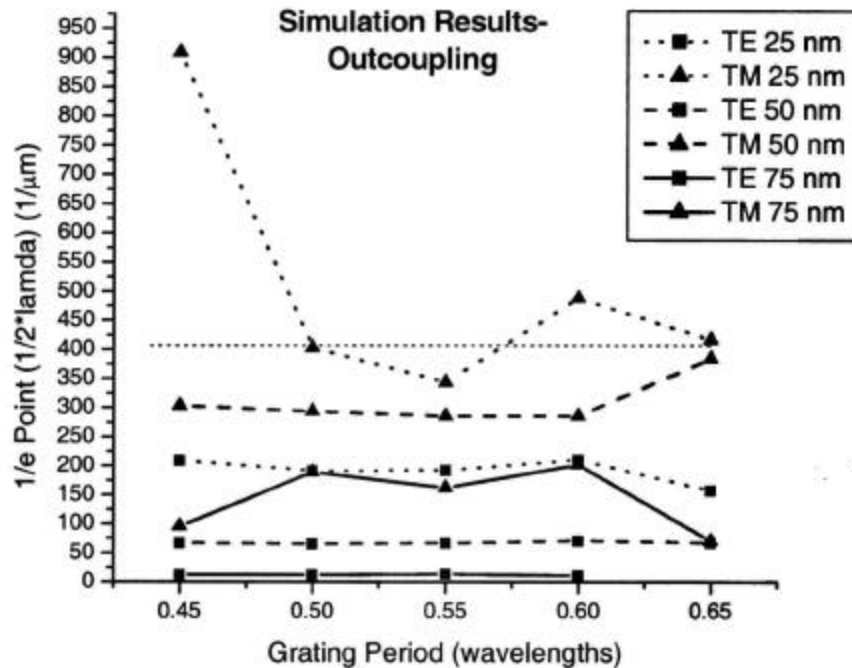


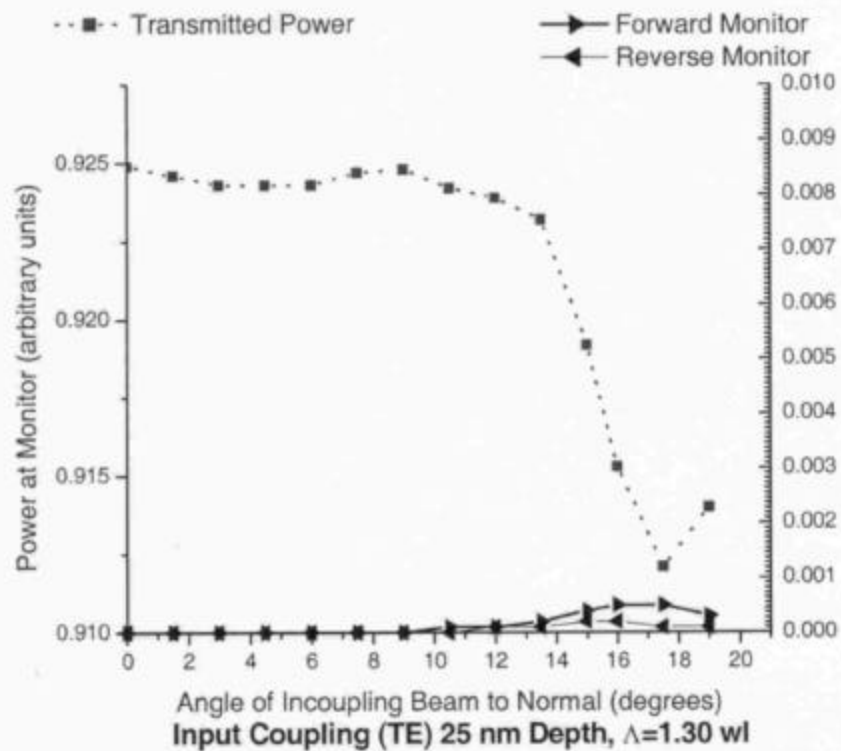
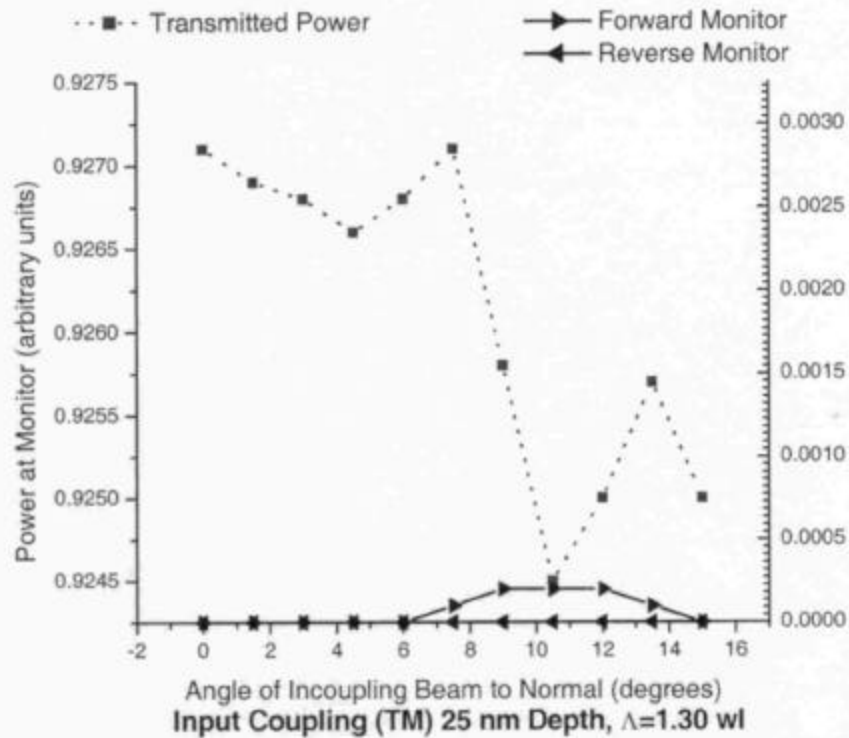
Figure 11: *First order outcoupling rate*: The above plot shows the loss of power from the waveguide mode due to outcoupling through the grating. The power flux in the waveguide was monitored at regular (spatial) intervals along the grating in the direction of propagation. The plots show an increase in outcoupling for deeper grating depths. There is not much change in the outcoupling rate as a function of the grating period (although the angle of the outcoupled light changes (see previous outcoupling plots)). First the natural log of the flux values was used to calculate the exponential decay coefficient of the grating mode. One over this value (plotted below as a function of grating period and grating depth) gives an estimate of the outcoupled beam size (in the longitudinal direction)

## Second order grating calculations and simulations:

There are technical fabrication difficulties associated with fabricating first order gratings. The difficulty is that direct e-beam write is necessary for the resolution of the  $\frac{1}{4}$  the period, which is what would be required. If alternative techniques like embossing or projection lithography are pursued, then e-beam could create the template or mask. Now, however, we are looking largely at contact lithography which has a minimum resolution of  $\sim 0.3$  microns. Thus we have also performed all of the above simulations and calculations for second order gratings, calculated to conform to the same input and output coupling angles as the first order to ensure platform compatibility.

Figures 12 and 13 display incoupling simulation results for second order coupling. The power coupled to the first TE and TM mode of the waveguide are shown as a function of the angle of the incident beam to the normal to the waveguide surface. The blue monitors indicate coupling in the forward direction. The red monitors show a corresponding drop in power transmitted past the waveguide at the correct coupling angles. From these and other simulations, we have determined the correct grating parameters of period and depth for second order coupling at the same angles as the first order coupling.

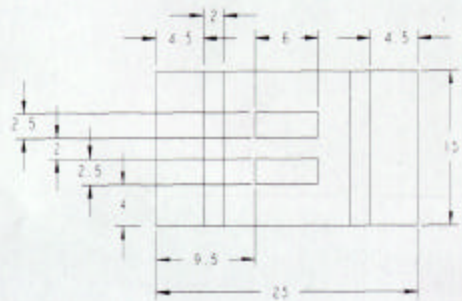
The last table shows the end results of the calculations for first and second order coupling.



Figures 11 and 12: *Incoupling simulation results for Second Order coupling*: The above two plots, show the power coupled to the first TE and TM mode, respectively, of the waveguide, as a function of the angle of the incident beam to the normal to the waveguide surface. The blue monitors indicate coupling in the forward direction. The red monitors show a corresponding drop in power transmitted past the waveguide at the correct coupling angles.

Order of Coupling	Fabrication Technique	Profile/ Duty Cycle	Period	Depth (directed into guiding layer)	Depth Uniformity across wafer	Coupling Angles	Tolerances
1st Order	e-beam direct write or Deep uv contact	square/ 50%	$0.411 \pm 0.010 \mu\text{m}$	$0.025 \pm 0.005 \mu\text{m}$	$0.025 \pm 0.002 \mu\text{m}$	7.0 deg TE, 12.0 deg TM	$\pm 1.0 \text{ deg}$
2nd Order	Lithography	square/ 50%	$0.822 \pm 0.010 \mu\text{m}$	$0.025 \pm 0.005 \mu\text{m}$	$0.025 \pm 0.002 \mu\text{m}$	7.0 deg TE, 12.0 deg TM	$\pm 1.0 \text{ deg}$

# **Appendix 4-D: Mechanical Layout of Grating Coupled Waveguides for Optical Switch, Corporation**

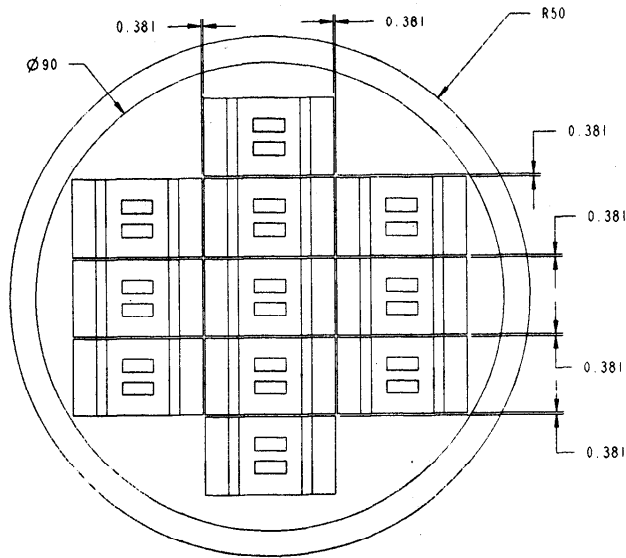


SCALE 4

ITEM NO.	QTY	PART NO.	NOMENCLATURE OR DESCRIPTION	REMARKS
1	1	114 SM-1094	WAVEGUIDE	SATCOM TECHNOLOGY 101 FIRST STREET CHANDLER, AZ 85226
<p><b>METRIC</b> UNLESS OTHERWISE SPECIFIED DIMENSIONS ARE IN MILLIMETERS DECIMALS OF MILLIMETERS FRACTIONS OF MILLIMETERS ANGLES 10° 30' 45' 60' 90' 120' 135° 180°</p> <p>DO NOT SCALE THIS DRAWING</p> <p>THIRD ANGLE PROJECTION</p>				
<p>SIZE: C 114894 SCALE: 4:1 SHEET: 1 OF 1</p>				

NOTICE: THIS DOCUMENT IS THE PROPERTY OF SATCOM TECHNOLOGY CORPORATION AND IS  
DELIVERED ON THE EXPRESS CONDITION THAT IT IS NOT TO BE DISCLOSED, REPRODUCED,  
IN WHOLE OR IN PART, OR USED FOR MANUFACTURE FOR ANYONE OTHER THAN SATCOM  
TECHNOLOGY CORPORATION WITHOUT ITS WRITTEN CONSENT, AND THAT NO RIGHT IS GRANTED  
TO DISCLOSE OR TO USE ANY INFORMATION CONTAINED IN THIS DOCUMENT. THIS RESTRICTION  
DOES NOT LIMIT THE RIGHT TO USE INFORMATION FURNISHED BY VENDORS OR OTHERS OUTSIDE  
SATCOM TECHNOLOGY CORPORATION.

# **Appendix 4-E: Original Waveguide Specification**



REVISIONS			
REV	DESCRIPTION	OWN	APPV/DATE

2	11	2005079	WAVEGUIDE	
1	1		SUBSTRATE	
ITEM NO.	QTY RECD	PART NO. IDENTIFICATION NO.	NOMENCLATURE OR DESCRIPTION	REMARKS
INTERPRET DRAWING PER ASME Y14.5M-1994			SATCON TECHNOLOGY 1st FLOOR BUREAU CAMBRIDGE MA 02142	
<b>METRIC</b> UNLESS OTHERWISE SPECIFIED: DIMENSIONS ARE IN MILLIMETERS TOLERANCE ON DECIMALS XX ± .25MM XXX ± .13MM		UNLESS OTHERWISE SPECIFIED: REMOVE ALL BIPS & SHARP CORNERS AND CONTAINING TIPPED HOLE TO ROOT SIZE FILLETS R 16 MAX. EXTERNAL CORNERS R 16 MAX. SURFACE ROUGHNESS: 6.3 DO NOT SCALE THIS DRAWING THIRD ANGLE PROJECTION MATERIAL SEE PARTS LIST		
4001		DRAWN D. HARRIS 6/6/02 CHECKED ENGINEER APPROVED APPROVED WAVEGUIDE PHOTOMASK		
USED ON NEXT ASST		SIZE CAGE NO. DRAWING NO. REV C 1JB94 2005077 - SCALE 2 CALC WT SHEET 1 OF 1		

NOTICE: THIS DOCUMENT IS THE PROPERTY OF SATCON TECHNOLOGY CORPORATION AND IS DELIVERED ON THE EXPRESS CONDITION THAT IT IS NOT TO BE DISCLOSED, REPRODUCED IN WHOLE OR IN PART, OR USED FOR MANUFACTURE FOR ANYONE OTHER THAN SATCON TECHNOLOGY CORPORATION WITHOUT ITS WRITTEN CONSENT, AND THAT NO RIGHT IS GRANTED TO DISCLOSE OR SO USE ANY INFORMATION CONTAINED IN SAID DOCUMENT. THIS RESTRICTION DOES NOT LIMIT THE RIGHT TO USE INFORMATION FURNISHED BY VENDORS OR OTHERS OUTSIDE SATCON TECHNOLOGY CORPORATION.

# Waveguide Specification

## I. General Description:

The fabrication specifications for an optical waveguide are described below. Each waveguide is derived from a wafer consisting of the following sandwich: 1.) An optical quality fused silica substrate, 2.) a silicon dioxide buffer layer 1.5  $\mu\text{m}$  thick, 3.) a silicon nitride guiding layer 166 nm thick, and 4.) a silicon dioxide cover layer two microns thick. Each waveguide device has two rectangular patterns (cuvettes) etched into the silicon dioxide top surface to expose areas of the silicon nitride guiding layer.

Coupling light in and out of the waveguide is accomplished by means of a grating integrated into the waveguide structure. Specifically, light is coupled into each waveguide from below (through the substrate) by directing a collimated light beam onto a grating etched into the guiding layer. Light travels through the quartz substrate and the waveguide layers, strikes the gratings in the guiding layer, and couples into the two modes (TE and TM) of the waveguide. The light traverses the length of the waveguide, encounters two identical second order gratings at the output end, and couples out the substrate.

A dimensioned drawing of each device is shown in Section II followed by the specifications for each of the various layers in Section III.

## II: Waveguide Dimensions

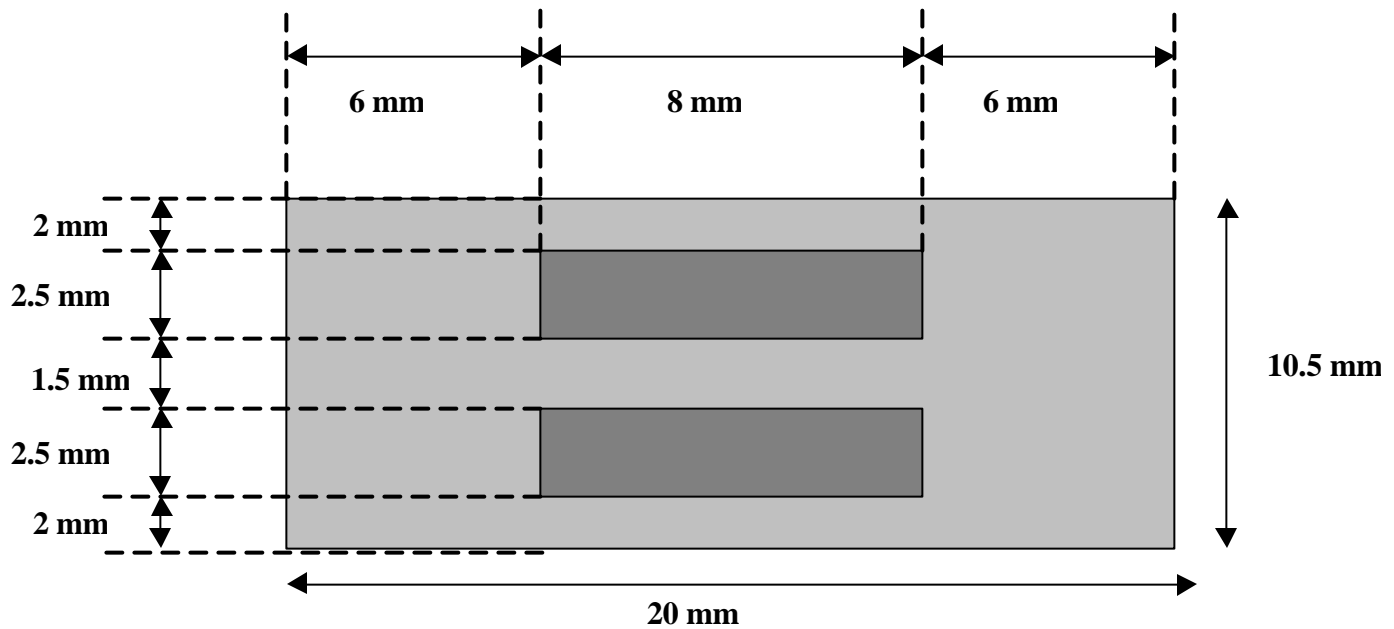


**Figure 4-3:** Top view of waveguiding structure. 2  $\mu\text{m}$  oxide layer is visible. Two 8 x 2.5 mm cuvettes are etched through the oxide to the silicon nitride surface.

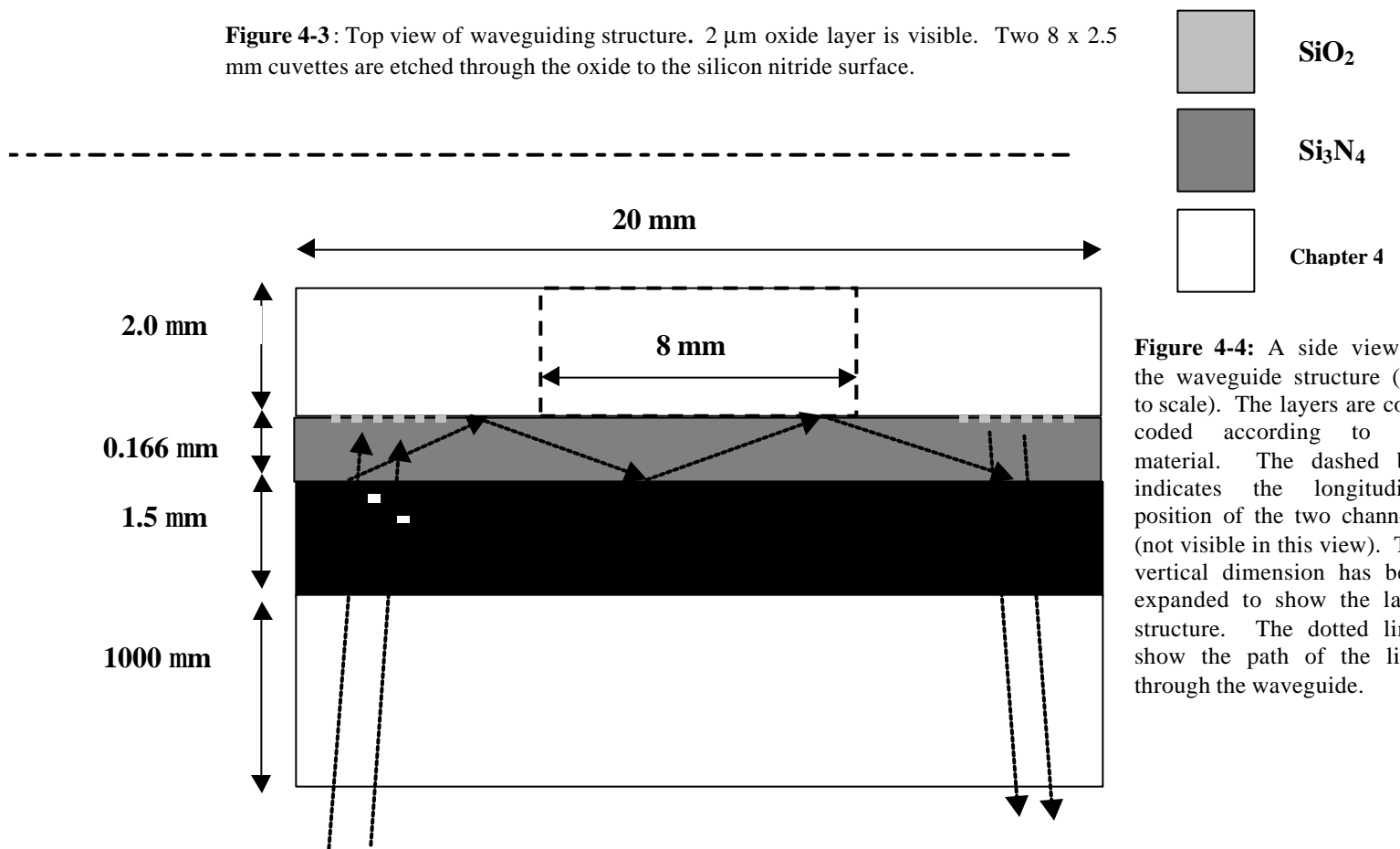


**Figure 4-4:** A side view of the waveguide structure (not to scale). The layers are color coded according to the material. The dashed line indicates the longitudinal position of the two channels (not visible in this view). The vertical dimension has been expanded to show the layer structure. The dotted line shows the path of the light through the waveguide.

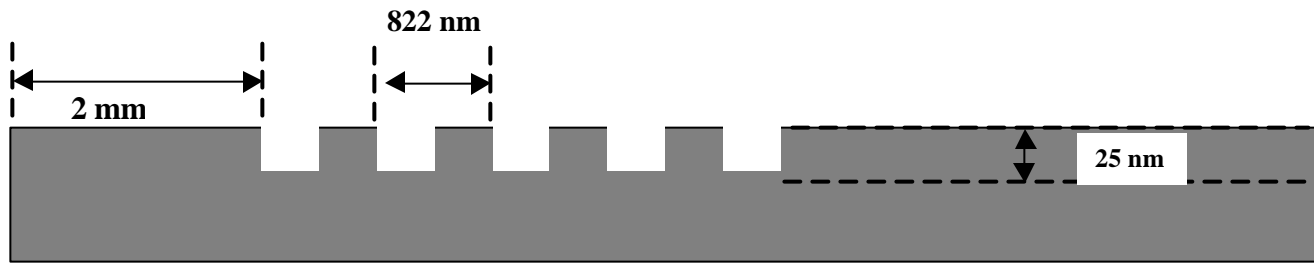


**Figure 4-5:** Grating profile. The gratings should be offset from the edge of the waveguide by 2 mm. This is commensurate with Figure 4-6, below.

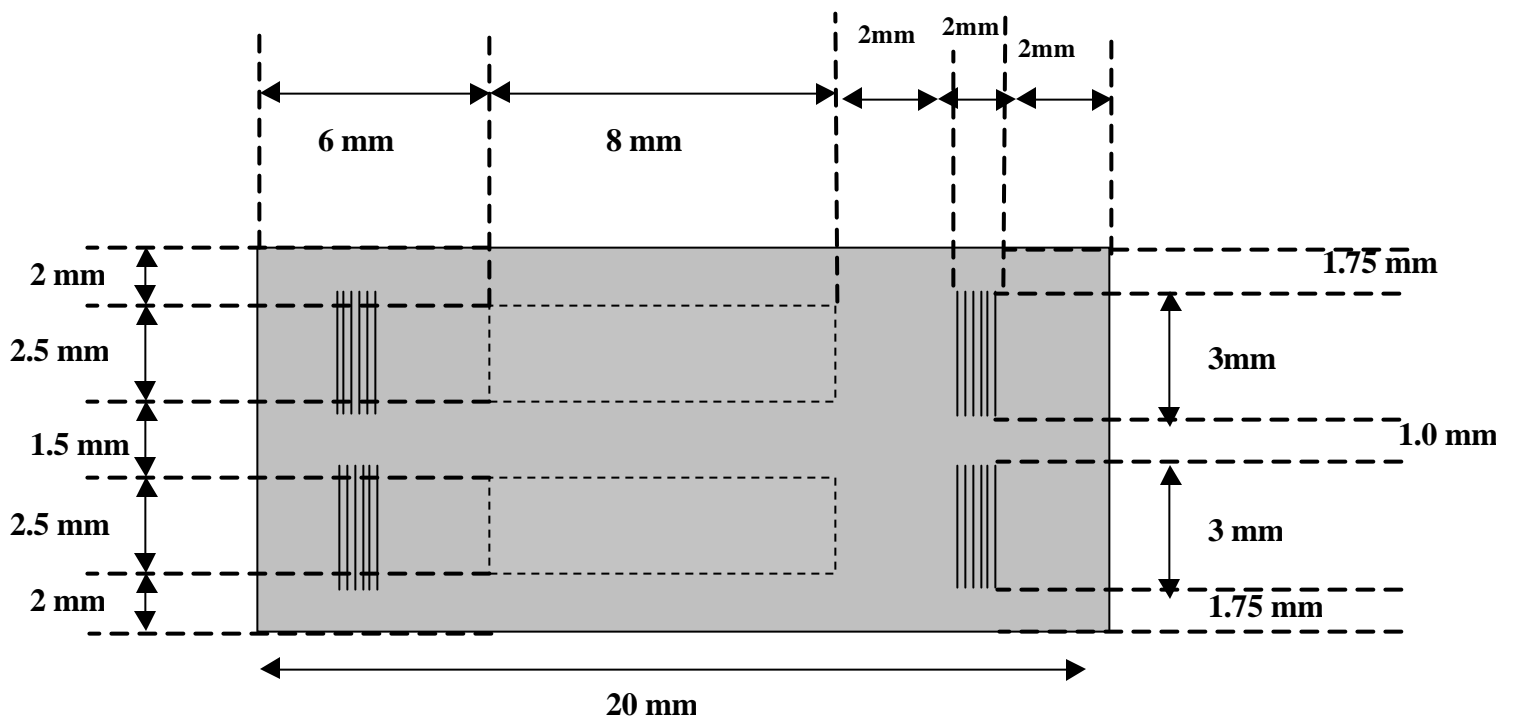


**Figure 4-6:** Bottom View of Waveguiding Structure. The cuvettes on the upper surface are drawn with dashed lines, not to scale. On the left, the dimensions of the surface channels are shown for comparison.

### III. Layer Description:

Please refer to *Section II, Figure 4-4* for this section.

**Layer #1: Substrate:** Corning high purity 7980 fused silica, optical quality (10/5 scratch/dig)

**Layer #2: Oxide Buffer Layer:** The lower silicon dioxide layer should be deposited by LPCVD, in order to create as flat and dense a surface as possible for the guiding layer. The tolerance for the thickness is  $1.5 \pm 0.2$  microns. The top surface should be flat to within  $\pm 5$  nm over the wafer, to ensure that it does not cause any subsequent variations in the guiding layer and thus scattering. The index of refraction for the  $\text{SiO}_2$  buffer layer is  $1.46 \pm 2\%$  at  $\lambda = 633\text{nm}$ .

**Layer #3: Silicon Nitride Guiding Layer:** LPCVD grown nitride layer thickness is  $166 \text{ nm} \pm 3$  nm with uniformity to within  $\pm 3$  nm over the wafer. The index of refraction of the layer  $n = 2.05 \pm 0.04$  at  $\lambda = 633 \text{ nm}$ . Uniformity of the index of refraction (to  $n = \pm 2\%$ ) and layer thickness is important to prevent scattering.

**Layer #4: Oxide Cover Layer:** LPCVD grown  $\text{SiO}_2$  cover layer should be  $2.0 \pm 0.1 \text{ } \mu\text{m}$  thick. The thickness should be uniform to within 5-10 nm. Again, a uniform index of refraction is important to maintain the properties of the guided modes. Can be PECVD.

**Table 4-2: Summary of Waveguide Layer Specifications**

Layer #	Material	Growth Technique	Thickness	Thickness Uniformity over wafer	Wafer-to-wafer Tolerance	Index of Refraction at $\lambda = 633 \text{ nm}$	Index uniformity
1	Fused Silica	Corning 7980 High Purity, optical grade (10/5 scratch/dig)					
2	$\text{SiO}_2$	LPCVD	$1.5 \pm 0.2 \mu\text{m}$	$\pm 0.010 \text{ m smooth}$	$\pm 0.1 \mu\text{m}$	$1.46 \pm 0.03$	$\pm 2\%$
3	$\text{Si}_3\text{N}_4$	LPCVD	$0.166 \pm 0.003 \mu\text{m}$	$\pm 0.003 \mu\text{m}$	$\pm 0.005 \mu\text{m}$	$2.05 \pm 0.04$	$\pm 2\%$
4	$\text{SiO}_2$	LPCVD	$2.0 \pm 0.1 \mu\text{m}$	$\pm 0.01 \mu\text{m}$	$\pm 0.1 \mu\text{m}$	$1.46 \pm 0.03$	$\pm 2\%$

#### Environmental Tolerances:

**Temperature:** The device is designed to be operated at room temperature, but should be able to withstand temperatures from 50-100 degrees Fahrenheit.

**Overall Dimensions:** Each device is 10.5 mm by 20 mm in size. The tolerance for each dimension is  $\pm 10$  microns.

## IV. Waveguide Patterning:

**Surface flow channels:** The rectangular cuvettes (as shown in *Section II, Figure 4-3*) can be etched using standard techniques. The edges of the cuvettes should be parallel to the grating. The tolerance is  $\pm 1$  degree. The edges (parallel to gratings) should be smooth with an average rms edge roughness of less than 20nm.

**Grating characteristics and fabrication:** Two types of grating coupling are possible, first order coupling and second order coupling. Each type requires its own set of grating parameters. Please refer to Table 4-3 below. First order coupling requires a nominal grating period of 411 nm with 50% duty cycle. The tolerance in grating period is  $\pm 10$ nm. Second order coupling requires a grating period of 822 nm and a similar tolerance. The grating depth (penetration into the guiding layer) in both cases is 25nm. The tolerance for grating depth accuracy is  $\pm 5$ nm. The variation across the wafer should be  $\pm 2$ nm.

The size (dimensions parallel to the waveguide surface), and position of each grating are specified in Figure 4-5. The tolerances indicated here are sufficient to ensure that the angle for the incoupled and outcoupled beams varies by less than one degree.

**Table 4-3: Summary of Grating Specifications for First and Second Order Coupling**

Order of Coupling	Fabrication Technique	Profile/Duty Cycle	Period	Depth (directed into guiding layer)	Depth Uniformity across wafer	Coupling Angles	Tolerances
1st Order	e-beam direct write or Deep uv contact	square/ 50%	$0.411 \pm 0.010\mu\text{m}$	$0.025 \pm 0.005\mu\text{m}$	$0.025 \pm 0.002\mu\text{m}$	7.0 deg TE, 12.0 deg TM	$\pm 1.0$ deg
2nd Order	Lithography	square/ 50%	$0.822 \pm 0.010\mu\text{m}$	$0.025 \pm 0.005\mu\text{m}$	$0.025 \pm 0.002\mu\text{m}$	7.0 deg TE, 12.0 deg TM	$\pm 1.0$ deg

## Chapter 5 : Surface Derivatization

**Overview.** A subcontract was let to the Laibinis group in the Department of Chemical Engineering at MIT to perform surface modification of the waveguides as a means to make them chemically selective in their adsorption characteristics. For sensing, the waveguide surfaces must be able to direct the adsorption of targeted analytes (here, cells) onto specified regions of the waveguide surface for detection while avoiding adsorption of the analytes onto other surfaces and avoiding the adsorption of untargeted species onto the active waveguide areas used for detection. The MIT approach has been to provide methods for incorporating molecular coatings onto the waveguide surfaces that include short lengths of oligo(ethylene glycol) units that provide inert surfaces. The coatings are to further provide sites for further immobilization of recognition sites. This latter goal—molecular coatings presenting reactive oligo(ethylene glycol) on the waveguide surface and their surface modification—has been the primary focus by MIT.

Three basic tasks were planned under Phase II for this effort: 1.) Develop and verify the basic attachment chemistry, 2.) Optimize the density of binding sites to minimize non-specific binding from Protein-A per se, and 3.) Patterning of the films on the waveguide surface. Task 1.) has been accomplished and is described below. Specifically, work accomplished to date by the Laibinis group at MIT is listed below:

- Provided surfaces to the SatCon biological group on waveguide mimics for screening their adsorption characteristics towards cells of interest.
- Prepared surfaces to the SatCon biological group on waveguide mimics that attach Protein A and antibodies for investigations of selective adsorption.
- Synthesized molecular agents that self-assembled onto the waveguide surface and provided surfaces that were inert towards the non-specific adsorption of agents (primarily proteins and other cells) and to include reactive sites for attaching Protein A and other species by employed chemistries to these layers.
- Pursued an optimization of the processing conditions required for assembling the molecular films onto the surfaces of waveguide mimics by examining the effects of time, temperature, and concentration on the structure and properties of films formed from in-house synthesized  $\text{Cl}_3\text{Si}(\text{CH}_2)_{11}[\text{OCH}_2\text{CH}_2]_3\text{O}_2\text{CCH}_3$ . These studies employed characterization methods including wetting, ellipsometry, x-ray photoelectron spectroscopy, and protein adsorption experiments.
- Examined the effects of processing conditions on the deprotection of the generated acetate-protected oligo(ethylene glycol) surface produced by adsorption of  $\text{Cl}_3\text{Si}(\text{CH}_2)_{11}[\text{OCH}_2\text{CH}_2]_3\text{O}_2\text{CCH}_3$ . Studies provided the means to produce hydroxyl-terminated oligo(ethylene glycol) surfaces and to set limits on the reaction conditions required in order to minimize loss of monolayer during the process.
- Initiated studies for reacting the generated hydroxyl-terminated oligo(ethylene glycol) for linking Protein A and antibodies to the layers.

**Chemical Synthesis.** To achieve the above goals, the MIT group conducted chemical synthesis, surface modification, surface reactions, surface characterizations, and studies of protein and cell adsorption (the latter with Hitesh Jindal of SatCon) on generated films. The effort in chemical synthesis focused on maintaining purified supplies of  $\text{Cl}_3\text{Si}(\text{CH}_2)_{11}[\text{OCH}_2\text{CH}_2]_3\text{O}_2\text{CCH}_3$  for surface studies. The chemical synthesis was developed and pursued during the first quarter, with some work during the second quarter directed to repurifying stock samples and resynthesizing precursors for expected future needs. The use of Krugelrohr distillation provided a convenient method for repurifying aging samples via a vacuum distillation process.

A critical development was establishing conditions for assembling the  $\text{Cl}_3\text{Si}(\text{CH}_2)_{11}[\text{OCH}_2\text{CH}_2]_3\text{O}_2\text{CCH}_3$  onto waveguide surfaces and to reveal the protected terminal hydroxyl-group contained in this molecule once adsorbed onto the surface. Studies were performed on silicon and glass samples to optimize this operation. In the former case of assembly onto the oxide surfaces, we were surprised to observe thinner films than expected by adsorption of this trichlorosilane. Examination of different solvents, concentration levels, times of exposure, and temperature lead to our establishing a preferred protocol for adsorbing the silane onto the oxide surfaces for preparing the most densely packed and thickest molecular film possible. We note that the resulting film remains less densely packed than the films formed from the  $\text{Cl}_3\text{Si}(\text{CH}_2)_{11}[\text{OCH}_2\text{CH}_2]_3\text{OCH}_3$  employed in the first quarter and the alkyltrichlorosilanes  $[\text{Cl}_3\text{Si}(\text{CH}_2)_n\text{CH}_3]$  often used for generating hydrophobized surfaces. The effect on performance of the pure monolayers is not yet clear. For the targeted mixed monolayers formed by reacting a surface with a solution containing both  $\text{Cl}_3\text{Si}(\text{CH}_2)_{11}[\text{OCH}_2\text{CH}_2]_3\text{O}_2\text{CCH}_3$  and  $\text{Cl}_3\text{Si}(\text{CH}_2)_{11}[\text{OCH}_2\text{CH}_2]_3\text{OCH}_3$  and subsequently deprotecting the former compound to reveal surface hydroxyl groups, we expect that films containing a majority of the latter species should show little effect on packing.

Figure 5-1 below shows results from x-ray photoelectron spectroscopy (XPS) on a film formed from  $\text{Cl}_3\text{Si}(\text{CH}_2)_{11}[\text{OCH}_2\text{CH}_2]_3\text{O}_2\text{CCH}_3$  and one subsequently reacted with  $\text{LiAlH}_4$  to remove the terminal acetate group.

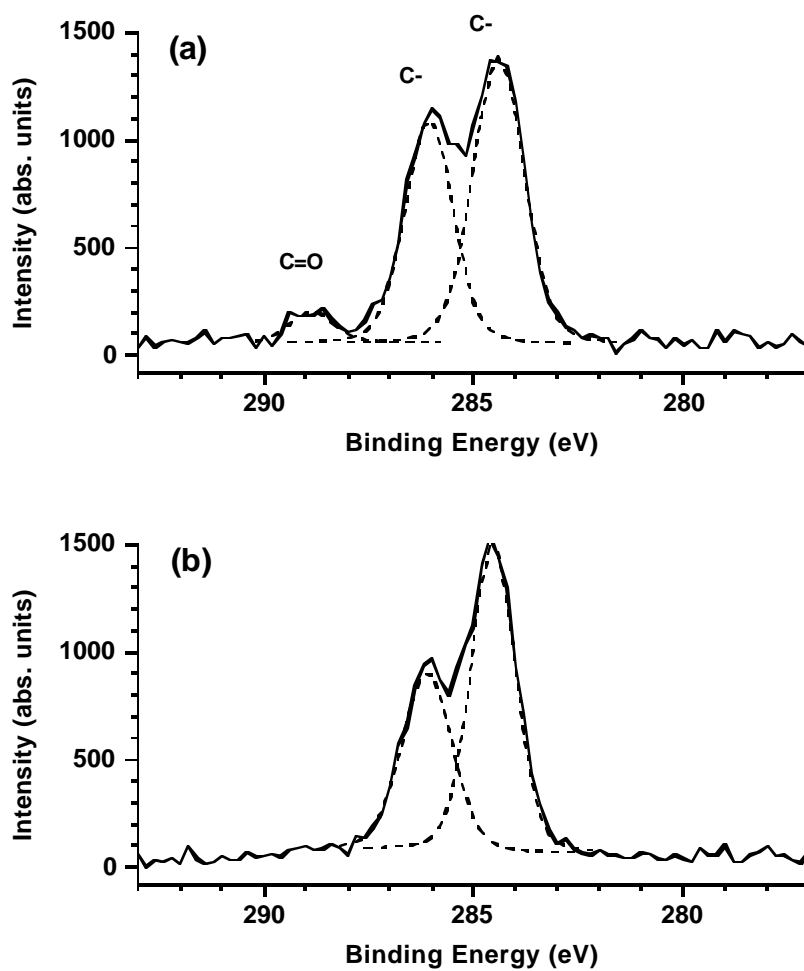


**Figure 5-1.** Results from x-ray photoelectron spectroscopy (XPS) on a film formed from  $\text{Cl}_3\text{Si}(\text{CH}_2)_{11}[\text{OCH}_2\text{CH}_2]_3\text{O}_2\text{CCH}_3$  and one subsequently reacted with  $\text{LiAlH}_4$  to removed the terminal acetate group.

In the upper spectrum, three peaks are observed for different carbon environments. Notable peaks are the peak at highest binding energy (corresponding to carbons connected to the most oxygen atoms) and the peak at an intermediate binding energy (corresponding here to carbons present in an oligo(ethylene glycol chain). The peak at lowest binding energy corresponds to carbon atoms attached solely to carbon and hydrogen atoms. After reaction with  $\text{LiAlH}_4$ , we observed a loss of the carbon peak at highest binding energy, consistent with deprotection of the terminal acetate group and the revelation of a terminal hydroxyl group. Under conditions where the reaction conditions were too long, we observed an overall decrease in the carbon signal, suggesting loss of the layer from the surface. Various reaction conditions were examined in order to provide a procedure that resulted in deprotection of the acetate and maintenance of the film. The results of these studies produce such a procedure that allows the

reproducible generation of hydroxyl-terminated oligo(ethylene glycol) surfaces on silicon oxide substrates. The next step in these studies would be the development of reaction protocols for activating these terminal hydroxyl group with Protein A (via coupling chemistry with carbonyl diimidazole), as we have done on related hydroxyl-terminated surfaces on the silicon dioxide substrates.

**Protein-A Attachment.** We also used X-ray Photoelectron Spectroscopy (XPS) to follow the reactions used for attracting Protein A to the hydroxyl-terminated surfaces (Figure 5-2 below).

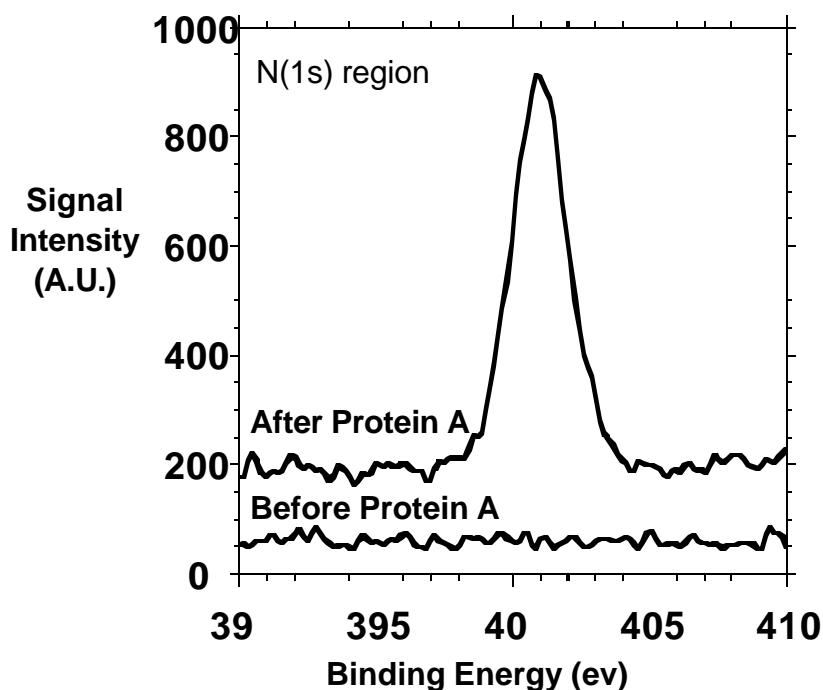


**Figure 5-2.** XPS spectrum for attracting Protein-A to the hydroxyl-terminated surfaces.

In these studies (performed concurrent with studies directed at optimizing the properties of the hydroxyl-terminated oligo(ethylene glycol) surfaces), we were able to demonstrate and optimize conditions for attaching the Protein A to hydroxyl-terminated surfaces on the silicon oxide substrates. In these experiments, we employed a glycidyl-terminated trichlorosilane to first derivatize the surface and generate a film containing terminal epoxide groups. These groups were hydrolyzed to reveal hydroxyl groups. A reaction sequence where the substrates were first exposed to a solution of carbonyl diimidazole and then to a solution of Protein A showed a dramatic change in the nitrogen signal (a unique element for the protein) that noted its attachment to the surface. Control experiments where the Protein A was exposed to the hydroxyl-terminated surface and the step of carbonyl diimidazole was stepped showed much less nitrogen signal. The evidence from XPS points to the reaction sequence providing a covalent coupling of Protein A to the molecular film, thereby providing a robust attachment. This chemical sequence will be adapted for use on the surfaces derived from  $\text{Cl}_3\text{Si}(\text{CH}_2)_{11}[\text{OCH}_2\text{CH}_2]_3\text{O}_2\text{CCH}_3$  and from mixtures of  $\text{Cl}_3\text{Si}(\text{CH}_2)_{11}[\text{OCH}_2\text{CH}_2]_3\text{O}_2\text{CCH}_3$  and  $\text{Cl}_3\text{Si}(\text{CH}_2)_{11}[\text{OCH}_2\text{CH}_2]_3\text{OCH}_3$ .

**Summary.** The development of the polyethylene (oxide) derived self-assembled monolayer and the covalent attachment of Protein-A by the Laibinis group provided a ‘teflon’ like surface to small proteins as well as a robust ligand for the generalized attachment of IgG immunoreceptors. Avoiding non-specific binding of small proteins is important to surface based detection methods to minimize the degradation of the desired signal. Preliminary laboratory characterization data of the surface’s ability to resist the non-specific binding of BSA is described in Chapter 10 (Suppression of Non-Specific Binding).

## Chapter 6 : Model Systems and Receptor Platform Development

**Model Systems.** A well characterized cell-antibody complex that could be used as a benchmark for all experiments was essential for clear interpretation of any experiments. Several strains of Gram-negative bacterium *E.coli* (*E.coli* O2, O10, O27 and O30) and their corresponding antibody were obtained from the *E.coli* Reference Center at Penn State University (State College, PA) and their binding affinities were characterized with both magnetic beads and on solid platform silicon oxide surfaces.

To accomplish this, the following experiments were conducted and described below:

- The model system was verified for its ability to efficiently capture *E. coli* cells in solution using magnetic beads;
- The binding of antibodies to a Protein-A coated solid surface was confirmed;
- The specific binding of cells to their corresponding antibodies attached to the solid support via Protein-A was demonstrated, and finally,
- The regeneration properties of the Protein-A coated surfaces using several protocols were explored and reuse of these surfaces was demonstrated.

Protein-A was chosen as an intermediate linker because it provides:

- High affinity to the Fc-receptor region of various classes of immunoglobulins (e.g. human IgG), thus acting as a specific non-covalent linker and ligand for a variety of different receptors with a single chemistry,
- Improved spatial and binding orientation of the antibody via Protein-A for improved binding activity and specificity with its target bacterium, and
- Non-covalent attachment to a wave-guide surface assuring the integrity of the variable binding region of the antibody and the specificity to its target epitope, often destroyed with harsh covalent chemistries.

Magnetic beads were purchased already functionalized with Protein-A. Coated oxide surfaces were provided by the MIT group with Protein-A covalently attached using carbonyldiimidazole-based surface derivitization (see Chapter 5). The initial experiments were conducted on silicon oxide surface; these experiment were repeated later once surfaces having a self-assembled monolayer of polyethylene oxide were available.

### Description of the Experiments

**Model System Verification.** The binding characteristics of the antibodies for the specific strain were assessed initially in solution to verify their binding properties for our future studies. This was accomplished by using Protein-A coated magnetic beads (BioMAG Iron Oxide Protein-A coated

Particles, approximately 1  $\mu\text{m}$  in size, Polysciences, Inc, Warrington, PA) in place of a solid surface. The procedure to bind the strain-specific antibodies and cells to the magnetic is depicted in Figure 6-1.

Briefly,  $8.75 \times 10^7$  Protein-A coated magnetic beads were used per experiment, and were incubated with strain specific anti-*E.coli* antibodies, followed by incubation with corresponding strain of cells ( $1.2\text{--}1.5 \times 10^8$  cells per experiment). This provided approximately one cell per bead; multiple cells bound to a bead was not observed. The cell-bead complex was collected using a simple magnet, washed, stained with fluorescence dye (Syto 9, fluorescein-conjugated dye, Molecular Probes, Eugene, OR), and visualized under the microscope.

We have predicted an average value of 59 cells in a 40X magnification microscope field of view (i.e. 40x objective lens) based on the number of magnetic beads, the number of cells per experiment, and amount of the Protein-A coated beads-antibody-cell complex (i.e. 7  $\mu\text{l}$ ). Cell counts in the range of 50-70 cells were observed, which is very much in accordance with the predicted range demonstrating that all binding sites were used effectively.

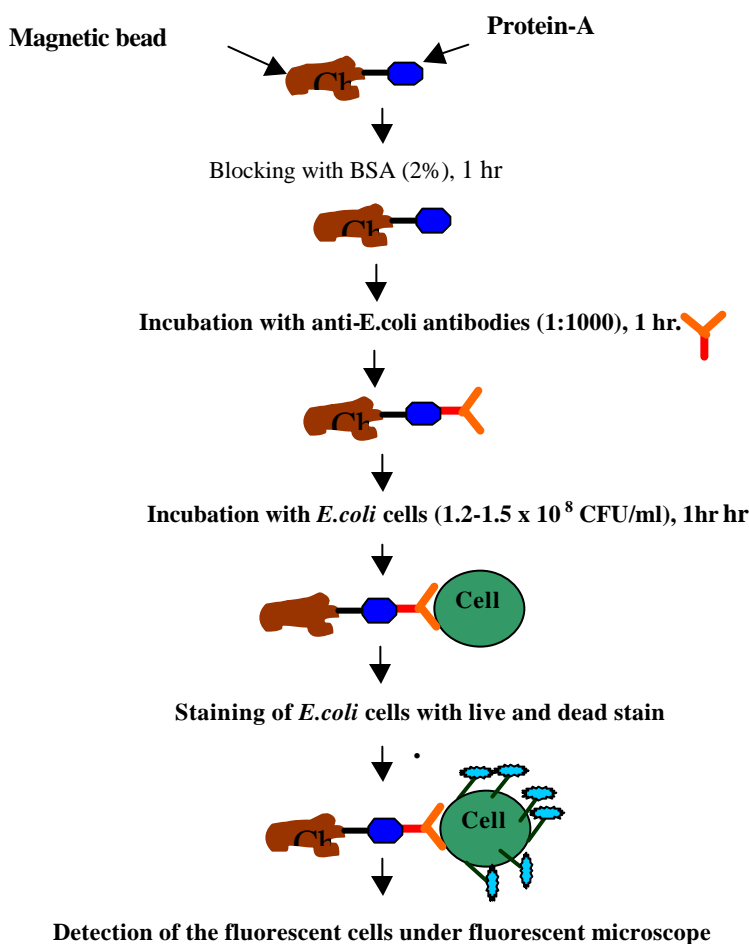


**Figure 6-1.** Cartoon showing procedure for obtaining magnetic bead-cell complex.

In order to determine the specific interaction of the cells, each immobilized antibody type was exposed to its corresponding strain of cell along with the other three different strains of *E.coli*. The binding combinations and their expected results are shown as a matrix in Table 6-1.

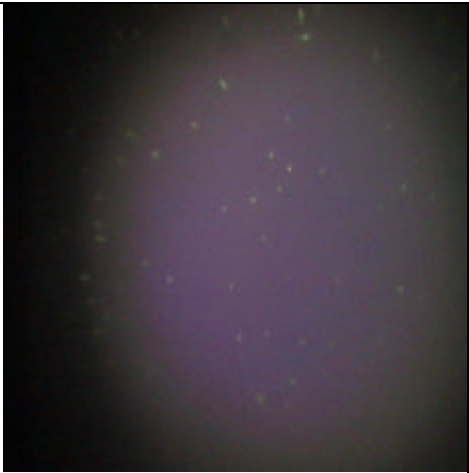



	Anti-strain#O2 antibody	Anti-strain#O10 antibody	Anti-strain#O27 antibody	Anti-strain#O30 antibody
<b>Strain # O2</b>	<b>Yes</b>	<b>No</b>	<b>No</b>	<b>No</b>
<b>Strain # O10</b>	<b>No</b>	<b>Yes</b>	<b>No</b>	<b>No</b>
<b>Strain # O27</b>	<b>No</b>	<b>No</b>	<b>Yes</b>	<b>No</b>
<b>Strain # O30</b>	<b>No</b>	<b>No</b>	<b>No</b>	<b>Yes</b>

**Table 6-1:** The results of the specific activity of the antibodies with the corresponding strains and cross-reactivity of the chosen antibodies on exposing to different strains of *E.coli*.

Results and Conclusions. The results from the model system verification showed that:

- There was no non-specific binding of the *E.coli* cells to the Protein-A coated magnetic beads alone.
- There was specific interaction of the antibodies with the corresponding strains of cells as shown in Figure 2 below.
  - The activities of anti-strain # O2 and O10 antibodies were several orders of magnitude lower than anti-strain # O27 and O30 antibodies.
  - Anti-strain # O30 antibody showed at least 3-4 fold higher activity than the anti-strain # O27 antibody in terms of capturing the cells (Figure 2).
  - There was no cross-reactivity of the antibodies when exposed to the three other different strains of *E.coli*.

Based on the above observations, we concluded that anti-strain #O30 antibody represents the best model system of the four systems tested followed by anti-strain # O27 antibody (Figure 6-2).

	Anti-strain # O27 antibodies	Anti-strain # O30 antibody
Strain # O27		
Strain # O30		

**Figure 6-2.** Specific interaction of anti-strain # O27 and strain # O30 antibodies attached to Protein-A coated magnetic with their corresponding strains of cells.

Titration Curves. The anti-strain # O30 antibody was titrated further to characterize its binding kinetics for the optimum binding of cells.

- Antibody Concentration. To determine the optimum concentration of the antibody required for the optimum binding of the cells to the antibody, various concentrations of anti-O30 antibody (as shown in Figure 6-3) were incubated with fixed number of magnetic beads ( $8.75 \times 10^7$  beads/experiments) coated with Protein-A. Collection, staining, and analysis of the magnetic beads with captured cells was done as described above. Enumeration of the analyzed cells revealed that the number of cells bound to the antibody was a function of the increasing concentration of antibody bound to the Protein-A coated beads, with the maximum binding obtained at 15  $\mu\text{l/ml}$  dilution of antibody, and further increments in the antibody concentration did not result in a significant increase in the number of cells captured.

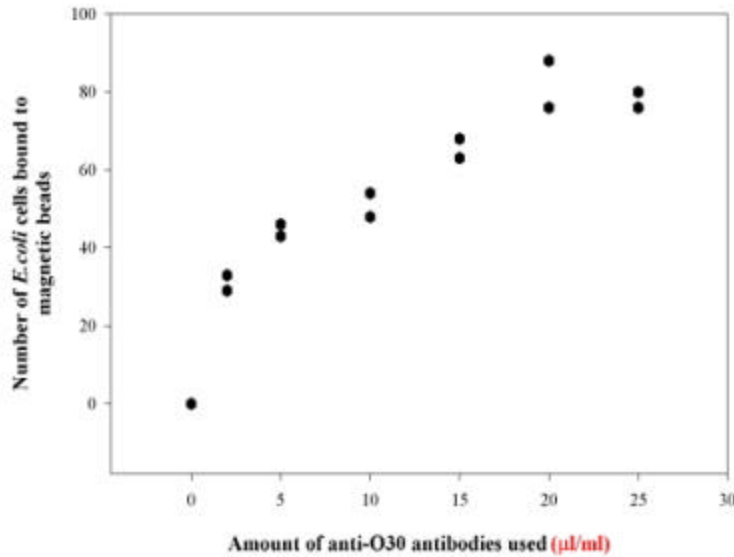


**Figure 6-3.** The concentration of anti-*E. coli* #O30 antibody immobilized to magnetic beads is plotted against the number of bound *E. coli* (strain #O30) cells.

- Time of incubation of antibody with Protein-A. In order to determine the optimum time of incubation with Protein-A, for the optimum number of the captured cells, the anti-O30 antibody was incubated for various periods of time (i.e. 15-180 min, Figure 6-4), with equivalent number of Protein-A coated beads ( $8.75 \times 10^7$  beads/experiments). It is evident from the Figure 6-4 that the number of cells bound to the antibody was also a function of the increasing time of incubation of the antibody with Protein-A, as it was linear up to 90 min of incubation of antibody with Protein-A and further increases in the time of incubation resulted in the leveling off of the capturing

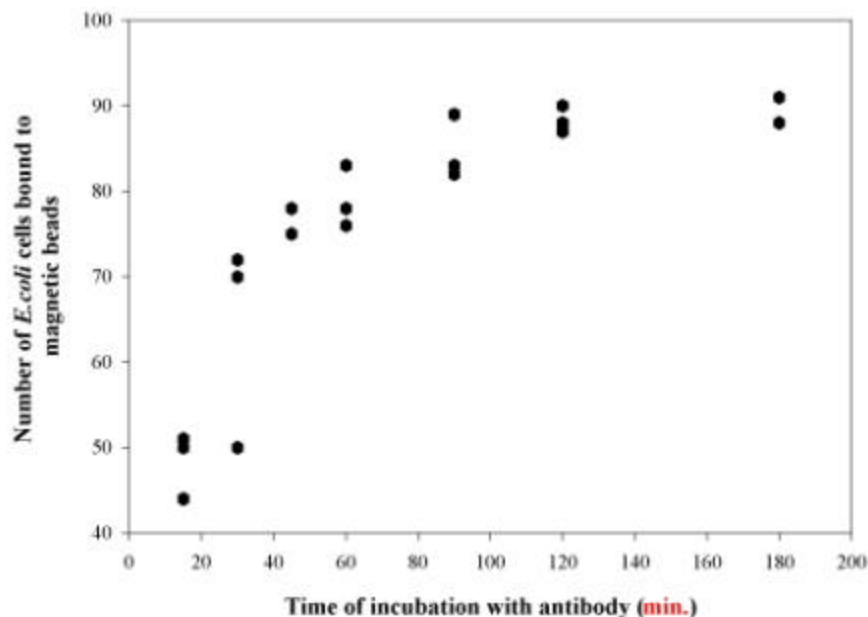


**Figure 6-4.** The time of incubation is plotted against the number of bound *E. coli* (#O30) cells bound to anti-*E. coli* (strain #O30) antibodies immobilized on magnetic beads.

efficiency of cells.

- **Conclusions.** The results from the titration experiment show that for the optimal binding of the *E.coli* strain #O30 cells with their corresponding antibody, concentration of the antibody needed was (15  $\mu\text{l/ml}$ ), and the antibody should have undergone incubation with Protein-A for about 90 min. For our further experiments we have chosen the amount of antibody at 10  $\mu\text{l/ml}$  dilution, and the time of incubation of antibody with Protein-A as 90 min. These two parameters fall very much within the linear ranges of the binding of cells with the corresponding antibody.

**Verify Activity of Protein-A on Solid Support.** After the model system was confirmed, the activity of the Protein-A on silicon chips (18 mm x 18 mm) provided by the Laibinis laboratory at MIT was determined by the direct binding of the FITC-conjugated immuno-pure polyclonal antibodies. These were either conjugated here in the laboratory using NHS-fluorescein according to the protocol from PIERCE or obtained already FITC-labeled from PIERCE, Rockford, IL. Upon binding of the

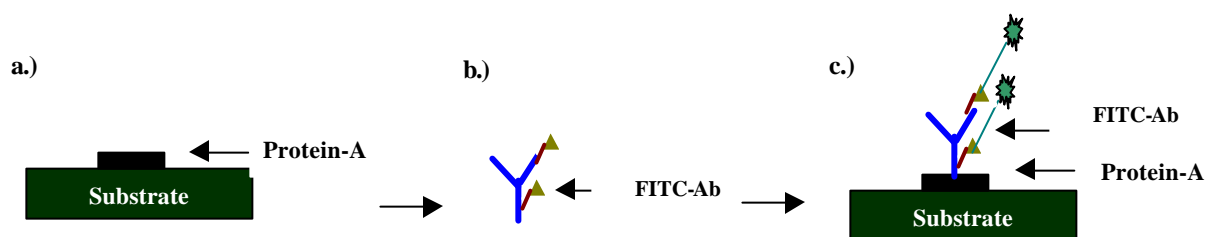


**Figure 6-5 Schematic representation of the detection of Protein-A activity.** a.) Chip's surface coated with Protein-A; b.) Incubation of the chips with FITC-conjugated antibodies; c.) Formation of Protein-A – antibody complex followed by monitoring of fluorescence under the fluorescent microscope.

fluorochrome labeled antibodies to active Protein-A the resulting fluorescence was monitored under the fluorescent microscope to reveal the activity and spatial distribution of the antibody-Protein-A interaction as shown in Figure 6-5. For the purpose of calibration BSA was labeled with FITC as described below.

This amount of Protein-A can be measured to within approximately 10 percent by monitoring the amount of fluorescence. The results are normalized by comparing the fluorescence from protein-A with the emission from an unlabelled chip (baseline) and the emission from a monolayer of FITC labeled antibodies (maximum signal). The latter data was obtained by incubating a hydrophobic chip surface with the labeled antibody. Microscope images of the respective emission are captured with a CCD camera and a frame grabber for latter analysis. Typical measurements indicate 30-40% coverage of active Protein-A on a wafer; these measurements are confirmed by independent measurements performed by the MIT group using XPS. Because the cell is large compared to the size of the antibody this amount of protein-A is tens of times larger than is necessary to capture a cell.

**Binding of Antibodies.** Activity of the Protein-A coated chips was further confirmed by checking the binding of specific anti-*E.coli* antibodies for the *E.coli* model systems obtained. First, the Protein-A surfaces were incubated with the anti-*E.coli* polyclonal antibodies (primary antibodies). To confirm the

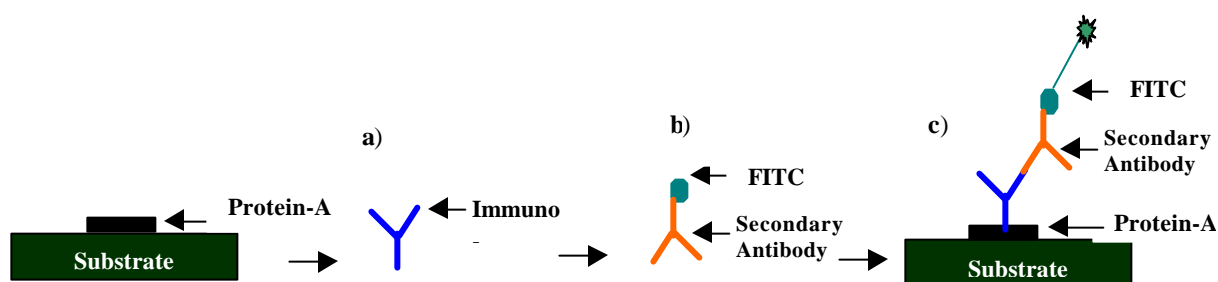


**Figure 6-6: Detection of the antibody binding to Protein-A coated surface.** a) Binding of primary antibody to Protein-A; b) Binding of secondary anti-body conjugated with FITC; c) Detection of the of the primary antibody-secondary body-FITC complex by monitoring.

binding of the primary antibodies, subsequent incubation of the surface with FITC-conjugated goat-anti rabbit antibodies (secondary antibodies) was carried out. The fluorescence from secondary antibodies bound to primary antibodies was monitored to determine the distribution of binding sites (Figure 6-6).

**Binding of Cells onto Solid Supports (Chips).** Based on the results from the magnetic bead measurements in solution, the specific binding of the *E.coli* strain # O27 and strain # O30 cells to their corresponding antibodies immobilized onto a solid support was measured. This was accomplished by first binding the antibody to the Protein-A coated surface followed by exposure to the corresponding strain of *E.coli* cells. The *E.coli* cell-anti-*E.coli* antibody complex was then stained with live/dead stain and monitored under the fluorescent microscope (Figure 6-7).

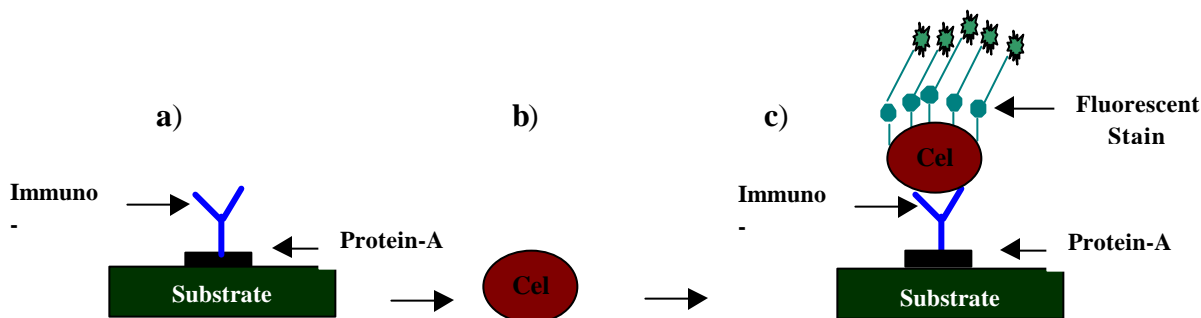


**Figure 6-7. Cell Binding.** a.) Binding of anti-*E.coli* antibody to Protein-A; b.) Capturing of *E.coli* cell; c.) Staining of the captured cells with fluorescent dye, (SYTO-9, live/dead stain) and monitoring of fluorescence under the fluorescent microscope.

**Results.** Figure 6-8 shows the results of the specific binding of the *E. coli* strain # O27 and strain # O30 cells to their corresponding antibodies. The 18 mm x 18 mm solid surface was exposed to  $3.5 \times 10^7$  cells for one hour. Subsequent experiments show the approximately 40% surface coverage (*E. coli* #O30) for similar conditions. If it is assumed that a cell will bind if it comes in contact with the surface, one can expect approximately  $1.4 \times 10^7$  interactions occur with the surface under our standard experimental conditions in one hour.

**Cross Reactivity and Non-Specific Binding.** In order to elucidate the cross-reactivity of these antibodies, the immobilized antibodies were exposed to corresponding strain and a different strain of *E.coli*. Results in Figure 6-5 show the cross reactivity of anti-strain O27 and anti- strain O30 antibodies to unmatched strains of *E.coli* so chosen for the model system. Note that the cells seen in

the off-diagonal pictures in Figure 6-8 represent the only cells seen after searching the entire 18 mm x 18 mm chip surface thus, non-specific interactions are of the order of one interaction in  $10^7$  cells.

The results of the binding of cells to the corresponding antibodies immobilized to the solid surface via Protein-A have indicated that there was:

- No non-specific binding of anti *E.coli* antibodies and *E.coli* cell to the chips (with diol derivitization), without Protein-A coated onto them.
- No non-specific binding of the *E.coli* cells to the Protein-A coated chips, in the absence of immobilized corresponding antibodies.
- Specific binding of the *E.coli* strain # O27 and strain # O30 to their corresponding antibodies, and
- No cross-reactivity of the anti-strain # O27 and anti-strain # O30 antibodies within the opposite strains.

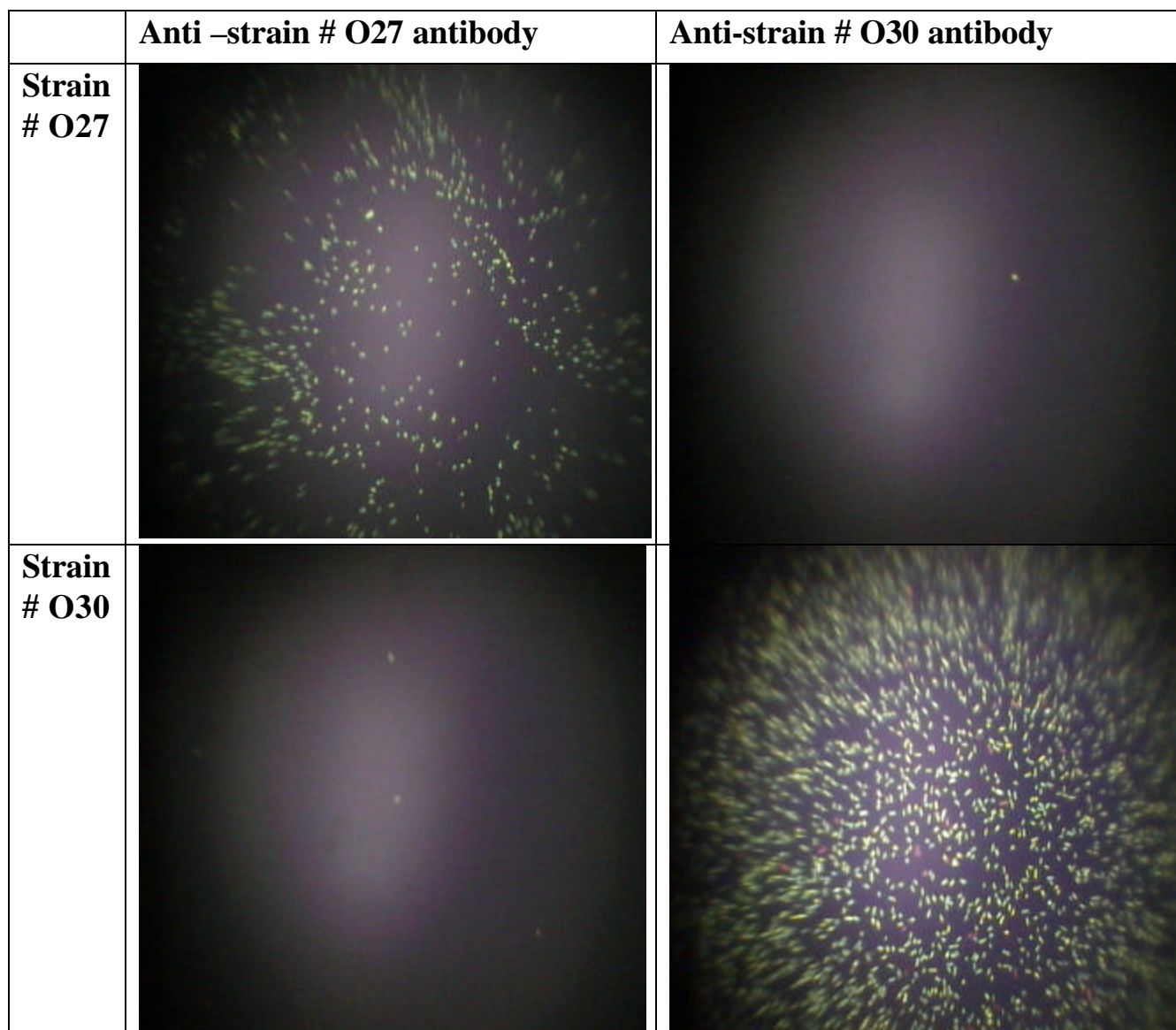


**Figure 6-8.** Specific interaction of anti-strain #O27 and strain #O30 antibodies with their corresponding strains of cells.

Effect of time of incubation of cells with antibodies attached to the solid surface via Protein-A. *E.coli* #O30 cells were incubated with anti-strain #O30 antibodies for 1 h, 4 h, and 22 h., and the numbers of cells captured were visualized under the microscope. Our standard protocol for such experiments is to place a 18 mm x 18 mm chip flat onto the bottom of a circular dish 37 mm in diameter. A solution of 1 ml PSB (containing typically  $3.5 \times 10^7$  cells) is added next and the dish is placed on a gyrating table at a speed of 60 rpm.

It is evident from Figure 6-9 that the number of cells binding to the antibody increased quite significantly from 1 h to 4 h. of incubation of cells with antibodies. However, prolonged incubation for 22 h. resulted in a decrease in the number of cells bound to the antibody, which may be attributed to death of the cells or dissociation of cells from the antibody during prolonged incubation.

Based on the results in Figure 6-9, and the assumption that if a cell comes into contact with the chip surface it will bind, we conclude that the surface is exposed to approximately 40% of the cells in a one hour period. In 4 hours, exposure to all of the cells at least once has occurred.

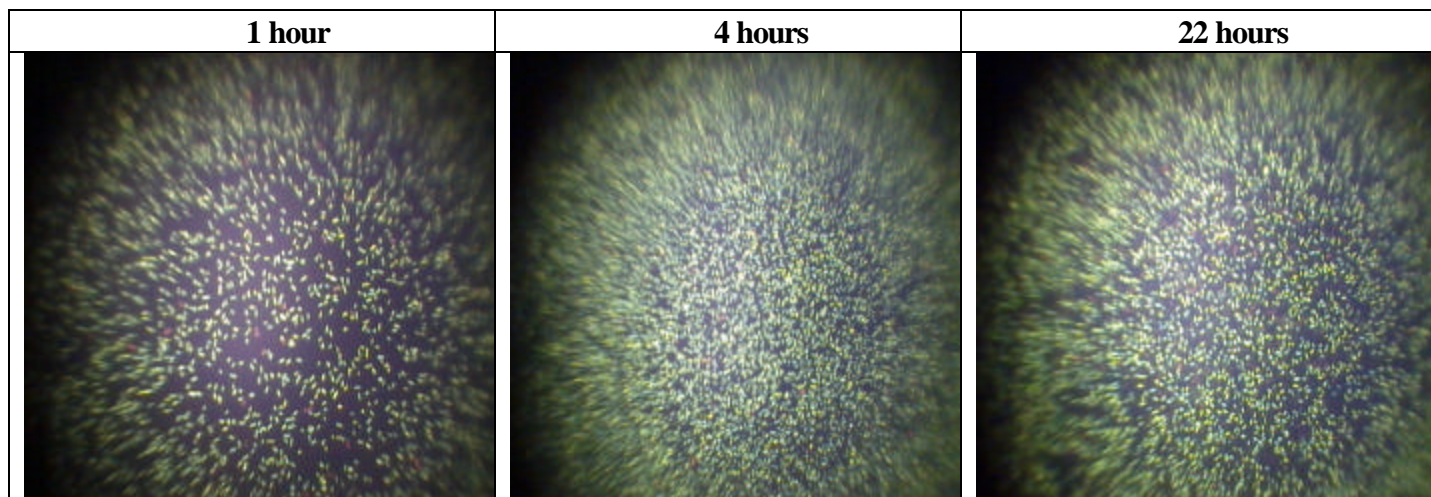


**Figure 6-9.** Binding of *E.coli* strain #O30 cells with anti-strain #O30 antibody-Protein-A complex on incubation of cells for various intervals of time.

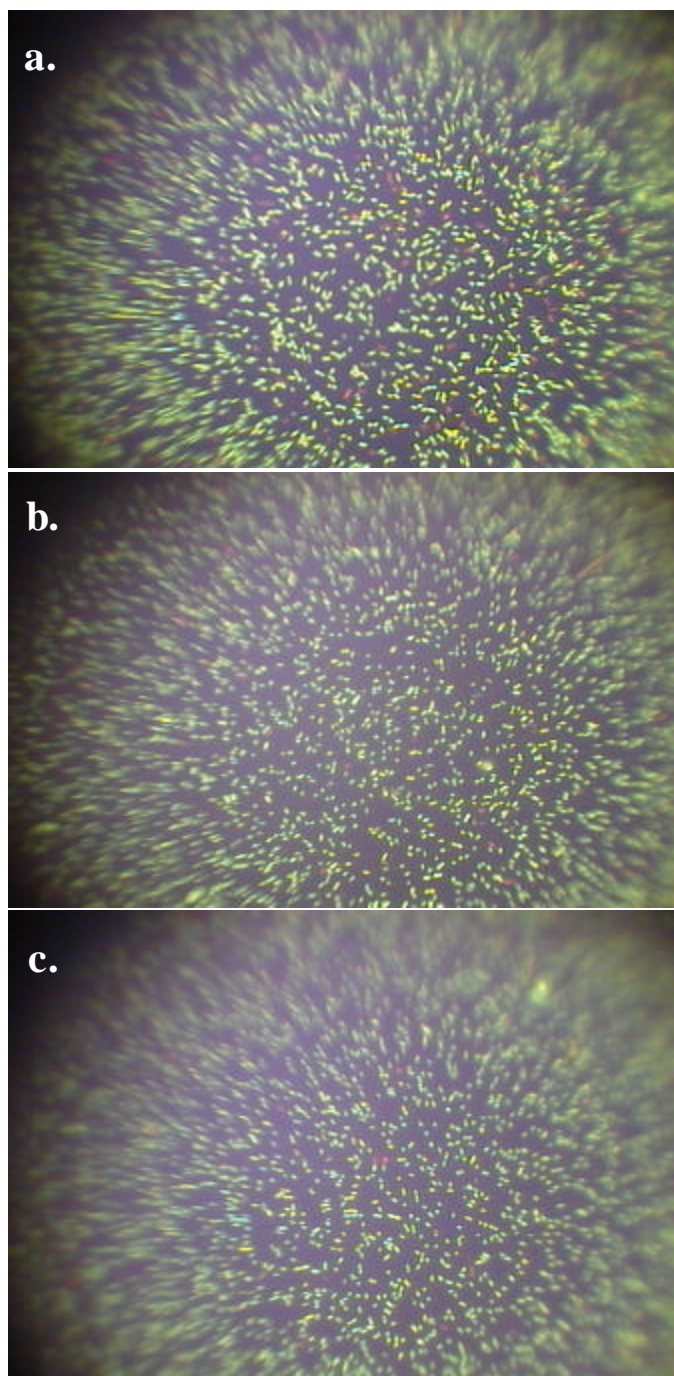
**Regeneration.** Regeneration of the Protein-A surface is very common in Protein-A columns (e.g. Agarose or Sepharose matrices conjugated with Protein-A) used to purify the antibody. The same principle of dissociating the bond between the antibody and the Protein-A was employed for the regeneration of the antibody-binding surfaces for re-usable sensor formats, with Protein-A immobilized onto the surface.

Two approaches for regeneration protocols were considered, successfully implemented, and listed below in order of harshness: Chips were treated with 20 mM HCl and 20 mM NaOH followed by washing with glycine-HCl (pH 1.7) and glycine-NaOH (pH 12.5). Alternately, the regeneration of

Protein-A coated chips was obtained by treating chips with 20% (v/v) acetonitril in 1 M ethanolamine, pH 12.0.

Chip surfaces coated with Protein-A attached to a polyethylene oxide (PEO) self-assembled monolayer were successfully regenerated numerous times using both methods. These chips were reanalyzed for the activity of Protein-A, the specific binding of antibodies, as well as cell binding. The final results are shown below in Figure 6-10.

**Figure 6-10.** Regeneration of PEO-Protein A coated chips using two different regeneration buffer systems. a.) The specific binding of the *E.coli* O30 cells to their corresponding antibody was first conducted on a new PEO-Protein-A surface. The resulting Protein-A-cell-antibody complex was then stained and monitored under the fluorescent microscope; b.) The chips with the bound cell complex (a) were then treated with 20 mM HCl and 20 mM NaOH for 2 min each, followed by washing with glycine-HCl (pH 1.7) and glycine-NaOH (pH 12.5). Following regeneration, the total absence of any residual complexes on the surfaces was verified with the fluorescent microscope. The cell binding protocol was then repeated to verify the Protein-A activity and the specific binding of the *E.coli* O30 cells. The bound cell population is seen to be virtually identical to that in figure a.). c.) The new chips from b.) were further subjected to regeneration by treating with 20% acetonitrile in 1 M ethanolamine (pH 12.0), and once again verified by specific binding of the *E.coli* cells to their corresponding antibodies. As before the resulting bound cell population is virtually identical to the experiments conducted with the fresh PEO/Protein-A surface.



**Summary.** *E. coli* O30 and its corresponding antibody obtained from the Penn State *E. coli* Reference Center was verified as a model system having good binding affinity, high specificity, and minimal non-specific binding. This system was used throughout the program as a reliable benchmark for a cell system. The successful implementation of the PEO/Protein-A based attachment system was experimentally demonstrated (including regeneration) providing a working generalized platform for the attachment of IgG immuno-receptors.

## Chapter 7 : Non-Specific Binding

**Introduction.** While carefully prepared laboratory test samples might be pure enough to allow sensitive unlabeled microbial detection, the real world is not. Non-specific binding (NSB) of proteins to active surfaces is a limiting problem for both labeled and unlabeled optical biosensors, reducing the S/N ratio by increasing the amount of background. This obstacle is typically addressed biochemically with limited results through the saturation of potential binding sites (e.g. through the application of BSA).

SatCon has addressed non-specific surface binding by exploring four different techniques:

- i.) Surface engineering through the application of polyethylene oxides (PEO) for a 'teflon-like' surface,
- ii.) The use of a reference binding area to subtract out any non-specific binding common to both the specific and the reference target areas,
- iii.) Tailoring the optical response to provide a desensitized region where small proteins bound to the surface become 'invisible', and
- iv.) Extraction of extraneous matter through the application of microfluidic diffusional filtering (H-filter).

Surface engineering of PEO is described elsewhere in Chapters 5 and 10 (Suppression of Non-Specific Binding). The effectiveness of a reference channel for reducing NSB, although automatically implemented when operating the interferometer, was not specifically quantified. The efforts made to demonstrate and characterize the optical desensitization technique and the H-filter are described below.

**Optical Suppression of Non-Specific Binding.** As their final task, the BU group was tasked with the demonstration of their optical desensitization technique invented in conjunction with SatCon . An experimental plan was generated by BU and experimental work was performed by BU in SatCon's laboratory to better supervise the work; in addition, a no-cost contract extension was granted to BU to complete this task. Waveguides having different guiding layer thicknesses were specially prepared by the BU group. However, the waveguides were constructed using the low-throughput PECVD wafers described in Chapter 4 (Wafer Processing at Boston University) and once again no results were obtained after significant effort was expended by the BU group. The experimental setup was transferred back to the Goldberg/Unlu laboratory at BU in April, 2002 for continued work and the BU group has promised to share any new results with SatCon. Although no laboratory result was obtained by the BU group, a peer-reviewed paper was published describing the concept<sup>1</sup>. It is assumed that this latter work was performed exclusively with funding other than SBCCOM/SatCon funds as no acknowledgements are made. A copy of this paper is included at the end of this chapter in Appendix 7-A.

---

<sup>1</sup> C. Worth, B. B. Goldberg, M. F. Ruane, M. S. Ünlü, "Surface Desensitization of Polarimetric Waveguide Interferometers," *IEEE Journal of Quantum Electronics*, vol. 37, no. 11, November 2001

Summary of Optical Suppression Technique. A direct consequence of measuring the difference between evanescent fields from two polarizations is the ability to block out signal at the immediate surface in a narrow nanoscale-controllable zone above the waveguide surface. This effectively makes the sensor invisible to non-specific binding and is not possible with any other techniques. While the evanescent interaction is the strongest for biolayers closest to the surface for each mode as is shown in

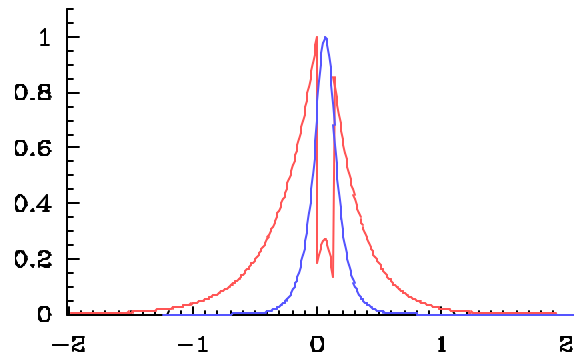
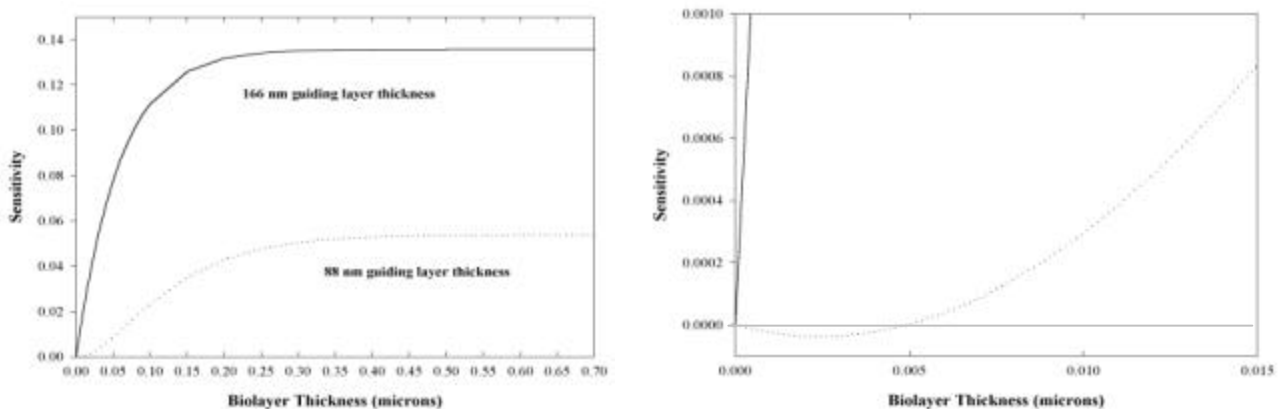


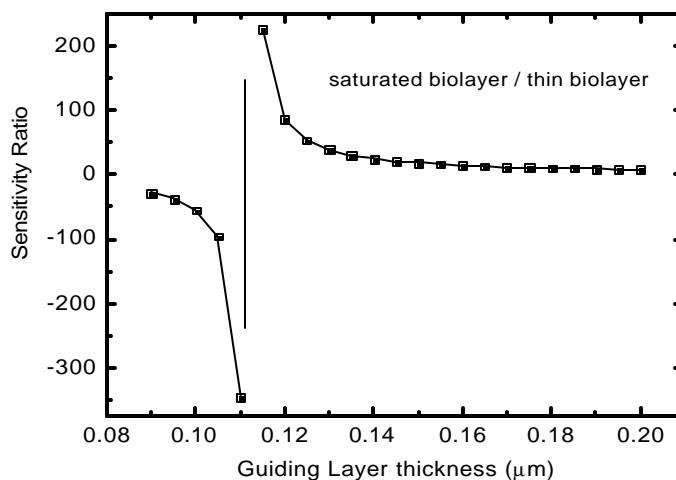
Figure 7-1, it is the difference in evanescent fields between the TE and TM modes phase method that matters. By controlling the thickness of the guiding layer, the relative response of the two modes, while each large, can be made to cancel each other out at or near the surface.

Figure 7-2 shows the integrated differential ( $TM_0-TE_0$ ) sensitivity plotted as a function of the thickness of the biomaterial situated on the surface of the waveguide for the two  $Si_3N_4$  guiding layer thickness values 166 nm and 88 nm. The sensitivity has been maximized for the former guiding layer thickness, however, the latter sensitivity goes through zero for 5 nm of biomaterial thickness.



This phenomenon is a result of the rapid change of decay of the TM evanescent mode above the mode cut-off condition. For very weak guiding (thin waveguide) the relative amplitude of the TM mode is smaller than the TE mode at the immediate surface, therefore, the phase change of TM-TE will have a negative sign. Hence, the optical response can be tailored to minimize the signal produced by an average thickness monolayer of protein making the instrument effectively blind to the non-specific binding of molecules onto the surface compared with the signal from large cell.

In Figure 7-2 left, the maximum sensitivity (166 nm guiding thickness) saturates with the increasing biomaterial thickness at around 300 nm reflecting the extent of penetration of the evanescent light field. The 88 nm thick guiding layer, optimized for immunity to non-specific binding, has only 40 percent of the overall sensitivity. Although the sensitivity is reduced the optical suppression of non-specific binding results in a larger S/N ratio. Figure 7-3 is a plot of the ratio of the saturated sensitivity of a thick biolayer (e.g. a cell) to a thin, 10 nm biolayer as a function of the guiding layer thickness. A several hundred-fold increase in the ratio of these sensitivities (i.e. S/N) is seen because for a 150 nm guide layer, the waveguide is insensitive to a 10 nm biolayer.



Boston University Experimental Plan. The plan proposed for this demonstration experiment along with the results received by the BU group are found in Appendix 7-B.

**Microfluidic Extraction.** To help limit non-specific binding it behooves one to remove as much extraneous matter as possible prior to entering the optical detection chamber. This can be implemented without the need of physical barriers such as conventional filters by employing diffusion within a microfluidic environment to separate small particles from large particles like cells. The principle behind diffusional filtering is shown schematically in Figure 7-4 where two inlet streams combine into an “Extraction” channel. Because there is no turbulence the two streams flow side by side in this channel

with absolutely no viscous or eddy mixing. The only transport of molecules from one stream to the other is purely by molecular diffusion, not requiring any external power sources. The major factors affecting diffusion are particle size, solution viscosity, and fluid temperature. Small molecules diffuse quickly from the sample stream to the waste stream (i.e., the outlet port on the top right) while the large molecules remain indefinitely in the sample stream and are collected as filtered output (i.e., the outlet port on the lower right of the H). Therefore, sample purification can occur by separating and isolating components without the need for centrifugation or filtration thus requiring no external equipment other than a small pump. Since no physical filter is required, there is no risk of clogging. Microfluidic diffusional filtering technology has been proven in the laboratory and tested with a variety of substances including human blood.<sup>2</sup>

**H-Filter Development.** A subcontract with Micronics, Inc (Redmond, WA) was let to design and provide SatCon with their proprietary H-filter microfluidic systems. The goal of this effort was to 1.) Evaluate the performance of the H-filter to separate unwanted analyte from a population of *E.coli* cells and 2) effectively separate toxins from cells within a sample in order to make quality simultaneous measurements. If successful the H-filter was envisioned to be eventually integrated into a disposable cartridge containing the waveguides for on-chip sample preparation. For these Phase II experiments all processing was to be performed serially in benchtop formats.

Two iterations of the filter were contracted from Micronics i.) an initial demonstration processing a 100  $\mu$ l sample and ii.) a scaling up in size to process a 1 ml sample within 30 minutes. In all, there were three batches of cartridges delivered by Micronics, Inc for testing plus additional samples with a proprietary hydrophilic surface. The cartridge developed for iteration ii.) was not able to be successfully scaled to the 1 ml volume in a usable format and the contract was fulfilled by producing additional cartridges from the first design (the '2<sup>nd</sup> batch').

Description of the H-filter. The main purpose of the tests was to verify performance of the H-filters. The tests also provided verification and calibration of the analytical models. This section describes the basic H-filter operation. A schematic representation of the H-filter is shown below in Figure 7-5:

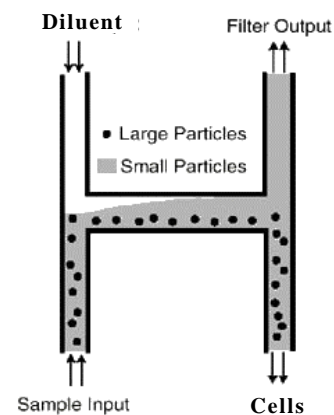


**Figure 7-4.** H-Filter: Two separate inlet streams, a reagent and a sample, combine into an Extraction channel that has the precise dimensions to separate large particles (non-diffusing) from small particles (diffusing) for a given low Reynolds number flow. The small particles are drawn off the top while the large particles are drawn off the lower leg<sup>2</sup>.

<sup>2</sup> Holl, M.R., P. Galambos, F.K. Forster, J.P. Brody, and P. Yager, "Optimal Design of a Microfabricated Diffusion-Based Extraction Device", Vol 4, 111-111, 1997.

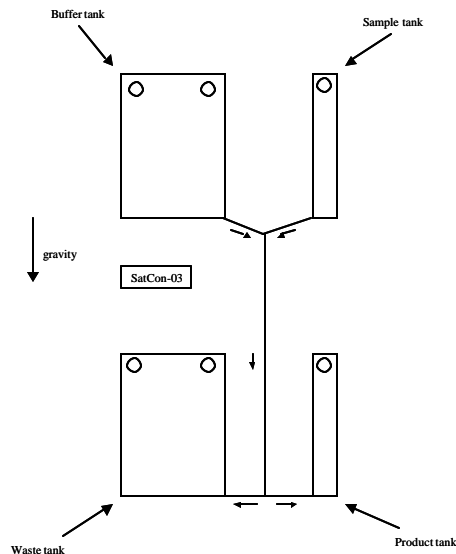


**Figure 7-5:** Schematic Diagram of the SatCon H-Filter.

The function of the device is to remove smaller particles from a sample solution, while recovering larger particles. The output or product of the H-filter is a solution that contains a reduced concentration of small particles, with nearly the same concentration of large particles. The success of the H-filter depends largely on the relative difference in particle sizes. Particles that are similar in size will not separate well, however, particles of very different sizes can be separated very efficiently.

The operation of the gravity-fed H-filter is straightforward. The fluid sample containing the analyte particles is inserted in the sample tank. The buffer tank is filled with the receiver solution, which serves as the solvent in the diffusion process. The cartridge is oriented vertically (or tilted at a specified angle) during operation and the sample and buffer streams flow into the main channel. The process is complete when the sample and buffer tanks are emptied, corresponding to the product and waste tanks being full.

The device performance measures are recovery and removal. The particle recovery is defined as the ratio of final concentration in the product tank to initial concentration in the sample tank. Likewise, the particle removal is defined as the ratio of final concentration in the waste tank to initial concentration in the sample tank. The design specifications for the first generation H-filter are given in Table 7-1.

**Table 7-1:** H-Filter Design Specifications.

Feature/Characteristic	Specification
Sample Volume	0.1 mL
Buffer Volume	1.0 mL
Processing Time	10 min
Large Particle Size	2 $\mu$ m
Small Particle Molecular Weight	70 g/mmol
Fluid Viscosity	1.0 cP
Fluid Specific Gravity	1.0
Removal of Small Particles	85%
Recovery of Large Particles	95%

The first generation H-filter was specified to handle fluids with properties similar to water. The tanks and channels in the device were designed to recover at least 95% of 2- $\mu$ m particles, and remove at least 85% of 70 g/mmol particles.

Preliminary Tests. Four basic experiments were performed to verify the initial performance of the first generation H-filter:

1. Test the recovery of 1.02- $\mu$ m polymer beads.
2. Test the removal of Bovine Serum Albumin (BSA, Molecular weight is 68 g/mmol).
3. Test the recovery of live *E.coli* 030 cells.
4. Test the removal of BSA in the presence of 1.02- $\mu$ m polymer beads (multiple species diffusion).

The first three tests were essentially binary diffusion processes, with a single diffusing species in the sample solution. The fourth test was a multi-component diffusion process, with two diffusing species in the sample solution (BSA and polymer beads).

Procedure.

1. Prepare a 0.1-mL sample and measure the particle concentration using a spectrophotometer.

2. Dispense the sample solution into the sample tank in the H-filter, and fill the buffer tank with the solvent fluid.
3. Place the H-filter on the test stand to initiate the run, and use a stopwatch to clock the run time.
4. At the end of the run, use a syringe to remove the product and the waste.
5. For measurements of large particle recovery, measure the concentration of the product solution using the spectrophotometer. Compare the recovered particles to the initial particles in the sample solution to assess the recovery.
6. For measurements of small particle removal, measure the concentration of the waste solution using the spectrophotometer. Compare the removed particles to the initial particles in the sample solution to assess the removal.

**Test Results and Discussion.** The results of the four basic tests are presented below in Table 7-2. In addition to the experimental results, the analytical estimates from the SatCon model are listed for the applicable tests.

**Table 7-2: Preliminary H-Filter Experimental Results**

Test Description	Test Results	Model Predictions
Recovery of 1.02- $\mu$ m polymer beads	91%	81%
Removal of 68 g/mmol BSA	62%, 69%	77%
Recovery of live <i>E.coli</i> 030 cells	85%	Not Applicable
Removal of BSA with suspended beads	No Test Data	77%

- **Test 1: Polymer Beads Recovery.** The result of the polymer beads test verifies the successful recovery of large particles. The H-filter was originally designed for 2- $\mu$ m particles with a 95% recovery specification. The recovery of 1.02- $\mu$ m beads was measured to be 91%; this is a good indication that the design specification of 95% recovery of 2- $\mu$ m particles would be realized in practice. The analytical model predicted a lower recovery than what was measured.
- **Test 2: BSA Removal.** The BSA removed during this test fell short of both the design specification and the analytical model. The device was designed to remove 85% of the small particles (70 g/mmol), but the measured removals were 62% and 69% from 2 independent tests. Additionally, the analytical model predicted a removal of 77%. The reason for these discrepancies is not understood.
- **Test 3: Live *E.coli* 030 Cell Recovery.** The usefulness of this particular test may not be obvious, but indeed this test served as an indication of the mobility of the live cells. Because the cell size (1-5  $\mu$ m, non-spherical) is similar to the polymer beads (1.02- $\mu$ m, spherical), it is expected that the recoveries of the two would be similar, and indeed they were (91% for the

beads, 85% for the cells). One possible explanation for the lower recovery of cells compared to beads is the mobility (swimming ability) of the live cells. Any significant cell mobility will effectively increase the apparent diffusivity of the cells therefore decreasing the cell recovery. Further tests should be performed to verify this hypothesis. If cell mobility is deemed important, then it should be addressed in future h-filter design generations by modifying the diffusivity value used in the design calculations.

- Test 4: BSA Removal with Suspended Polymer Beads: Unfortunately this test was unsuccessful. It is believed that the procedure used for this test was flawed. The test involved the same basic steps described previously, except that the product solution was spun down with a centrifuge, and the liquid components were manually separated from the solid beads prior to analysis in the spectrophotometer. Apparently, the product solution was not spun down long enough, and there were trace amounts of solid beads still in the spectrophotometer sample. This led to an erroneous BSA concentration measurement.

Test Results for All Batches. Similar experiments were performed for the other batches of 100 µl sample cartridges. Again, three basic measurements were performed to test:

1. The removal of BSA.
2. The recovery of live *E. coli* O30 cells.
3. The removal of BSA and recovery of *E. coli* cells from the mixture of BSA and viable *E. coli* cells.

The first two tests involved single diffusing species in the sample solution, whereas the third and fourth tests had two diffusing species in the sample solution (BSA and *E. coli* cells). The basic experimental protocol common to all tests is summarized as given below.

- a. Prepare BSA solution as well as suspension of the overnight grown *E. coli* cells in PBS and observe the absorbance (for BSA at 280nm and for *E. coli* cells at 600 nm, respectively) using spectrophotometer.
- b. Fill the buffer tank with PBS and dispense 100 µl of sample into the sample tank.
- c. Place H-filter at 30°, 45 ° degree or at vertical position to initiate the run.
- d. At the end of the run, use a syringe to remove the product and the waste. In order to determine the removal of small molecules (i.e. BSA), measure the absorbance of the waste solution and compare it that of the staring/ initial sample solution. To determine recovery of large particles (i.e. *E. coli* cells), measure the absorbance of the product solution and compare it with the absorbance of the sample solution.

Results and Discussion. The results of the first two tests are presented below in Table-7-3 and the results of the third test are given in Table-7-4.

**Table-7-3.** Recovery of *E. coli* cells and removal of bovine serum albumin (BSA) using three different batches of H-filter cards.

Recovery of <i>E. coli</i> Cells				Removal of BSA		
Card Orientation	1 <sup>st</sup> Batch	2 <sup>nd</sup> Batch	Hydrophilic Coating	1 <sup>st</sup> Batch	2 <sup>nd</sup> Batch	Hydrophilic Coating
30 <sup>0</sup>	57%	77%	72%	79%	79%	82%
45 <sup>0</sup>	60%	68%	74%	84%	88%	87%
90 <sup>0</sup>	54%	64%	67%	62%	84%	78%

**Table 7-4.** Separation of *E.coli* cells from BSA in the mixture of BSA and *E.coli* cells.

Recovery of <i>E. coli</i> Cells				Removal of BSA		
Card Orientation	1 <sup>st</sup> Batch	2 <sup>nd</sup> Batch	Hydrophilic Coating	1 <sup>st</sup> Batch	2 <sup>nd</sup> Batch	Hydrophilic Coating
30 <sup>0</sup>	60%	75%	70%	86%	91%	82%
45 <sup>0</sup>	62%	70%	66%	87%	94%	88%
90 <sup>0</sup>	60%	67%	67%	84%	92%	78%

Test-1: Removal of BSA: The BSA removal using all three batches of H-filter cards was between 78 - 88%. In all the batches of filter cards, the maximum BSA removal was achieved when the cards were operated at 45° degree. However, the cards from the 1<sup>st</sup> batch gave very poor removal of BSA when operated in vertical orientation. Of all the filter cards, the cards with hydrophilic coating were very convenient to handle and there was no difficulties with bubbles or air pockets in the main channels.

Test-2: Recovery of live *E.coli* cells: Recovery of live *E.coli* cells using H- filter cards from 2<sup>nd</sup> batch as well as with hydrophilic coating was to the order of between 67% and 77%, whereas, the card from 1<sup>st</sup> batch gave very poor recovery of *E.coli* cells (i.e. between 54-60%). The overall recovery of live *E.coli* cells using all three batches of H-filter cards was very significantly lower than the 95% specification.

Test-3: Removal of BSA and Recovery of *E. coli* from a mixture. Products from the product tank containing recovered *E.coli* cells as well as from the waste tank containing removed BSA were drawn out. The product from the waste tank was spun down at maximum speed in clinical centrifuge to pellet down the *E.coli* cells (unrecovered cells) and the absorbance of the supernatant was taken to determine the BSA removal. Surprisingly the values for the removal of BSA from the *E.coli* cells suspension were comparatively higher than the values of the removal of BSA without *E.coli* cells, using filter cards from 1<sup>st</sup> batch (84%-87% as compared to 62%- 79%) as well as from 2<sup>nd</sup> batch (91%- 94% as compared to 79%- 88%). However, the removal of BSA using filter cards with hydrophilic coating was same in the absence of presence of *E. coli* cells.

Recovery of live *E.coli* cells in the absence or presence of BSA, using all three batches of filter-cards, at all three orientations didn't show any substantial difference.

**Summary.** Significant testing was performed to evaluate the Micronics H-filter as a method for 'on-chip' sample preparation. The design of the system depends critically on the viscosity and specific density of the constituent, thus, the sample must be very well characterized for effective use. No clogging was observed with the cell suspensions used and difficulties with trapped air were minimized with experience. The devices tested were more effective at separating out the small molecules than recovering the larger cells. Typically, cell recovery was only 70% of the originally specified 95% recovery. Improved cell recovery can be obtained but at the expensive of significantly less small

molecule cleanup. We have concluded that the H-filter as tested would serve no obvious advantage for automated sample preparation. However, the laser fabrication process used for making inexpensive disposables is an ideal candidate for the consumable cartridge including the waveguide.

# **Appendix 7-A: Surface Desensitization of Polarimetric Waveguide Interferometers**

# Surface Desensitization of Polarimetric Waveguide Interferometers

Colin Worth, Bennett Goldberg, Michael Ruane, Selim Unlu

## Abstract

Non-specific surface binding of small protein molecules presents a major obstacle to surface bio-sensing techniques attempting to detect very low concentrations ( $< 1 \text{ pg/mm}^2$ ) of large biological objects such as cells and bacteria. Desensitization of a polarimetric waveguide interferometer eliminates the background noise from non-specific surface binding. We demonstrate the ability to tune the phase sensitivity of a waveguide interferometer as a function of the distance of the biological or chemical analyte from the waveguide surface. It is possible to design a sensor that has zero sensitivity at a particular distance where non-specific surface binding occurs without significantly reducing the sensitivity to larger, target biological species.

## Keywords

Surface Sensing, Evanescent Wave Biosensing, Waveguide Interferometry

## I. INTRODUCTION

OPTICAL techniques for detecting low concentrations of cells or bacteria in solution have become popular over the past few years[1], [2]. In particular, waveguide interferometry has the potential to become an effective approach for biosensing[3], [4]. Waveguide interferometry exploits changes in the guided modes of a waveguide caused by biological particles above the waveguide surface. The biological particles affect the waveguide modes by interacting with the evanescent electromagnetic fields above the waveguide. While other optical biosensing techniques, e.g. Total Internal Reflection Fluorescence(TIRF)[5], [6], select particles for detection with processes such as tagging with fluorescent markers, waveguide interferometry detects a particular species with chemically selective surface binding sites. Because any particle bound to the surface causes a change in the local index of refraction and evanescent fields, the effectiveness of selective binding chemistry determines how well the biosensor can distinguish small numbers of the desired particle type. Perfecting selective chemical binding techniques for specific particles is a major challenge facing biosensors.

This paper describes a purely optical method of distinguishing between specifically and non-specifically bound particles, based on particle size and distance above the waveguide surface. In most biosensing applications, specifically bound particles—such as bacteria—are much larger (several microns across) than non-specifically bound particles—typically proteins (several nm across). We show that tuning the evanescent field polarization modes desensitizes a thin (20-30 nm) layer above the waveguide surface, reducing the response to non-specific binding by a factor of one hundred or more.

## II. MODE BEHAVIOR OF AN EVANESCENT WAVEGUIDE INTERFEROMETER

### A. Waveguide Modes

A slab waveguide consists of multiple dielectric layers, each with different refractive indices, stacked along the x dimension (Fig. 1) to form a guiding layer with upper and lower buffer layers. The slab has infinite extent in the remaining y and z dimensions. The guiding layer supports a propagating light wave with evanescent tails. Solving Maxwell's equations shows that the propagating light has a stationary sinusoidal amplitude profile in the x-direction (Fig. 2) with exponentially decaying evanescent fields in the buffer layers and beyond. The electric field in the guiding layer is given by:

$$E = \cos(k_x x) e^{ik_z z - i\omega t} \quad (1)$$

The total wavevector of the light,  $\vec{k}$  is determined by the index of refraction of the guiding medium according to:

$$k_x^2 + k_z^2 = n_g^2 k_0^2, \quad (2)$$

where  $k_0 = \frac{2\pi}{\lambda_0}$  is the free-space wavevector. The boundary conditions at each interface require the z-component of

Colin Worth is a graduate student at the Boston University Physics department. email: cworth@ultra.bu.edu

Bennett Goldberg is Professor of Physics and Professor of Electrical and Computer Engineering at Boston University. email: goldberg@bu.edu

Michael Ruane is Professor of Electrical & Computer Engineering at Boston University. email: mfr@bu.edu

Selim Unlu is Professor of Electrical & Computer Engineering at Boston University. email: selim@photon.bu.edu

the wavevector to be conserved.  $k_z$  is called the propagation constant,  $\beta$ , of the mode. A fundamental property of waveguides is that mode solutions exist only for particular, discrete values of  $\beta$ . The guiding layer thickness,  $t_g$ , is chosen to allow only two propagating modes,  $TE_0$  and  $TM_0$ , which have orthogonal polarizations.  $t_g$  is typically on the order of 100 nm for  $\lambda = 633$  nm.

### B. Measuring Changes in the Propagation Constant of Waveguide Modes

Interferometry measures relative phase shifts between two coherent beams of light by observing their interference fringe pattern. Any change in the optical path length of one of the beams causes a resultant shift in the interference pattern. In waveguide interferometry, the two beams correspond to the two lowest order waveguide modes,  $TE_0$  and  $TM_0$ . Binding of many biological particles to the waveguide surface changes the index of refraction of a thin layer above the surface, leading to a change in the dielectric boundary conditions that determine the mode propagation constants. The change in the propagation constants leads to a change in the optical path length of the light, and a total phase shift,  $\Delta\phi$ , proportional to the average change in the propagation constant per unit length,  $\Delta\beta$ , times the interaction length,  $L$ .

$$\Delta\phi = \Delta\beta L, \quad (3)$$

When the two modes are interfered, the overall phase shift in the interference pattern is equal to the *relative* phase shift between the two modes:

$$\Delta\phi = \Delta\phi_{TM} - \Delta\phi_{TE} = (\Delta\beta_{TM} - \Delta\beta_{TE})L \quad (4)$$

### C. Formulation of Sensitivity

Modal phase shifts due to binding of biological particles to the waveguide surface can be estimated by representing the biological matter by a uniform dielectric layer located above the waveguide. For widespread binding of many small particles, as in non-specific binding of proteins, this uniform model is appropriate.

To determine the response of the waveguide to changes in the biolayer index, for particular values of the layer indices and thicknesses,  $n_i$  and  $t_i$ , we numerically obtain the propagation constants[8],  $\beta_{TM}$  and  $\beta_{TE}$  for two cases. First, we consider  $n_b$  without the nonspecific binding species. Next, we change  $n_b$ , by a small amount,  $\Delta n_b$  (1% typically) to represent the effect of non-specific binding, and again solve for the propagation constants. The sensitivity for each mode is proportional to the change in the propagation constant divided by the change  $\Delta n_b$ . To define the sensitivity, we first define a normalized propagation constant or effective index:

$$n_{eff} = \frac{\beta}{k_0} \quad (5)$$

The sensitivity of each mode is defined as the change in the effective index of the mode divided by the change in the biolayer index.

$$S_{TE} = \frac{\Delta n_{eff;TE}}{\Delta n_b} \quad (6)$$

$$S_{TM} = \frac{\Delta n_{eff;TM}}{\Delta n_b} \quad (7)$$

The differential sensitivity,  $\Delta S$ , is then

$$\Delta S = S_{TM} - S_{TE}. \quad (8)$$

## III. RESULTS AND DISCUSSION

Both the  $TM_0$  and  $TE_0$  modes respond to refractive index changes near the waveguide surface. However, the interferometric measurement signal responds to *relative* changes between the two modes. To maximize interferometric sensitivity, we vary waveguide thickness to maximize the difference between the responses of each mode. Fig. 3 shows the sensitivity of the  $TE_0$  and  $TM_0$  modes as a function of  $t_g$ , the thickness of the guiding layer for a materials system consisting of a silicon nitride-silicon dioxide waveguide ( $n_i = n_u = 1.465$ ,  $n_g = 2.02$ ), operating at  $\lambda = 632.8$  nm, and a biolayer thickness  $t_b$  of 10 nm. The biolayer index is varied around  $n_b = 1.333$ , the index of water, to determine the sensitivities. The maximum differential sensitivity occurs at  $t_g \approx 166$  nm. A similar value of  $t_g$  gives the maximum sensitivity for thicker biolayers as well, due to the fact that the  $TE_0$  mode is significantly more confined within the guiding layer than the  $TM_0$  mode.

Fig. 4 shows the variation of the differential sensitivity,  $\Delta S$ , with the thickness of the biolayer,  $t_b$ , for several values of  $t_g$  including  $t_g = 166$  nm. The sensitivity saturates with increasing biolayer thickness at around half a wavelength (300 nm to 400 nm) because the evanescent field strength decays significantly at this distance. For lower values of  $t_g$ , Fig. 4 shows an unexpected result. Not only do the steepness and the saturation point of the sensitivity curves change, but the curvature changes as well. For a guiding layer thickness,  $t_g = 84$  nm the differential sensitivity is negative (the TE mode is more sensitive than the TM mode) for biolayer thicknesses,  $t_b$ , from 0 to 60 nm. At  $t_b = 60$  nm, the TE and TM modes respond equally to changes in the biolayer index. Thus, although the response of each mode is finite, the differential response is zero. This represents a new desensitization effect for thin biolayers that we have discovered.

Fig. 5 shows an enlarged plot of Fig. 4 for biolayers between 0 and 60 nm thick. Take, for example, the curve corresponding to a guiding layer thickness  $t_g = 87$  nm. Although the saturated differential sensitivity (important for detection of large particles) is reduced by a factor of 60%, Fig. 5 shows that the biosensor is essentially blind to binding of small particles from a few Angstroms to 20 nm in thickness. A comparison of the curves for  $t_g = 87$  nm and  $t_g = 166$  nm shows that the average sensitivity to small particles in the range  $5 \text{ nm} < t_b < 20 \text{ nm}$  has been reduced by a factor of 100, and proteins or cells as large as 30 nm produce a signal almost twenty times less than they would have in a non-desensitized system.

The sensitivity of a waveguide mode to a particular uniform biolayer is related to the proportion of the mode intensity contained in the evanescent fields interacting with the biolayer. To examine closely the mechanism of the desensitization, the two normalized  $TE_0$  and  $TM_0$  mode profiles for a waveguide optimized for high differential sensitivity ( $t_g = 166$  nm) are shown in Fig. 6. Fig. 6 also shows the mode profiles for a guiding layer  $t_g = 87$  nm. The most significant difference between the two modes is the large electric-field discontinuities for the TM mode at the guiding layer boundaries due to the component of the electric field normal to the boundaries, resulting in a higher evanescent field strength for the TM mode than for TE mode, for both thinner and thicker biolayers. Fig. 3 displayed the relative sensitivities of the TE and TM mode for a thin 10 nm biolayer for this value of  $t_g$ , showing that the TM mode has a much greater response. For a guiding layer thickness,  $t_g = 87$  nm, the field intensity of each mode relative to the total mode intensity is identical at a distance of 21 nm above the waveguide. Thus, the change in the optical path length is identical, leading to zero sensitivity at this point.

#### IV. CONCLUSIONS

Polarimetric waveguide interferometers use the differential phase shift between two orthogonal waveguide modes to detect biomaterials bound to the waveguide surface. The differential interference technique and the complex response of waveguide modes to changes in waveguide thickness allow us to tailor the optical phase response of the biosensor to discriminate against non-specific binding of small molecules such as proteins. Interferometric optical sensors are fundamentally limited not by their optical phase resolution, but by chemical processes at the waveguide/biolayer interface, especially non-specific binding of proteins. We believe that the method of surface desensitization reported here will allow results several orders of magnitude better than previously reported for the detection of large molecules such as bacteria bound to a waveguide surface. We are also implementing a doubly-differential technique to compensate for thermal and concentration gradients within the waveguide and sample. The latter effects may play a greater role once the signal due to non-specific binding is reduced by desensitization.

#### REFERENCES

- [1] Abel, P.A., M. G. Weller, G.L. Duveneck, M. Ehrat, and H. M. Widmer, *Fiber-Optic Evanescent Wave Biosensor for the Detection of Oligonucleotides*, Anal. Chem., 68, 2905-2912, 1996.
- [2] James, E.A., K. Schmelzer, and F.S. Ligler, *Detection of Endotoxin Using an Evanescent Wave Biosensor*, Applied Biochemistry and Biotechnology, 60, 189-202, 1996.
- [3] Lukosz, W. Sensors and Actuators B 29, 37-50, 1995; Lukosz, W., Sensors and Actuators B, 38-39, 316-323, 1997.
- [4] Hartman, N.F., J. C. Wyvill, D.P. Campbell, and P. Edmonds, *Rapid Response Biosensor for Detection and Identification of Common Foodborne Pathogens*, SPIE Proceedings Vol. 2345, 128-137, 1995; Hartman, N.F., J. Cobb, J.G. Edwards, *Optical System on-a-chip for Chemical and Biochemical Sensing: the Platform*, SPIE Proceedings, Vol. 3537, 302-308, 1998; Hartman, N.F., U.S. Patents 5,623,561, 4,940,328.
- [5] Zhou C., P. Pivarnik, S. Anjou, A. Rand, and S. Letcher, *A Compact Fiber-Optic Immunosensor for Salmonella Based on Evanescent Wave Excitation*, Sensors and Actuators B (Chemical), 1997.
- [6] Rockhold, S.A., R.D. Quinn, R.A. Van Wegenen, J.D. Andrade, M. Reichert, *Total Internal Reflection Fluorescence (TIRF) as a quantitative probe of protein adsorption*, J. Elect. Chem. Vol. 150, pp 261-275; 1983.
- [7] Walt, D.R., V. Agayn, K. Bronk, S. Barnard, *Fluorescent Optical Sensors*, Applied Biochemistry and Biotechnology, 41, 129-139, 1993.
- [8] Numerical simulation software by Optiwave Corp., Nepean, Ontario.
- [9] Bluestein, B.I., I.M. Walczak, and S. Chen, *Fiber-Optic Evanescent Wave Immunosensors for Medical Diagnostics*, Tibtech, 8, 161-168, 1990.

## FIGURE CAPTIONS:

[Figure 1] Generic slab waveguide structure. Thicknesses,  $t_x$ , and refractive indices,  $n_x$ , in each layer vary. BOX is buffered oxide layer and forms first buffer layer. Typical thickness values:  $t_l \simeq 1500$  nm,  $t_g \simeq 150$  nm,  $t_u \simeq 5$  nm,  $t_b \simeq 10$  nm. Mode propagates in  $+z$  direction.

[Figure 2] Electric field for lowest order TE guided mode of a slab waveguide.

[Figure 3] Waveguide sensitivities vs. guiding layer thickness for a silicon nitride-silicon dioxide waveguide ( $n_l = n_u = 1.465$ ,  $n_g = 2.02$ ,  $t_l = 1500$  nm,  $t_u = 4$  nm), operating at  $\lambda = 632.8$  nm, and a biolayer thickness  $t_b = 10$  nm.

[Figure 4] Waveguide sensitivity vs. biolayer height for several guiding layer thicknesses.  $\Delta n_b = 0.005$

[Figure 5] Waveguide sensitivity vs. biolayer thickness, enlarged for thin biolayers for several guiding layer thicknesses. For  $t_g = 87$  nm,  $|\Delta S| < 10^{-4}$  for  $0 < t_b < 25$  nm. Compare to  $\Delta S$  for  $t_g = 166$  nm.

[Figure 6]  $TE_0$  and  $TM_0$  mode electric field profiles for guiding layer thicknesses of 166 nm and 87 nm. a)  $TM_0$  mode. b)  $TE_0$  mode.  $x=0$  in center of guiding layer. Asymmetry is due to unequal buffer thicknesses.

# **Appendix 7-B: Experimental Plan for Optical Surface Desensitization**

**October 11, 2001**

**Plan for measuring surface desensitization in optical polarimetric waveguide biosensors**

These experiments will demonstrate optical surface desensitization in polarimetric waveguide biosensors. We will use a HeNe laser to end-fire couple into waveguides with three different guiding layer thicknesses to measure the dependence of the phase sensitivity measured with both surface layers and bulk media on guiding layer thickness. Bulk measurements will be carried out with a sucrose solution. Surface measurements will be done for several protein types. Our purpose is to show that the near-surface phase sensitivity is reduced by several orders of magnitude for the thinner waveguides, whereas the bulk (saturated) sensitivity is only reduced by a factor of 2-3. The latter reduction applies to measurements of large biological molecules and cells attached to the waveguide surface, such as bacteria, whereas the former reduced sensitivity applies to non-specific protein binding near the surface.

There are two general types of experiments that must be performed in order to acquire the needed data and show the intended surface desensitization. Task 1 is the characterization of the biolayer specifically bound to the waveguide surface. Both the height and the index of refraction of the layer must be measured for the most accurate determination of the effect of the waveguide guiding layer thickness on the differential phase. Task 2 is the characterizing of the experimental setup and taking of data with the polarimetric waveguide interferometer for both bulk solutions and surface-bound proteins.

These two experimental paths can be carried out in parallel. Pieces will be prepared for characterization in parallel with the waveguide interferometry work. In addition, once successful results have been obtained using the biosensor, at least one waveguide of each type will be put through the same characterization process described below and compared with results on previous samples.

Appendix A lists our inventory of waveguides and samples, and the work required to complete the samples necessary for the experiments. Appendix B lists the protein types available for testing. Appendix C shows predicted outcomes of the interferometry experiments for each biolayer/waveguide thickness combination, and a plot of the biosensor sensitivity with crosses indicating data points that will be hopefully determined experimentally.

**Task 1: Biolayer Characterization:**

**General:** Characterization of the biolayer requires preparation of test samples at Satcon, and analysis at BU (AFM, Reflectometry) and at MIT (Ellipsometry). AFM measurements, if successful, will measure the height of the biolayer. If the height is

known, Reflectometry and/or Ellipsometry can determine the index of refraction of the biolayer. In addition we will try to determine the uniformity of the layer to find out if we have a monolayer of protein. Ellipsometry has a beam size of about one square millimeter and will thus be limited to measuring the gross uniformity. We will scan small areas of the surface ( $\sim 5\text{ }\mu\text{m}$ ) with the AFM to determine local uniformity. This will be performed on four different sections of each sample surface.

In the sections below, we describe the sample preparation, the required samples and configurations for the characterization steps for both AFM and Ellipsometry experiments.

*Sample Preparation for Characterization:* The following is a step-by-step outline of sample preparation for each of the characterization experiments. In all cases, the waveguides are prepared at Satcon by the following procedure.

- 1) Immerse in a Piranha solution for cleaning.
- 2) Immerse in an OTS solution until saturation occurs (10 hours is sufficient). The OTS forms a thin (1-2 nm) layer which creates a hydrophobic surface for protein binding.
- 3) Expose the surface to a solution consisting of the protein and a PBS buffer. In the biosensor experiments, the protein will be applied dynamically by flowing across the waveguide surface. Therefore several samples should be coated with biolayer in this fashion (see below). For characterization only, protein can also be added by immersing the waveguide in the protein solution. This result can be compared to the result obtained using the flow cell.

*Ellipsometry:* Ellipsometry will be carried out by Paul Lebinas at MIT. To obtain data by this method, the biolayer must be applied to a silicon substrate (without a guiding or buffered oxide layer). Data will be taken with an ellipsometer with and without the protein monolayer. Therefore silicon pieces coated with protein, and silicon pieces coated with OTS only are required. The protein will be applied through both the immersion coating at Satcon and flow cell coating to compare the two protein application methods. The labeling refers to the particular silicon piece, S1-S6. The experiments require 6 silicon pieces (S1-S6) for each protein. The following set of procedures will be applied to each protein, with the samples reused in between experiments. Following the experiments, we expect to obtain height and refractive index, as compared to the bare OTS surface for each protein. We expect also to be able to test for any differences in the protein coating methods.

- 1) Coat all with OTS at Satcon
- 2) Coat 2 w/PROTEIN in lab at Satcon (S1,S2)
- 3) Coat 2 w/PROTEIN using flow cell at Satcon (S3,S4)
- 4) S5, S6 are left with OTS only
- 5) Samples taken to MIT for analysis of protein height and gross uniformity.

*AFM and Reflectometry:* AFM and reflectometry measurements will be carried out at BU. Professor Chasen of the BU physics department will assist with the AFM work.

Reflectometry will be carried out in our lab at BU on the setup of Professor Swan. The AFM will determine the height of the biolayers, which together with the reflectometry, can determine also the refractive index. The experiments require 6 166 nm waveguides, labeled R1-R6, which again can be reused for each of the proteins.

- 1) At BU, do one reflectometry measurements on each waveguide in a cuvette region prior to coating the surface. Make sure that the color of the facets are uniform.
- 2) At Satcon, coat all 6 waveguides with OTS
- 3) At Satcon, Coat 2 with PROTEIN in lab (R1, R2)
- 4) At Satcon, Coat 2 with PROTEIN using flow cell (R3,R4)
- 5) R5,R6 OTS are left with OTS only.
- 6) Repeat reflectometry on each to determine thickness to obtain thickness/index data.
- 7) Perform AFM measurements of the biolayer height for waveguides R1 and R3. Professor Chasen has suggested a method of removing a piece of the biolayer using the force of the AFM tip in tapping mode (wet), and then measuring the depth of the removed section. We have demonstrated this technique, which removes a local section with the added AFM tip force of tapping mode. This will provide a step edge for measuring the biolayer height. In addition, we will scan the surface in four places (10 micron scans) to look at local layer uniformity on several sections of the surface.

**Outcome of Task 1:** Data from the ellipsometry and AFM and reflectometry experiments will be compared. We expect to have a determination of the height to within +/- 0.5nm, and index to within about 3%. These numbers will provide sufficient resolution to use the data to demonstrate surface desensitization.

### **Task 2: Waveguide Interferometry:**

**General:** In the following, we describe the requirements of phase resolution necessary to show the effects of surface desensitization, the characterization of the interferometric setup, and the waveguide biosensing experiments we will perform. The latter experiments look for surface desensitization by measuring the phase response of the biosensor to different proteins for three different guiding layer heights. Figure 3 in the first appendix shows the theoretical waveguide sensitivity as a function of biolayer height and waveguide thickness, and the crosses indicate the points on each curve that these experiments will map out. By comparing the points on the 85 nm and 103 nm waveguide curves to the results for 166 nm waveguides, for proteins and bulk solution measurements, we will demonstrate the desensitization effect.

*Required Phase Resolution:* Our phase resolution must be high enough to measure the phase response for each protein and waveguide. Predicted phase results are given in Appendix C, Table 1. The minimum expected phase shift is  $-3.2 \times 10^{-1}$  cycles for an 85 nm waveguide response to lysozyme. To make this measurement, we require a phase

resolution of at least  $10^{-2}$  to  $10^{-3}$  cycles. In past work, Dr. Ron Rieder of Satcon obtained a phase resolution of  $10^{-4}$  cycles.

*Characterization of interferometric setup:* In order to determine the accuracy of our measurements, and consequently the minimum detectable phase signal, we will take a half-hour set of interferometric data for an open path interferometer and measure the RMS noise of the signal from the detector. If necessary, we will take 10 minutes of unfiltered data at 40 kHz to obtain the PSD spectrum in order to identify specific noise sources. Finally, we will estimate the long-term DC offset drift of the detector.

*Bulk Solution experiment:* The following experiment will be performed first once the characterization of the setup is complete. The experiment measures the response of each waveguide to a bulk sucrose solution with a known refractive index. This data measures the biosensor sensitivity to samples large enough to saturate the evanescent fields at the waveguide surface, such as bacteria. The experiment will be performed first because it produces the largest phase response and can be repeated without removing and cleaning the waveguides. Therefore, we will be able to easily make a number of trial runs to ensure that the setup is producing consistent data.

*Method:* The following experiment will be performed at Satcon on three waveguides, one with 166 nm guiding layer height, one with 103 nm guiding layer height, and one with ~85 nm guiding layer height. The solutions used will be de-ionized water (as a buffer), and a sugar solution of known refractive index.

Process steps:

- a) flow buffer through flow cell for 20 seconds and record phase
- b) flow sugar solution for twenty seconds and monitor change in phase
- c) flow buffer solution for twenty seconds and monitor change in phase
- d) repeat b and c using different flow rates and compare results

*Outcome:* This experiment will give us the bulk phase sensitivity for each type of waveguide, providing the three data points shown on the first plot in Figure 3. The phase response will be determined with an accuracy of 1% or better.

*PROTEIN layer experiment:* The following experiment measures the phase response of the biosensor for different protein and guiding layer heights. Each experiment described below must be repeated for each protein type, reusing the waveguides inbetween experiments. A list of proteins and approximate layer heights are given in Appendix B. These experiments will provide the data points indicated by crosses on the second plot in Figure 3.

*1. Thick (166 nm) waveguides:* In this experiment, protein is flowed across a 166 nm waveguide and the phase response is measured. Experiments on thick waveguides will be carried out first because the phase response will be the larger than for thin proteins, and therefore easier to detect. If necessary, we will repeat

the experiment and vary the flow rate of the protein to determine the flow rate that induces the most surface binding. This experiment requires 2 polished thick (166 nm guiding layer) waveguides (labelled R7 and R8, see Appendix A). The buffer solution is PBS.

- a) At Satcon, coat waveguides with OTS as described in the characterization section.
- b) Mount waveguide in interferometry setup.
- c) Flow buffer solution through flow cell for one minute
- d) Flow PROTEIN solution until phase measurement saturates
- e) Flow buffer solution for thirty minutes to clean bulk solution
- d) Experiment may need to be repeated with different flow rates. If more than two runs are required, surfaces must be regenerated overnight.
- e) once successful results are obtained, one waveguide will be characterized as described in Task 1 in order to compare with previously characterized samples.

*2. Thin (103 nm, 85 nm) waveguides:* This experiment is identical to the first, except that a 103 nm waveguide (labelled D1), and an ~85 nm (labelled E1) waveguide replace the 166 nm waveguide. The flow rate used is the same as determined in the previous experiment.

- a) At Satcon, coat waveguides with OTS as described in characterization section.
- b) Flow buffer solution through flow cell for one minute
- c) Flow PROTEIN solution until phase measurement saturates
- d) Flow buffer solution for thirty minutes to clean bulk sln
- e) After the experiment, the waveguides will be characterized as described in the characterization section.

**Outcome of Task 2:** The data from these experiments will map out the sensitivity curves in Figure 3. The phase resolution of the measurements will have an accuracy of  $10^{-2}$  or better, as determined by the characterization of the optical setup. For the smallest data point, this corresponds to an accuracy of 1%.

## **Conclusion:**

Comparison of the data obtained in bulk solution biosensing experiments and protein layer biosensing experiments for different guiding layer heights will demonstrate surface desensitization. Characterization of the biological sample layer will allow us to improve upon our estimates for the height and index of the biolayer, thereby raising the accuracy of our simulation results. In addition, characterization will verify that we are in fact creating a uniform protein layer of a specific height on the waveguide surface. The resolution of the interferometric data and characterization data will be sufficient to allow

comparison of the experimental data to theoretical predictions. Comparison of the data obtained for different waveguides thicknesses will demonstrate the desensitization effect.

## Appendix A: Sample preparation

The following is a record of our current waveguide inventory and a list of waveguides and samples necessary for the experiments. The purpose of each of the sample and waveguide types listed below is described in the experiments above. In some cases, several steps are needed to create the necessary waveguides and samples. Reflectometry (performed at BU on Anna Swan's instrument) is used to identify guiding layer heights where necessary. In some cases, etching of SiO<sub>2</sub> (using Buffered Oxide Etch (BOE), performed at BU, in the Optoelectronics Processing Facility (OPF)) is required. Wafer dicing is done at BU using our own wafer dicing saw. Polishing is done at BU using a fiber and waveguide polisher shared with the Photonics Center at BU. Samples are listed by type. The steps following each sample type describe the work needed to complete the particular sample type.

- 1) Current inventory of processed and partially processed samples:
  - 2 180 nm waveguides, C1-C2, C1 polished
  - 3 103 nm waveguides, D1-D3, D1 polished
  - 3 etched 103 nm waveguides, E1-E3, E1 polished
- 2) Additional samples needed and work required to fabricate and/or characterize them:
  - a) Measure the etched 103 nm waveguides (E1-E3) (estimated guiding layer height 85 nm) using reflectometry to determine the actual guiding layer height using reflectometry at BU.
  - b) Prepare 6 silicon pieces (S1-S6)
    - At BU, dice oxide-on-silicon-substrate wafer into quarters
    - At BU, etch oxide to silicon on one quarter
    - At BU, dice six 1.5 cm x 1.5 cm pieces S1-S6
  - c) Prepare 8 166 nm waveguides, (R1-R8), two polished
    - At BU*, identify 166 nm wafer with reflectometry (wafers became mixed in MIT processing)
    - At BU*, etch oxide to completion if necessary (not all wafers were etched to completion, probably due to the variation in oxide height I observed and relayed to Matt for different wafers)

*At BU, dice eight 166 nm waveguides R1-R8*

*At BU, polish R7,R8*

d) Prepare 2 103 nm polished waveguides (D1,D2)

*At BU, polish D2*

e) Prepare 2 etched 103 nm polished waveguides, (E1,E2)

*At BU, polish E2*

## Appendix B: Protein types

The following lists the name of the protein, the weight (in kiloDaltons), and approximate size (italic numbers are interpolated values). Based on the two data points (supplied by Hitesh at Satcon), the weight of each protein type is proportional to the dimension raised to the power 2.38

Type	weight	dimensions
BSA	67 kD	<i>5.0 nm</i>
IGG (Ab)	150 kD	7.0 nm
Lysozyme	13 kD	2.5 nm
HRP	43 kD	<i>4.1 nm</i>

## Appendix C: Simulation results

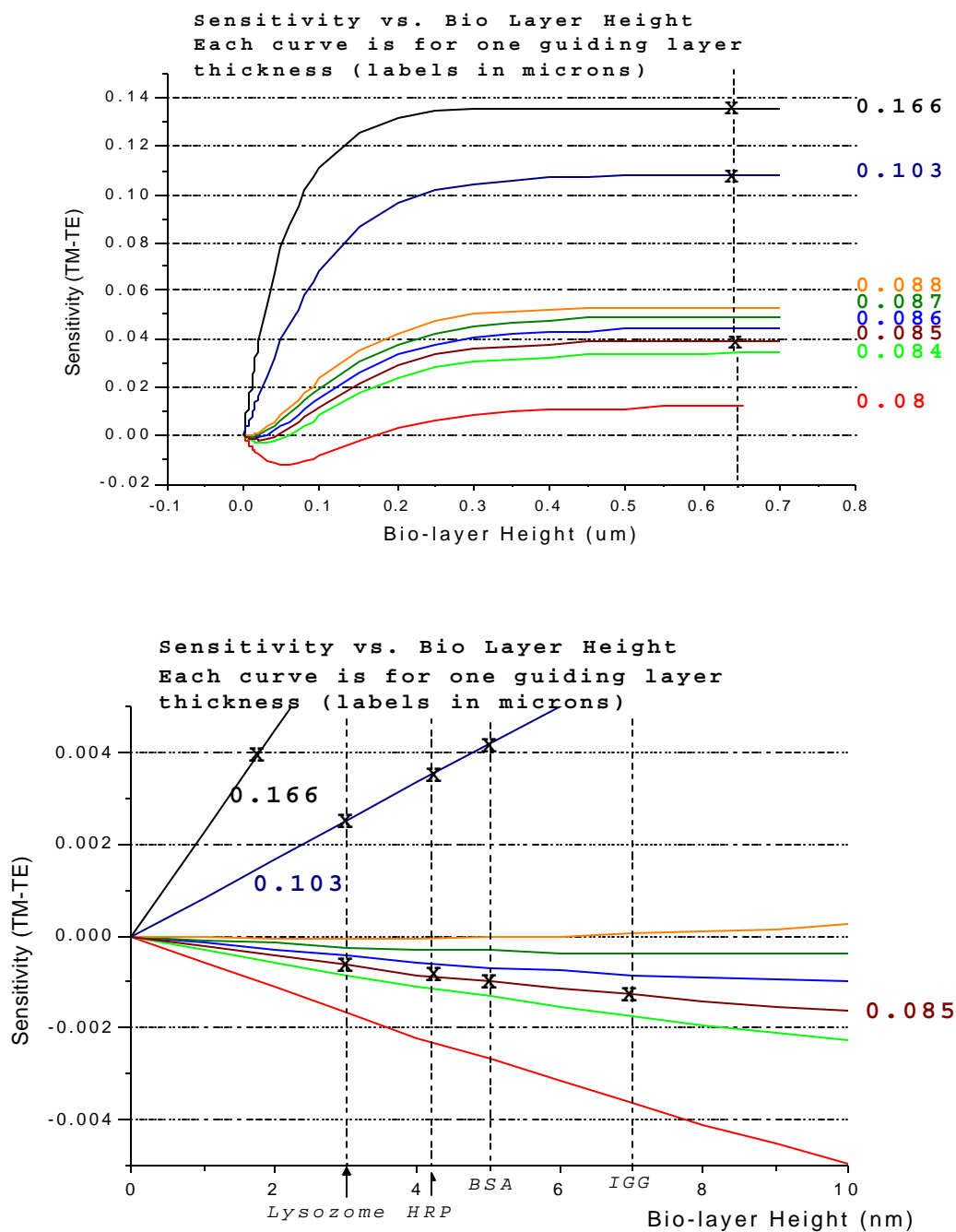


Fig. 3: Sensitivity curves for various waveguide thickness. The first plot shows the response over the entire range of biolayer heights. X's indicate sensitivity expected for a bulk solution measurement for experimentally available waveguide thicknesses. The second plot shows a detailed view for small biolayer heights. The estimated height of the four available proteins are labeled in italics. The X's mark the points on each curve mapped out by these four proteins. The expected experimental phase shifts for each of these points, calculated from the sensitivity curves, are given in Table 1 below.

### Predicted Biosensor Phase Response (in cycles)

<u>Protein</u>	Guiding layer Thickness (nm)		
	166	103	85
Lysozyme	3.30	1.20	-0.32
HRP	5.22	1.98	-0.49
BSA	6.47	2.48	-0.59
IGG (Ab)	8.92	3.47	-0.76
Sucrose Solution	18.55	14.70	5.32

### Desensitization Factor (compared to an optimized waveguide)

<u>Protein</u>	Guiding layer Thickness (nm)	
	103	85
Lysozyme	0.36	-0.10
HRP	0.38	-0.09
BSA	0.38	-0.09
IGG (Ab)	0.39	-0.09
Sucrose Solution	0.79	0.29

Table 1: Phase shifts expected for three guiding layer heights ( $t=166$  nm,  $t=103$  nm,  $t=85$  nm) for the four available proteins. The phase shifts are derived from the predicted sensitivity curves, and the estimated thickness of each protein monolayer. The desensitization factor is the phase response of the biosensor divided by the phase response of a biosensor optimized for highest sensitivity ( $t=166$  nm). A negative number indicates that the phase shift of the former is in the opposite direction from the latter.

## Chapter 8 : Microfluidic Primer

**Introduction** A major component of the biosensing platform is the fluidic transport of the sample to the optical detection chamber. The approach we have taken in this project is the use of microfluidics both for sample preparation as well as for cell capture. The following sections describe the basic elements of flow at low Reynolds number (i.e the microfluidic regime) and its application to sample extraction and cell capture.

**Overview of Microfluidics.** Microfluidics is the flow of liquids in microchannels with dimensions on the order of microns. Fluid motion in microchannels exhibits special behavior that is distinctly different from fluid flow in our common macroscopic environment. The difference between microfluidics and macro fluid flow is the scale of the flow regime. All fluid flow can be scaled based on the relative effects of inertial and viscous forces. Microfluidics is the special case when channel dimensions are so small that inertial forces are insignificant compared with viscous forces. Even with low viscosity liquids such as water, because of the small flow dimensions the fluid in motion will appear extremely viscous.

Flow at the microfluidic scale introduces new possibilities for fluid devices, many of which would be impossible with full-scale fluid handling systems. Consider a device that joins two fluid streams in a microfluidic channel, shown in Figure 8-1.

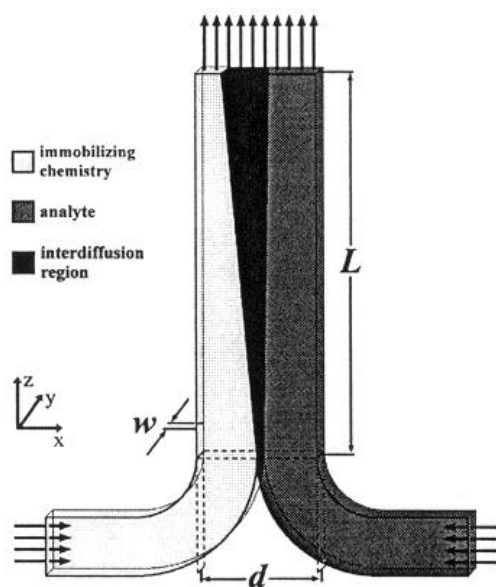


**Figure 8-1:** A diffusion-based microfluidic extraction device.

Because the flow is laminar, the two fluid streams will flow side-by-side with no mixing. The utility of this scenario is that diffusion of particles will occur from one stream to the other. Although there is no physical mixing, the two streams will interact by diffusion mass transfer.

Diffusion mass transfer is the transport of a chemical species in the presence of a concentration gradient (species will tend to migrate from spatial regions of high concentration to regions of lower concentration as a result of random molecular motion). The practical utility of diffusion in a microfluidic device is to separate particles based on size. Thus, the microfluidic device can be used as a particle filter as shown in the previous chapter (see Figure 7-4). A microfluidic filter can efficiently discriminate between particles of different sizes, because diffusion in liquids is based primarily on particle size. Diffusion mass transfer is one of the primary processes that make microfluidic devices useful for the optical biosensor.

Another practical use of microfluidics is hydrodynamic focusing. Separate fluid streams will flow side-by-side in a microchannel, and there will be some stream interface between adjacent streams. In the case of two adjacent streams, the location of the streamline interface can be made such that one stream is focused tightly near a surface while the other occupies the majority of the channel volume. This type of focusing is accomplished by regulating the ratio of flow rates in the two streams. For example, if one wishes to focus a stream of analyte particles into a layer which is  $1/5$  the total channel thickness, then the flow rates must be controlled such that the flow associated with the particle stream is  $1/5$  the total flow rate in the channel<sup>1</sup>. This process can be visualized using Figure 8-2, which illustrates pathlines in a fluid junction, the output of a numerical fluid simulation. In this case, the flow rate ratio is 4:1, so the analyte fluid stream occupies about  $1/5$  the total volume.

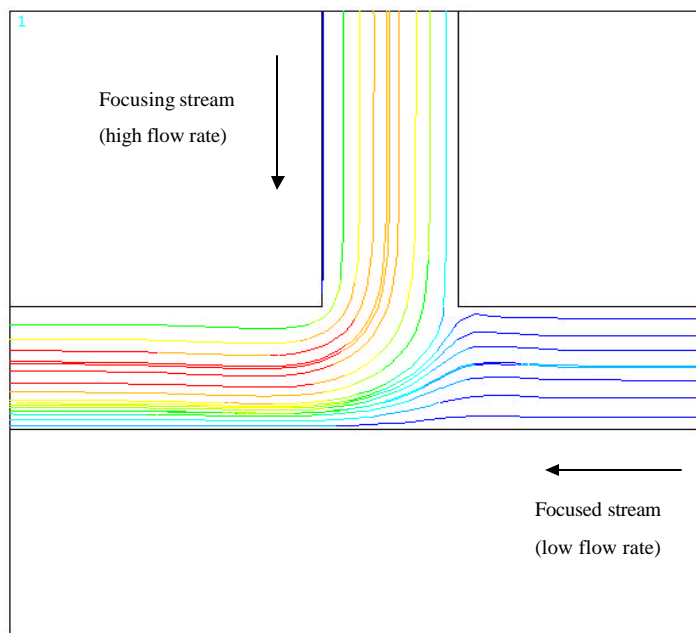


**Figure 8-2:** Illustration of hydrodynamic focusing. The horizontal stream is focused to about  $1/5$  its original thickness.

<sup>1</sup> It should be mentioned that this is an approximation. An exact relationship between focusing and flow rate ratio must take into account the viscous velocity profile. While the statement presented here is strictly valid only for an inviscid velocity profile, the approach is reasonable and appropriate for system-level calculations.

The practical use of hydrodynamic focusing is to pass analyte cells very close to the reception sites in a flow cell. This should increase the probability of capturing cells on the surface.

With the current fabrication techniques available, microfluidic devices will enjoy a wide range of applications in biotechnology. There has been tremendous research in recent years in this field, and a number of excellent references are available in the literature. While there are many applications for microfluidic technologies, our purpose for the optical biosensor is to use a microfluidic device as a particle separator to differentiate particles of different sizes, and also to perform hydrodynamic focusing of fluid layers.

**Analytical Modeling Tools for Microfluidic Devices.** The analysis of microfluidic devices serves the purpose of understanding of the physical phenomena and developing models that can be used for device design. The analysis of microfluidics follows from an understanding of basic transport phenomena, particularly momentum transfer and mass transfer. The approach here is to consider the two basic transport phenomena separately<sup>2</sup> in the context of a microfluidic device.

*Fluid Dynamics.* The goal is to develop an analytical model that can be used to predict pressure and velocity distributions in a microchannel. Both of these performance parameters can be obtained using basic momentum and continuity principles.

Consider the geometry of a microchannel shown in Figure 8-3. The channel has length  $L$ , width  $w$ , and depth  $d$ . A Cartesian coordinate system is used, with the origin at the center of the microchannel.

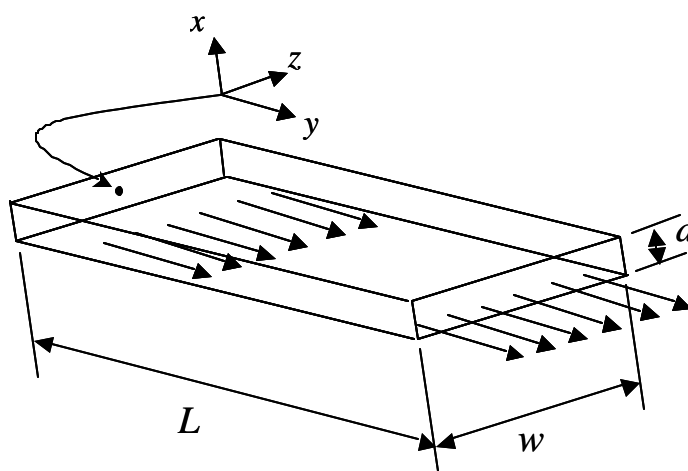


**Figure 8-3:** Geometry used in the fluid dynamics analysis of a rectangular microfluidic channel.

---

<sup>2</sup> Analyzing the momentum and mass transfer separately is valid in a dilute mixture, where each diffusing species behaves as if it was in a binary mixture, and the diffusion has no effect on the flow field. On the other hand, a composite mixture is one in which the momentum and mass transfer phenomena are strongly coupled.

The momentum equation for an incompressible, Newtonian fluid is written in Cartesian coordinates as

$$\boldsymbol{m}\nabla^2\mathbf{V} - \nabla P = \boldsymbol{r}\frac{\partial\mathbf{V}}{\partial t} + \boldsymbol{r}(\nabla\cdot\mathbf{V})\mathbf{V}, \quad (8-1)$$

where the velocity vector is given as  $\mathbf{V} = [V_x \ V_y \ V_z]$ . Equation 8-1 is commonly known as the Navier-Stokes equation. Each term in the momentum equation is actually a force per unit volume of fluid. The first and second terms on the left-hand side of the equation are the viscous shear forces and the pressure forces, respectively. The right-hand side includes the inertial forces. Additional body forces acting on the fluid would contribute terms on the left-hand side of Equation 8-1 (e.g., gravity would contribute a term  $\boldsymbol{r}\mathbf{g}$ ).

All fluid motion is scaled by considering the ratio of inertial forces to viscous shear forces. When this ratio is formed in steady state the time-derivative vanishes, and we get a very useful dimensionless group known as the Reynolds number:

$$\frac{\text{inertial forces}}{\text{viscous forces}} = \frac{\boldsymbol{r}(\nabla\cdot\mathbf{V})\mathbf{V}}{\boldsymbol{m}\nabla^2\mathbf{V}} \propto \frac{\boldsymbol{r}VD}{\boldsymbol{m}} = Re. \quad (8-2)$$

The Reynolds Number is used to determine the nature of one-dimensional fluid motion. In general, all flow can be classified as laminar, turbulent, or transitioning. Turbulent flow can be thought of as a rich and complicated flow pattern with interacting vortices. Turbulent flow can only occur at Reynolds Numbers greater than about  $10^3$ , but typically occurs at  $Re > 10^4$ . Laminar flow, which normally occurs at Reynolds Number less than about 2000, can be thought of as orderly flow with predictable, smooth pathlines.

Microfluidics is a special case of laminar flow, with typical Reynolds Numbers less than one. For example, if water at room temperature flows at 5 mm/s in a microchannel with effective diameter of 100  $\mu\text{m}$ , the Reynolds Number would be about 0.5. At this scale, the flow field is dominated by viscous shear forces and pressure forces – inertial effects are insignificant.

In light of the fact that inertial forces are relatively small at the microfluidic scale, Equation 8-1 can be simplified by dropping the inertial forces, and the resulting expression is the Stokes flow model (also known as creeping flow, or low-Reynolds Number flow):

$$\boldsymbol{m}\nabla^2\mathbf{V} = \nabla P. \quad (8-3)$$

The Stokes equation is further simplified by considering a 1-D flow field in the y-direction. Taking only the y-direction scalar equation and eliminating insignificant terms leads to

$$\boldsymbol{m}\left(\frac{\partial^2 V_y}{\partial x^2} + \frac{\partial^2 V_y}{\partial z^2}\right) = \frac{\partial P}{\partial y}. \quad (8-4)$$

Equation 8-4 provides a differential equation that can be used to determine the velocity profile  $V_y = f(x, z)$  in terms of the pressure gradient  $\partial P / \partial y$ . The pressure drop must be related to the fluid flow rate  $Q$ . If we use the concept of a hydraulic or effective diameter for the rectangular channel, defined as  $D = 2dw / (w + d)$ , we get the following expression for pressure drop:

$$\frac{\partial P}{\partial y} = - \frac{bm(w+d)^2}{(2wd)^3} Q. \quad (8-5)$$

The constant  $b$  is a function of the channel aspect ratio, and is reported in the Handbook of Heat Transfer (Rohsenow et al. 1985) as:

$$b = 96 \left( 1 - 1.3553a^* + 1.9467a^{*2} - 1.7012a^{*3} + 0.9564a^{*4} - 0.2537a^{*5} \right), \quad (8-6)$$

where

$$a^* = \min \left( \frac{d}{w}, \frac{w}{d} \right). \quad (8-7)$$

In addition, the flow rate is expressed in terms of the average velocity as  $Q = Vwd$ . Equation 8-5 indicates a linear relationship between pressure drop and flow rate, which is always true for laminar flow. The negative sign indicates that fluid motion in the  $y$ -direction occurs with decreasing pressure gradient.

With an expression for the pressure drop now available (Equation 8-5), the field equation (Equation 8-3) can be solved for the velocity profile in the microchannel. Four boundary conditions are required, all of which are based on a no-slip condition at the four channel walls. The boundary conditions are

$$V_y \left( x, -\frac{w}{2} \right) = V_y \left( x, \frac{w}{2} \right) = V_y \left( -\frac{d}{2}, z \right) = V_y \left( \frac{d}{2}, z \right) = 0, \quad (8-8)$$

and the solution to Equation 8-3 is

$$V_y(x, z) = - \left( \frac{\partial P}{\partial y} \frac{d^2}{8m} \right) \frac{32}{p^2} \sum_{n=0}^{\infty} \frac{(-1)^n}{(2n+1)^3} \left[ 1 - \frac{\cosh[(2n+1)pz/d]}{\cosh[(2n+1)pw/2d]} \right] \cos[(2n+1)px/d]. \quad (8-9)$$

Equation 8-9 gives a closed-form solution to the field equation, which can be plotted to visualize the velocity profile. Figure 8-4 shows a typical velocity profile in a microchannel.

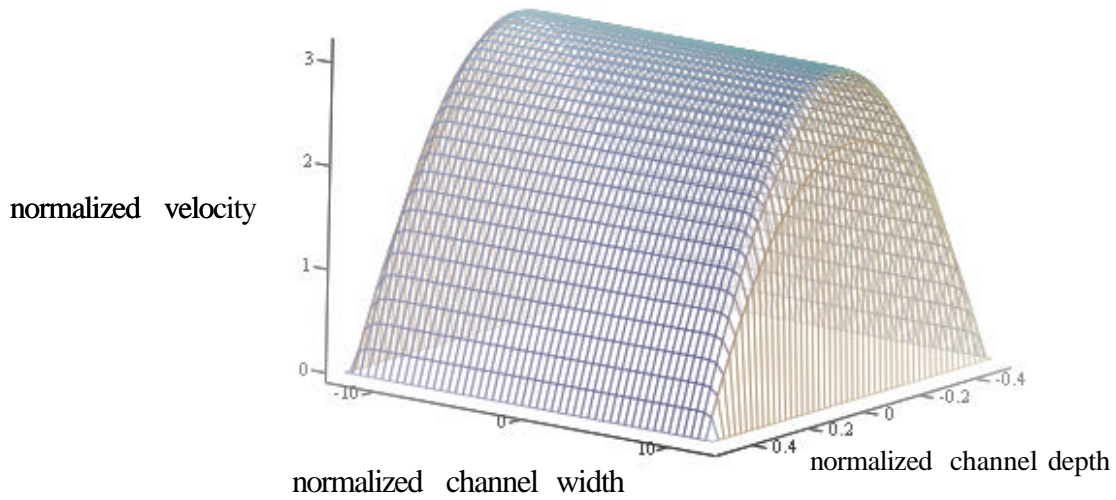


**Figure 8-4:** Velocity profile in a typical microchannel (plot of equation 8-9).

Figure 8-4 gives insight into the nature of the flow in a microchannel. In the  $x$ -direction (depth direction) not close to the two edges, the profile looks parabolic, which is typical for laminar flow in a pipe, or laminar flow between flat plates. In fact, if we take the limit of the velocity profile as the width goes to infinity while maintaining constant depth (which is the limiting case of flow between two flat plates), we indeed get a parabolic velocity profile in the  $x$ -direction:

$$\lim_{a \rightarrow 0} V_y(x, z) = \frac{\partial P / \partial y}{8m} (4x^2 - d^2) \quad (8-10)$$

This analysis provides closed-form expressions for velocity profile and pressure drop. It is worth noting that the analysis was developed with no regard to the diffusion that will take place in the channel. This simplification is very useful and valid for dilute mixtures.

Mass Transfer. Mass transfer by diffusion is the transport of chemical species because of species concentration gradients. The analysis of mass transfer is often analogous to heat transfer, with the fundamental equations and solutions taking similar forms.

The transport equation for diffusion mass transfer is Fick's Law, written as

$$\mathbf{j} = -\mathbf{r} D_i \nabla c_i, \quad (8-11)$$

where the mass flux vector is given as  $\mathbf{j} = [j_x \ j_y \ j_z]$ . The transport property in mass transfer is the mass diffusivity  $D_i$ , which is interpreted as the diffusion coefficient of species  $i$  with respect to a unique solvent. In general, the diffusion coefficient of a species will always depend on the particular solvent being used. There are both analytical and empirical correlations available for estimating diffusion coefficients, and in general, the techniques differ for liquids and gases. Cussler (Cussler 1984) provides a good amount of diffusion coefficient data for both liquids and gases. For microfluidic systems (liquid systems) with diffusing particle sizes large compared to the solute, the Stokes-Einstein equation provides a good analytical expression:

$$D_i = \frac{k_B T}{6\pi\eta R_i}. \quad (8-12)$$

The key feature of the Stokes-Einstein equation is the relationship between the diffusion coefficient  $D_i$  and the particle size  $R_i$ . In a given solvent, smaller particles have higher diffusion coefficients than larger particles. This is the basis for microfluidic separation – a device will efficiently separate particles based on diffusion coefficients, and hence particle size. In some cases, the particle size is not known, but the molecular weight is known. In these cases the particle size may be estimated using Equation 8-13:

$$\frac{4}{3}\pi R_i^3 = l \frac{M_i}{N_A r_i}. \quad (8-13)$$

The ultimate goal in the mass transfer analysis is to predict the concentration distributions in the microchannel. This is accomplished by considering the continuity (mass balance) of each diffusing species in the mixture. Consider the geometry of a microchannel shown in Figure 8-5. The channel has length  $L$ , width  $w$ , and depth  $d$ . A Cartesian coordinate system is used, with the origin at a corner at the inlet of the channel.

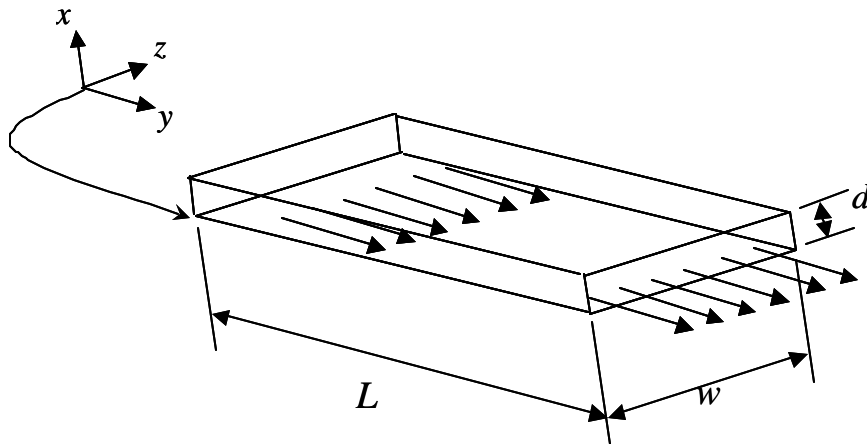


**Figure 8-5:** Geometry used in the mass transfer analysis of a rectangular microfluidic channel.

The species continuity equation is written as:

$$D_i \nabla^2 c_i = \mathbf{V} \cdot \nabla c_i + \frac{\partial c_i}{\partial t} \quad (8-14)$$

Equation 8-14 is a general-purpose equation and can be simplified for a specific situation. If we consider steady state operation of a separation device, the time derivative term vanishes. Furthermore, a microfluidic separator would be designed such that only one dimension would be used for diffusion (called the primary diffusion direction). With this in mind, Equation 8-14 simplifies to:

$$D_i \frac{\partial^2 c_i}{\partial x^2} = V_y \frac{\partial c_i}{\partial y}. \quad (8-15)$$

The first term includes the effect of diffusion in the  $x$ -direction, while the second term includes the effect of advection (bulk fluid motion) in the  $y$ -direction. The typical boundary conditions include impermeable walls (zero flux at the walls), and some specified initial concentration distribution at the inlet:

$$\frac{\partial c_i}{\partial x}(0, y) = \frac{\partial c_i}{\partial x}(d, y) = 0, \text{ and } c_i(x, 0) = f(x). \quad (8-16)$$

The solution to Equation 8-15 with these boundary conditions takes the following form:

$$c_i(x, y) = \frac{F_0}{2} + \sum_{n=1}^{\infty} F_n \exp\left(-\frac{(n\mathbf{p})^2 y}{Pe} \frac{y}{d}\right) \cos\left(n\mathbf{p} \frac{x}{d}\right), \quad (8-17)$$

where the harmonic coefficients are given by

$$F_n = \frac{2}{d} \int_0^d f(x) \cos\left(n\mathbf{p} \frac{x}{d}\right) dx, n = 0, 1, 2, \dots \infty, \quad (8-18)$$

and

$$Pe = \frac{V_y d}{D_i} \quad (8-19)$$

is the dimensionless Peclet Number. Equations 8-17 and 8-18 provide a closed-form solution for the concentration distribution in the microchannel. For a given microfluidic device, the only input necessary to determine the concentration distribution is the initial distribution at the inlet,  $c_i(x, 0) = f(x)$ . This analytical model for diffusion is used to design and analyze both the flow cell and the microfluidic separator cartridge described in Chapter 9.

## Chapter 9 : Microfluidic Flow Cell for Enhanced Capture Efficiency

**Introduction.** A highly sensitive transducer alone is not enough to detect small numbers of microorganisms. A key issue for all biosensors is the capture of the targets prior to detection, which depends on both the quality of receptors and capture mechanism. We have addressed the capture mechanism through a novel laminar flow cell employing the use of microfluidics to focus the organisms for efficient capture. This following text describes the design, fabrication, and laboratory characterization of the flow cell.

The ideal flow stream for differential detection would expose both the reference and the specific binding areas to identical amounts of NSB while only exposing the specific receptors to the target cells. Arbitrarily flowing a sample stream containing a uniform distribution of cells over an area containing both the reference and the specific binding regions has the fundamental problem that the target cells will often miss the specific receptors as shown in Figure 9-1.

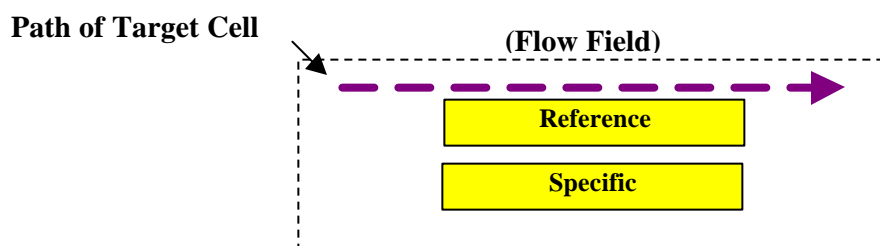


**Figure 9-1.** Schematic showing a flow field (area within dashed line) containing a uniform distribution of cells and the path of an arbitrary target cell missing the receptors.

**SatCon Concept.** This problem can be rectified by using microfluidic techniques to alter the flow field as shown below in Figure 9-2. First, the cells are spatially confined so that they flow across the specific receptors, and then the small analytes are diffused across the flow field again to provide a common

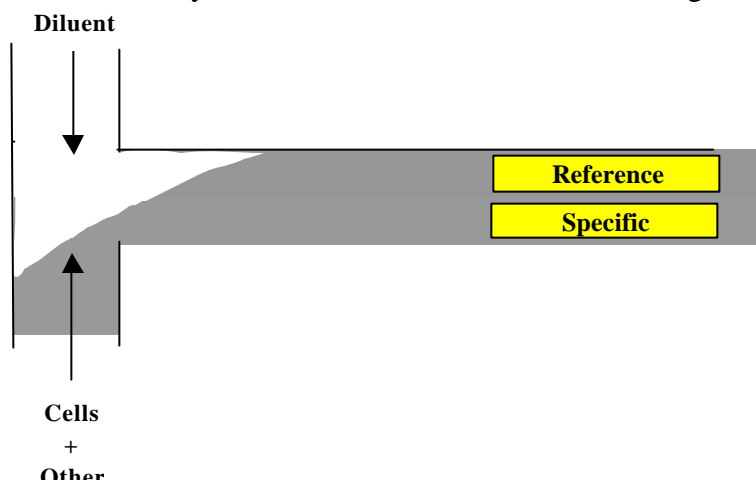


**Figure 9-2.** Altering the flow field with microfluidics to confine the cells (white dots) to the region containing the specific receptors while diffusing the small analytes to provide uniform distribution across the sample stream.

distribution to both the reference and the specific binding regions.

The final element of this approach is to use hydrodynamic focusing to create a thin sheath of cells close to receptor surface. This is accomplished by introducing a third stream flowing significantly faster to push the cells onto the receptor surface for binding as is shown in Figure 9-3.

**Analysis of the Flow Cell.** The flow cell was analyzed for both hydrodynamic stability and diffusion

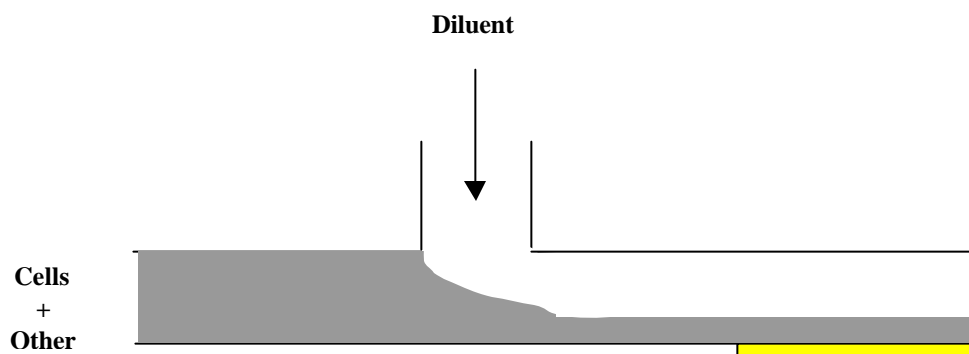


**Figure 9-3.** Hydrodynamic Focusing. A third stream is introduced at a significantly higher flow rate to focus the cells onto the receptor surface.

performance. The analytical model presented in the previous section was used to predict the diffusion performance and design the device accordingly. The fluid dynamics were analyzed using numerical techniques due to the relatively complex flow cell geometry (channels with varying areas, varying aspect ratios, junctions, etc.). The numerical solution was obtained using FLOTRAN, a general-purpose computational fluid dynamics (CFD) package (the CFD solver provided finite element solutions to Equation 8-1, combined over the entire flow cell fluid domain).

Table 9-1 lists the design parameters of the flow cell. The parameters listed in Table 9-1 are those that were used in the flow cell design, prior to any experiments or fluid property measurements.

**Table 9-1:** Parameters for the design and analysis of the flow cell.

Parameter	Value
Mixture type: dilute of concentrated	dilute
Solvent properties	aqueous
Molecular weight of diffusing particles (small particles)	70,000 g/mol
Analyte particle size (large particles)	5 $\mu\text{m}$
Sample specific gravity	1
Sample viscosity	1 cP
Mixture temperature	20°C
Depth of the diffusion channel	0.1 mm
Width of the diffusion channel	2.5 mm
Length of the diffusion channel	40 mm
Output flow rate (total flow rate)	0.044 mL/min
Focusing stream flow rate	0.036 mL/min
Analyte flow rate	0.008 mL/min

The function of the flow cell is twofold: (1) bifurcate the analyte stream by flowing an adjacent solvent stream in equal proportion, while simultaneously providing a uniform background of diffusing particles, and (2) focusing the analyte stream close to the receptor surface. The two functions are performed sequentially in the flow cell. The bifurcation/diffusion step is analyzed using the mass transfer model presented earlier.

The design of the diffusing region of the flow cell requires a prediction of the species concentrations. Equation 9-1 provides a functional form for the species concentrations. For each species in the sample stream, the boundary condition at the inlet of the diffusion channel is given as:

$$f(x) = c_i(x,0) = \begin{cases} c_{i,o}, & 0 \leq x < x_1 \\ 0, & x_s < x \leq d \end{cases}, \quad (9-1)$$

where  $c_{i,o}$  is the initial species concentration, and  $x_1$  is the streamline interface location for the diffusing species. The streamline interface location is related to the flow rates of the two streams<sup>1</sup>:

---

<sup>1</sup> It should be mentioned that this is an approximation. An exact relationship between streamline interface and flow rate ratio must take into account the viscous velocity profile. While the Equation 1.21 is strictly valid only for an inviscid velocity profile, the approach is reasonable and appropriate for system-level calculations.

$$x_1 \approx \frac{Q_1}{Q_1 + Q_2} d \quad (9-2)$$

The goal of the flow cell is to bifurcate the sample flow, so the streamline interface must be one-half the overall channel dimension,  $x_1 = d/2$ , and the flow rates  $Q_1$  and  $Q_2$  must be equal. With this boundary condition specified, the concentration distribution of the analyte is given in Figure 9-4.

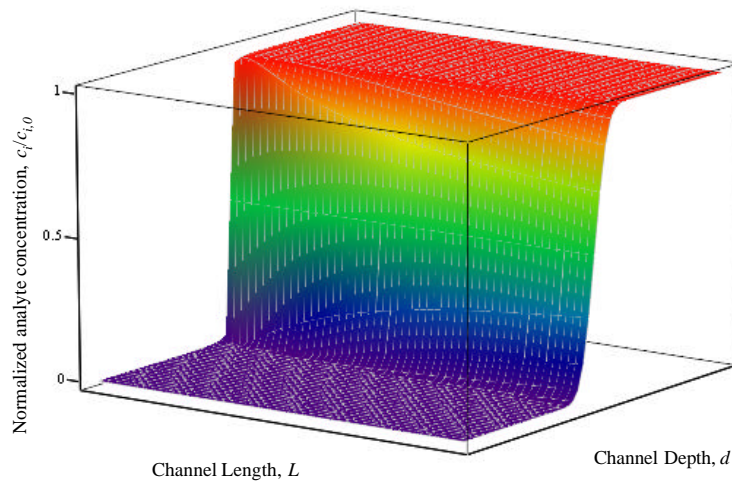


**Figure 9-4:** Plot of the analyte concentration distribution in the diffusion channel.

The concentration distribution shown in Figure 9-4 indicates that the analyte particles diffuse only slightly through the diffusion channel. This is an important design objective. Ideally, we would like no diffusion of the analyte particles. Realistically there will always be some amount of analyte diffusion, but the majority of the cells will remain on the same side of the channel that they entered. If the analyte particles were any smaller, there would of course be more diffusion.

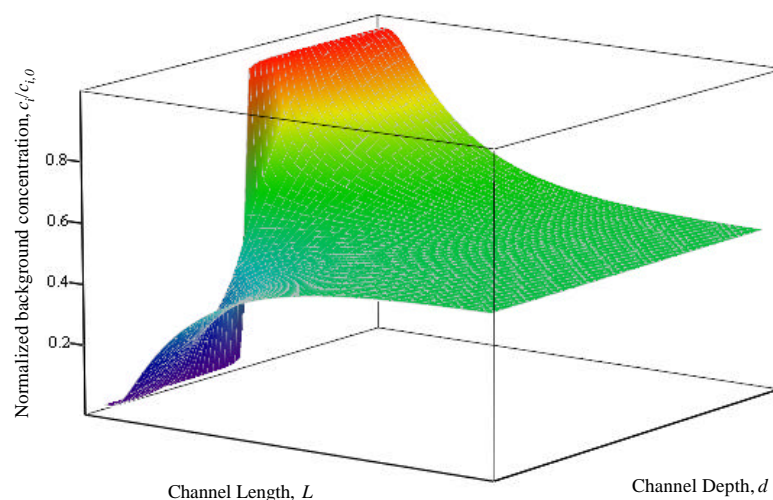


**Figure 9-5:** Plot of the background concentration distribution in the diffusion channel.

Figure 9-5 shows the same concentration plot for the other species in the sample mixture, the small diffusing particles, which we will call the background for obvious reasons. The background particles behave quite differently than the analyte particles, because of the small particle size (i.e., low molecular weight) of the background species. Diffusion takes place very quickly and the concentration distribution becomes uniform at the channel outlet. This uniform distribution provides the necessary ‘background’ for differential optical measurements. In summary, the goal of the diffusion channel is to provide a uniform background by diffusing small particles, while maintaining a required distribution of analyte with minimal diffusion.

The second function of the flow cell is hydrodynamic focusing. We wish to focus the analyte stream close to the chemical surface for optimal cell capture. The simple expression that can be used to estimate focusing is Equation 9-2. Using this equation with the flow rate data presented in Table 9-1, the thickness of the focused analyte stream would be  $x_1 = (0.1 \text{ mm})(0.008 \text{ mL/min}) / (0.008 \text{ mL/min} + 0.036 \text{ mL/min}) = 0.018 \text{ mm}$ . This concept of using flow rates to regulate stream thickness was verified using a 2D CFD model, with the result shown in Figure 9-2. In this figure the horizontal stream moving from right to left gets focused to about 18% of its original thickness. The flow cell was designed for a focused thickness of about 0.018 mm, but thinner layers can be focused if necessary by adjusting the relative flow rates.

Additional fluid analysis was performed to study the effect of geometry variations in the microchannels. The flow cell must interface with tubing, which is one example of geometry variations in the flow cell. The other variation is the transition region, where the channel goes through a variable-area passage to ‘invert’ the aspect ratio. Figure 9-6 illustrates the geometry of the flow cell.

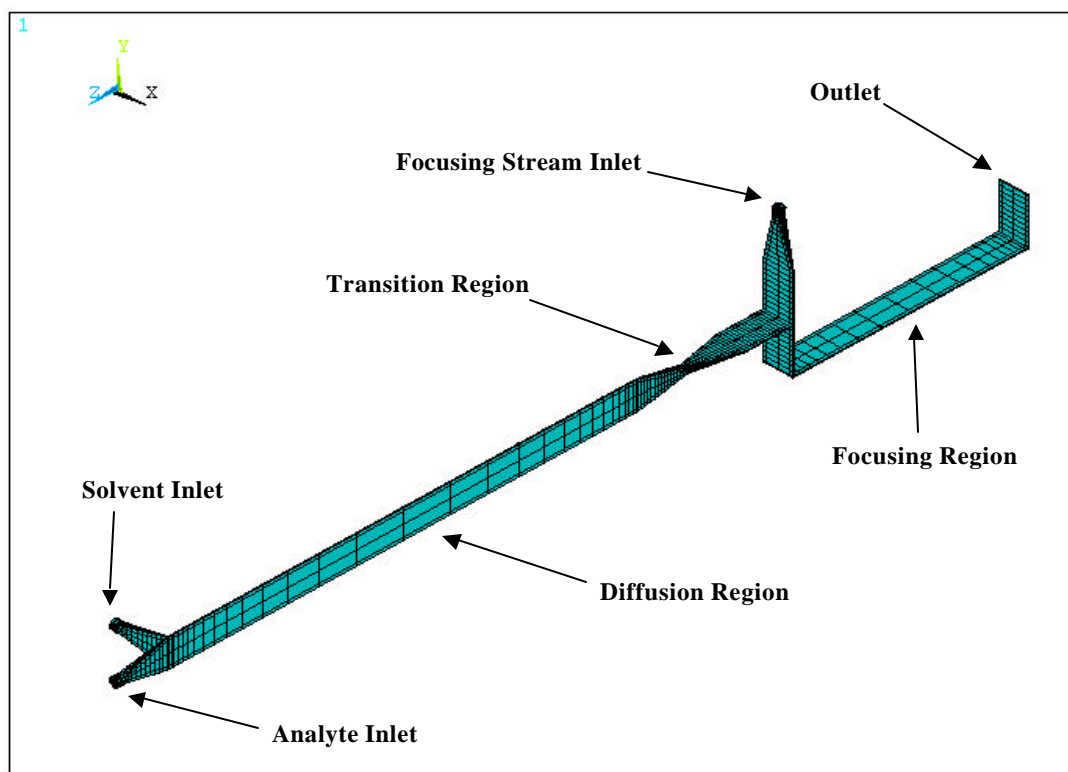


**Figure 9-6:** Geometry of the flow cell.

The goal of this additional analysis was to verify that no instabilities were introduced in the flow field because of the various geometry changes. For this analysis, a three-dimensional CFD model was used. A powerful post-processing technique for fluid systems is to view the velocity vectors at key locations in the fluid domain. Figures 9-7 and 9-8 show the velocity vectors at the flow cell inlets and at the transition region, respectively.

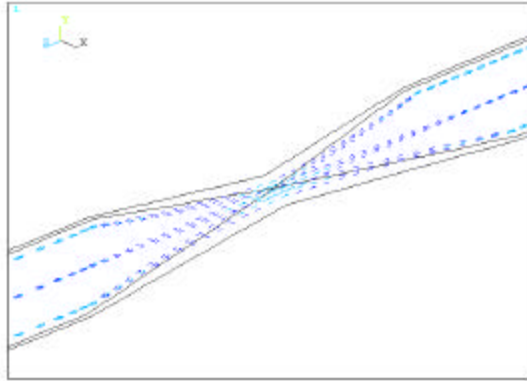


**Figure 9-7:** Velocity vectors at the transition region.

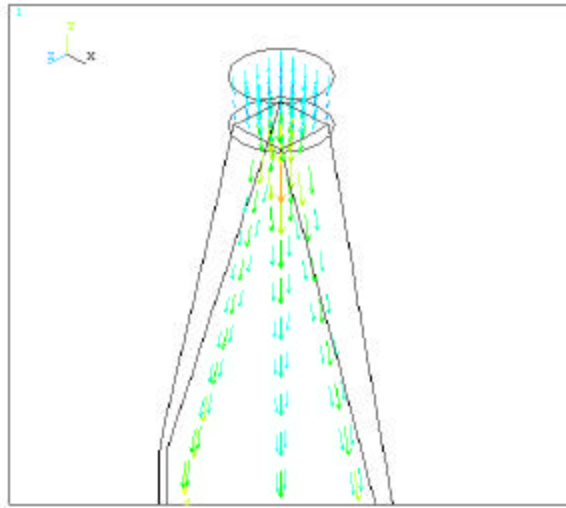


**Figure 9-8:** Velocity vectors at the interface between tubing and microchannels.

From inspection of the two figures, the analysis predicts that the flow patterns will not be disrupted by the geometry changes. In other words, there will be no irregular flow conditions such as boundary layer separation, or circulatory flow at sudden enlargements. The reason there are no irregular flow patterns is the low-Reynolds Number operating range of the device.

Finally, the numerical model predicted the overall pressure drop<sup>2</sup> to be around 150 Pa at 0.044 mL/min. At this low flow rate, the pump power requirements are about  $10^{-7}$  W, which is negligible. At higher

---

<sup>2</sup> The pressure drop stated here assumes a completely filled device. The pressure requirements during device startup could be much greater due to capillary forces in the microchannel. For this reason, additional sources of energy are sometimes used to startup a microfluidic device, such as vacuums at the outlet and low surface tension prefill fluids.

flow rates however, pumping power and pressure drop could become more important, because pressure drop is proportional to the flow rate, and power is proportional to the square of the flow rate.

#### List of Symbols Used

$c_i$	concentration (mass fraction) of species $i$ [kg/kg]
$c_{i,o}$	concentration (mass fraction) of species $i$ at the diffusion channel inlet [kg/kg]
$d$	depth of the microchannel [m]
$D$	diameter or effective diameter for non-circular channel [m]
$D_i$	mass diffusivity (diffusion coefficient) for species $i$ [m <sup>2</sup> /s]
$F_n$	Fourier coefficients [dimensionless]
$\mathbf{g}$	gravitational acceleration vector ( $\mathbf{g} = [g_x \quad g_y \quad g_z]$ ) [m/s <sup>2</sup> ]
$\mathbf{j}$	mass flux vector [kg/s/m <sup>2</sup> ]
$j_x$	mass flux in the $x$ -direction [kg/s/m <sup>2</sup> ]
$j_y$	mass flux in the $y$ -direction [kg/s/m <sup>2</sup> ]
$j_z$	mass flux in the $z$ -direction [kg/s/m <sup>2</sup> ]
$k_B$	Boltzmann's constant [ $1.380 \cdot 10^{-23}$ J/K]
$L$	length of the microchannel [m]
$M_i$	molecular weight of species $i$ [kg/kmol]
$n$	summation index used in Fourier series [dimensionless]
$N_A$	Avagadro's number [ $6.024 \cdot 10^{23}$ particles/mole]
$P$	static pressure [Pa]
$Pe$	Peclet number [dimensionless]
$Q$	volumetric flow rate [m <sup>3</sup> /s]
$Q_I$	volumetric flow rate of the focused stream [m <sup>3</sup> /s]
$Q_2$	volumetric flow rate of the focusing stream [m <sup>3</sup> /s]
$R_i$	radius of a diffusing particle associated with species $i$ [m]
$Re$	Reynolds Number [dimensionless]
$T$	temperature of the bulk fluid [K]
$V$	average channel velocity, $V = Q/wd$ [m/s]
$\mathbf{V}$	velocity vector [m/s]
$V_x$	$x$ -component velocity [m/s]
$V_y$	$y$ -component velocity [m/s]
$V_z$	$z$ -component velocity [m/s]
$w$	width of the microchannel [m]
$x$	coordinate aligned with the depth dimension [m]
$x_1$	streamline interface location (thickness of a focused stream) [m]
$y$	coordinate aligned with the length dimension [m]
$z$	coordinate aligned with the width dimension [m]
$\mathbf{a}^*$	inverse channel aspect ratio: (shortest side)/(longest side) [dimensionless]
$\mathbf{b}$	constant used to evaluate pressure drop [dimensionless]
$I$	close-packing factor for calculating molecular volume [dimensionless]
$\mathbf{m}$	dynamic (absolute) viscosity of the bulk fluid [Pa·s]
$\mathbf{r}$	mass density of the bulk fluid [kg/m <sup>3</sup> ]
$\mathbf{r}_i$	mass density of the species $i$ [kg/m <sup>3</sup> ]

#### References

1. Cussler, E. L. (1984). Diffusion, Mass Transfer in Fluid Systems. Cambridge, Cambridge University Press.
2. Rohsenow, W. M., Hartnett, J. P., and Ganic, E. N. (1985). Handbook of Heat Transfer, Fundamentals. McGraw-Hill.

**Flow Cell Fabrication.** After the flow cell channel geometry was defined (Figure 9-6) the fabrication of the device was addressed. This includes material selection, fabrication methods for prototype and volume production. The technical challenges associated with the proposed flow cell design are now discussed, along with results of a literature search, micro-fabrication techniques survey, material trades and bonding investigation.

**Technical Challenges.** The proposed flow cell design has a channel width or depth of 2500  $\mu\text{m}$ ; more than 10 times geometries discussed in published literature ( $<100 \mu\text{m}$ ). Large channel width, by itself, is not an issue for many traditional micro-machining methods. However, the large channel aspect ratio (25:1) coupled with a transition in channel orientation (25:1 to 1:25) requires application of different fabrication methods. The three intersecting, orthogonal flow channel for the two parallel flow circuits present fabrication challenges as well.

**Background.** A general review of published papers, patents and commercial product literature for biosensor, flow cell and micro fluidics was performed and a few of the key papers are summarized below. Ward and Winsor<sup>3</sup> summarize commercial optical biosensors used to study macromolecules and their interactions with biospecific partners; Table 1 summarizes commercial biosensor products and suppliers. Madou and Florkey<sup>4</sup> conclude that miniaturized biosensors are best fabricated from plastics using lamination, plastic molding and electroplating techniques. They believe low cost, disposable devices with no moving parts should be used for handling wet chemistry. The wet chemistry device interfaces with permanent instrumentation containing power, heating, pumping, sensor and electronic functions. Buttgenbach and Robohm<sup>5</sup> present a review of silicon based micro fluidic component/device fabrication and implementation of a flow-diffusion system for gas-phase ethanol. Feldstein et al.<sup>6</sup> with the Naval Research Laboratory provide a detailed description of a complete optical and fluidic system implementation using a multi-channel flow cell made out of CNC machined plastic. Guenat, et al<sup>7</sup> presents their work with channels, electrosmotic nanopumps and micromixers implemented in ultrasonically eroded or HF etched, fusion bonded, Pyrex<sup>TM</sup> wafers.

Wurmus<sup>8</sup> describes a static micromixer that can be used to mix two separate fluids. This mixer can also be adapted diffuse the transition in concentration and/or index of refraction separating two fluids in series in a single flow channel. Ramsey<sup>9</sup> has a patent for an apparatus and method for electrically

---

<sup>3</sup> Ward, Larry D., Winzor, Donald J., (2000) Relative Merits of Optical Biosensors Based on Flow-Cell and Cuvette Designs *Analytical Biochemistry*, 285, 179-193

<sup>4</sup>Madou, Marc, Florkey, John, (2000) From Batch to Continuous Manufacturing of Micro Biomedical Devices *Chem. Rev.* 100, 2679-2692

<sup>5</sup> Buttgenbach, S., Robohm, C. (1998) Microflow Devices for Miniaturized Chemical Analysis Systems *SPIE Vol 3539 0277-786X/98*

<sup>6</sup> Feldstein, Mark J. et al., (1999) Array Biosensor: Optical and Fluidics Systems *Journal of Biomedical Microdevices* 1:2, 139-153

<sup>7</sup> Guenat, O.T., et al., (2000) Partial Electosmotic Pumping in Complex Capillary Systems Part 2 *Sensors and Actuators B* 3637 1-10

<sup>8</sup>Hurmus, H. (2001) [www.maschinenbau.tu-ilmenau.de/mb/wwwmm/inhalt/german/6-5.htm](http://www.maschinenbau.tu-ilmenau.de/mb/wwwmm/inhalt/german/6-5.htm)

<sup>9</sup> Ramsey, M. J. (1999) Apparatus and Method for Performing Microfluidic Manipulations for Chemical Analysis and Synthesis *Patent Number* 5,858,195

controlled flow redirection in micromachined channels. This method can be used as a valve and has no moving parts.

Wang<sup>10</sup> et al. report on a low temperature bonding process developed at Oak Ridge National Laboratory for glass using spin-on sodium silicate as an adhesive. Channel sealing was successful with a 12-hour cure at room temperature or a 1 hour, 90° C cure. Bond strength is lower than high temperature bonding processes such as anodic bonding but adequate for most chemical microchip applications.

**Table 9-2:** Commercial Biosensors

Biosensor	Manufacturer	Location	Fluid System	Detector
BIOS-1	Artificial Sensing Instruments	Zurich, Switzerland	Flow Cell	Evanescent Wave (I/O Optical Grating)
IAsys	Thermo BioAnalytics	Cambridge, UK	Stirred Cuvette	Resonant Mirror
IBIS	Intersens	Amersfoort, The Netherlands	Cuvette	Evanescent Wave (Surface Plasmon Resonance)
BIACORE BIALITE BIACORE-X/J	Biacore	Uppsala, Sweden	Flow Cell	Evanescent Wave (Surface Plasmon Resonance)
TRACE Flowcell	TRACE Biotech AG	Braunschweig, Deutschland	Flow Cell	Electrochemical

**Survey of Micro-Fabrication Techniques.** Fabrication of a flow cell device with microfluidic channels requires investigation and application of appropriate microfabrication techniques. A good understanding is needed for successful selection of prototype and production flow cell materials and fabrication methods. Prototype and production materials and methods will most likely be different, based on cost and risk factors. Lower risk, higher cost methods and materials are justified for prototype development.

There are many microfabrication techniques available, including the following:

- Bulk Micromachining
- Surface Micromachining
- Traditional Mechanical Machining

---

<sup>10</sup> Wang, H.Y. et al., (1997) Low Temperature Bonding for Microfabrication of Chemical Analysis Devices *Sensors and Actuators B* 45 199-207

- LIGA
- Deep UV Photoresist
- Laser
- Stereo Lithography
- Lamination
- Electro Discharge Machining (EDM)
- Surface Micromachining
- E-Beam Machining
- Plasma Beam Machining
- Focused Ion Beam Machining
- Water Jet
- Ultrasonic Machining
- Photofabrication
- Electrochemical Machining
- Chemical and Photochemical milling

The first seven techniques were investigated in detail and are summarized as follows.

#### 1) Bulk Micromachining

- Bulk micro machining is a removal process done predominantly in Silicon using IC fabrication techniques and is the predominant micromachining method. Several techniques also apply to glass.
- Silicon is crystalline and as a result has direction dependent properties defined by Miller indices (unit vectors in x, y and z). Glass, however is isotropic.
- Starting from a flat surface (e.g., wafer) material is removed by lithographic and chemical etching techniques
- Masks (Silicon Oxide - SiO<sub>2</sub>) created using photolithography are used to prevent etching on selected surfaces
- Etching methods include
  - Wet Etch
    - Isotropic – Acid Etchant – Etch rate same in all directions
    - Anisotropic – Base Etchant – Etch rate direction dependent
  - Dry Etch - Isotropic
    - Reactive Ion Etch (REI)
    - REI with Inductive Coupled Plasma (ICP REI)
    - Electron Cyclotron Resonance (ERC REI)
    - Plasma Etch (PE) Isotropic
    - Geometry and tolerances limited by control of the etching process and can take up 4 to 8 hrs for deep structures

Channels with 25:1 aspect ratio can be accomplished economically with shallow and wide etches. This limits the 3D channel geometries needed for the proposed flow cell. These

methods may be used for prototype development in glass, but it is unlikely they would apply to volume production. These methods can be used to fabricate moulds.

## 2) Surface Micromachining

- Surface micro machining is done on a Silicon substrate with material added and removed using deposition and bulk micromachining techniques in multiple layers
- Two layer types
  - Structural -- of which the final microstructures are made
  - Sacrificial -- which separate the structural layers and are dissolved in the final stage of device fabrication
- Fabrication relies on encasing the structural parts of the device in layers of a sacrificial material during the fabrication process.
- The sacrificial material is then dissolved away with a chemical etchant that does not attack the structural parts.
- Process temperatures can range from 450 to 1050 °C
- Can be used to create micromachines and micromoulds

This technique favors wide and shallow features and can be used to make moulds. It is unlikely this method would be used for prototype fabrication.

## 3) Traditional Mechanical Machining

- Micro Milling is similar to conventional machining of 2D and 3D structures and uses custom microfabrication CNC controlled multi axis mills, grinders, lathes, inspection equipment, etc.
- Reproducible machining to better than 0.05 µm.

Methods used to fabricate glass and optical devices are prime candidates for fabrication of a prototype flow cell. Moulds from many isotropic materials can also be made.

## 4) LIGA

- LIGA is German acronym standing for
  - Lithography
  - Electroforming
  - Molding
- Lithography – X-Ray radiation (synchrotron) is used to penetrate a photoresist (PMMA) supported on a conductive substrate. The substrate is then developed dissolving voids in the substrate
- Electroforming - Voids in the substrate are electroplated with metals (e.g., Nickel) and the remaining substrate is removed, leaving the metal structure
- Molding – The metal structure is used as a molding tool for hot embossing or injection molding for mass production

LIGA is costly, is excellent for high aspect ratio geometries (500:1), and produces very smooth, nearly vertical walls. This method could be used to fabricate channels of any aspect ratio but would not work well for the transition region.

#### 5) Deep UV Photoresist

- This method is a lower cost version of LIGA with lower resolution and height.
- Photosensitive polyimide (i.e., Kapton) is used in place of PMMA for the photoresist
- UV light is used in place of X-Ray radiation for exposure of the photoresist
- 50  $\mu\text{m}$  high with 3-5  $\mu\text{m}$  resolution
- 0.25-.18  $\mu\text{m}$  resolution for lower features
- Method favors shallow and wide features
- Used to produce ink jet printer heads

This technique cannot produce the aspect ratios needed or the transition region.

#### 6) Laser

- Lasers can machine materials by one of two processes
  - Thermal process – Uses the lasers ability to deposit a great amount of energy into a small amount of material to melt or vaporize the material in a short period of time
  - Photo-ablation – Uses UV radiation to break the bonds of organic materials at the surface.
- Laser cutting, drilling and welding examples used in medical devices
- Cut width - 35 microns
- Groves – 5-50 micron deep, 10-200 microns wide
- Hole sizes - 700 micron
- Spot Weld sizes - 100 microns

Laser machining has been used to make flow channels but not to the depth and aspect ration needed. Machining channels is time consuming and therefore costly. It could be used for prototype fabrication if surface smoothness can be improved with a secondary process (i.e. HF etch of glass).

#### 7) Stereo Lithography

- Stereo Lithography (SLA) is the most common Rapid Prototype technique, and produces acrylic and epoxy parts
- Almost unlimited geometry possibilities, fine geometric details and high accuracy (tolerances lie between 0.05% to 0.2%)
- Resolution of less than 5  $\mu\text{m}$  is possible
- The required geometry is produced in thin layers (0.1-0.25 mm). A CNC-controlled laser beam cures a pattern in the surface of a fluid photosensitive polymer. The hardened layer is then stepwise lowered allowing the fluid to cover the part.

**Materials.** Madou and Florkey <sup>11</sup> present a comparison of materials used for micro biomedical applications, which is reproduced in Table 9-3. A quick survey of the material costs show glasses and plastics are the lowest cost materials suitable for the flow cell application. The baseline flow cell design uses a large volume of material and with a low cost goal; silicon is eliminated. Isotropic materials are also favored, given the channel geometry. Properties for three low cost, isotropic materials, glass, plastic and stainless steel are compared in Table 9-4. Stainless has been eliminated because high thermal conductivity is unsuitable for a flow cell. Another materials concern is water absorption. Figure 9-9 illustrates the relative permeability of several materials. Glass is the best choice for the flow cell, given that metals prohibited.

The majority of flow cells to date have used comparatively small channel geometry (<100 µm) created with bulk or surface micro machining methods in glass and silicon. More recently, structures made from PMMA (polymethylmethacrylat), PEEK(), PDMS (polydimethylsiloxane) and Polycarbonate (Lexan™) plastic have been molded or embossed from surface machined structures. While polycarbonate is a good candidate, glass is preferred for prototype fabrication.

**Table 9-3:** Comparison of Substrate Properties

Manufacturing of Microbiomedical Devices

Chemical Reviews, 2000, Vol. 100, No. 7 2681

Table 1. Comparison of Substrate Properties<sup>a</sup>

		cost	pack-aging	fracture	metallization	installed equipment base (access)	web	machinability (common methods)	dielectric constant	E GPa	thermal conductivity W/mK
single crystals	silicon	\$	difficult	b,s	good	very large	no	very good	11.8	165	150
	quartz	\$	easy	b,s	good	small	no	poor	4.4	87	7
	GaAs	\$\$\$	difficult	b,f	good	small	no	poor	13.1	119	50
	sapphire	\$\$\$	easy	b,s	good	small	no	poor	9.4	490	40
amorphous	fused silica	\$-\$\$	easy	b,f	good	small	yes	poor	3.9	72	1.4
	plastic	c	very easy	t,s	poor	very large	yes	fair			
	paper/cardboard	c	easy	t,s	poor	very large	yes	fair			
	glass	c-\$	easy	b,f	good	large	yes	poor	4.6	64	1.1
polycrystalline	alumina	cc-\$\$	easy	b,s	fair	fair	yes	poor	9.4	400	~30
	aluminum	\$	difficult	t,s	good	very large	yes	very good	77	~240	

<sup>a</sup> b brittle, t tough, s strong, f fragile; \$ = dollars, \$\$ = more dollars, \$\$\$ = most dollars, c = cents, cc = more cents.

<sup>a</sup> b brittle, t tough, s strong, f fragile; \$ = dollars, \$\$ = more dollars, \$\$\$ = most dollars, c = cents, cc = more cents.

**Table 9-4:** Flow Cell Material Candidate Properties

Property	Units	Borosilicate Glass (Pyrex™)	Polycarbonate Plastic (Lexan™)	304 Stainless Steel
Optical		Transparent	Transparent	Opaque
Density	g/cm <sup>3</sup> Lb/in <sup>3</sup>	2.2 0.08	1.2 0.04	8.0 0.29
Modulus of Elasticity	Pa	6.27E10	2.34E9	1.93E11
Thermal Coefficient of Expansion	cm/cm/°C in/in/°F	3.24E-7 1.8E-7	6.8E-5 3.8E-5	1.7E-5 9.6E-6
Thermal Conductivity	W/m-°C Btu ft/hr ft <sup>2</sup> °F	1.1 0.65	0.20 0.12	16 9.4

<sup>11</sup> Madou, Marc, Florkey, John, (2000) From Batch to Continuous Manufacturing of Micro Biomedical Devices *Chem. Rev.* 100, 2679-2692

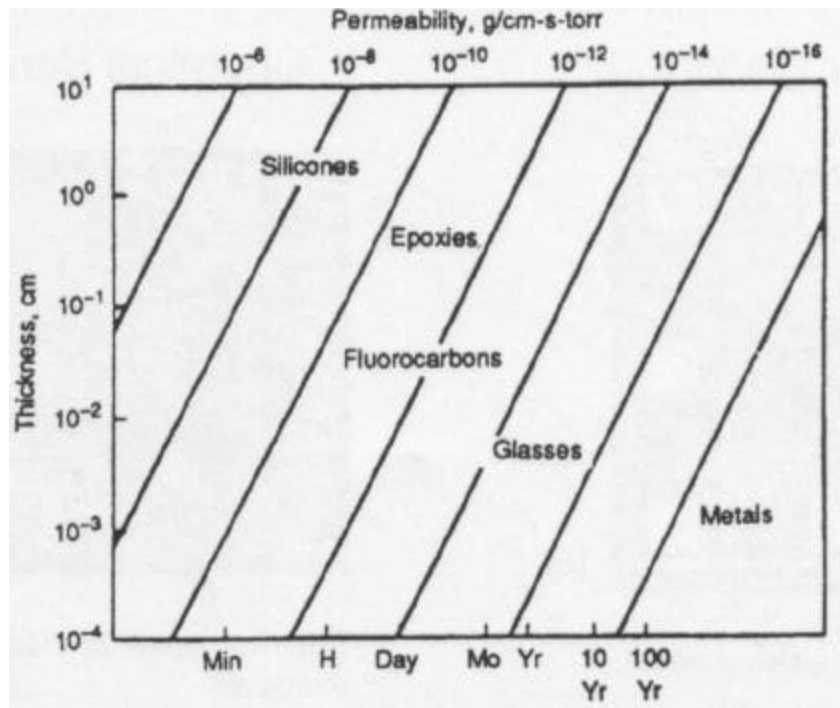


**Figure 9-9:** Water Permeability of Several Materials

Bonding. A list of bonding methods and materials for common material choices is given below.

- Glass and Silicon
  - Anodic Bonding – High Temperature and Voltage
  - Fusion Bonding – High Temperature and Pressure
  - Sodium Silicate – Low Temperature
  - UV Cure Adhesives – Low Temperature
  - Cyanoacrylates (Super Glue)

- Plastics
  - Ultrasonic
  - Thermosonic
  - Thermocompression
  - Epoxy
  - Solvents
  - Cyanoacrylates (Super Glue)

**Fabrication of the Flow Cell.** After examining many different fabrication techniques it was determined to fabricate the prototype flow cell using precision standard machining techniques instead of resorting to MEMS techniques. While standard rectangular channels (typical dimensions  $\sim 100\mu\text{m} \times 2500\mu\text{m}$ ) can be readily etched, the transition region requiring angles other than 90 degrees is difficult. A full set of engineering drawings for the final design of the flow cell are found in Appendix E of this document.

The flow cell is a stand-alone device fabricated from many glass blocks which will have the necessary channels precision machined into the surface. Precision machining was performed by Mindrum Precision Inc, (Rancho Cucamonga, Ca) and confined to one to two mating surfaces. The other surface was a flat plate whose function was to make a seal and provide the fourth wall of any channel. To create the three dimensional channel system needed for our flow cell required 9 different blocks, 5 of which had machined channels and 4 smooth blocks along with 7 inlet and outlet orifices and provisions for a custom seal assembly to seal the flow cell to the silicon wafer. A 3-dimensional drawing of the flow cell is shown in Figure 9-10 and a set of mechanical drawing is found in Appendix 9-A.

Initially, it was thought that the flow cell blocks would be bonded by spin coating sodium silicate onto the surface for low temperature bonding as reported by Wang et al. at Oak Ridge Laboratory.<sup>12</sup> However, after testing it was determined that a more reliable approach was the use of UV curing cement. The cement was painted on the bonding surfaces with a fine brush, positioned in a jig, and subjected to a UV lamp for several hours for curing.

**Laboratory Characterization.** As was described previously a microfluidic flow cell was designed to increase the capture efficiency of cells by focusing the cells selectively onto the receptor surface. The diffusion constant for bacterial cells is as much as 1000 times smaller than for proteins and other small particles and the cells deviate minimally from their path in a laminar stream. For this reason conventional laminar flow cells are generally inefficient for the capture of microorganisms. The SatCon flow cell exploits the small diffusion constant of a cell to hydrodynamically focus cells in close proximity to a receptor-laden surface to increase the capture efficiency.

Experiments were performed to monitor the capture of *E.coli O30* cells onto a solid platform for different flow rates. The objective of this work was to characterize the probability of capturing a single cell from a flowing suspension with a microfluidic flow cell. In all experiments the *E.coli O30* model system was used because of its minimal non-specific binding and demonstrated high affinity for its corresponding immuno-receptor. Two basic experiments were carried out as described below: 1.) cell capture using a standard laminar flow cell and 2.) cell capture using hydrodynamic focusing to enhance the capture rate.

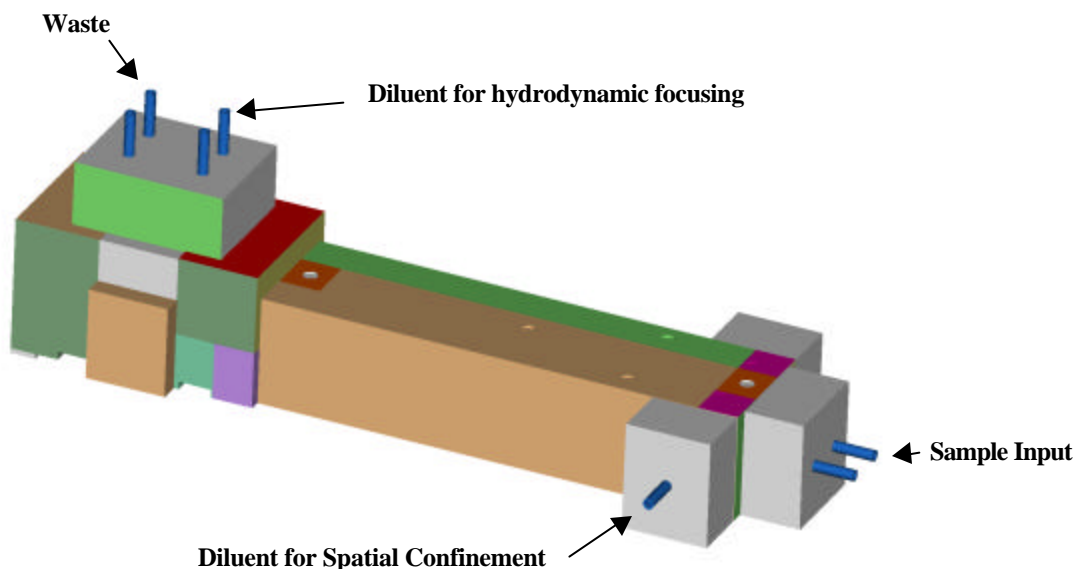


**Figure 9-10.** Prototype flow Cell. The cell contains two independent flow cells separated by 4.5 mm. The overall dimension of the device is approximately 4 inches in length.

<sup>12</sup> Wang, H.Y. et al., (1997) Low Temperature Bonding for Microfabrication of Chemical Analysis Devices *Sensors and Actuators B* 45 199-207

Experimental Description. A plexiglass fixture was designed to hold the flow cell against a chip 18 mm x 18 mm in size in a sandwich-like format. The flow cell was mounted on a secure post and attached to either the peristaltic or syringe pump (or both). The PEO/Protein-A chips prepared by the MIT group were incubated with anti-*E.coli* O30 as is described in the protocol below and exposed to sample streams having different flow rates. After flowing a fixed number of cells the exposed chip was removed from the flow cell, the captured cells were stained and examined under a fluorescence microscope for enumeration.

The general protocol used was:

- a) Silicon chips with Protein-A covalently attached to the polyethylene oxide monolayer (PEO) were incubated with anti-O30 antibody (1:100 dilution) for 90 min at room temperature.
- b) Chips were washed twice with PBS containing 0.2% Tween-20 for 5 min each, followed by one washing with PBS alone to wash off the unbound antibody.
- c) A Chip was assembled into the flow cell, and was made sure that there was no leak by flushing the PBS. Since the flow cell has two channels/cuvettes, each chip was subjected to two different flow rates of the cell suspension.
- d) Overnight grown *E.coli* O30 cells were washed twice with PBS and were resuspended in PBS to create a cell suspension with a concentration of  $1.75 \times 10^9$  CFU/ml.
- e) 2 ml of *E.coli* O30 cell suspension ( $3.5 \times 10^9$  cells) were flowed through the flow cell at various flow rates (i.e. 16, 32, 64, 96, 128, 160, 200, 300, 400  $\mu$ l/min).
- f) Unbound cells were removed by washing with PBS with 0.2% Tween-20 for 5 min at a flow rate of 100  $\mu$ l/min, followed by washing with PBS alone for 5 min at a flow rate of 100  $\mu$ l/min.
- g) Cells captured on the surface of the chips were stained with live and dead stain (BacLight Syto-9, fluorescein) for 20-30 min at room temperature, and were visualized under fluorescent microscope.
- h) Several images were taken corresponding to each flow rate and cells were enumerated.

A photograph of a flow cell used for these experiments is shown in Figure 9-11. The flow cell was constructed of glass and has two adjacent and fully independent chambers each 2.5 mm wide x 8 mm long x 100  $\mu$ m high (2 $\mu$ l volume) as was mentioned previously. In addition to a sample input port, each chamber had two diluent input ports for lateral and vertical focusing.

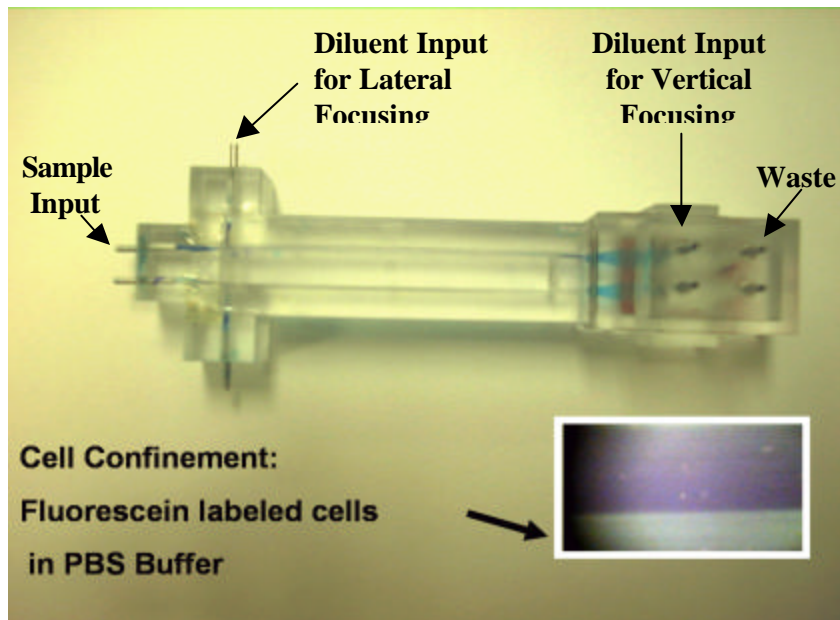


**Figure 9-11. Microfluidic Flow Cell for Focusing Cells.** The insert shows the lateral focusing of fluorescently labeled cells.

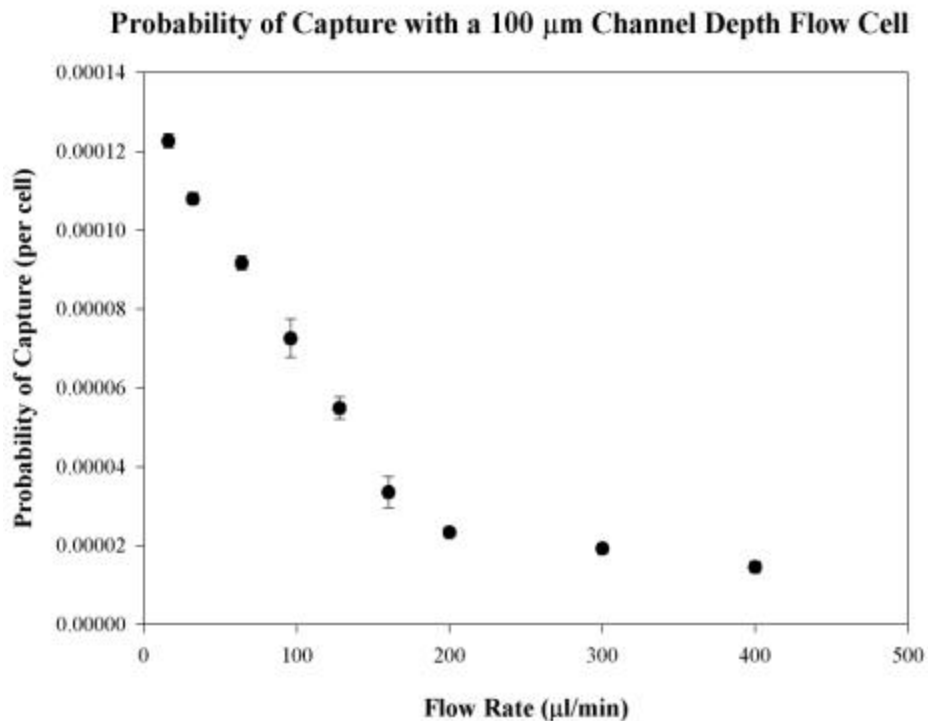
**Experiment #1: Unfocused Flow Cell Results.** In this experiment only cell suspension ( $1.75 \times 10^9$  CFU/ml) was flowed through the flow cell, thus the entire  $2\mu\text{l}$  volume was filled a uniform density of cells. A concentration of  $1.75 \times 10^9$  CFU/ml corresponds to a nearest neighbor distance of  $8.3\text{ }\mu\text{m}$ ; thus, on average cells are approximately 4 body lengths apart.

A fixed number of cells ( $3.5 \times 10^9$ ) were always flowed and data for 9 independent flow rates were collected. The peristaltic pump was used for all but the lowest two flow rates (16 and  $32\text{ }\mu\text{l}/\text{min}$ ) because of limitations in flow rate where a syringe pump was used. The analysis of the bound cells involved first scanning the entire region before choosing 3 representative areas within the microscope field of view, enumerating the cells, and averaging these results. These averages were then scaled to obtain the total bound cells over the  $20\text{ mm}^2$  active area. The probability of capture was calculated by the equation:

$$\text{Probability} = (\text{Total number of bound cells})/(\text{Total number of cells available for binding})$$

These data are plotted in Figure 9-12.

A clear



Discussion.

**Figure 9-12. Probability of Capture for a Conventional Laminar Flow Cell:** All measurements were obtained by flowing  $3.5 \times 10^9$  CFU's at the different rates and counting the number of organisms captured onto the 2.5 mm x 8 mm receptor laden surface. The capture probability was calculated by dividing the number of organisms captured by  $3.5 \times 10^9$ .

dependence on the flow rate is seen increasing linearly from 150 μl/min to 16 μl/min and plateauing for flow rates in excess of 200 μl/min. At a flow rate of 16 μl/min the measured probability is  $1.226 \times 10^{-4}$ . Thus at this rate only one cell in 8156 will be captured and at 200 μl/min only one in 42,735 cells. This is because the majority of cells in the fluid stream is not at the receptor interface and diffuse very little from their flow stream. This measurement clearly demonstrates the inefficiency expected for cell capture with a conventional laminar flow cell. The probability of capturing discrete numbers of cells from a suspension using such a device and without *very significant* pre-concentration is impractically small.

The increase in capture probability with lower flow rate can be understood qualitatively. As the flow rate is slowed down the cells at the receptor interface proportionally spend more time near the surface and have many more opportunities to bind. Naively, one might expect that doubling the residence time of the cell would result in twice as much binding. However, the slope does not have a value of one although it appears linear, thus time is only one of many parameters needed to describe the capture process.

At a flow rate of 200 μl/min the probability flattens out, inferring a binding threshold. This suggests that there is a minimum duration of time required for the interaction to occur between cells and their receptors and that the drag or shear forces by virtue of high flow rate of the cells might prevent these interactions from taking place. One might also expect that this inflection point will vary with the binding affinity of the immuno-receptor.

**Experiment #2: Hydrodynamic Focusing.** Hydrodynamically focusing the cells to create a thin sheath at the receptor interface is an improvement to a conventional flow cell. Focusing does not concentrate the cells, instead it makes for an efficient use of the cells moving each organism closer to the surface to improve its probability of binding. For example, consider a volume of cells transported at flow rate  $Q$ . If the sample volume is focused to occupy only half its previous volume and the rate  $Q$  is kept constant then it will take twice as long to transport the same number of cells. That is, the volume of cells has been effectively squashed in the vertical direction and displaced to the longitudinal direction. Therefore, twice as many cells would be expected to be bound at the surface because the volume of cells, from what previously would have had almost zero probability of capture, now can compete more effectively for a binding site.

Experiment #2 was conducted to verify this improvement in capture efficiency. To implement the focusing element a second stream of diluent (PBS) was added so there are now two independent flow parameters instead of one. The total flow rate is given by the sum of the two inputs

$$Q_{\text{Total}} = Q_{\text{cell}} + Q_{\text{diluent}}$$

The thickness of the sheath is given by

$$x \approx \frac{Q_{\text{cell}}}{Q_{\text{cell}} + Q_{\text{diluent}}} d$$

where  $d$  is the height of the flow cell and  $x$  is thickness of the sheath.

For the experiment performed the total flow rate was kept constant at 200  $\mu\text{l}/\text{min}$  and the flow rates of the sample and diluent were varied according to the above formulas. Because of the geometry of the flow cell no visual confirmation of the stratification was possible with this experiment.

A plot of these data points along with the theoretical prediction is shown in Figure 9-13. Only three data points were able to be collected as will be described below, all in excellent agreement with predictions.

**Discussion.** The absolute capture probability for a total flow rate of 200  $\mu\text{l}/\text{min}$  (enhancement factor of one) is  $2.34 \times 10^{-5}$ , the same as that measured in Figure 9-12. For every value of the total flow rate there exists a similar hyperbolic enhancement curve observed by varying the sheath size. Thus, one can imagine a different hyperbolic curve for each of the data points in Figure 9-13.

Two independent flow streams were required as inputs to the flow cell for focusing. The peristaltic pump provided the supply of PBS as the diluent stream while a syringe pump was used to flow cell suspension. It is crucial that the respective flow rates be steady to ensure a regular and predictable interface between the two streams. As can be seen from the above equation, any variations in  $Q_{\text{cell}}$  or  $Q_{\text{diluent}}$  will lead to variations in  $x$  and hence unstable fluids interface. It is for this reason that Micronics, Inc. has resorted to gravity feed for their microfluidic devices to ensure regular flow and avoid these difficulties.

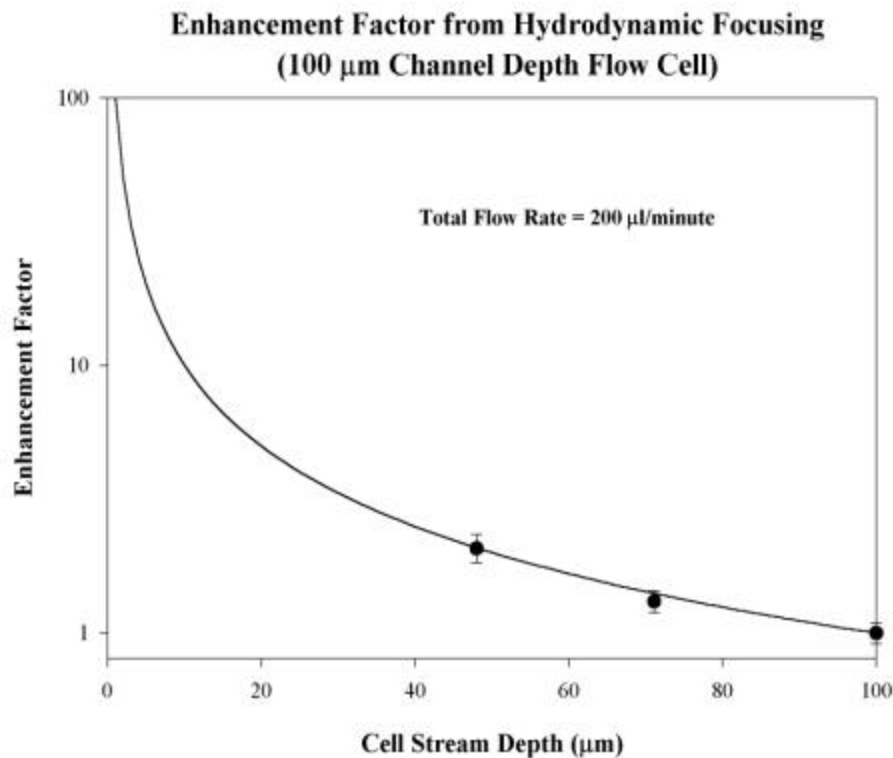


**Figure 9-13.** *Enhancement in Capture Probability from Hydrodynamic Focusing:* Empirical data (solid circles) and a theoretical curve (solid line) are plotted showing the factor increase in the probability of capture from confining the sample to different percentage volumes of the flow cell. The flow cell has a total cell stream depth of 100  $\mu\text{m}$ , so a depth of 100  $\mu\text{m}$  corresponds to flow through the full volume, 50  $\mu\text{m}$  corresponds to flow filling only half the volume and so on. The total flow rate for these experiments was 200  $\mu\text{l}/\text{minute}$ . The absolute capture probability for these points is obtained by multiplying the respective enhancement factor by  $2.34 \times 10^{-5}$ , the probability for the 200  $\mu\text{l}/\text{minute}$  data point (see Figure 9-12). For example, the enhancement factor for a 50  $\mu\text{m}$  cell stream depth equals 2, therefore, the capture probability equals to  $4.68 \times 10^{-5}$ . Note that while twice as many organisms were captured when the sample stream was confined to only half of the flow cell volume, the throughput was also halved.

The pump types used for this experiment both have inherent irregularities as part of their operation limiting the experiment. For the syringe pump it is the discreteness of the stepper motor driving the lead screw; for the peristaltic pump it is the repeated compression of the tubing driving the fluid. The output of the peristaltic pump was modified by i.) combining the flow with a second stream  $180^\circ$  out of phase and ii.) adding a large (200 ml) fluid buffer that acts as a low pass filter or ‘shock absorber’ to significantly reduce any oscillations.

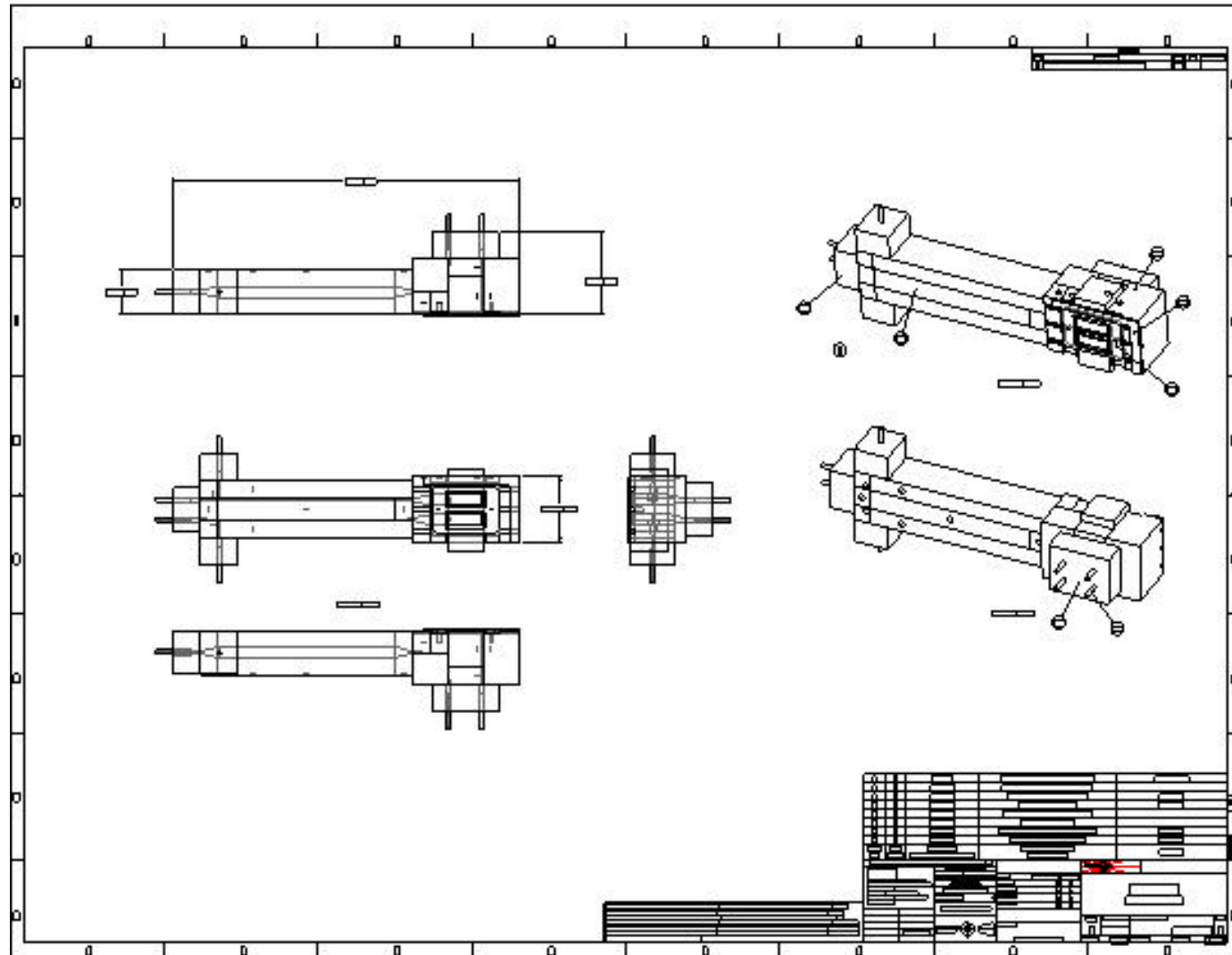
Within the limits of the experimental apparatus, the sample stream was reliably able to be compressed to 50  $\mu\text{m}$  or half the height of the flow cell providing the expected factor of two enhancement in capture efficiency. Because the dependence on the sheath thickness is hyperbolic, the majority of benefit is gained at very small thicknesses that were not obtainable with the experimental pumps used. Once a stable pump system is obtained, a factor of 50 enhancement should be within reach. Please note that

the overall flow time will be increased by the same factor. This would increase the probability of capture to 0.6% at a flow rate of 16  $\mu\text{l}/\text{min}$  - a significant increase over conventional flow cells. While this technique makes a significant contribution to the capture problem, there remains further advances needed before the capture of a single cell from a large suspension is possible.

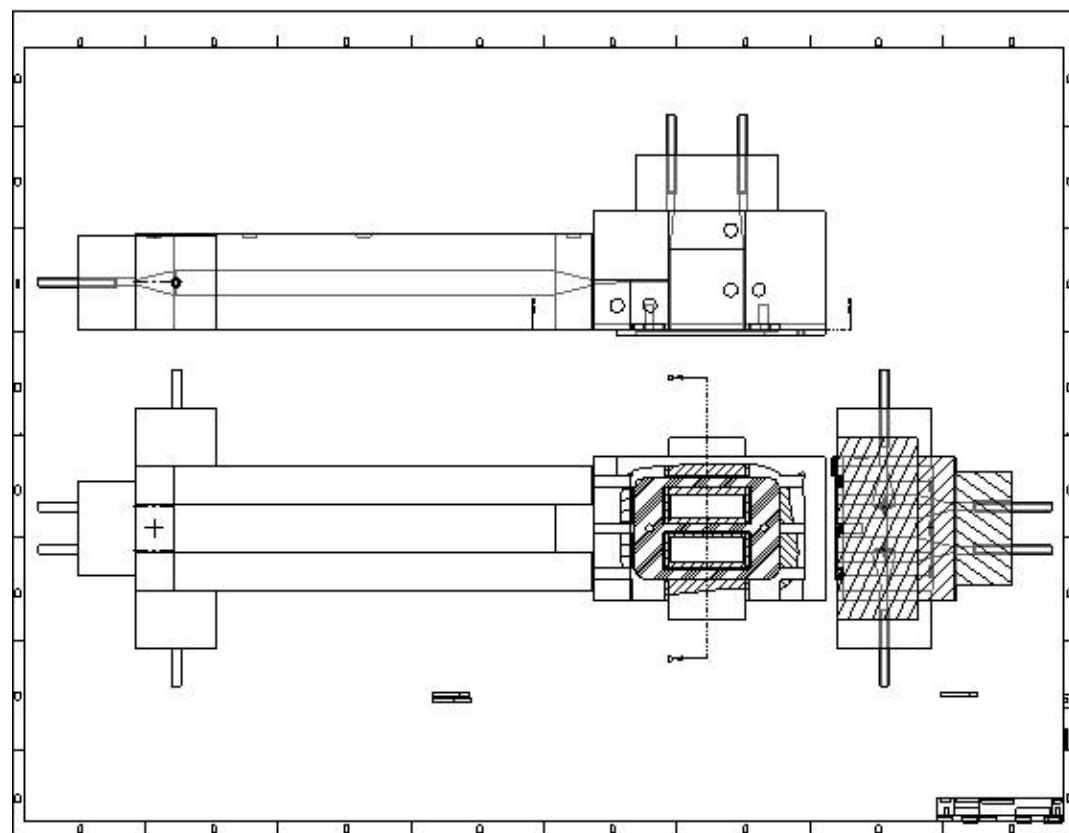
**Lateral Confinement.** A last measurement was made to verify the ability to align the cells in the lateral direction. This purpose of this alignment is to ensure that the desired organisms all flow over the specific receptors and not the reference area. *E.coli* cells ( $>10^9$  CFU/ml) were first stained with fluorescein and flowed against a second stream of PBS. The goal was to displace the cells halfway across the flow path, thus the two flow rates should be equal. Two syringes loaded with cells and PBS, respectively, were mounted together in the syringe pump to ensure equal rates. The flow cell was mounted to a transparent microscope slide instead of the opaque silicon chips enabling viewing of the flow cell chambers. The entire flow cell was able to be placed in the field of view of the fluorescence microscope and monitored with the attached CCD camera. A typical result is shown in the insert in Figure 9-11. The fluorescein green cells are confined as expected demonstrating the ability to spatially align the cells. The volume occupied by the cells is seen to be less than half indicating unequal flow rates. This was likely due to different impedances of the flow streams from different tube lengths, connectors, or unknown impediments within the flow cell channels from manufacturing.

**Summary.** Although a stable and sensitive transduction method is important, the most pressing problem facing all cell detecting biosensors is the capture of the cells. Our measured probability distribution using a standard laminar flow cell geometry demonstrates their poor capture efficiency and inability to satisfy in a practical way the need to monitor small numbers of cells. A new flow cell design relying on the dynamics of microfluidic transport to spatially realign the cell concentration to enhance the capture efficiency was designed, fabricated and tested by SatCon in order to increase the probability of cell capture and binding. In the approach taken the cells were aligned both in the lateral direction and the vertical dimension to create a thin sheath of cells in close proximity to the active receptor surface. The new flow cell was characterized experimentally and shown to be fundamentally sound although measurements were ultimately limited by the stability of the pumps driving the flow. While effective, the tradeoff for this alignment procedure is processing time. Thus, while this approach alone will not adequately solve the capture problem, it is an important contribution to its ultimate solution.

# **Appendix 9-A: Mechanical Drawings for Microfluidic Flow Cell**

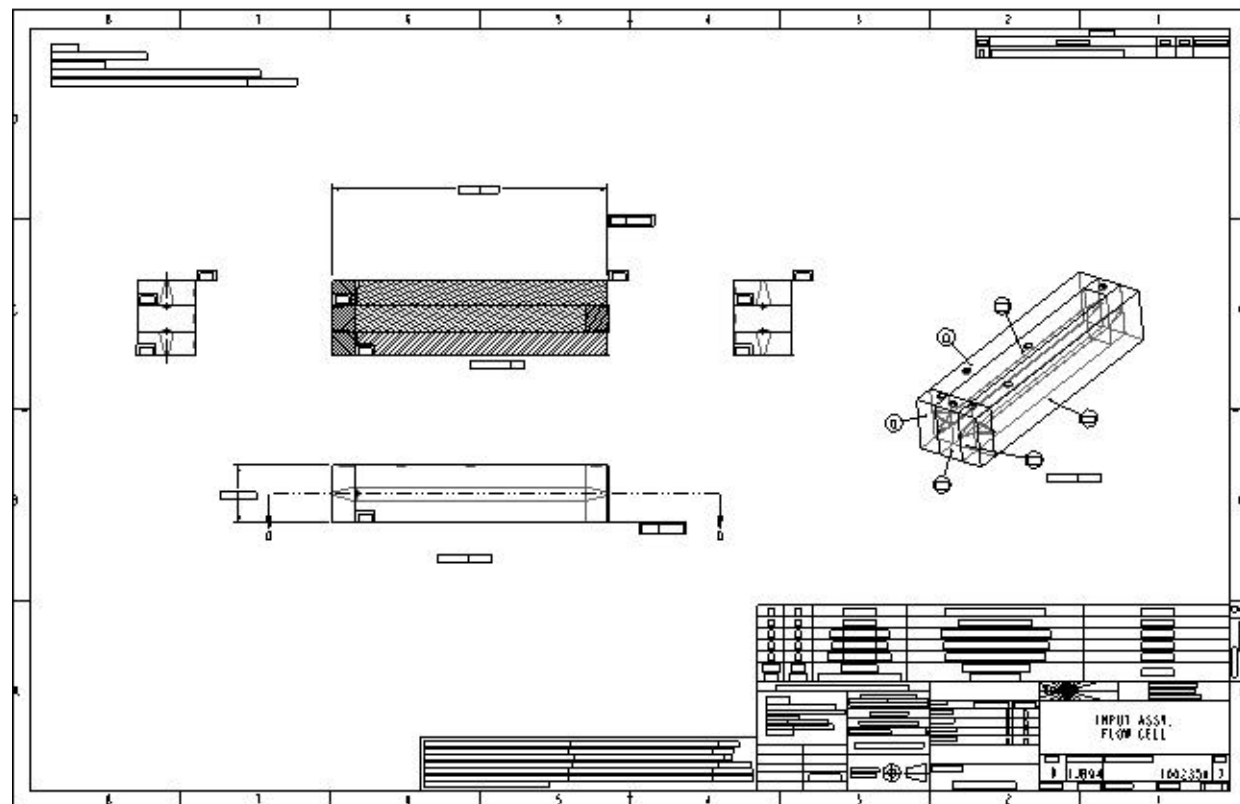


X X 1-0 1  
 X.XX 1-0.01  
 X.XXX 1-0.001  
 ANG 1-0.5



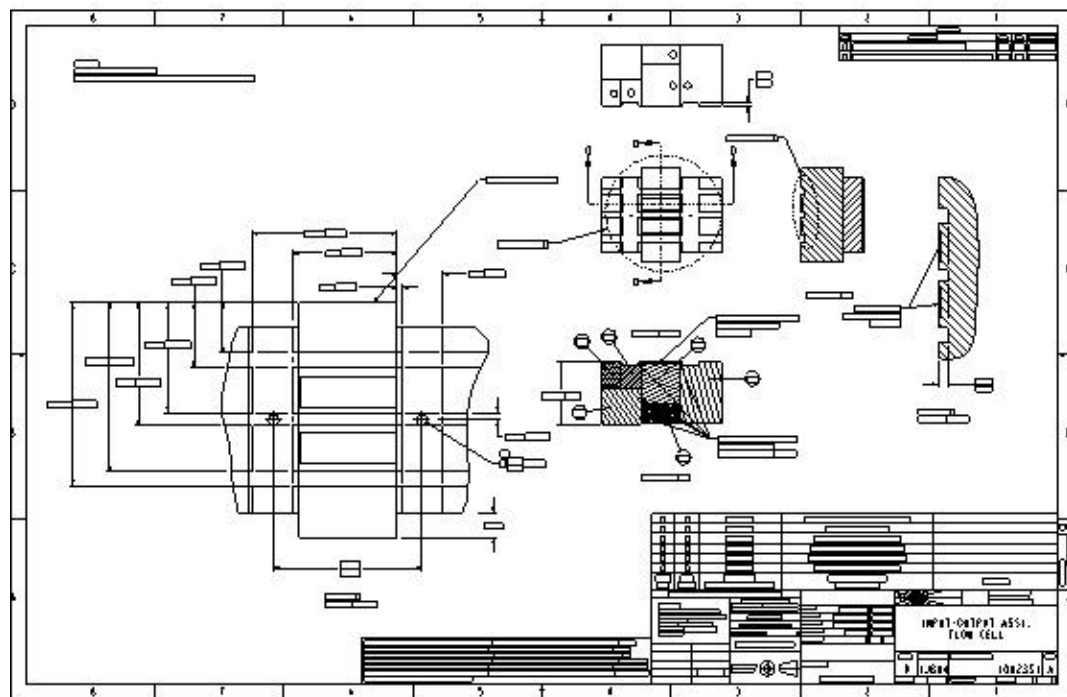
X X 1-0 1  
 X.XX 1-0.01  
 X.XXX 1-0.001  
 ANG 1-0 5

SCALE : 2.000 TYPE : ASSEM NAME : 1002343 SIZE : E SHEET 2 OF 2



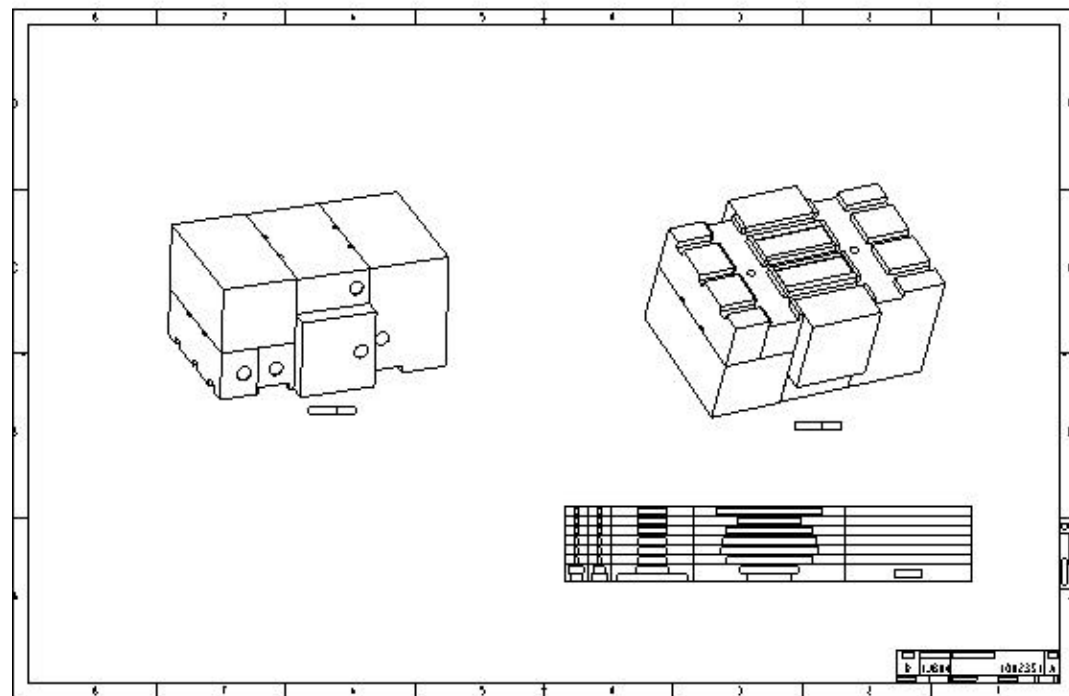
X.X    +-0.1  
 X.XX   +-0.01  
 X.XXX +-0.001  
 ANG   +-0.5

SCALE 3.000 TYPE : ASSEM NAME 1002350 SIZE D



X X 1-0 1  
 X XX 1-0 01  
 X XXX 1-0 001  
 ANG 1-0 5

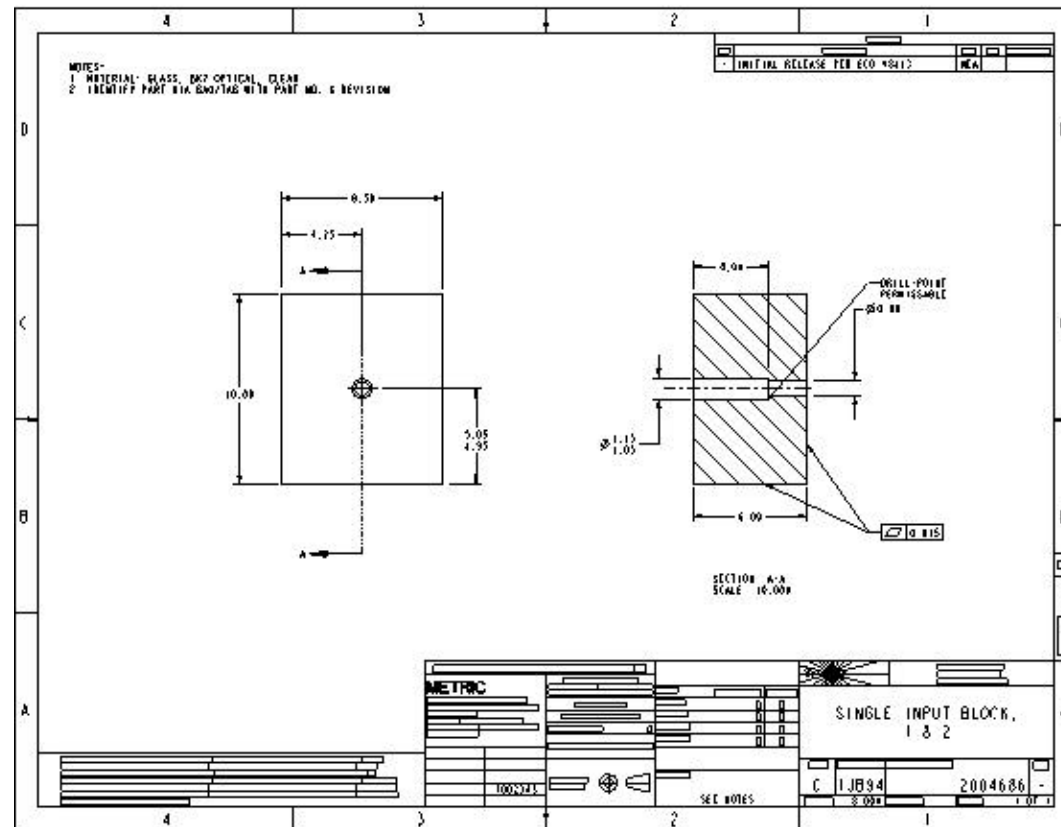
SCALE : 4.000 TYPE : ASSEM NAME : 1002351 SIZE : D SHEET 1 OF 2



X X 1-0 1  
 X.XX 1-0.01  
 X XXX 1-0.001  
 ANG 1-0 5

SCALE : 4.000 TYPE : ASSEM NAME : 1002351 SIZE : D SHEET 2 OF 2

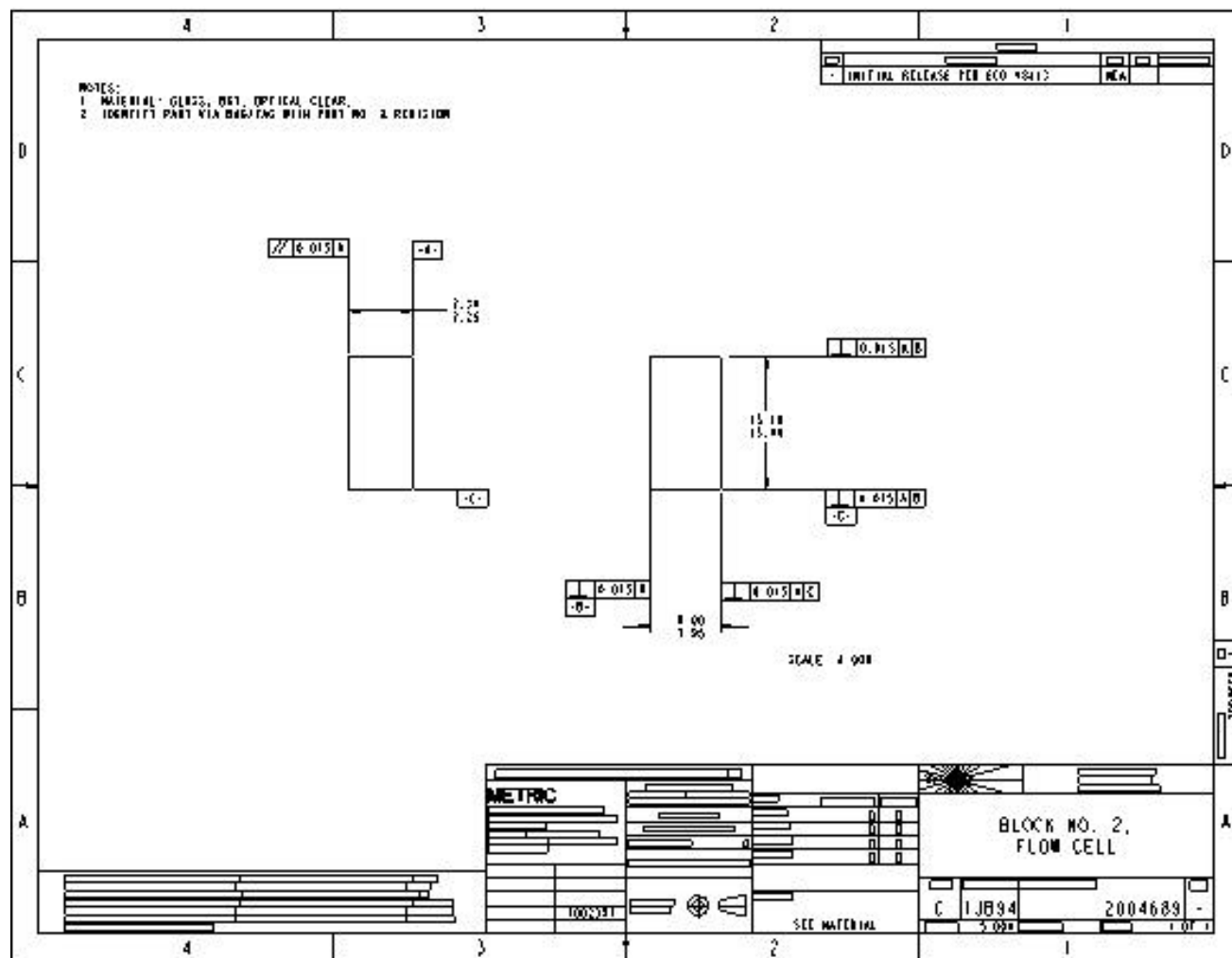




SCALE : 8.000 TYPE : PART NAME : 2004686 SIZE : C

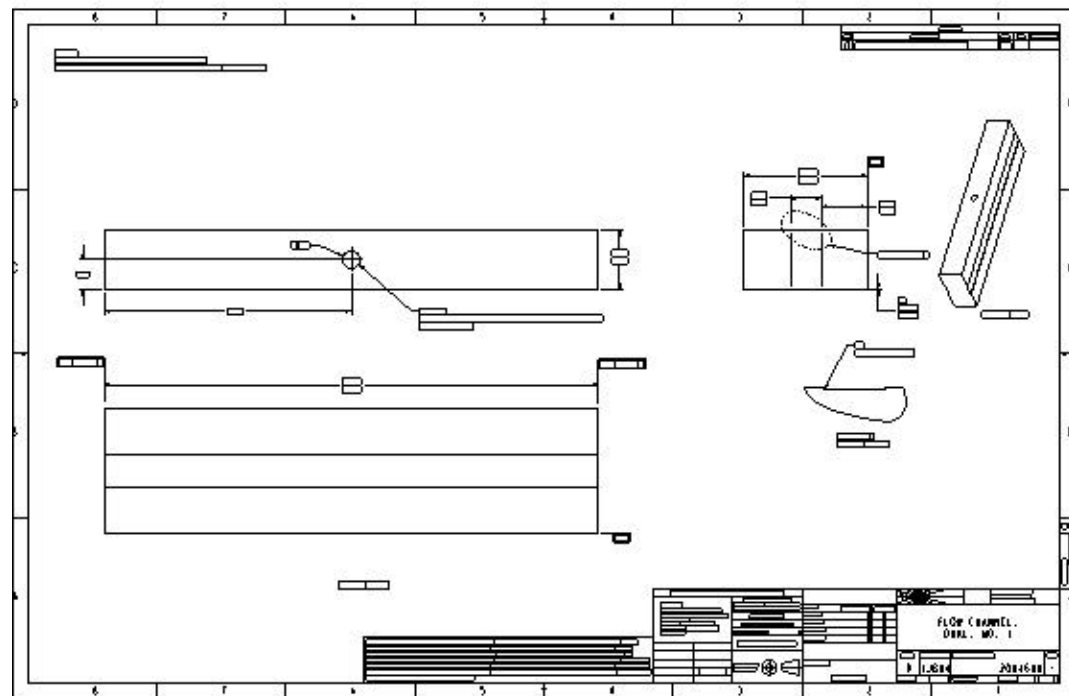
X X 1-0 1  
 X XX 1-0 01  
 X XXX 1-0 001  
 ANG 1-0 5





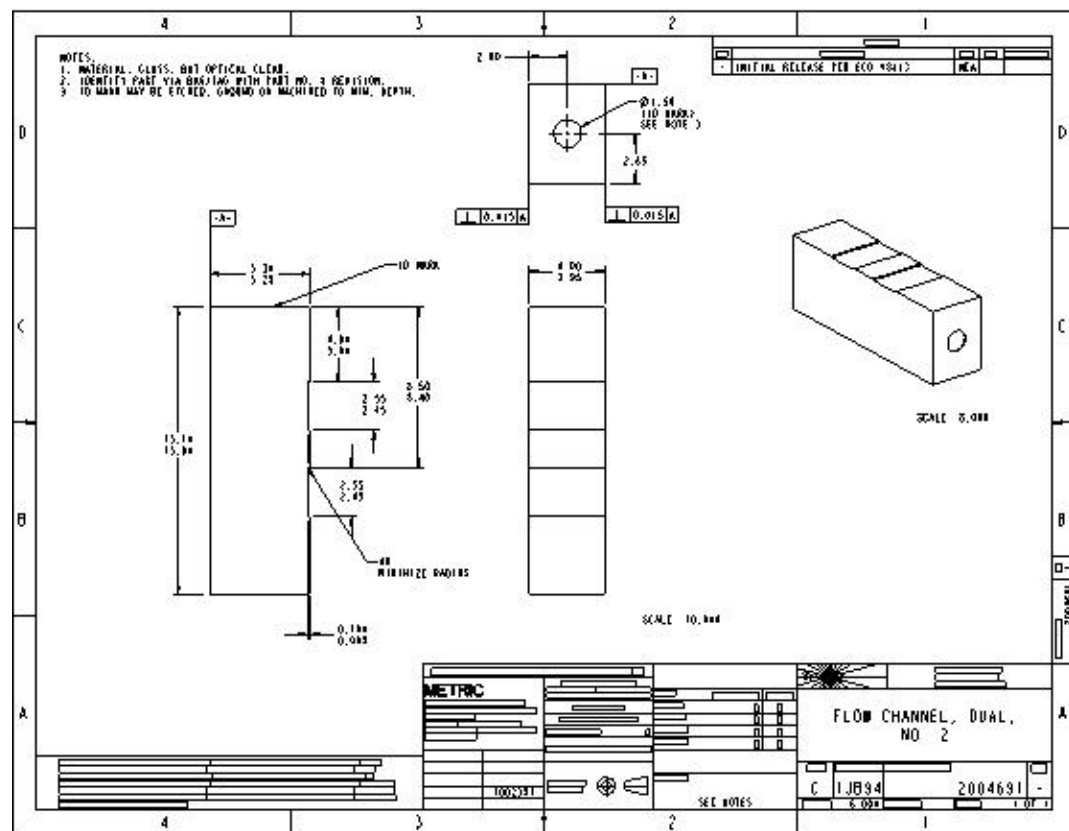
X X 1-0 1  
 X XX 1-0.01  
 X XXX 1-0 001  
 ANG 1-0 5

SCALE : 5.000 TYPE : PART NAME : 2004689 SIZE : C



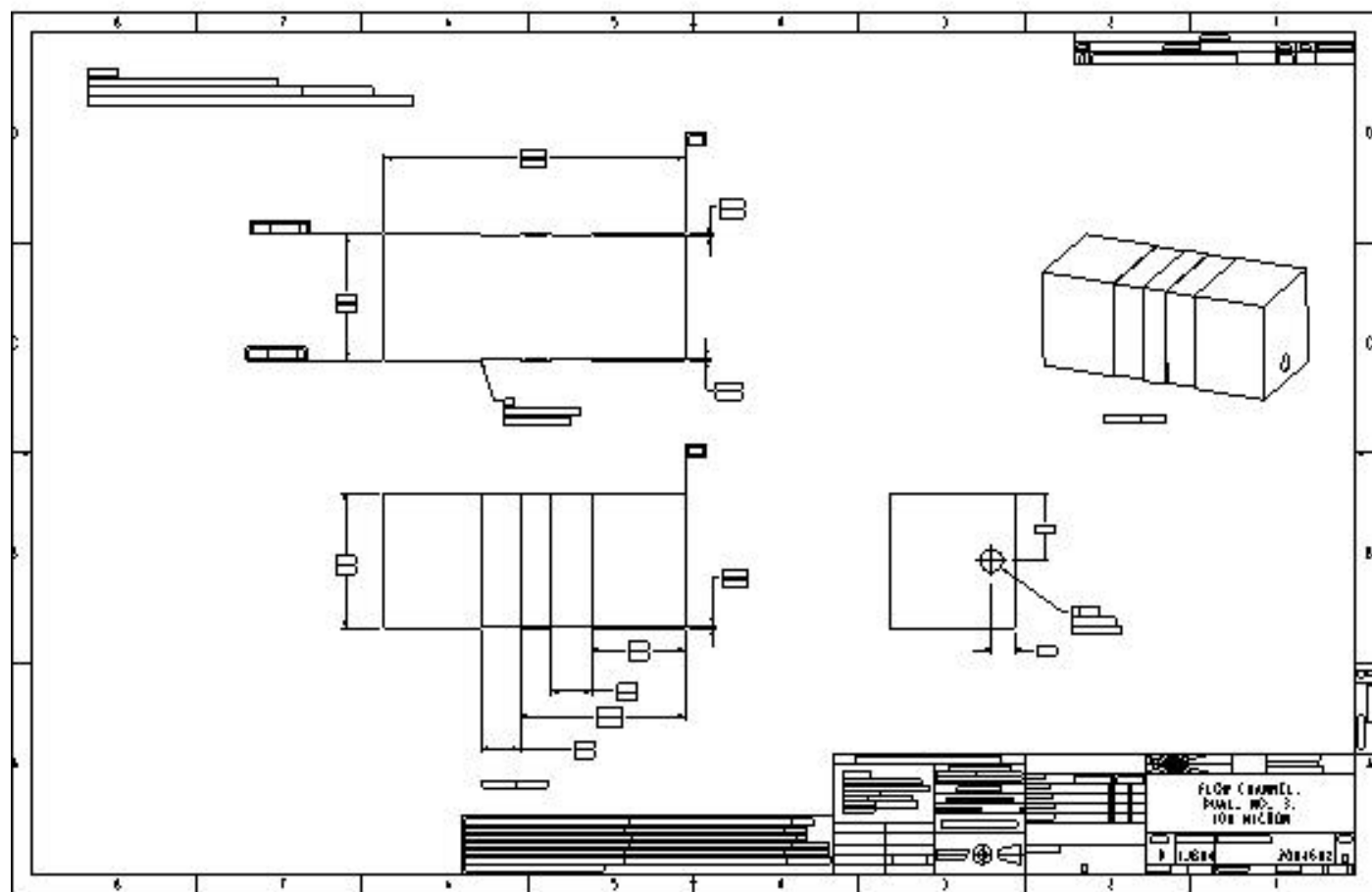
SCALE : 3.000 TYPE : PART NAME : 2004690 SIZE : D

X X 1-0 1  
 X.XX 1-0.01  
 X.XXX 1-0.001  
 ANG 1-0 5



SCALE : 0.000 TYPE : PART NAME : 2004691 SIZE : C

X X 1-0 1  
 X.XX 1-0.01  
 X.XXX 1-0.001  
 ANG 1-0 5



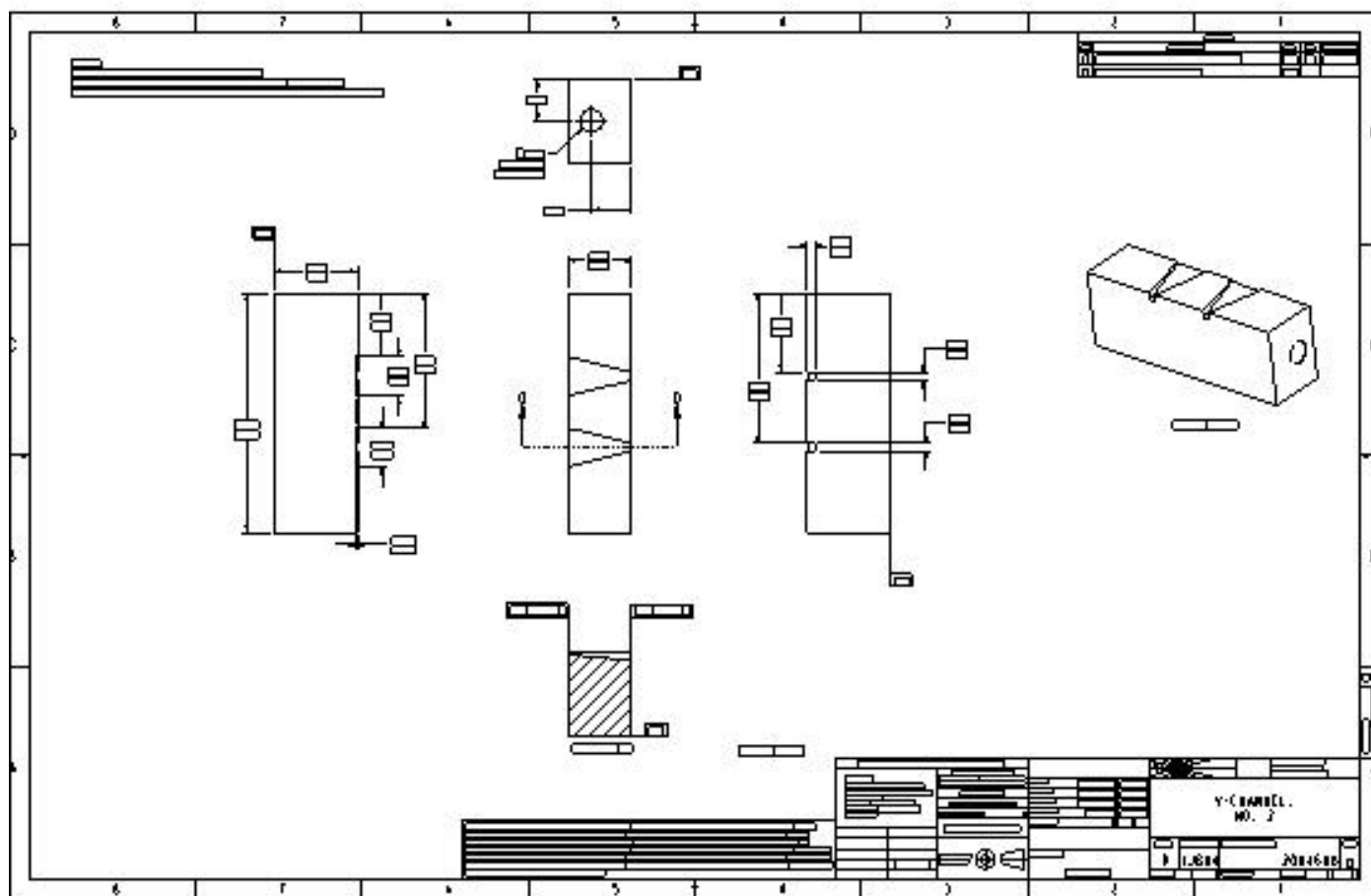
SCALE : 5.000 TYPE . PART NAME . 2004692 SIZE . D

X X 1-0 1  
 X.XX 1-0.01  
 X XXX 1-0 001  
 ANG 1-0 5

X X	F-0 1
X.XX	F-0.01
X.XXX	F-0.001
ANG	F-0.5

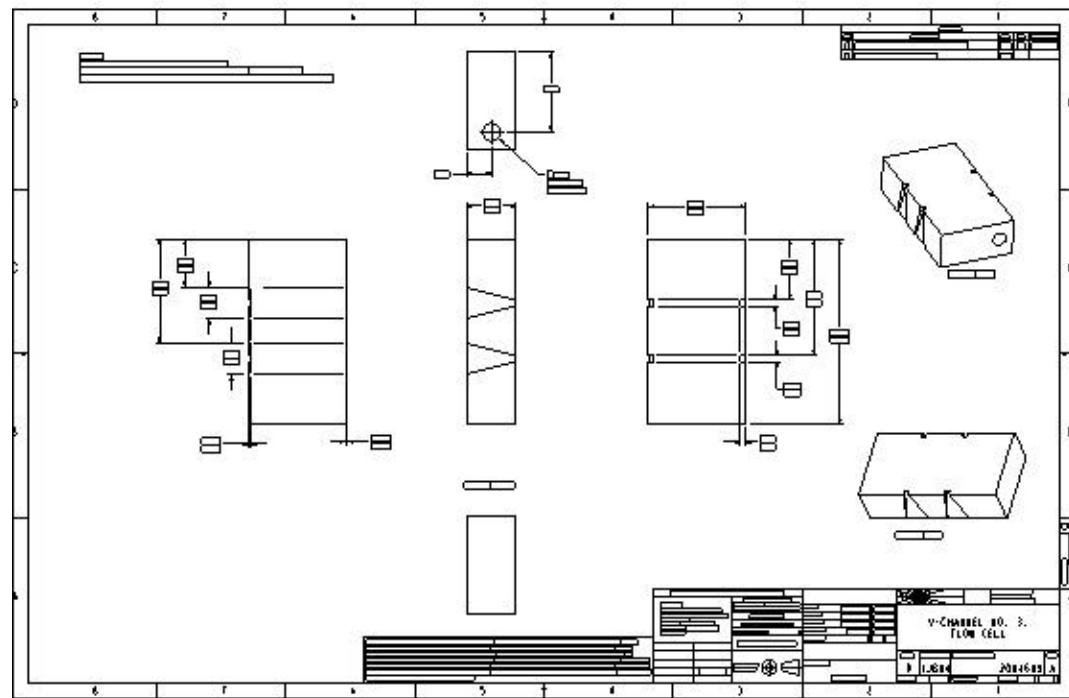






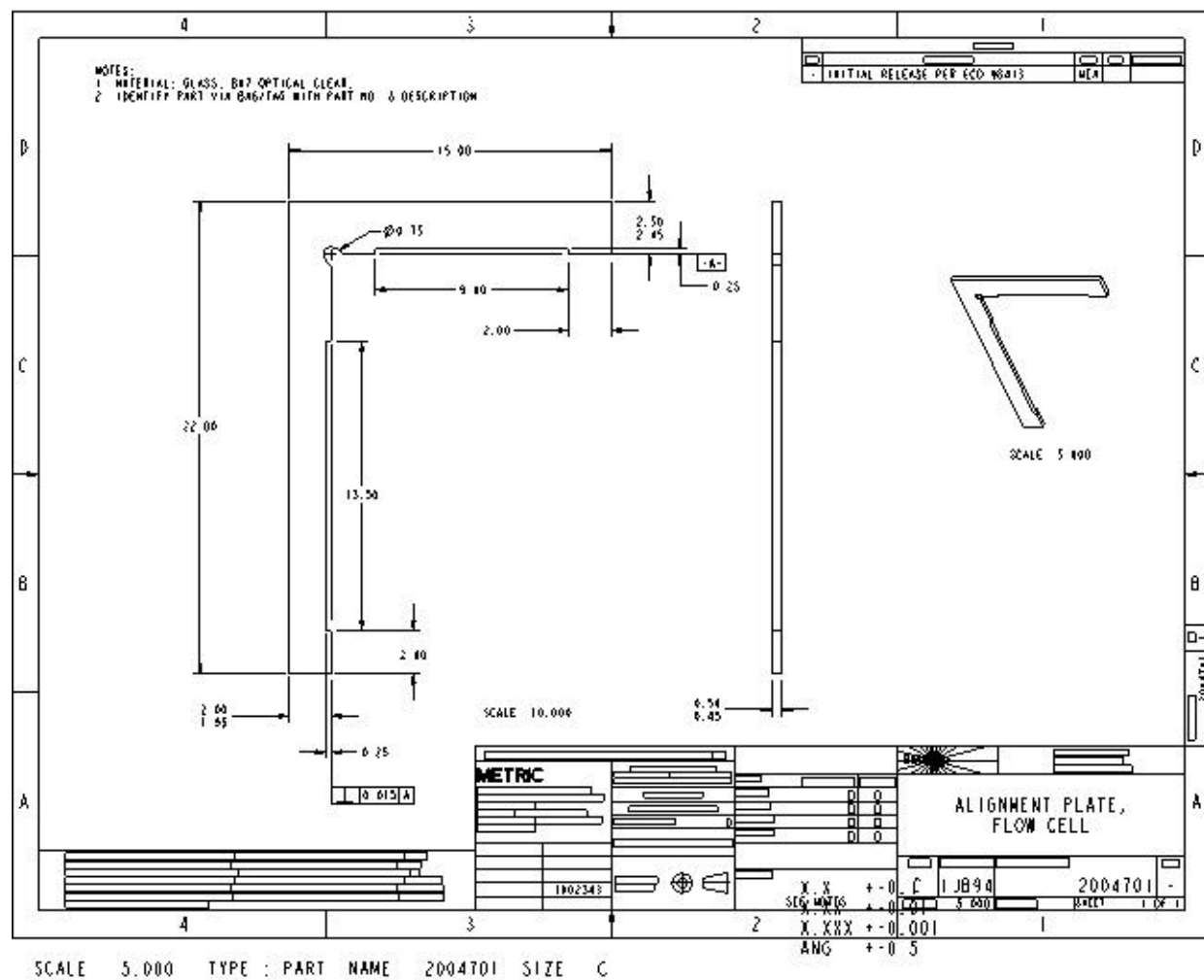
SCALE : 7.000 TYPE . PART NAME . 2004698 SIZE . D

X X 1-0 1  
 X.XX 1-0.01  
 X.XXX 1-0.001  
 ANG 1-0 5

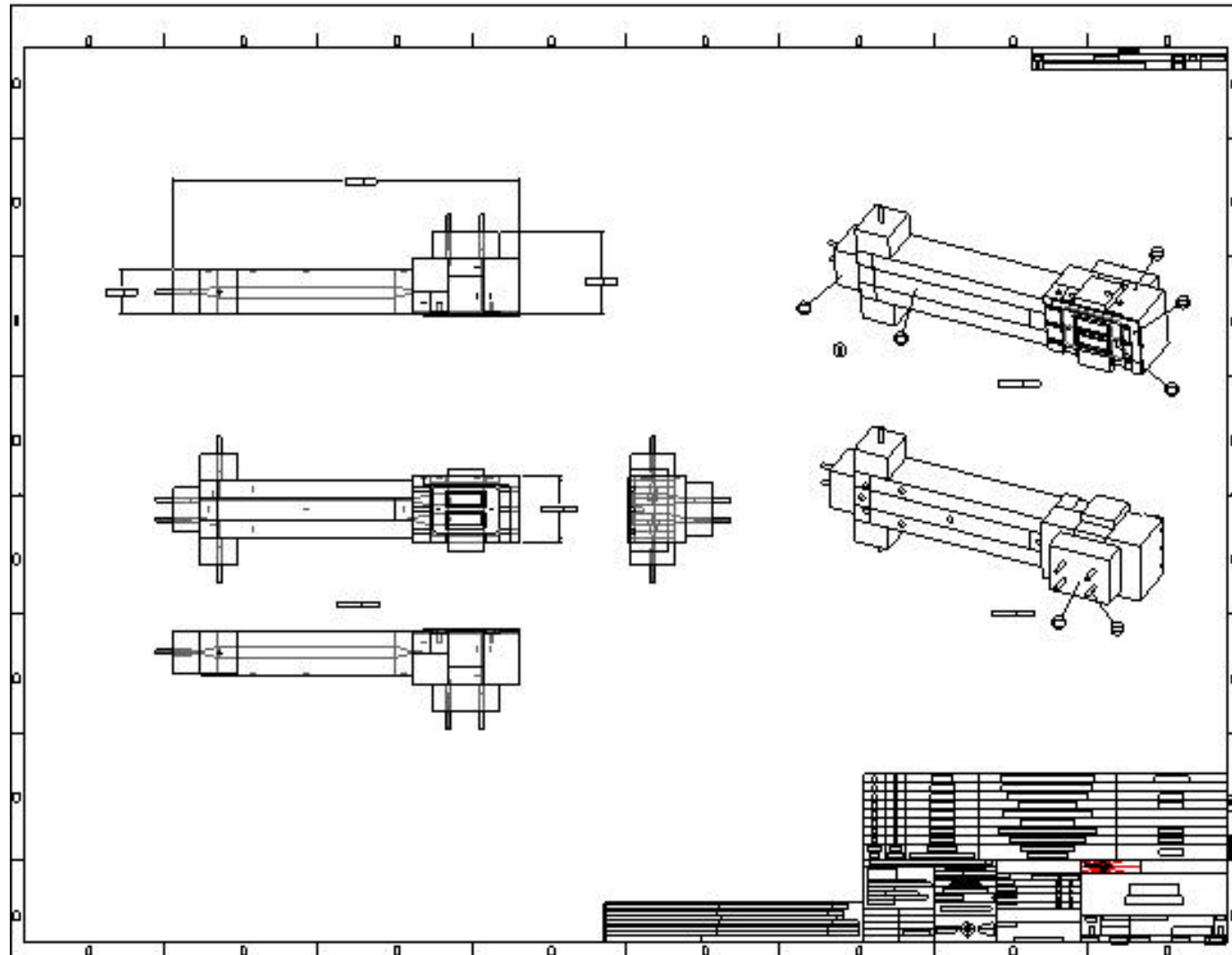


X X 1-0 1  
 X.XX 1-0.01  
 X.XXX 1-0.001  
 ANG 1-0 5

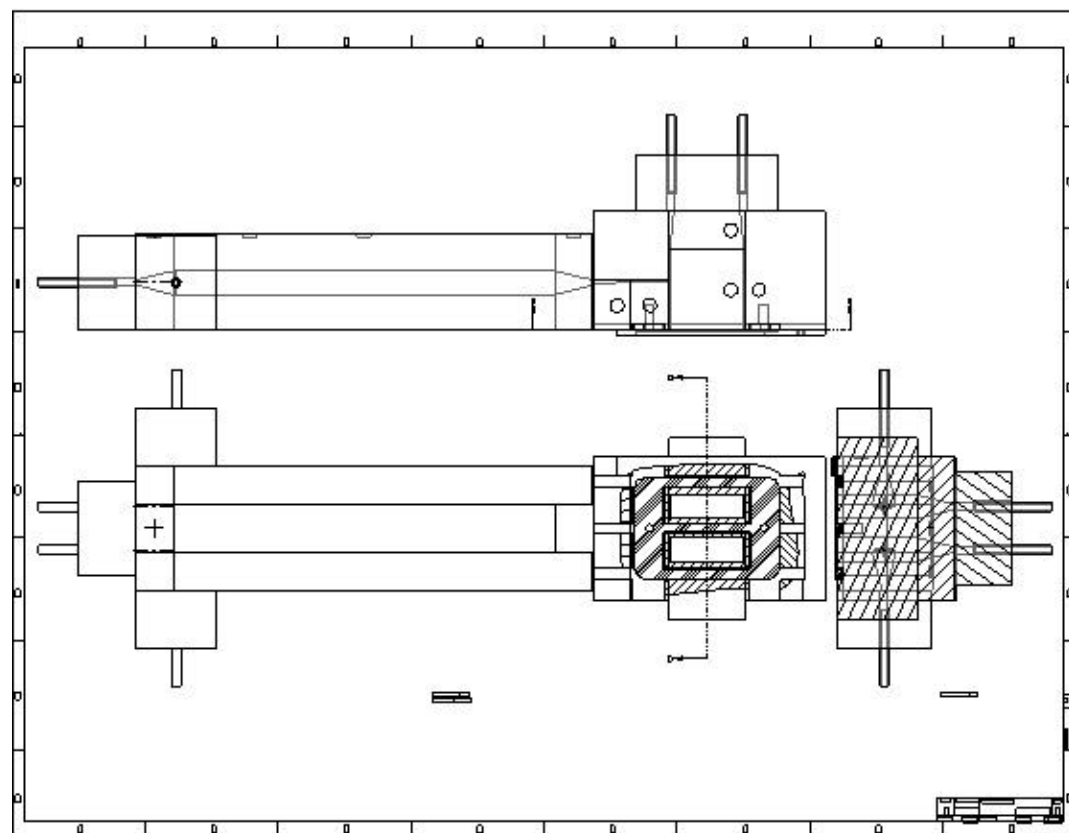
SCALE : 6.000 TYPE : PART NAME : 2004699 SIZE : D





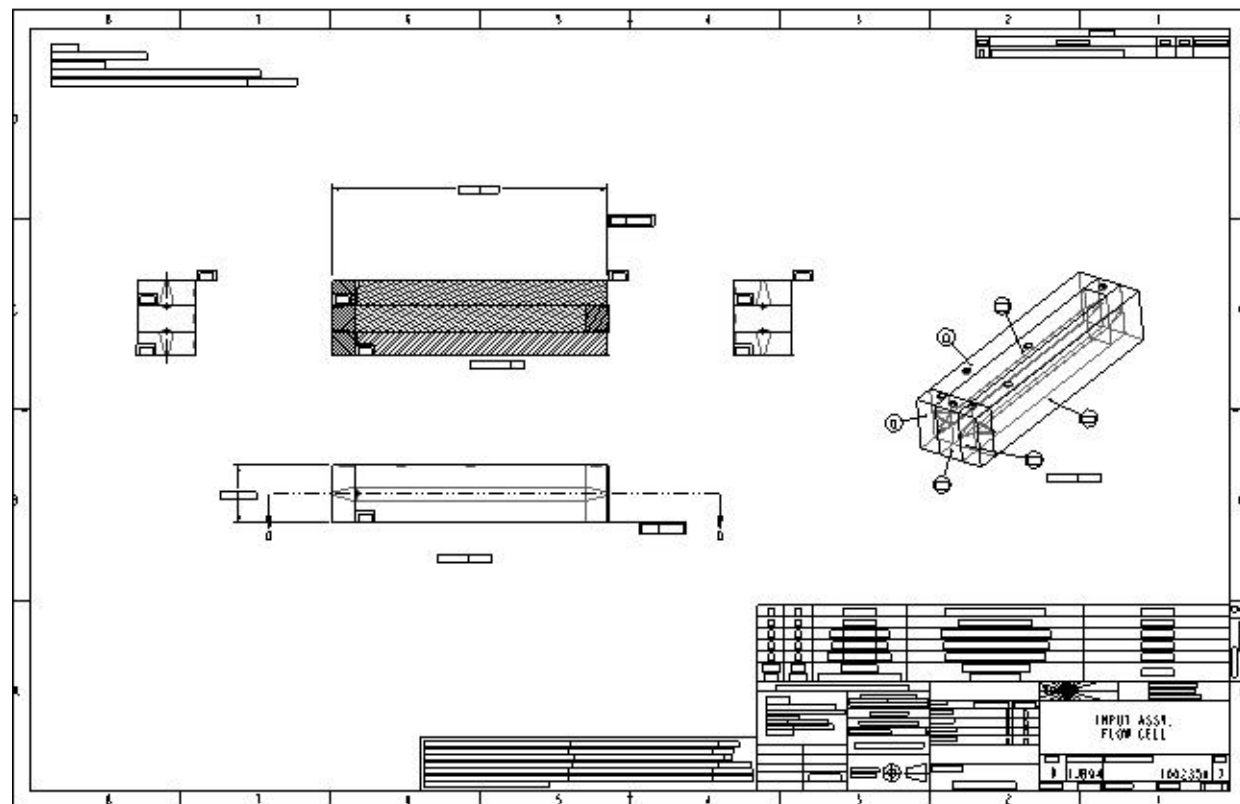


X X 1-0 1  
 X.XX 1-0.01  
 X.XXX 1-0.001  
 ANG 1-0.5



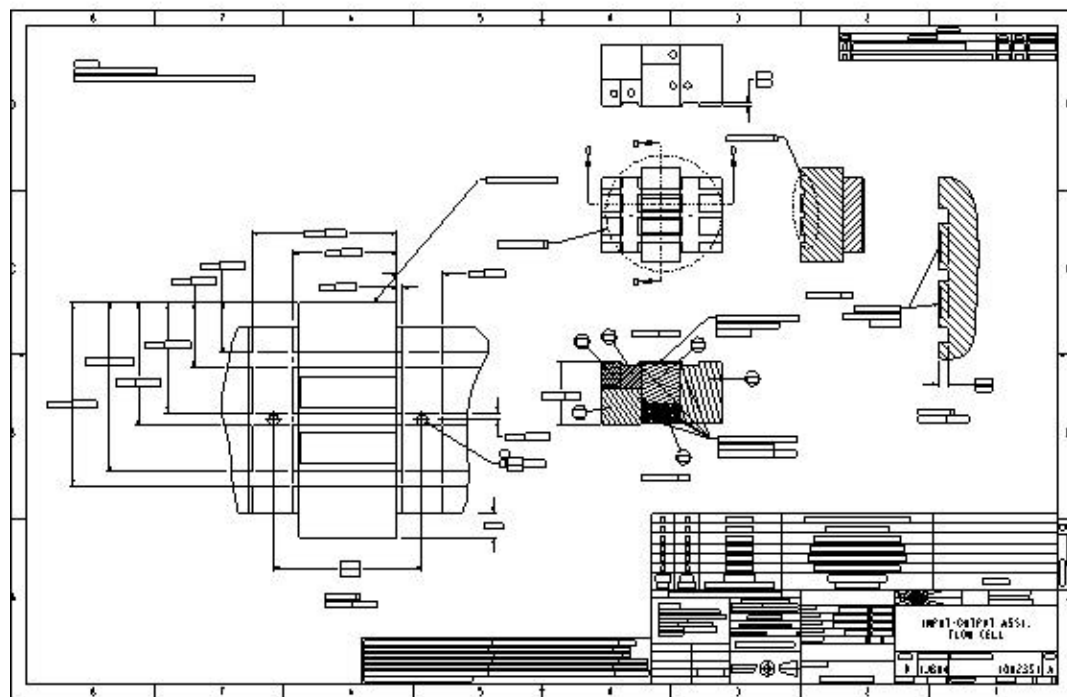
X X 1-0 1  
 X.XX 1-0.01  
 X.XXX 1-0.001  
 ANG 1-0 5

SCALE : 2.000 TYPE : ASSEM NAME : 1002343 SIZE : E SHEET 2 OF 2



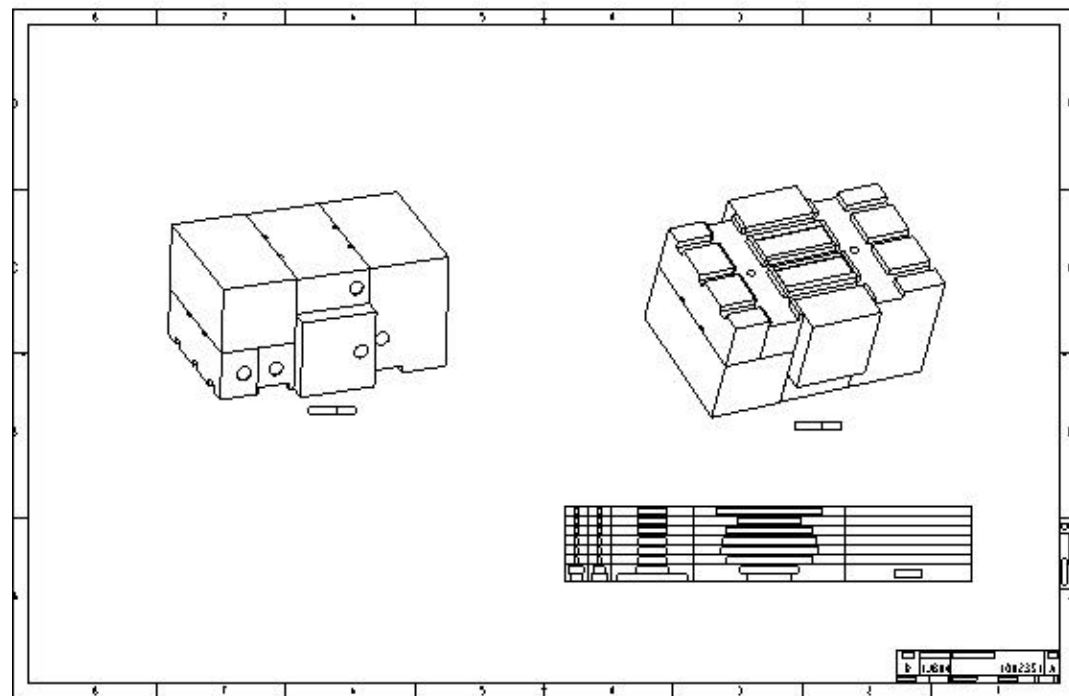
SCALE 3.000 TYPE : ASSEM NAME 1002350 SIZE D

X.X +-0.1  
X.XX +-0.01  
X.XXX +-0.001  
ANG +-0.5



X X 1-0 1  
 X XX 1-0 01  
 X XXX 1-0 001  
 ANG 1-0 5

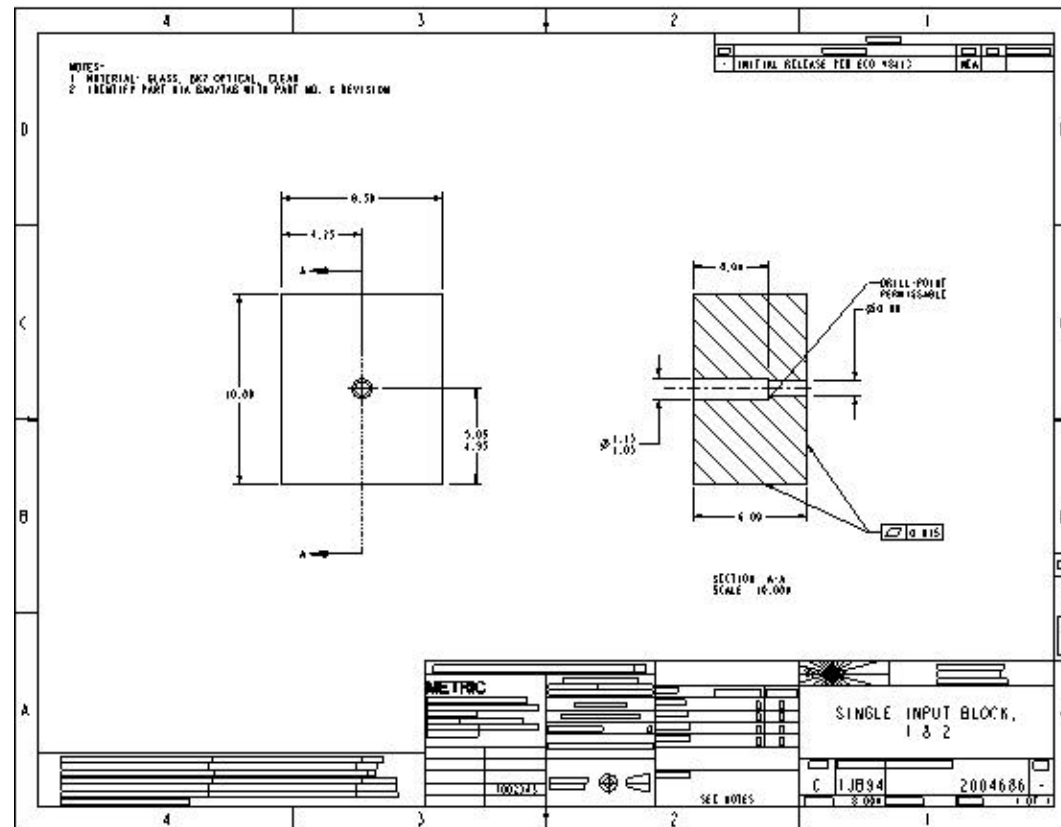
SCALE : 4.000 TYPE : ASSEM NAME : 1002351 SIZE : D SHEET 1 OF 2



X X 1-0 1  
 X.XX 1-0.01  
 X.XXX 1-0.001  
 ANG 1-0 5

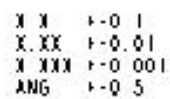
SCALE : 4.000 TYPE : ASSEM NAME : 1002351 SIZE : D SHEET 2 OF 2



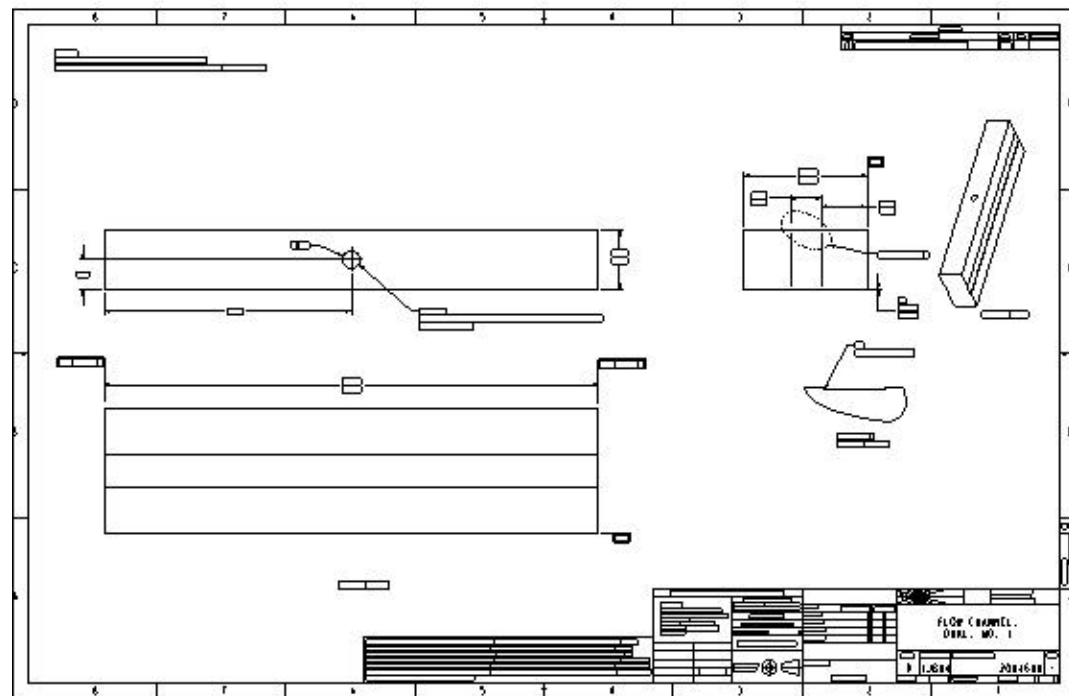


X X 1-0 1  
X XX 1-0 01  
X XXX 1-0 001  
ANG 1-0 5



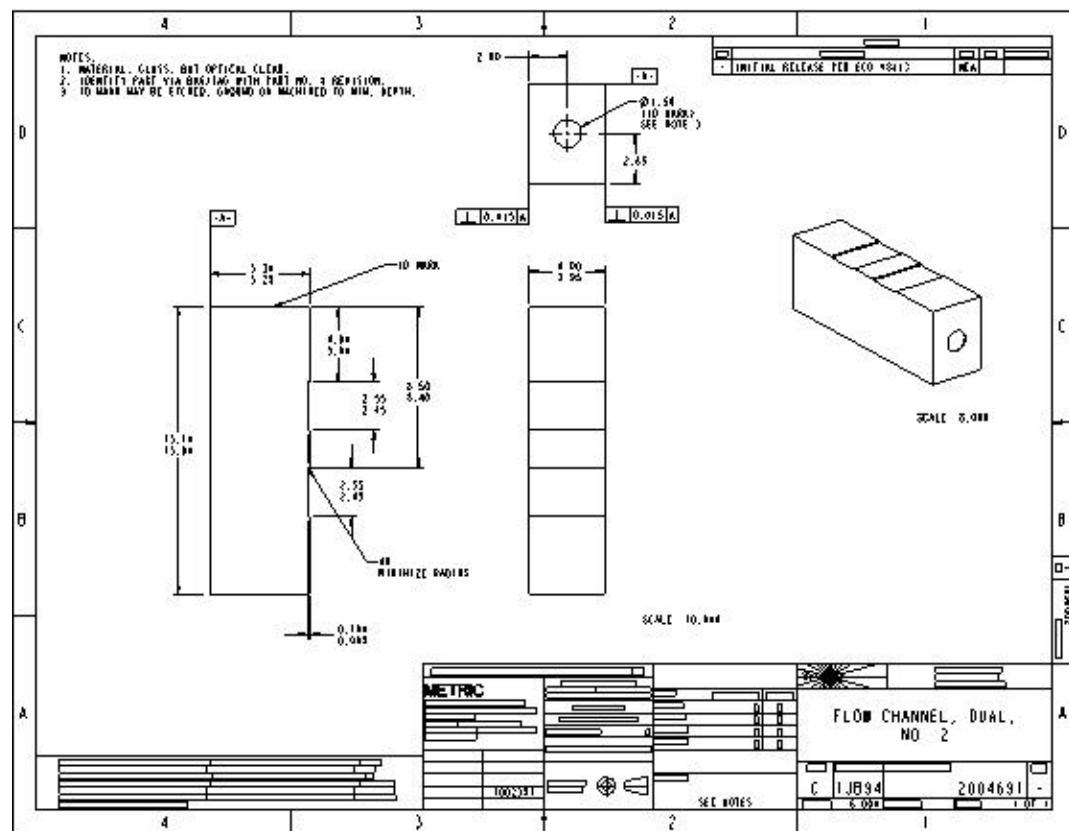


SCALE : 5.000 TYPE . PART NAME . 2004689 SIZE . C



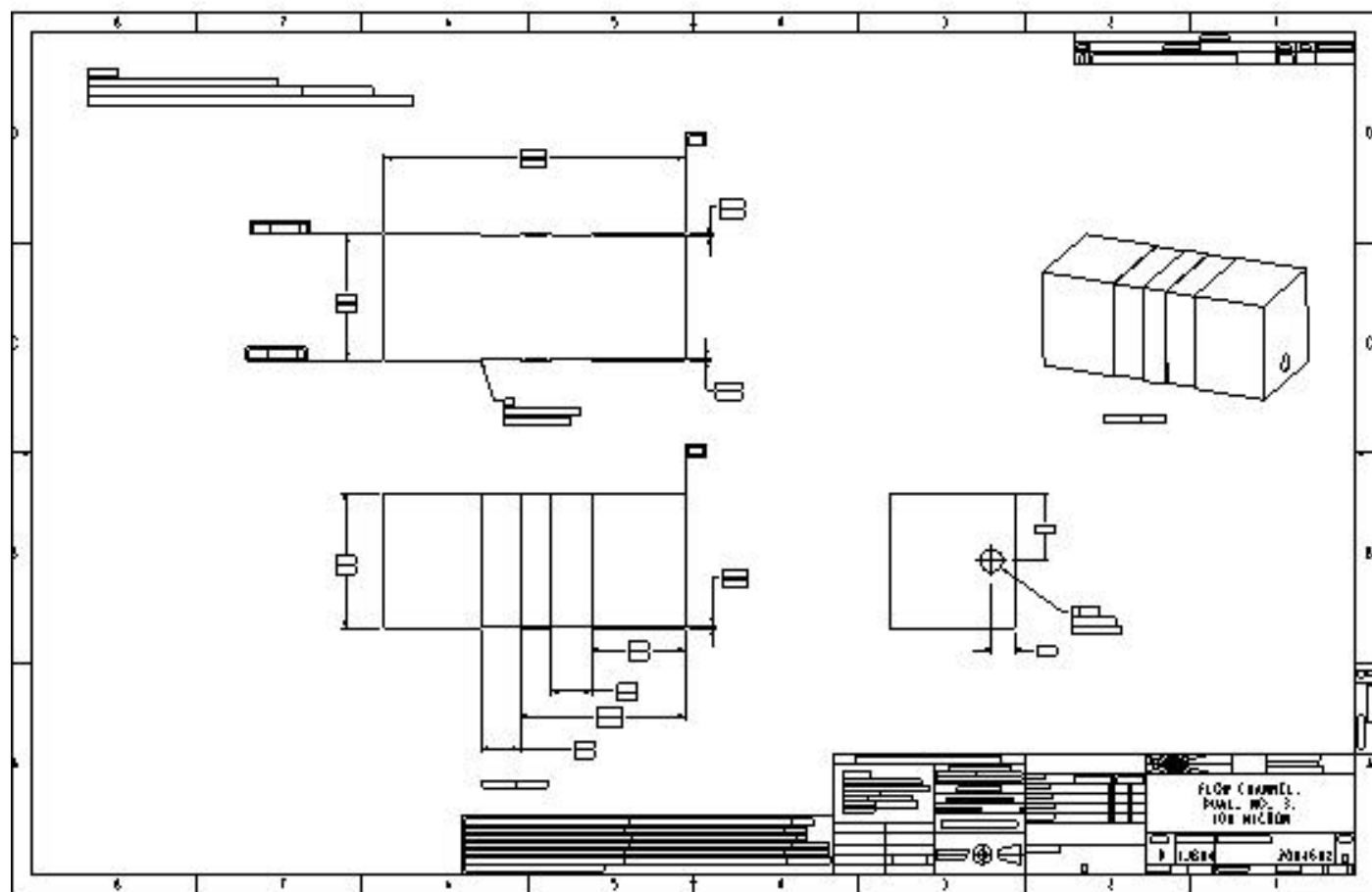
SCALE : 3.000 TYPE : PART NAME : 2004690 SIZE : D

X X 1-0 1  
 X.XX 1-0.01  
 X.XXX 1-0.001  
 ANG 1-0 5



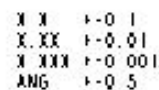
SCALE : 5.000 TYPE : PART NAME : 2004691 SIZE : C

X X 1-0 1  
 X XX 1-0 01  
 X XXX 1-0 001  
 ANG 1-0 5



SCALE : 5.000 TYPE . PART NAME . 2004692 SIZE . D

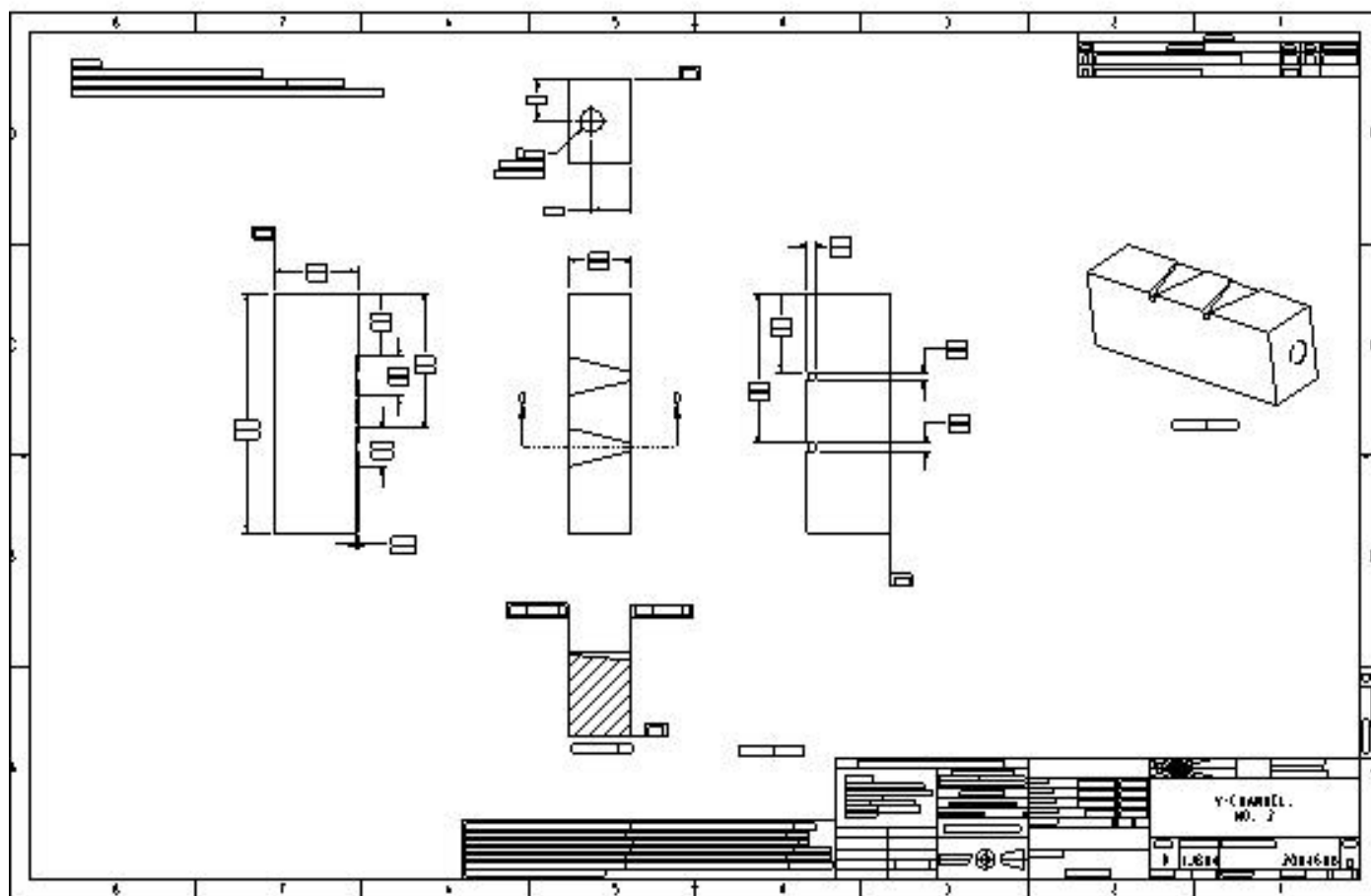
X X 1-0 1  
 X.XX 1-0.01  
 X XXX 1-0 001  
 ANG 1-0 5



SCALE : 5.000 TYPE : PART NAME : 2004693 SIZE : C

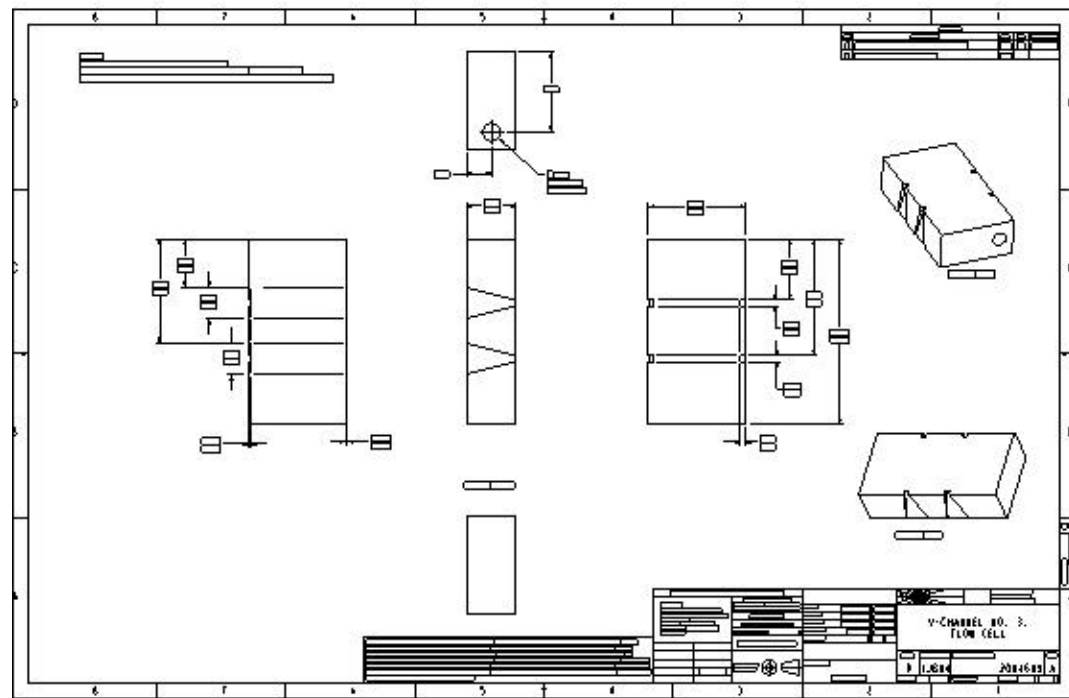






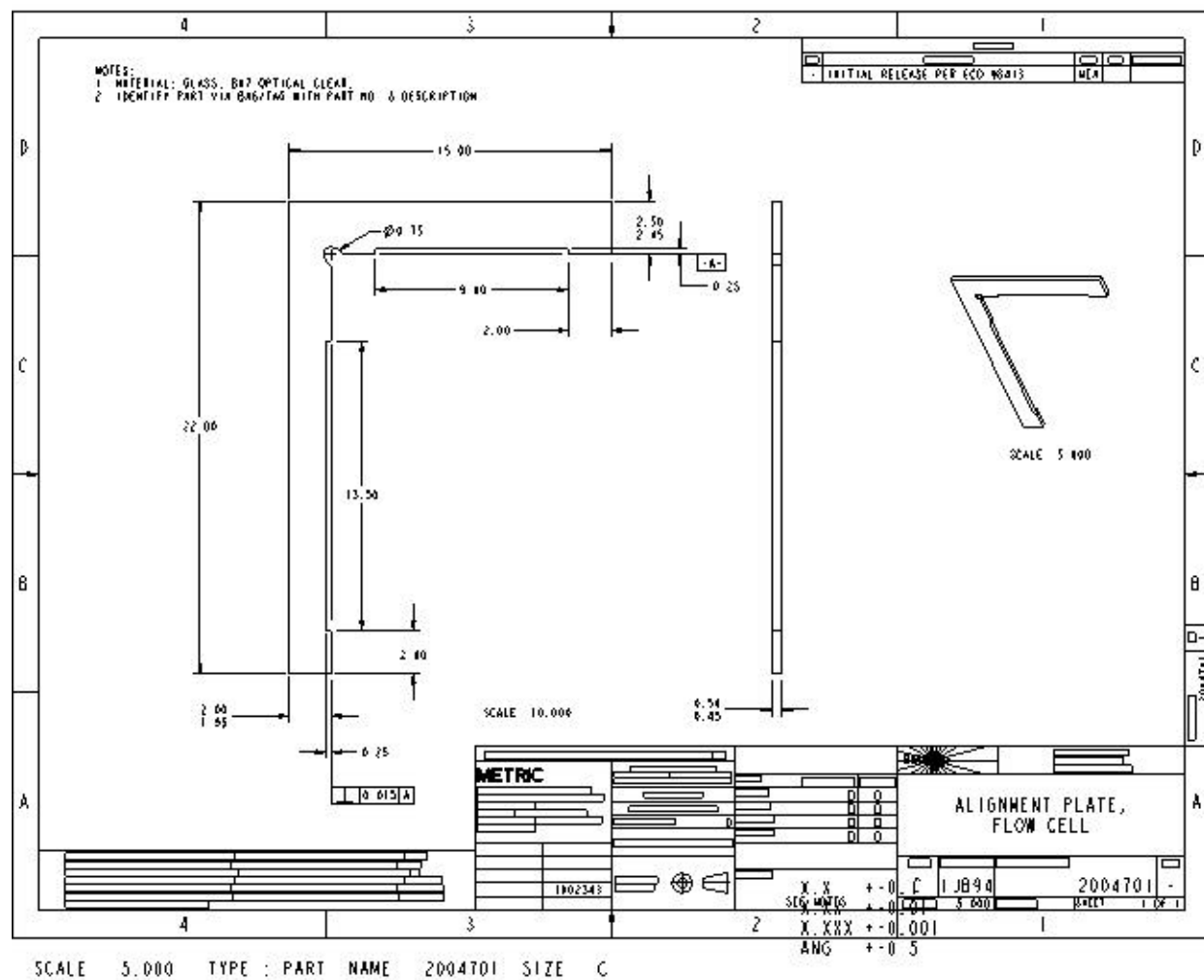
SCALE : 7.000 TYPE . PART NAME . 2004698 SIZE . D

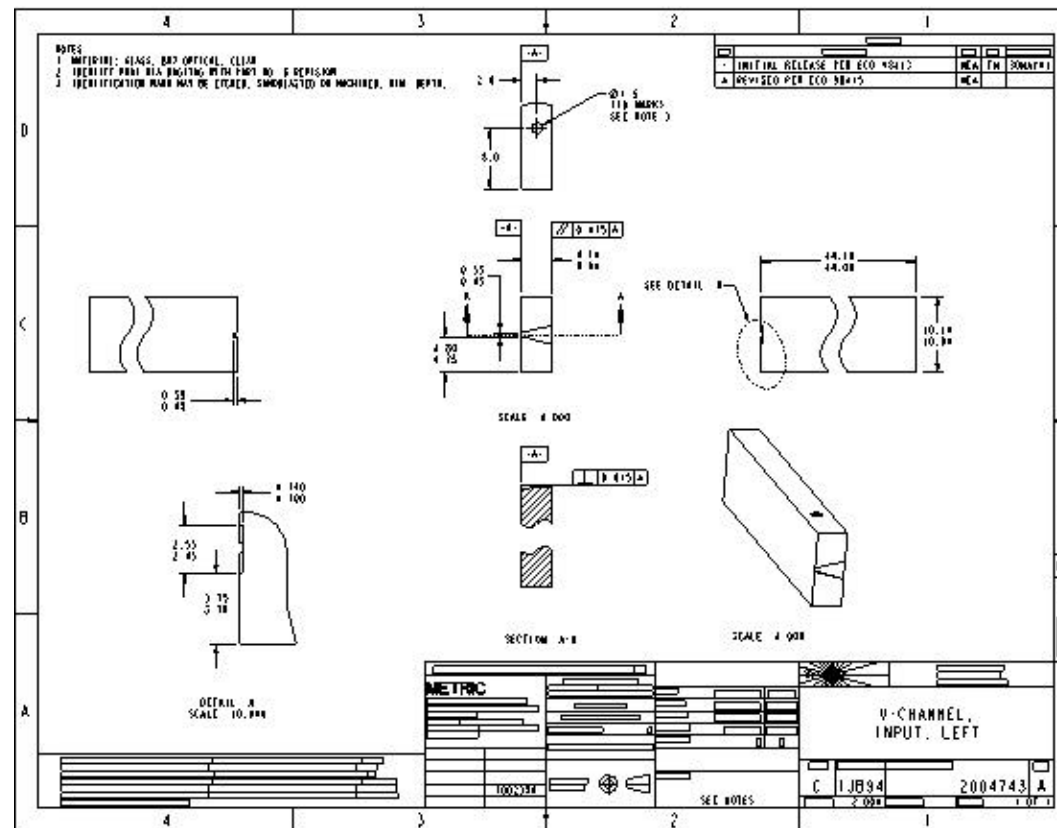
X X 1-0 1  
 X.XX 1-0.01  
 X.XXX 1-0.001  
 ANG 1-0 5



SCALE : 6.000 TYPE : PART NAME : 2004699 SIZE : D

X X 1-0 1  
 X.XX 1-0.01  
 X.XXX 1-0.001  
 ANG 1-0 5





SCALE : 2.000 TYPE : PART NAME : 2004743 SIZE : C

X X 1-0 1  
 X XX 1-0 01  
 X XXX 1-0 001  
 ANG 1-0 5

## Chapter 10 : Laboratory Characterization.

Beginning in January of 2002 a series of experiments were undertaken to combine the subsystems developed to characterize their ability to operate together as a functional biosensor. A description of this effort follows.

**Experimental Setup.** A mechanical fixture was constructed to hold the waveguide, flow cell, and associated folding mirrors. A photograph of the setup is shown in Figure 10-4 and mechanical drawings for the reproduction of the fixture are found in Appendix 10-A. The waveguide was held in a recessed area (having the exact dimensions as the waveguide) machined into the mounting plate for repeatable performance after many removals and replacements. The flow cell shown in Figure 10-2 was placed on top of the waveguide and held in position with precision mechanical stops and secured with pressure onto the top of the cell.

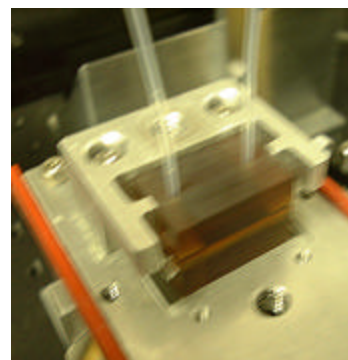


**Figure 10-1.** Photograph of mechanical fixture holding the flow cell. The flow cell is sitting on top of the waveguide.

**Pump Station.** Two pumping systems were available and used for driving the flow into the flow cell; 1) the computer controlled peristaltic pump described at the end of this chapter and 2) a simple syringe pump arrangement. The syringe pump (Cole Parmer) incorporated a manual mixing valve for switching between syringes containing different fluids.

A source of problems for both flow devices was the presence of bubbles. This problem was significantly reduced by adding a small buffering chamber capable of being vented. This chamber serves the dual purpose of removing troublesome bubbles as well as providing a degree of mixing for a gentle transition from one fluid to another avoiding scattering from abrupt changes in refractive indices.

**Waveguides and Flow Cells.** As was described previously the first generation design employing 2<sup>nd</sup> order diffraction gratings and fabricated by Sarnoff Corporation (Princeton, NJ) had inadequate throughput to conduct any experiments. In order to carry out the laboratory characterization, several waveguides were obtained from the Georgia Tech Research Institute. These devices were built with 1<sup>st</sup> order diffraction gating coupler and had very good throughput. Since the dimensions and cuvette regions were designed to fit the GTRI geometry, they were not compatible with the SatCon flow cell devices. Consequently, a specially sized flow cell was designed and built from polyetherimide (GE ULTEM 1000) in order to use the GTRI waveguides. Additionally, the mechanical fixture holding the waveguide and flow cell was altered to accommodate these design changes.

The flow cell design was based on SatCon's standard design used for the Phase I work. The sample chamber is a rectilinear volume approximately 100  $\mu\text{m}$  high, 15 mm long (corresponding to the length of the GTRI cuvette), and either 3 mm (single chamber) or 1 mm wide (two independent chambers). The input and output were tapered in both dimensions to i.) transition between 1/32" tubing and the cuvette region, and ii.) maintain a constant area for uniform flow. Mechanical drawings to construct this flow device are found in Appendix 10-B.

Photographs of the mechanical fixture, flow cell, and GTRI waveguide, and are shown in Figures 10-1, 10-2, and 10-3, respectively.

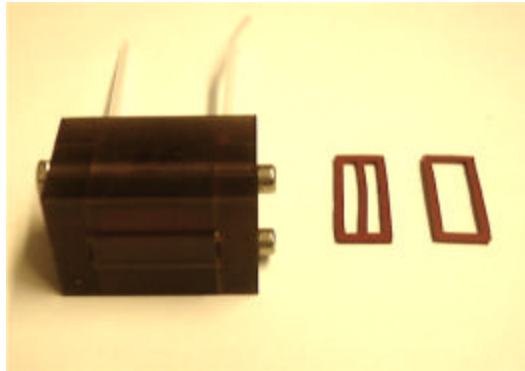


**Figure 10-2.** Flow Cell for GTRI Waveguides. The flow cell was machined from polyetherimide. Two cells were constructed with: a large chamber containing both cuvettes and two independent chamber side-by-side for independent flows. Dye cut gaskets for the respective cells are shown to the right in the photograph. The height of the chambers was typically 100  $\mu\text{m}$  for highly laminar flow.

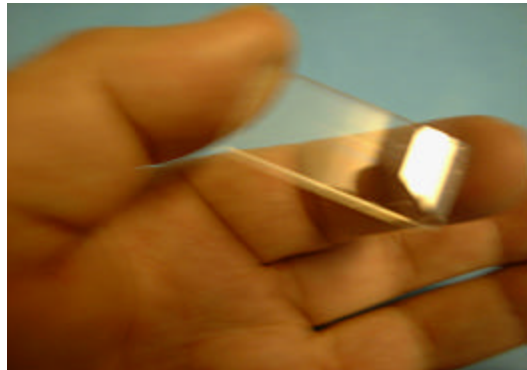


**Figure 10-3.** Photograph of a standard GTRI waveguide used for the laboratory characterizations.

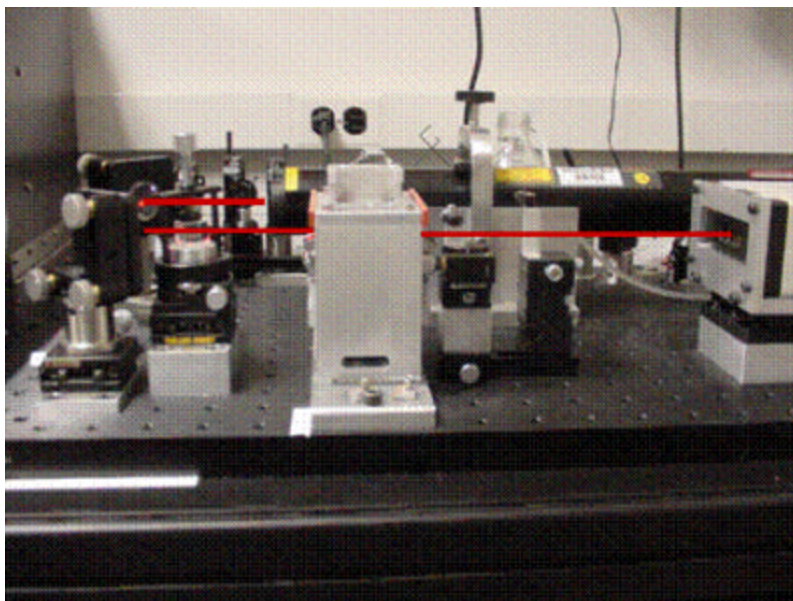
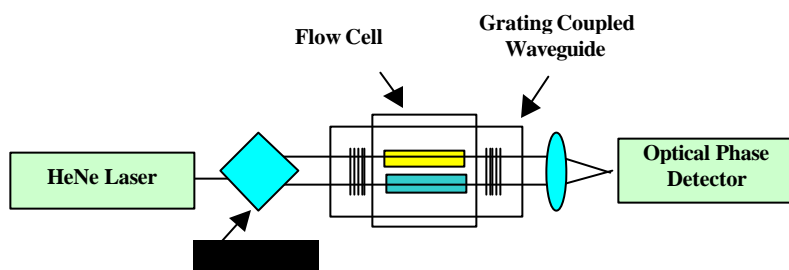
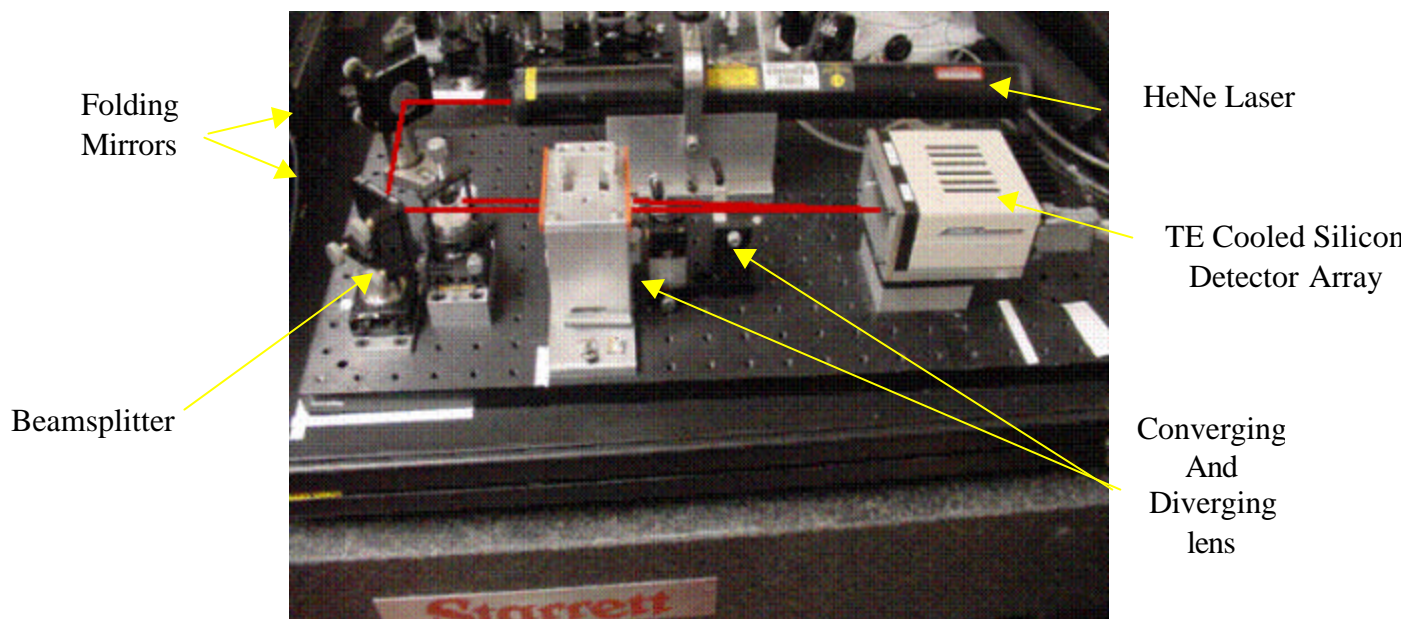


**Figure 10-4.** Photographs of the top and side views of the experimental apparatus used to obtain the data acquired for the laboratory characterization.

**Gaskets.** An important component for providing a robust, uniform, and repeatable mechanical interface between the flow cell and the waveguide is the development of the flow cell gasket. The gasket must provide a good seal between the respective sensing chambers and the outside world to prevent leakage of the sample outside of the flow path, to prevent contamination from flowing into the sample, and to maintain a constant flow pressure.

The gasket designs developed for the SatCon flow cells were designed to conform to the rectangular shaped cuvette regions. The flow cell sensing chamber volume was defined by a continuous precision height fence-like structure surrounding the footprint of the waveguide cuvette. One to two millimeters of gasket material fit around this fence to form the seal. A soft silicone material was chosen for the gasket material because of its pliability in conforming to the spacing determined by the mechanical height of the fence. A special dye was constructed to cut these gaskets. While the mechanical properties of the silicone were desirable it was found initially that the material leached a contaminating film that compromised the waveguide response. This was alleviated by triple washing the gasket in a sonicated acetone bath.

**Integration Effort.** The goal of these experiments was to integrate the flow cell, waveguide, surface chemistry, and receptor system together and to learn how to use the apparatus in order to design test runs. No attempt was made to integrate the Micronic's H-filter into these experiments. All experiments described below were conducted with homogeneous solutions. A significant learning curve was encountered and the obstacles were examined, understood, and overcome. Obstacles worthy of note were:

- *Gasket Positioning.* It was discovered that the gasket would creep and often overlap the edge of the flow cell, interfering with the propagating light beam and scattering the light crossing from the exposed cuvette region into the buried oxide. This was rectified by stretching the gasket slightly and reseating it before applying the flow cell.
- *Trapped Air.* Since the mode of detection is sensing of the surface, any imperfection or perturbations of the surface are typically deleterious. The accumulation or generation of small bubbles collecting at the surface caused havoc in a number of experiments. This was alleviated by de-gassing of all buffers prior to experimentation and by purging the flow and pump system of any gas prior to use. This was accomplished by attaching a syringe to the fluid waste line and gently drawing it out to create a negative pressure and overcome the surface energy of the bubbles. Care had to be taken not to draw the syringe too hard and break the gasket seal. When performed successfully one could easily see the release of a large amount of air (unknowingly trapped in the flow cell) from the output line. Once all of the air was removed, the resulting fringe pattern returned to a stable pattern.
- *Cleaning.* The performance of the waveguide depends heavily on the cleanliness of the exposed surface as expected. Unwanted thin films from oils and salt precipitates act as optical absorption or scattering centers significantly impairing the performance of the sensor. A three-pronged Teflon sleeved holder was built, based on a design used by Campbell at GTRI, to grip the waveguide. The following cleaning procedure was then performed to ensure no surface contamination:

- Douse the waveguide with standard MicroKlean solution, while rubbing the waveguide with a soft cloth, and rinse with a copious amount of deionized water.
- Transfer the waveguide into chromic acid heated to 110C for 10 to 20 minutes.
- Rinse with a copious amount of deionized water and dry thoroughly with purified N<sub>2</sub>.

**System Integration.** The different sub-systems were developed and individually tested, however, not all of the optimum components were able to be integrated together as a system. Because a working waveguide patterned to fit the SatCon microfluidic flow cell (Chapter 9) has not yet been fabricated, it was not possible to test these two components together. Instead, the integration effort was limited to the use of the intermediate flow cell (Figure 10-2), with the GTRI waveguides described above. The effort did however integrate the testing of the PEO/Protein-A surface derivatization and the incorporation of immuno-receptors using the GTRI waveguides. The results from these laboratory experiments are described in the following sections of this chapter.

The integration of the microfluidic filter for extraction of extraneous matter was planned as a separate step, not fully integrated into the flow cell as a complete hands-off process. A gravity feed system for the extraction process was developed by Micronics, Inc and tested by SatCon (Chapter 7) using a stand-alone cartridge, where the product was collected in a reservoir. Although not executed, the plan called for the contents of the reservoir to be emptied and transferred to a flow cell for optical measurements as a separate step.

**Automated pump station.** A new computer-controlled pump station was designed and built for conducting experiments. The new automated hardware eliminated the pressure discontinuities and overall difficulty in use experienced with the single channel syringe pump used previously.

The pump station is a continuous flow source based on a modular, COTS, peristaltic (positive displacement) pump (Cole Parmer, MasterFlex Model 4111). Peristaltic pumps are known for oscillatory flow rates from the repeated compression and expansion of the tubing driving the fluid. This pump was chosen because it operates by pumping two streams in parallel, the second being 180° out of phase with the first. The two streams are mixed together to cancel out the peristaltic artifacts for a constant flow.

The pump station can handle up to six different fluids and has one or two outputs. (Independent output flow rates are obtained by varying tubing sizes at the output). Flow from any of the six inputs is independently switched from a re-circulating mode when no flow is desired to one output by means of computer controlled solenoid valves. Additionally, the 5<sup>th</sup> and 6<sup>th</sup> input can be redirected from the first to the second output. A schematic diagram of the pump function is shown below in Figure 10-5 and a photograph of the pump station is shown in Figure 10-6.

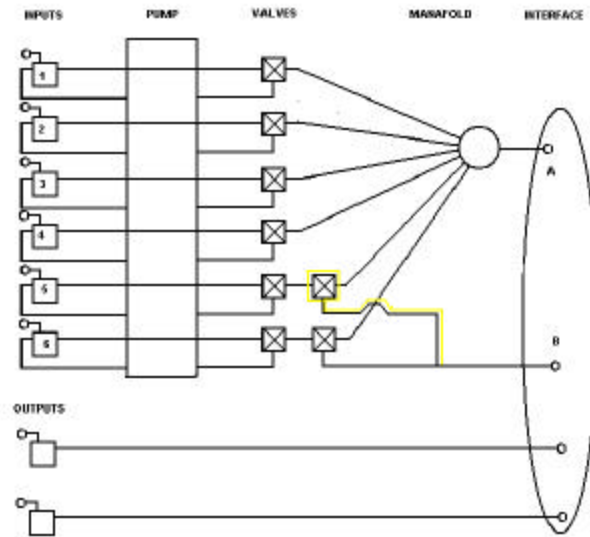


**Figure 10-5:** Schematic of automated flow station function.

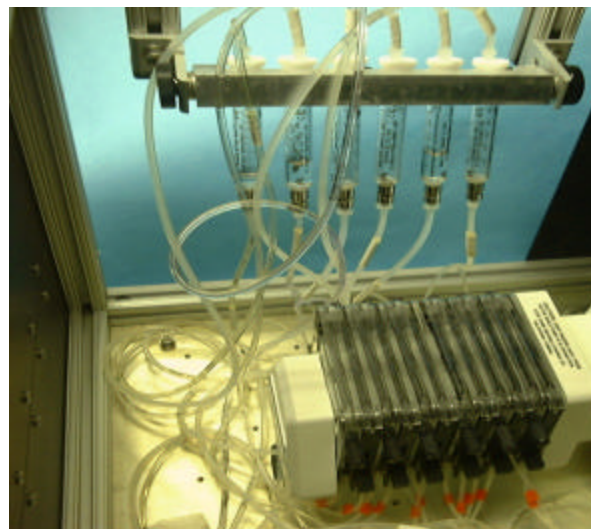


**Figure 10-6.** Photograph of peristaltic pump mounted in the automated flow station

Commands to select and control the desired fluids are input into a graphic user interface designed for transparent operation to provide accessibility to any individual. The interface allows the user to program all the information needed to conduct a complete experiment and repeat it any number of times. The resulting fluid and pump speed is plotted as a function of time. A picture of the interface is shown in Figure 10-7 below.

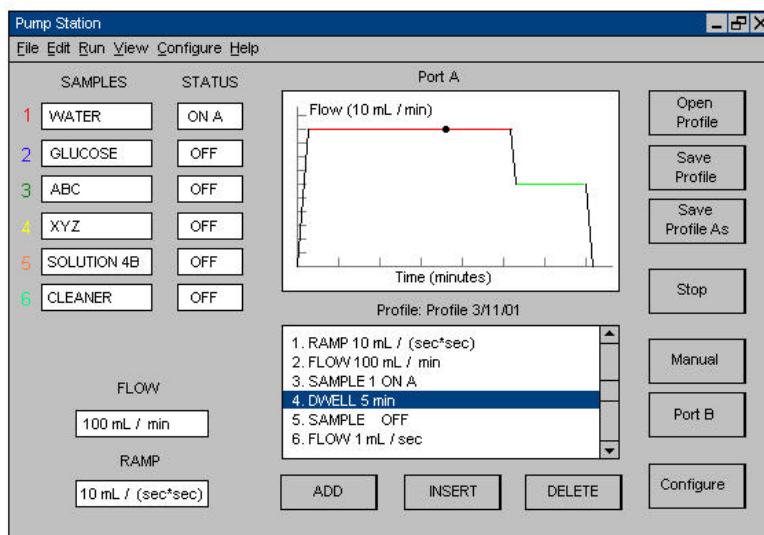


**Figure 10-7.** Computer interface for automated pump station.

## Laboratory Results

**Bulk Index Changes.** As a first test of the biosensor, the monitoring of bulk indices was undertaken to demonstrate its operation as a refractometer. For this set of experiments the computerized pump station was used to switch between the different fluids tried. Judicious choices of fluid samples were Phosphate Buffer Saline (PBS) and deionized water.

The waveguides from GTRI only allow for a reference beam that passes through the middle of the cuvette, so the experiment had to be carried out using the split flow cell. Here, deionized water was introduced into a reference cell and left static. The flow was continuous through the other target channel and controlled by the pump. This configuration allows for the comparison of refractive indices of two different fluids in a differential format, however, because the two fluids are independent they are at different temperatures thus limiting the quality of the measurement.

Figure 10-8 shows typical refractive data curve for deionized (DI) water and Phosphate Saline Buffer (PSB). Deionized water was initially flowed followed by PBS and then back to DI water. The total response was equal to 4.953 cycles; the standard deviation monitored between 1900 and 2250 seconds was calculated to be  $5.1 \times 10^{-3}$  cycles.

The difference in refractive indices can be obtained from the formula  $\Delta n = \Delta \phi \lambda / l$  where  $\lambda = 633 \times 10^{-9}$  m and  $l = 18 \times 10^{-3}$  m (the length of the active area). Plugging in these number one obtains a difference in refractive index between PBS and deionized water of  $\Delta n = 1.742 \times 10^{-4}$ .

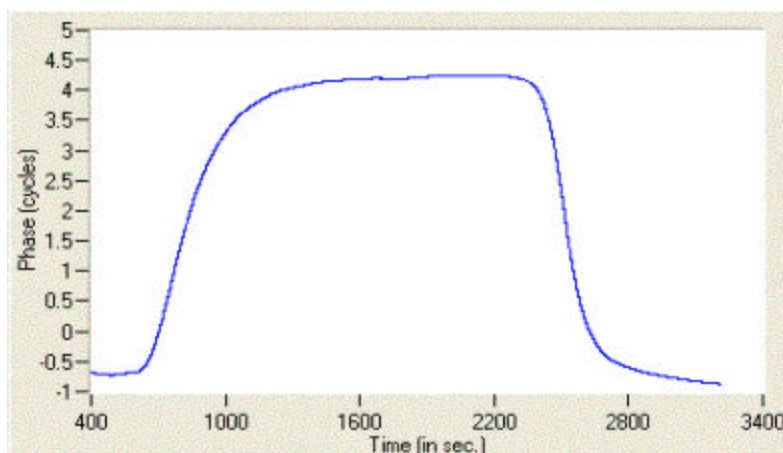


**Figure 10-8** Bulk flow of deionized water and phosphate saline buffer (PBS). The reference cell was filled with a static solution; the flow rate in the other arm was 2 ml/hr.

**Surface Detection: Protein Adsorption.** Measuring the bulk index demonstrates the ability of the interferometer to monitor volume effects but does not confirm where the phenomenon is taking place. To demonstrate that the interferometer is measuring surface phenomena, a set of experiments to monitor the non-specific adsorption of a protein was undertaken. In this way, the optical performance of the system was characterized for its sensitivity to surface bound mass. This was accomplished by coating the native nitride with Octadecyltrichlorosilane (OTS) to form a hydrophobic surface for the adsorption of a monolayer of protein and monitoring the resulting phase response. The OTS solution was provided by the Laibinis group at MIT. After a thorough cleaning, the waveguide was submerged in the OTS solution for a few hours to form a coating estimated to be tens of angstroms thick. Hydrophobicity was readily confirmed visually by observing the large contact angle of drops of water placed on the surface.

An estimate of the signal size from such an experiment was obtained from the data shown in Figure 10-9. After establishing a baseline flowing PBS, lysozyme was introduced (1350 s) and began to bind to the OTS coated surface. The initial rise in signal is due primarily to diffusion of the protein within the flow cell. (The velocity profile of the flow is laminar and thus parabolic; therefore, the flow is ‘creeping’ at the nitride surface.) The essentially linear increase from 2000 to 4000 seconds is interpreted as due the ‘creeping’ interface slowly covering the nitride surface and the accumulation of any loosely bound protein. At 4000 seconds the loosely bound protein is washed from the surface with PBS and a monolayer of lysozyme molecules remain bound to the surface.

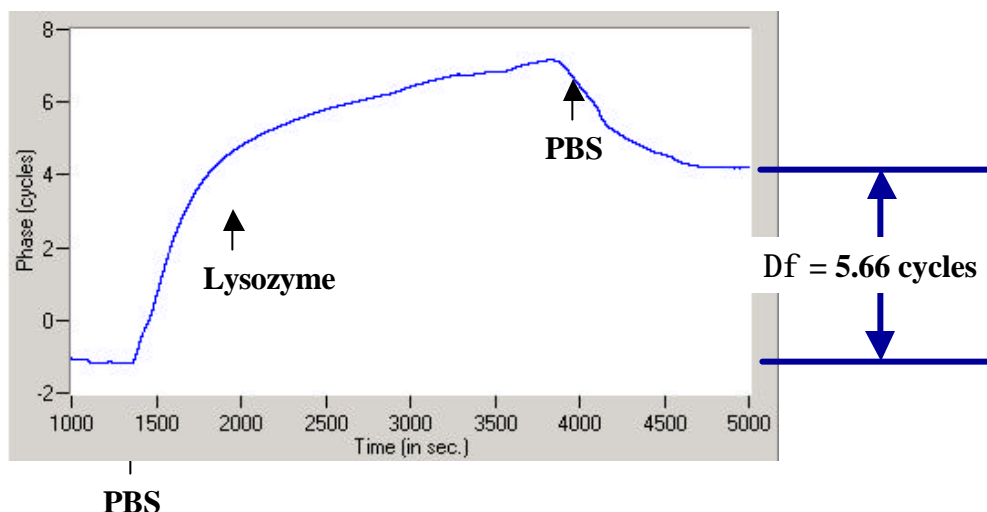


**Figure 10-9.** Non-Specific Binding. These data show the amount of phase shift from non-specifically bound lysozyme adsorbed onto an 18 mm<sup>2</sup> hydrophobic surface. At 4000 sec the surface was washed removing any loose or unbound protein. The response from the remaining bound protein is 5.66 cycles, which is assumed to be due to a monolayer of lysozyme coating of active region.

The total mass of the assumed adsorbed monolayer of lysozyme is estimated to be approximately 2.1 ng/mm<sup>2</sup> corresponding to a response of 371 (pg/mm<sup>2</sup>)/cycle. The standard deviation of the signal between 4500 and 5000 seconds was calculated (to accurately portray any 1/f noise from the bound surface) as  $\sigma_\phi \sim 6 \times 10^{-3}$  cycles and used as the detection threshold. These data are shown in expanded form in Figure 10-10. The mass detection threshold is obtained by multiplying  $\sigma_\phi$  by the responsivity to get:  $\sigma_{\text{Mass}} \sim 2$  pg/mm<sup>2</sup> for these data. Extrapolating this measurement to a baseline of  $\sigma_\phi \sim 10^{-6}$  cycles (the goal of the doubly differential configuration) suggests a detection threshold of 0.4 fg/mm<sup>2</sup>.

*Discussion.* The average flow rate for this experiment was 50  $\mu$ l/min through a 4.5  $\mu$ l chamber volume (15 mm long x 3 mm wide x 0.1 mm high) thus the total transit time for a plug of fluid is 3.6 seconds. However, the rise time of this binding response is ~500 seconds and the signal was increasing for several thousand seconds. The microfluidic character of the flow necessitates that the flow rate is laminar and therefore its corresponding velocity profile is parabolic. This means that the flow rate at interaction surface (assume the OTS coating is 10 nm thick) is creeping at the value of 0.0017 mm/s so that while the fluid at the center of the flow cell is moving at maximum speed (4.17 mm/s), the lysozyme-PBS interface at the interaction surface is creeping along at a rate 2453 times slower! Thus the binding interactions for small proteins (in contrast to cells) is dominated by diffusion.

The diffusion length can be estimated with the equation

$$l \approx \sqrt{Dt}$$

where D is the diffusion constant and t is the time for a molecule to traverse the length of the flow cell. The diffusion constant was calculated using the CLAMP program available for free

from the University of Utah<sup>1</sup> {ref}. For lysozyme at 25 C the value of  $D = 1.5 \times 10^{-5} \text{ cm}^2/\text{s}$ ; the relevant diffusion length is  $\sqrt{(1.5 \times 10^{-5})(5.5 \text{ s})} = 93 \text{ }\mu\text{m}$  or the approximate height of the flow cell confirming diffusion as the main transport mechanism for binding.

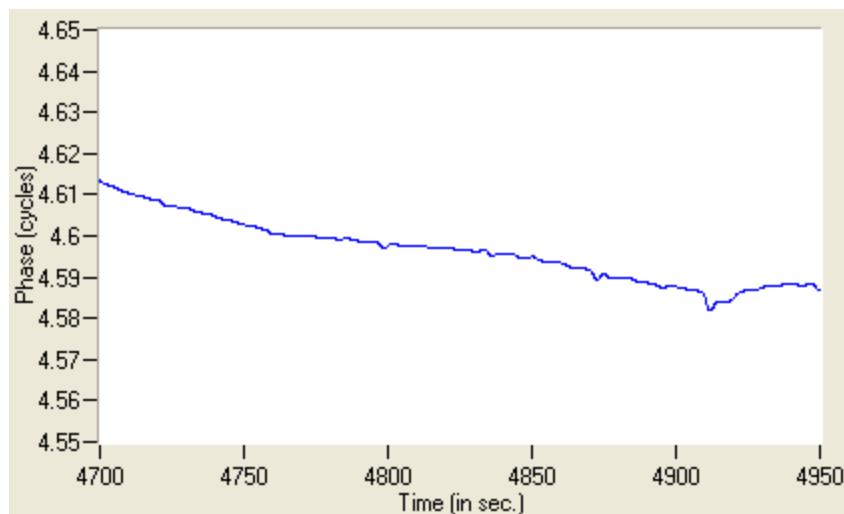


**Figure 10-10.** Detection Threshold. The baseline was determined with a signal from bound molecules to accurately portray any  $1/f$  noise from the bound surface. The standard deviation was calculated to be  $\sigma_p \sim 6 \times 10^{-3}$  cycles.

**Specific Binding.** The next set of experiments were undertaken to incorporate the receptor system developed and demonstrate the specific capture of a protein. A logical choice for this is lysozyme allowing a comparison with the previous non-specifically bound lysozyme data from Figure 10-11. Once again a single flow cell chamber covered both channels so that the reference channel is subjected to the same flow stream encouraging common mode rejection between to two.

It was found that the syringe pump arrangement was more effective for this set of experiments because of its ability to operate at very low flow rates combined with its ease in cleaning.

Two waveguides were delivered to MIT for surface modification. The waveguides were derivatized in bulk with the self-assembled monolayer of PEO thus the entire waveguide surface was coated. Next the ‘split’ flow cell was mounted on the waveguide to be able to operate on each cuvette independently. For this experiment it was desired to attach Protein-A on only one of the cuvettes. After surface activation followed by incubation with Protein-A the waveguides were returned to SatCon for further experimentation.

The waveguide was next mounted in the interferometer while keeping the surface wet and mounting the flow cell to contain a solution of PBS during alignment and other preparation steps.

<sup>1</sup> Morton & Myszka (1998) *Methods Enz.*, 295, 268-294

Anti-lysozyme (Biodesign, Kennebunkport, MA) at a dilution of 1:50 was flowed at a rate of 3 ml/hr for a typical period of one hour followed by a wash step with PBS. The binding was usually observable with the biosensor.

Next, a 1-2 mg/ml solution of lysozyme (Sigma, St. Louis, MO) was prepared and loaded into the syringe pump. The experiment was started with the flow of PBS to establish a baseline. Variations at the onset were typically seen requiring tens of minutes to settle. These are interpreted as thermal perturbations resulting from the temperature differential between the fluid, the flow cell, and the waveguide material. Although the apparatus was enclosed by 1.5" insulating foam, the mechanical instabilities of this setup still dominate. After a stable baseline was established the flow was switched over to the lysozyme solution. A similar response to the non-specific case was observed.

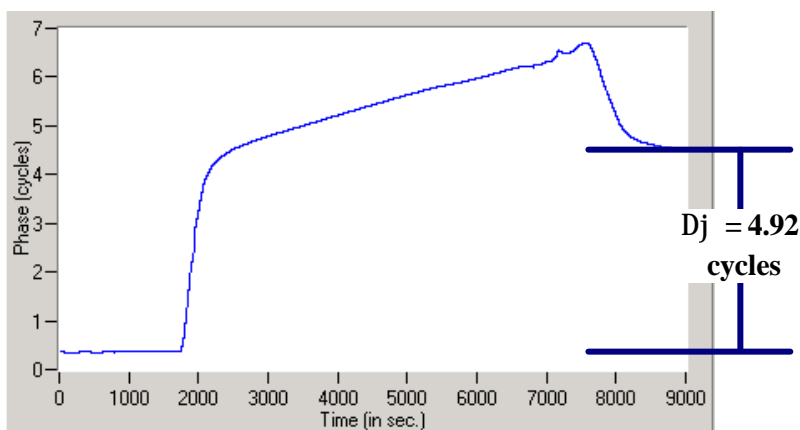


**Figure10-11.** Specific Binding of Lysozyme.

**Discussion.** Two data sets have been obtained for the binding of the small protein lysozyme. In the first experiment a monolayer of adsorbed protein was formed and in the second the biomolecule was specifically bound to an immobilized affinity probe. The magnitude of the response for the specific case (4.92 cycles) is 87% smaller than for the non-specific case (5.66 cycles). Based on earlier studies of the active coverage of the protein-A, estimates based on fluorescence were 30-40% active coverage. Combining this estimate with the fact that two binding sites are available per antibody a value between 60-80% was anticipated in marginal agreement with the actual data. Differences could be attributed to

- Improved coverage of Protein-A,
- Use of different waveguides having different sensitivities
- Non-specific adsorption is less than the assumed 100% coverage
- Non-specific binding on the reference region.

**Suppression of Non-Specific Binding.** A measurement of the adsorption from BSA onto the PEO self-assembled monolayer surface developed by the MIT group was made as a further demonstration of its ability to resist non-specific binding of proteins. This measurement was carried out using the 'split' flow cell containing two separated flow cells and allowing a different flow stream for each cuvette.

The cuvette for the reference arm was filled with a static solution of PBS + 0.1% Tween 20 while the a 1 mg/ml solution of BSA in PBS + 0.1% Tween 20 was continuously flowing in the other cuvette. A plot of the data is shown in Figure 10-12. PBS was flowed to establish a baseline and then the BSA mixture was introduced (1300 s). A response of 0.85 cycles is observed from a combination of both the change in index from the bulk solution as well as any BSA bound to the surface. Note that for typical experiments such as those from Figure 10-9 the bulk index is optically subtracted and the response from adsorption only would be seen. At 3200 s the surface is washed with PBS and the signal is seen to return to the baseline indicating a 'Teflon'-like surface consistent within the experimental uncertainty of virtually no bound protein.

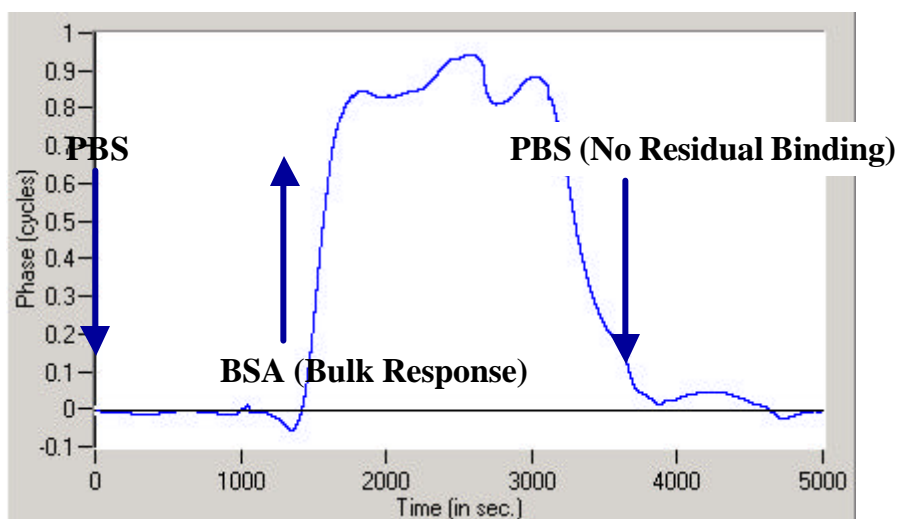
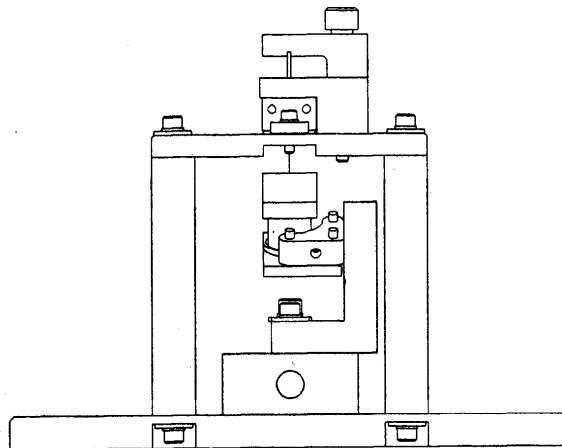
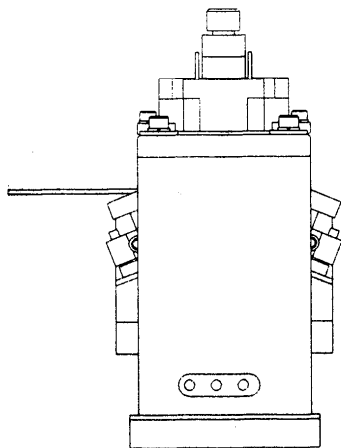
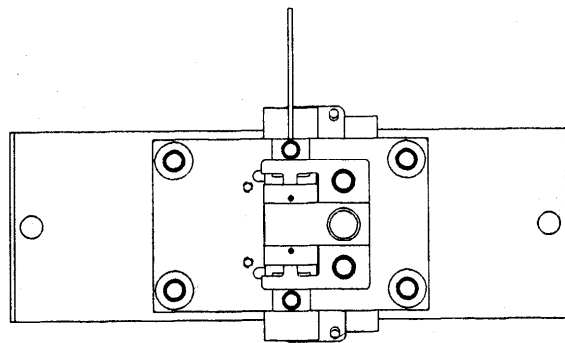
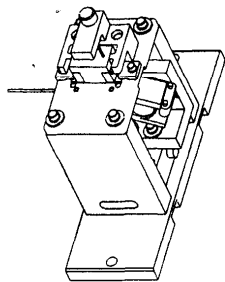
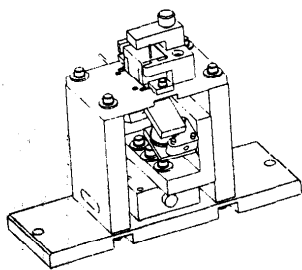


**Figure 10-12.** Adsorption of BSA onto a self-assembled monolayer of polyethylene oxide. For the reference channel, the cuvette volume was filled with PBS buffer in a stopped flow configuration.

**Cell Detection Effort.** Several attempts were made to monitor the specific binding of cells. These efforts were thwarted by the limited performance of the GTRI waveguides used for these experiments. Six waveguides were obtained from GTRI. Of these six, three were of high quality and three were of marginal quality. Unfortunately, during the integration process the three highest quality waveguides were destroyed through handling and only the marginal waveguides that suffered from low throughput and scattering were available for these experiments. The two best remaining waveguides were evaluated and brought to MIT for protein-A attachment. Once again the 'split' flow cell was used to pattern the waveguide immobilizing Protein-A on one cuvette only. The waveguide was then placed on the optical fixture and very significant attempts were made to couple light into and out of these waveguides with no success. The observed results were an irregular distribution over a wide angular range, the result of severe scattering. This was in contrast to the well defined tight beam spot typically seen in all previous experiments. Both waveguides were tried with the same results and the experiment was finally abandoned.

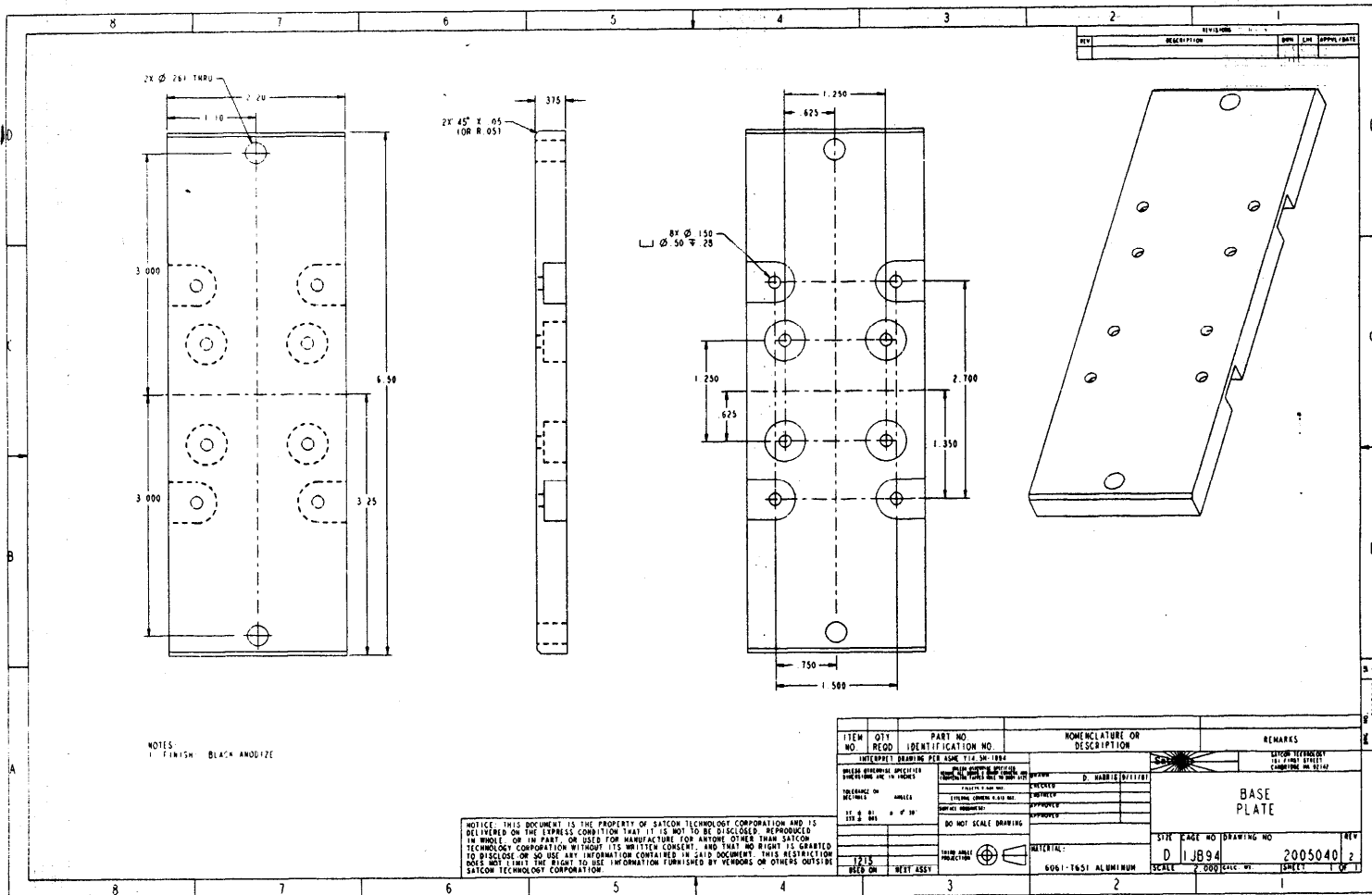
**Summary.** Preliminary laboratory characterization of the evanescent detection technique was performed using waveguides provided by the GTRI group. The basic interfacing of the flow cell and the waveguides was accomplished. The laboratory systematically demonstrated the operation of a device as a refractometer. Next, the non-specific adsorption of lysozyme was monitored confirming its ability to respond to surface phenomena. Finally, the waveguide interferometer was combined with the Protein-A/PEO derivitized surfaces incubated with anti-lysozyme to demonstrate the specific capture of a protein. Although it was not possible to obtain measurements of bacteria, a noise threshold of  $2 \text{ pg/mm}^2$  was obtained with this system inferring a threshold of  $\text{sub-fg/mm}^2$  once the doubly differential interferometer is operational.

# **Appendix 10-A: Mechanical Drawings for Waveguide-Flow Cell Mounting Fixture**



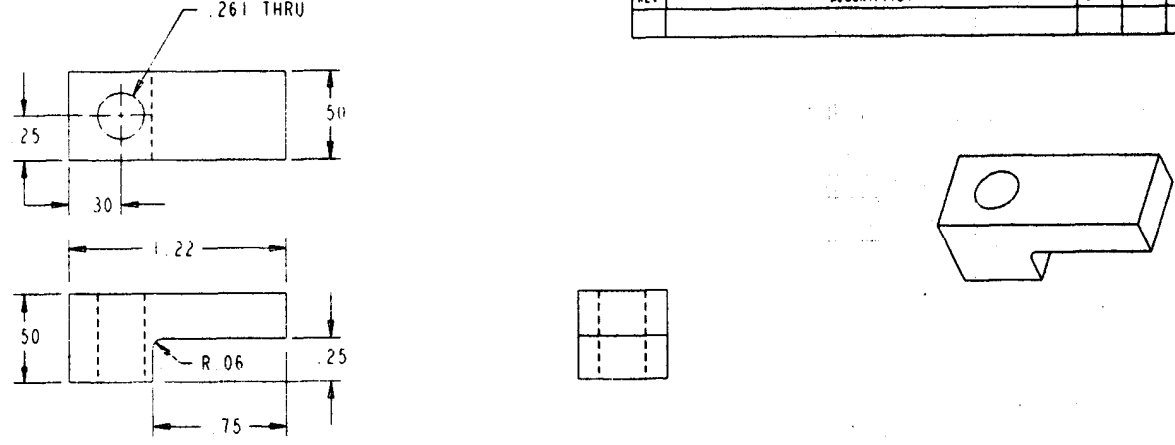
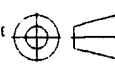




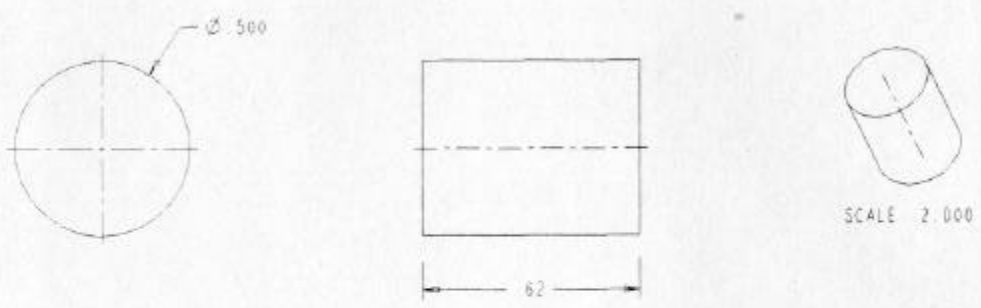




NOTICE: THIS DOCUMENT IS THE PROPERTY OF SATCON TECHNOLOGY CORPORATION AND IS LOANED TO YOU IN THE EXPRESS CONDITION THAT IT IS NOT TO BE DISCLOSED, REPRODUCED, COPIED, OR IN PART OR USED FOR MANUFACTURE FOR ANYONE OTHER THAN SATCON TECHNOLOGY CORPORATION WITHOUT ITS WRITTEN CONSENT, AND THAT NO RIGHT IS GRANTED TO DISCLOSE OR SO USE ANY INFORMATION CONTAINED IN THIS DOCUMENT. THIS RESTRICTION DOES NOT LIMIT THE RIGHT TO USE INFORMATION FURNISHED BY PERSONS OR OTHERS OUTSIDE SATCON TECHNOLOGY CORPORATION.

4		3		2		1	
DWG. NO 2005042				SH 1		1	
REVISIONS							
REV		DESCRIPTION				DWN CHK APPVL/DATE	
							
A							
ITEM NO		QTY REQD		PART NO. IDENTIFICATION NO.		NOMENCLATURE OR DESCRIPTION	
						REMARKS	
						SATCON TECHNOLOGY 161 FIRST STREET CAMBRIDGE MA 02142	
NOTICE: THIS DOCUMENT IS THE PROPERTY OF SATCON TECHNOLOGY CORPORATION AND IS DELIVERED ON THE EXPRESS CONDITION THAT IT IS NOT TO BE DISCLOSED, REPRODUCED IN WHOLE OR IN PART, OR USED FOR MANUFACTURE FOR ANYONE OTHER THAN SATCON TECHNOLOGY CORPORATION WITHOUT ITS WRITTEN CONSENT. AND THAT NO RIGHT IS GRANTED TO DISCLOSE OR SO USE ANY INFORMATION CONTAINED IN SAID DOCUMENT. THIS RESTRICTION DOES NOT LIMIT THE RIGHT TO USE INFORMATION FURNISHED BY VENDORS OR OTHERS OUTSIDE SATCON TECHNOLOGY CORPORATION.		UNLESS OTHERWISE SPECIFIED DIMENSIONS ARE IN INCHES TOLERANCE ON		UNLESS OTHERWISE SPECIFIED REMOVE ALL BURRS & SHARP CORNERS AND COUNTERSINK TAPPED HOLE TO BODY SIZE		DRAWN D. HARRIS 3/26/02	
		DECIMALS XX ± .01 XXX ± .005		ANGLES ± 0° 30'		CHECKED	
						ENGINEER	
						APPROVED	
						APPROVED	
				DO NOT SCALE THIS DRAWING			
		THIRD ANGLE PROJECTION				MATERIAL	
		4001		1002499		ALUMINUM 6061-T6	
		USED ON		NEXT ASSY			
SIZE		CAGE NO.		DRAWING NO.		REV	
B		1JB94		2005042		2	
SCALE		2.000		SHEET		1 OF 1	
4		3		2		1	

DWG. NO.		2005043		SR	1	REVISONS	
REV	DESCRIPTION				DWN	CHK	APPV/DATE



ITEM NO.	QTY REQD	PART NO. IDENTIFICATION NO.	NOMENCLATURE OR DESCRIPTION	REMARKS
INTERPRET DWG PER ASME Y14.5M-1994				
NOTICE: THIS DOCUMENT IS THE PROPERTY OF SATCON TECHNOLOGY CORPORATION AND IS LOANED TO YOU FOR YOUR INFORMATION ONLY. IT IS NOT TO BE REPRODUCED, COPIED, OR USED FOR MANUFACTURE FOR ANYONE OTHER THAN SATCON TECHNOLOGY CORPORATION WITHOUT ITS WRITTEN CONSENT. AND THAT NO RIGHT IS GRANTED TO REPRODUCE OR TO USE ANY INFORMATION CONTAINED IN THIS DOCUMENT. THIS RESTRICTION DOES NOT LIMIT THE RIGHT TO USE INFORMATION FURNISHED BY MEMBERS OR OTHERS OUTSIDE SATCON TECHNOLOGY CORPORATION.		SATCON TECHNOLOGY 161 FIRST STREET CAMBRIDGE MA 02142		
UNLESS OTHERWISE SPECIFIED: DIMENSIONS ARE IN INCHES TOLERANCE ON DECIMALS: .01 ± .01 ANGLES: .01 ± .01		DRAWN: D. HARRIS 1/25/02 CHECKED: [ ] ENGINEER: [ ] APPROVED: [ ] APPROVED: [ ]		
4001 USED ON		1002499 NEXT ASSY		
THIRD ANGLE PROJECTION		MATERIAL: ALUMINUM 6061-T6		
SIZE: B		CAGE NO: 1JB94		DRAWING NO: 2005043
SCALE: 2.000		SHEET: 1 OF 1		REV: 2

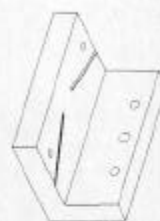
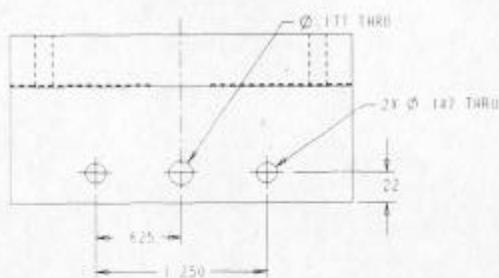
4

3

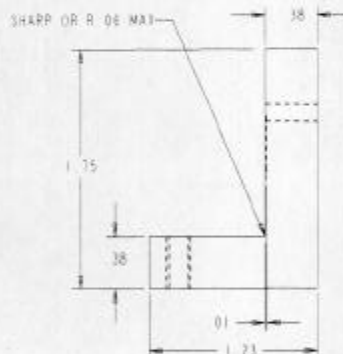
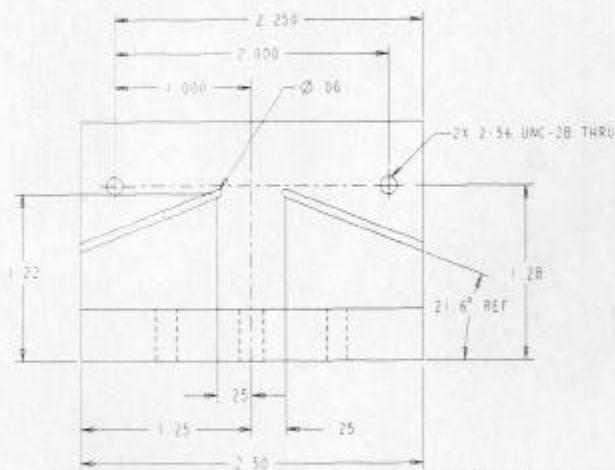
2

1

REVISIONS				
REV	DESCRIPTION	OWN	CHK	APPROV DATE



SCALE 1.000

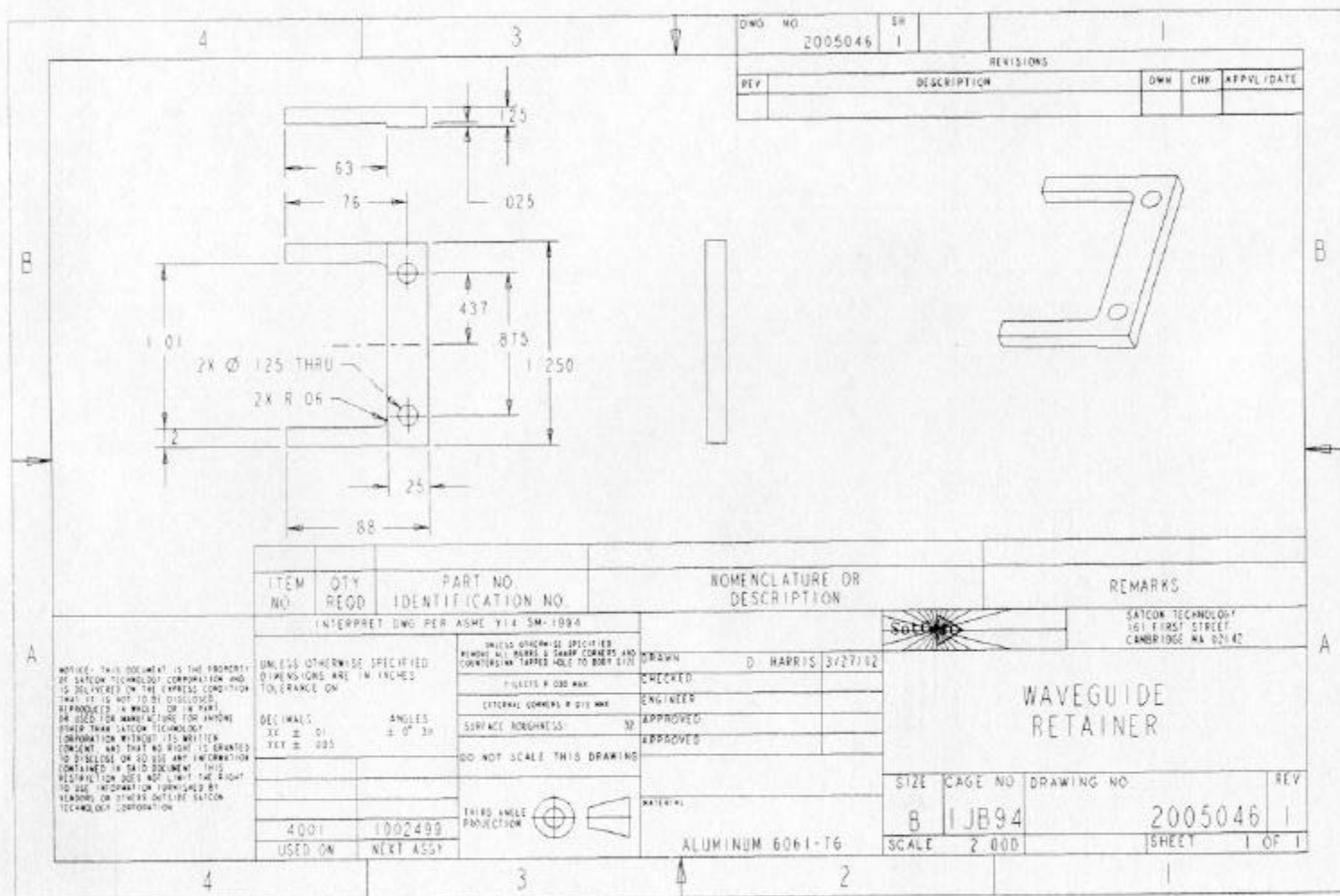


ITEM NO	QTY REQD	PART NO. IDENTIFICATION NO	NOMENCLATURE OR DESCRIPTION	REMARKS
INTERPRET DRAWING PER ASME Y14.5M-1994				
UNLESS OTHERWISE SPECIFIED DIMENSIONS ARE IN INCHES		SPECIAL DIMENSIONAL SPECIFICATIONS: DIMENSIONS ARE SHOWN UNLESS OTHERWISE SPECIFIED. DIMENSIONS ARE TO BE TO DIMENSIONS UNLESS OTHERWISE SPECIFIED.		
TOLERANCES ON		DIMENSIONS ARE SHOWN UNLESS OTHERWISE SPECIFIED. DIMENSIONS ARE TO BE TO DIMENSIONS UNLESS OTHERWISE SPECIFIED.		
DECIMALS		ANGLES		
XX.XX		± 0° 30'		
XXX.XXX		± 0° 05'		
DO NOT SCALE THIS DRAWING		DO NOT SCALE THIS DRAWING		
4001		1002489		
USED ON		NEXT ASSY		
DRAWN		D. HARRIS 3/26/00		
CHECKED		D. HARRIS 3/26/00		
EXTERNAL DIMENSIONS		EXTERNAL DIMENSIONS		
SURFACE FINISH		SURFACE FINISH		
DO NOT SCALE THIS DRAWING		DO NOT SCALE THIS DRAWING		
MATERIAL		ALUMINUM 6061-T6		
SIZE		C 1JB94		
SCALE		2.000 SCALE WT		
DRAWING NO		2005045		
REV		2		
SHEET		1 OF 1		

NOTICE: THIS DOCUMENT IS THE PROPERTY OF SATCON TECHNOLOGY CORPORATION AND IS DELIVERED ON THE EXPRESS CONDITION THAT IT IS NOT TO BE DISCLOSED, REPRODUCED, IN WHOLE OR IN PART, OR USED FOR MANUFACTURE FOR ANYONE OTHER THAN SATCON TECHNOLOGY CORPORATION WITHOUT ITS WRITTEN CONSENT. AND THAT NO RIGHT IS GRANTED TO DISCLOSE OR TO USE ANY INFORMATION CONTAINED IN SAID DOCUMENT. THIS DISTRIBUTION DOES NOT LIMIT THE RIGHT TO USE INFORMATION FURNISHED BY VENDORS OR OTHERS OUTSIDE SATCON TECHNOLOGY CORPORATION.

MIRROR MOUNT

A

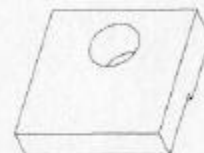
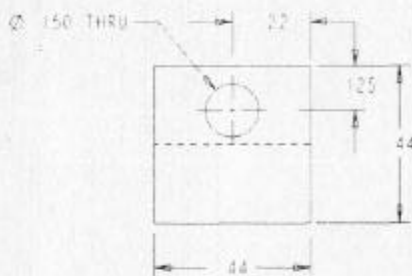


DWG NO.	2005046	SR	1	REVISIONS					
REV		DESCRIPTION	DWN	CHK	APPV	DATE			

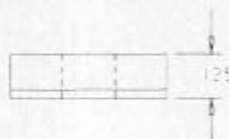
ITEM NO.	QTY REQD	PART NO. IDENTIFICATION NO.	NOMENCLATURE OR DESCRIPTION	REMARKS
INTERPRET DWG PER ASME Y14.5M-1994			SOLD	
UNLESS OTHERWISE SPECIFIED DIMENSIONS ARE IN INCHES TOLERANCE ON			SATCON TECHNOLOGY 161 FIRST STREET CAMBRIDGE MA 02142	
DECIMALS: XX ± .01 XXX ± .005			DRAWN D. HARRIS 3/27/62	
ANGLES: ± 0° 30'			CHECKED	
SURFACE ROUGHNESS: 32			ENGINEER	
DO NOT SCALE THIS DRAWING			APPROVED	
THIRD ANGLE PROJECTION			APPROVED	
MATERIAL: ALUMINUM 6061-T6			SIZE CAGE NO DRAWING NO REV	
4001 1002499			B 1JB94 2005046 1	
USED ON NEXT ASSY			SCALE 2.000 SHEET 1 OF 1	

WAVEGUIDE  
RETAINER

DWG. NO.	2005047	SR	1	REVISIONS		
REV.	DESCRIPTION			OWN	CHK	APPROVAL DATE



SCALE 4 000



ITEM NO.	QTY REQD	PART NO IDENTIFICATION NO	NOMENCLATURE OR DESCRIPTION	REMARKS
INTERPRET DWG PER ASME Y14.5M-1994				
UNLESS OTHERWISE SPECIFIED DIMENSIONS ARE IN INCHES TOLERANCE ON		UNLESS OTHERWISE SPECIFIED FINISHES ARE SHOWN IN CIRCLES AND CONTAINED TAPERS MUST TO BODY SIZE		
DECIMALS		ANGLES		
10 ± .01		± 0° 30		
100 ± .005		DO NOT SCALE THIS DRAWING		
400 ± .002		THIRD ANGLE PROJECTION		
USED ON		NEXT ASSY		
1000499		ALUMINUM 6061-T6		
1000499		DRAWN O. HARRIS 3/26/02		
1000499		CHECKED		
1000499		ENGINEER		
1000499		APPROVED		
1000499		APPROVED		
1000499		MATERIAL		
1000499		SIZE CAGE NO DRAWING NO REV		
1000499		B 1JB94 2005047 1		
1000499		SCALE 4 000 SHEET 1 OF 1		

WAVEGUIDE  
RETAINER

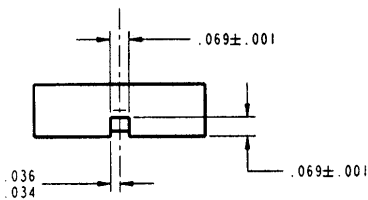
SATCON TECHNOLOGY  
161 FIRST STREET  
CAMBRIDGE MA 02142

NOTICE: THIS DOCUMENT IS THE PROPERTY OF SATCON TECHNOLOGY CORPORATION AND IS DELIVERED ON THE EXPRESS CONDITION THAT IT IS NOT TO BE DISCLOSED, REPRODUCED IN WHOLE OR IN PART, OR USED FOR MANUFACTURE FOR ANYONE OTHER THAN SATCON TECHNOLOGY CORPORATION WITHOUT ITS WRITTEN CONSENT. AND THAT NO RIGHT IS GRANTED TO DISCLOSE OR TO USE ANY INFORMATION CONTAINED IN THIS DOCUMENT. THIS RESTRICTION DOES NOT LIMIT THE RIGHT TO USE INFORMATION DISCLOSED BY MEMBERS OR OTHERS OUTSIDE SATCON TECHNOLOGY CORPORATION.

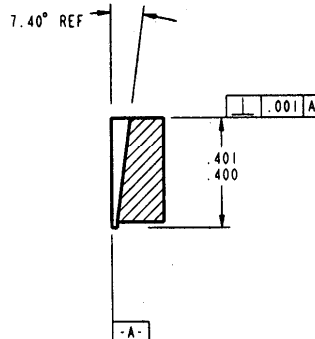
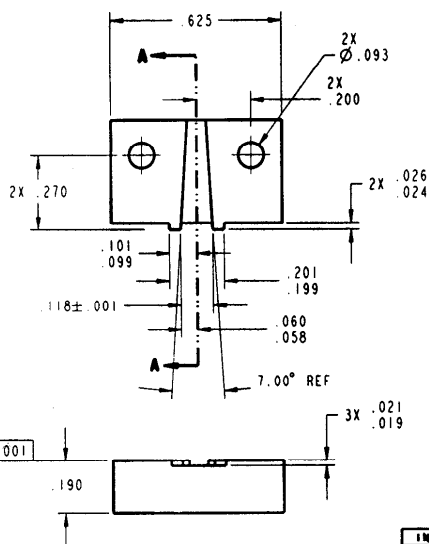
# **Appendix 10-B: Flow Cell Mechanical Drawings**

- NOTES:  
 1. MATERIAL: ULTEM.  
 2. ALL EDGES OF PART TO BE SHARP AS POSSIBLE, YET BURR-FREE.  
 3. IDENTIFY PART VIA BAG/TAG WITH PART NO. & REVISION.

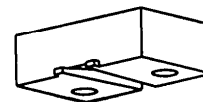
REVISIONS				
REV	DESCRIPTION	DWG	CHK	APPROV/DATE
3	PRELIMINARY 12AUG99 M.E. AMARAL			



SCALE 4.000



SECTION A-A



SCALE 4.000

SCALE 4.000

INTERPRET DRAWING PER ANSI Y14.5M-1982	
UNLESS OTHERWISE SPECIFIED DIMENSIONS ARE IN INCHES	UNLESS OTHERWISE SPECIFIED DIMENSIONS ARE IN INCHES
TOLERANCE ON	TOLERANCE ON
DECIMALS	ANGLES
.XX ± .01	± 0° 30'
.XXX ± .005	
DO NOT SCALE THIS DRAWING	
THIRD ANGLE PROJECTION	THIRD ANGLE PROJECTION

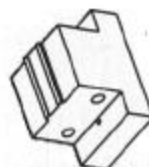
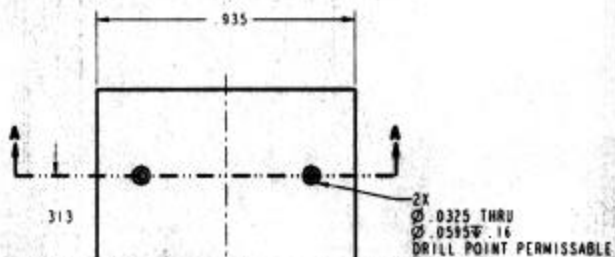
DRAWN	M.E. AMARAL 15JUN99
CHECKED	
DESIGNED	
APPROVED	
APPROVED	
SEE NOTES	

SATCON TECHNOLOGY 101 FIRST STREET CAMBRIDGE MA 02142	
FLOW CHANNEL NO1, FLOW CELLS NO1 & NO2	
SIZE	CAGE NO. DRAWING NO.
C	IJB94
SCALE	CALC WT.
5.000	
SHEET	1 OF 2
REV	4
FC001	

NOTICE: THIS DOCUMENT IS THE PROPERTY OF SATCON TECHNOLOGY CORPORATION AND IS  
 DELIVERED ON THE EXPRESS CONDITION THAT IT IS NOT TO BE DISCLOSED, REPRODUCED  
 IN WHOLE OR IN PART, OR USED FOR MANUFACTURE FOR ANYONE OTHER THAN SATCON  
 TECHNOLOGY CORPORATION WITHOUT ITS WRITTEN CONSENT. AND THAT NO RIGHT IS GRANTED  
 TO DISCLOSE OR TO USE ANY INFORMATION CONTAINED IN SAID DOCUMENT. THIS INSTRUCTION  
 DOES NOT LIMIT THE RIGHT TO USE INFORMATION FURNISHED BY VENDORS OR OTHERS OUTSIDE  
 SATCON TECHNOLOGY CORPORATION.

1. MATERIAL: ULTEM.  
2. ALL EDGES OF PART TO BE SHARP AS POSSIBLE, YET BURR-FREE.  
3. IDENTIFY PART VIA BAG/TAG WITH PART NO. & REVISION.

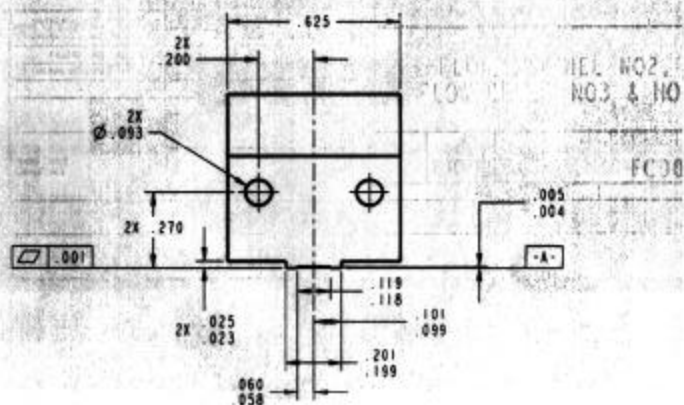
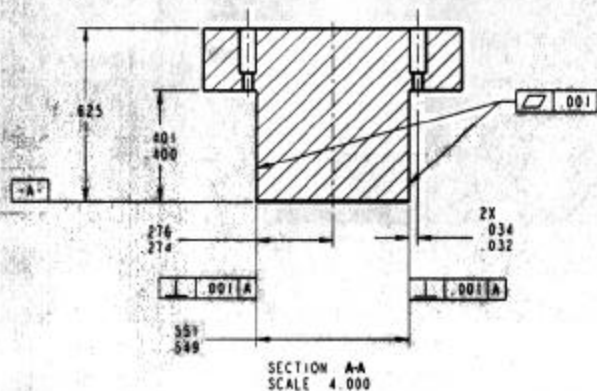
REVISED				
REV	DESCRIPTION	DOB	CM	APPROBATE
2	PRELIMINARY 12AUG99 M.E. AMARAL			



SCALE 2,000



SCALE 2.000



NOTICE: THIS DOCUMENT IS THE PROPERTY OF SATECON TECHNOLOGY CORPORATION AND IS  
 LOANED TO YOU ON THE EXPRESS CONDITION THAT IT IS NOT TO BE REPRODUCED, REPRODUCED  
 IN WHOLE OR IN PART, OR USED FOR MANUFACTURING FOR ANYONE OTHER THAN SATECON  
 TECHNOLOGY CORPORATION WITHOUT ITS WRITTEN CONSENT, AND THAT NO RIGHT IS GRANTED  
 TO ANYONE OR TO DO ANY INFORMATION CONTAINED IN THIS DOCUMENT. THIS RESTRICTION  
 DOES NOT LIMIT THE RIGHT TO THE INFORMATION FURNISHED BY YOU OR OTHERS OUTSIDE  
 SATECON TECHNOLOGY CORPORATION.

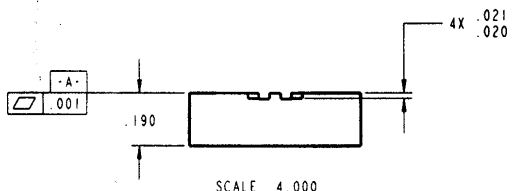
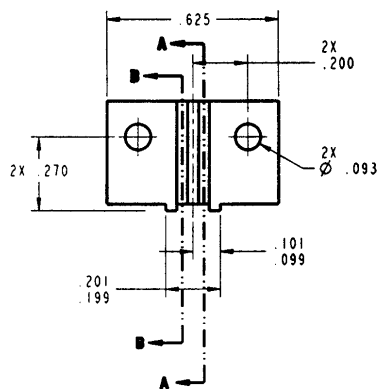
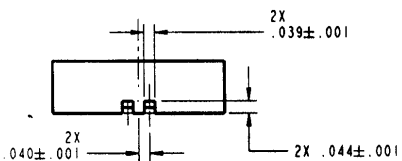
CHANNEL INTERFACE,  
FLOW CELL NO2

SIZE	CASE NO.	DRAWING NO.	REV
C	IJB94	FC003	3
SCALE	5.000	CALC BY	DATE

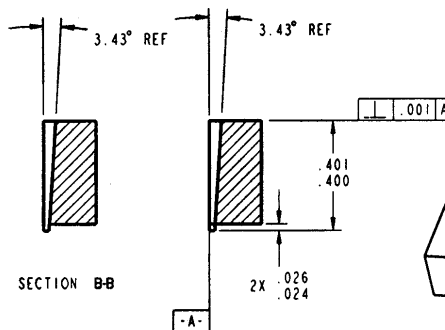
NOTES:

1. MATERIAL: ULTEM.
2. ALL EDGES OF PART TO BE SHARP AS POSSIBLE, YET BURR-FREE.
3. IDENTIFY PART VIA BAG/TAG WITH PART NO. & REVISION.

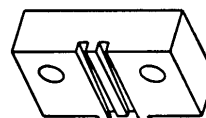
3 PRELIMINARY 12AUG99 M.E. AMARAL



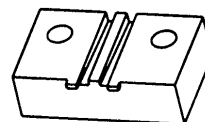
SCALE 4.000



SECTION A-A



SCALE 4.000



SCALE 4.000

		M. E. AMARAL 15 JUL 99		FLOW CHANNEL NO2, FLOW CELLS NO3 & NO4	
PULSED CURRENT SOURCE EXEMPT FROM GDSN EXEMPT FROM GDSN					
F L A T T E N E D WAVE					
EXEMPT FROM GDSN					

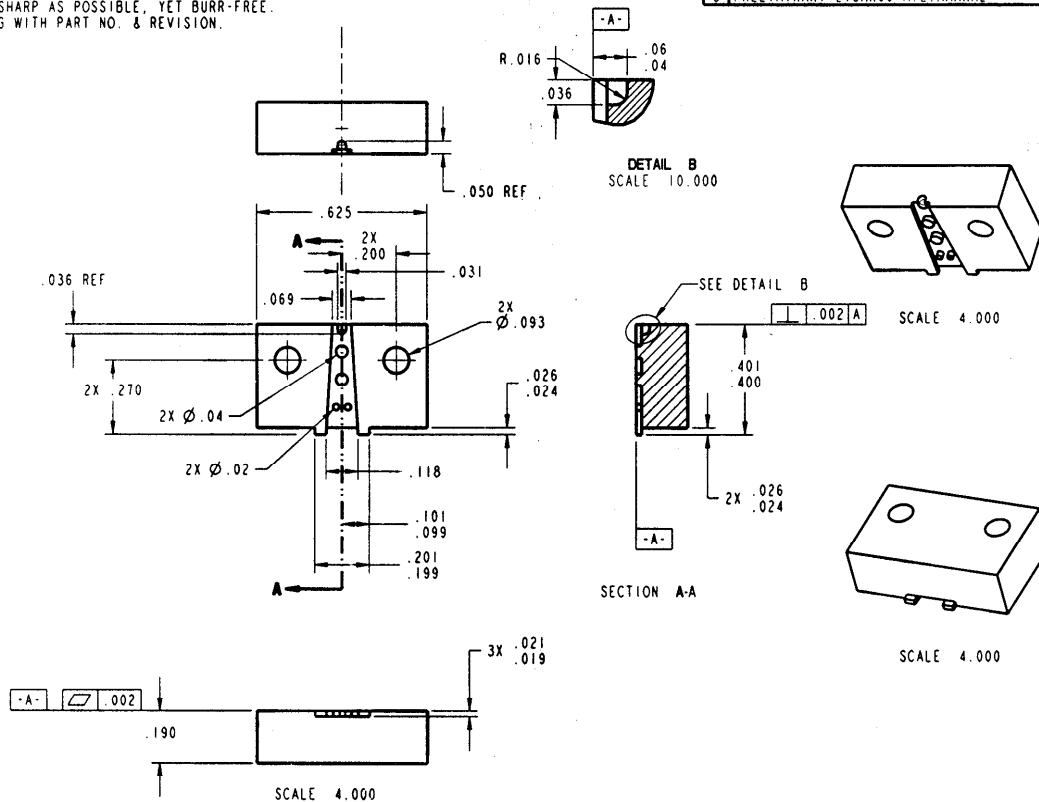
FC004 1



# NOTES

1. MATERIAL: ULTEM 1000
2. ALL EDGES OF PART TO BE SHARP AS POSSIBLE, YET BURR-FREE.
3. IDENTIFY PART VIA BAG/TAG WITH PART NO. & REVISION.

REVISIONS				
REV	DESCRIPTION	DWN	CHE	APPLY/DATE
3	PRELIMINARY 21 JAN 00 M.E. AMARAL			



## INTERPRET DRAWING PER ANSI Y14.5M-1982

UNLESS OTHERWISE SPECIFIED  
DIMENSIONS ARE IN INCHES  
TOLERANCE ON  
DECIMALS .01  
ANGLES 0° 30'

UNLESS OTHERWISE SPECIFIED  
DIMENSIONS ARE IN INCHES  
TOLERANCE ON  
DECIMALS .01  
ANGLES 0° 30'

DESIGNED BY M.E. AMARAL 15 JUL 99  
CHECKED  
DRAWN  
APPROVED  
DO NOT SCALE THIS DRAWING

SALCON TECHNOLOGY 181 FIRST STREET CAMBRIDGE MA 02142	
FLOW CHANNEL NO1, FLOW CELLS NO1 & NO2	
SIZE C	DRAWING NO. IJB94
SCALE 5.000	CALC WT. FC007 3
SHEET 1 OF 2	

NOTICE: THIS DOCUMENT IS THE PROPERTY OF SALCON TECHNOLOGY CORPORATION AND IS  
DELIVERED ON THE EXPRESS CONDITION THAT IT IS NOT TO BE DISCLOSED, REPRODUCED  
IN WHOLE, OR IN PART, OR USED FOR MANUFACTURE FOR ANYONE OTHER THAN SALCON  
TECHNOLOGY CORPORATION WITHOUT ITS WRITTEN CONSENT, AND THAT NO RIGHT IS GRANTED  
TO DISCLOSE OR TO USE ANY INFORMATION CONTAINED IN THIS DOCUMENT. THIS RESTRICTION  
DOES NOT LIMIT THE RIGHT TO USE INFORMATION FURNISHED BY VENDORS OR OTHERS OUTSIDE  
SALCON TECHNOLOGY CORPORATION.

SEE NOTES

## Chapter 11 : Application to Food System Testing.

**Food System Testing.** The goal of the effort was the application of the SatCon evanescent wave biosensor to the detection of foodborne pathogens. This work was intended to be subcontracted to Dr. Jianming Ye in the Department of Food Science and Nutrition at the University of Rhode Island. However, because of internal problems within URI (i.e. the dissolution of the research group) URI was forced to refuse the subcontract. Drs. Andre Senecal and Phillip Pivarnic at the U.S. Army Soldier and Biological Chemical Command, Soldier System Command, Natick, MA subsequently agreed to complete the work intended for URI.

Three experiments were planned to accomplish this effort:

1. Verify binding of the model antibody-antigen systems.
2. Develop sampling methods to recover *S. aureus*, staphylococcal enterotoxins, and *E. coli* O157:H7 from food extracts and clarify the extracts that will be introduced into the microfluidic circuitry of the SatCon system.
3. Evaluate the performance of the sensor for *S. aureus*, *E. coli* O157:H7, and staphylococcal enterotoxins in spiked food samples.

The completion of all three tasks was impeded by the unavailability of waveguides to make any optical measurements. Nonetheless, Experiments 1 and 2 were planned and are described below. In Experiment 1, progress was made toward the verification of the model system, but this experiment was hampered by the logistics of transferring biological substances onto a US Army base during a time of heightened security.

Additionally, the non-specific binding of three food systems spiked with *E. coli* O30 onto the PEO-Protein-A coated surfaces was monitored.

The model systems intended for this effort were:

### Food-borne Pathogens and Toxin:

- *E.coli* O157 cells & (Anti-*E. coli* O157 antibody, KPL Inc. Gaithersburg, MD))
- *S.aureus* cells & (Anti-*S. aureus* polyclonal antibody, ViroStat Portland, ME)
- *S. enterotoxin A* (SEA) & (Anti-SEA polyclonal antibody, Toxin Technology, Inc. Sarasota, FL)

### Food Matrices:

- Low lipid content (apple/lettuce)
- Medium lipid content (milk)
- High lipid content (burrito/ground beef)

All testing with pathogenic cell lines and toxin was performed by Dr. Pivarnic at the Natick laboratories. *S. aureus*, purchased from ATTC (Manassas, VA) was sent directly to the Natick

facility; *E.coli* 0157 and SEA were already available in-house to Dr. Pivarnic. The corresponding antibodies listed above were purchased and stored at SatCon.

## Description of Experiments

Confirmation of Specific Binding of the Model Systems. The first task was to verify the binding of the pathogenic target cells to the immobilized immuno-receptors and characterize the specific binding; cross reactivity, and non-specific binding of the model systems. PEO Protein-A surfaces were prepared by MIT on 18mm x 18 mm silicon chips, incubated with antibody by SatCon. All chips were immersed in PBS solution, packaged in a plastic multi-well container, and sealed thoroughly with parafilm.

A summary of the intended experiments is shown in the matrix below:

	<b>Non-Specific Binding (PEO)</b>	<b>Non-Specific Binding (PEO + Prot-A)</b>	<b>Specific Binding (PEO + Prot-A + Antibody)</b>	<b>Cross Reactivity (PEO + Prot-A + Antibody)</b>
<i>S.aureus</i> (#1)	<b>X</b>	<b>X</b>	<b>ViroStat Ab</b>	<b>ViroStat x <i>E.coli</i></b>
<i>S.aureus</i> (#2)	<b>X</b>	<b>X</b>	<b>ViroStat Ab</b>	
<i>E. coli</i> 0157	<b>X</b>	<b>X</b>	<b>KPL Ab</b>	<b>KPL Ab x <i>S.aureus</i></b>
<b>SEA</b>	<b>X</b>	<b>X</b>	<b>Toxin Tech Ab</b>	<b>Toxin Tech Ab x <i>S. aureus</i></b>

The general protocol used for these pathogen binding studies is given by:

- Incubate the respective individual silicon chips with cultured cells ( $2-4 \times 10^8$  CFU/ml) for 60 to 90 minutes.
- Remove unbound cells by washing three times for 5 min each with PBS containing 0.2% Tween-20 followed by one washing with PBS alone.
- Stain bound cells with fluorescein based live/dead stain (Syto 9, Molecular Probe, Cat #L-7007) for 15-30 min and detection of fluorescent cells under fluorescent microscope. In order to do staining, component A and component B of the staining kit are mixed in equal volumes and 5  $\mu$ l of stain mixture is added to each ml of PBS. Live cells emit green fluorescence; dead cells emit red fluorescence.
- Monitor bound cells by visualizing and counting stained cells with a fluorescent microscope, normalizing the number to estimate the amount of coverage, and comparing with initial population.

N.B.S. Enterotoxin A must be treated differently. After initial binding of SEA, a second incubation with FITC-labeled anti-SEA antibody to form a sandwich assay is needed followed by the detection of the complex fluorometrically.

*E.coli* O157 Model System. Two chips were prepared with anti-*E.coli* O157 (KPL Inc. Gaithersburg, MD) along with two control chips containing Protein-A only. All four chips were incubated at SatCon with heat killed *E.coli* O157 cells (KPL Inc. Gaithersburg, MD) and fluorescently stained for monitoring. Photographs of these fluorescent bound heat killed cells are shown in Figure 11-1. Marginal binding is seen especially when compared with the *E.coli* O30 model system (Figure 6-8). This K&P antibody has shown good success in other biosensor laboratories<sup>1</sup> and according to the manufacturer 'good binding' is routinely seen with the heat killed cells. A possible explanation for this result is that the manufacturer's studies were performed successfully by agglutination methods but the heat-killed cells have very weak affinity that is manifested in the different binding dynamics encountered with a solid support platform. Consequently, if the SatCon experiment had been performed with live cells significantly better results would have been seen.

Additional measurements were performed by Dr. Pivarnic at the Natick facility using viable *E. coli* O157:H7 cells (strain B6-914 from the CDC and also ATCC strain 43888). Antibody laden surfaces were incubated with a cell concentration of  $5.1 \times 10^7$  CFU/ml and very little binding was reported likely due to corrupted surfaces (see below).



**Figure 11-1. *E.coli* O157 Heat-Killed Cells.** Surfaces were incubated at SatCon with heat killed *E.coli* O157 cells for 2 hours. *Left:* Control surface contained active Protein-A but was not incubated with antibody; *Right:* Active Protein-A surface was incubated with anti-*E.coli* O157.

Two attempts were made to deliver these chips in working order to SBCCOM with limited success. An attempt to deliver these chips in person was thwarted by the initial confiscation due to heightened security, resulting in the eventual drying out and spoilage of the surfaces. More chips were prepared and a second attempt was made shipping the package via FedX. These chips were successfully received by Dr. Pivarnic but several surfaces were again spoiled showing cracking of the surface indicating drying had occurred.

*S. aureus* Model System. Again two Protein-A chips were incubated with anti-*S. aureus*, and the two others were not and used as controls. All four chips were incubated with *Staphylococcus aureus* (ATCC strain 13567) at concentration of  $6.5 \times 10^7$  CFU/ml. The surfaces were stained

---

<sup>1</sup> D. Lim, Univ. S. Fl, Tampa, FA, *Private Communication.*, 2001.

with fluorescence (Live/Dead, Molecular Probes) and visualized with a fluorescent microscope. Images were obtained with a magnification of 400X through a #1 coverslip. The CCD camera on our microscope was designed for taking bright field images and doesn't work as well with the low light fluorescent images. The *Staphylococcus aureus* control chip (Figure 11-2 Left) had a few areas of high concentration and more areas of lower concentration. The *Staphylococcus aureus* IgG chip (Figure 11-2, Right) had many more areas of high concentration showing single, double and some small clusters of cells, a characteristic of *Staphylococcus aureus*. A quantitative estimate was difficult to make due to the irregularity of the cell density and small field of view.

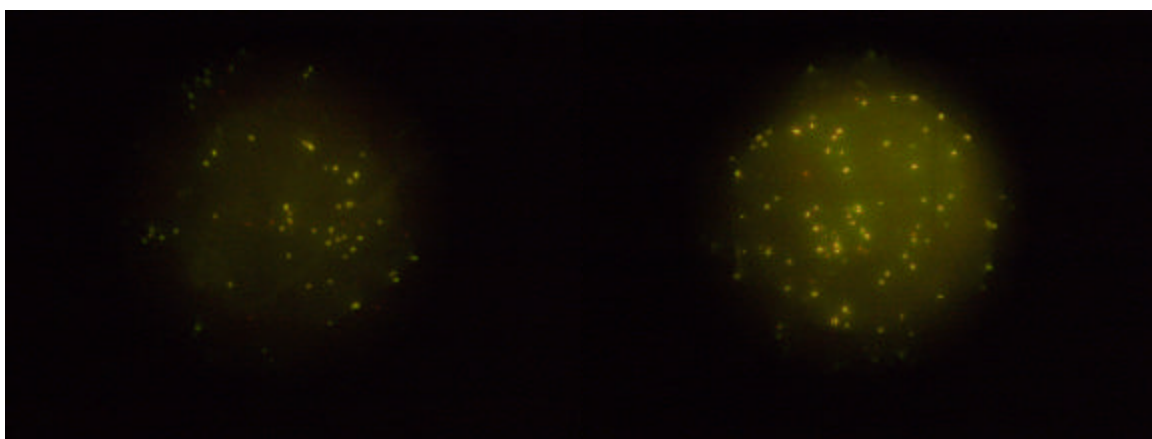


**Figure 11-2.** Results of *S.aureus* Model System. Surfaces were incubated with *Staphylococcus aureus* (ATCC strain 13567) at concentration of  $6.5 \times 10^7$  CFU/ml and stained with fluorescence for visualization.. *Left:* Protein-A control surface (no IgG receptors); *Right:* Protein-A surface was incubated with anti-*S.aureus*.

**Capture from Spiked Food Matrices.** A demonstration of the specific binding of *E.coli* O157, *S. aureus* and SEA in spiked food samples was planned but not executed. Spiked and non-spiked food samples were to be provided by the Natick laboratories. For each food system both non-specific and specific binding must be checked. For each food matrix a total of 12 incubated chips (PEO surfaces with Protein-A and antibodies) are required. A summary of these experiments is shown below.

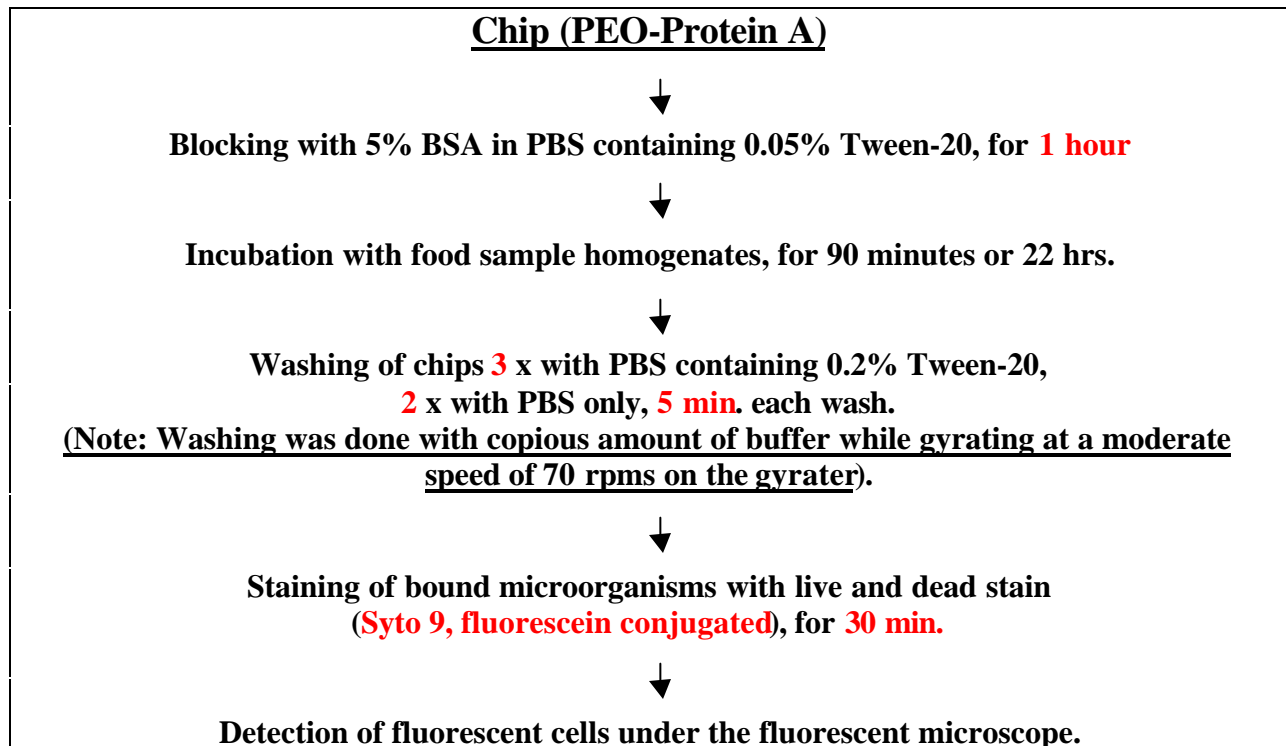
	Food Matrix – Unspiked (PEO + Prot-A)	Food Matrix – Spiked (PEO + Prot-A)	Food Matrix – Unspiked (PEO + Prot-A + Antibody)	Food Matrix – Spiked (PEO + Prot-A + Antibody)
<i>E. coli</i> 0157	X	X	KPL Ab	KPL Ab
<i>S.aureus</i>	X	X	ViroStat	ViroStat
SEA	X	X	Toxin Tech Ab	Toxin Tech Ab

**Non-Specific Binding (NSB) of Food Samples.** Previous NSB testing of cells onto PEO surfaces was conducted with our *E.coli* 030 model system and found to be void of any non-specific binding. We have repeated these tests with food samples prepared by Dr. Phillip Pavarnic at the Army SBCCOM facility in Natick, MA; PEO/Protein-A coated surfaces were provided by the Labinis lab at MIT. The homogenates of the food samples namely, bread, clam chowder and BBQ brisket were kept frozen at  $-20^{\circ}\text{C}$  until analyzed. PEO-coated chips with and without Protein-A were incubated with the food homogenates for either 90 min or 20-22 hours at room temperature as outlined in the protocol description below. The presence of any surface binding of the microorganisms was determined by fluorescent staining and visual monitoring.

Significant non-specific binding of microorganisms to the PEO-coated surfaces in the presence as well as in the absence of Protein-A was observed and is shown in Figure 11-3. Much of this binding has subsequently been determined to be caused by yeasts and mold likely originating from the building air conditioning system. Additional experiments are needed to determine the exact cause of this binding. However, it is strongly suspected that the NSB cells and food fibers are attaching to proteins and lipids, non-specifically coating the chip surface. It is important to note that these tests were performed as benchtop experiments in small gyrating containers. These conditions are significantly different from the dynamics of the flow stream that will be encountered within the flow cell.

The protocol used for these experiments is provided below:

**Detection of the non-specific binding of microorganisms present in the food samples with or without Protein-A coupled to PEO surfaced chips.**



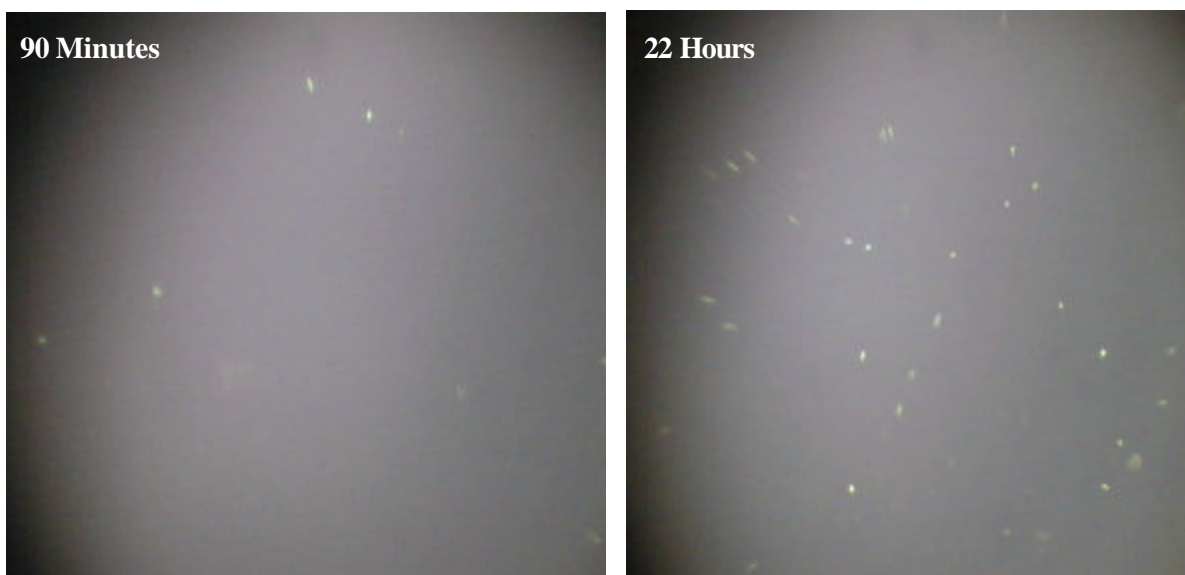


**Figure 11-3a:** Non-specific binding of microorganisms in the bread homogenate with PEO-Protein-A chips

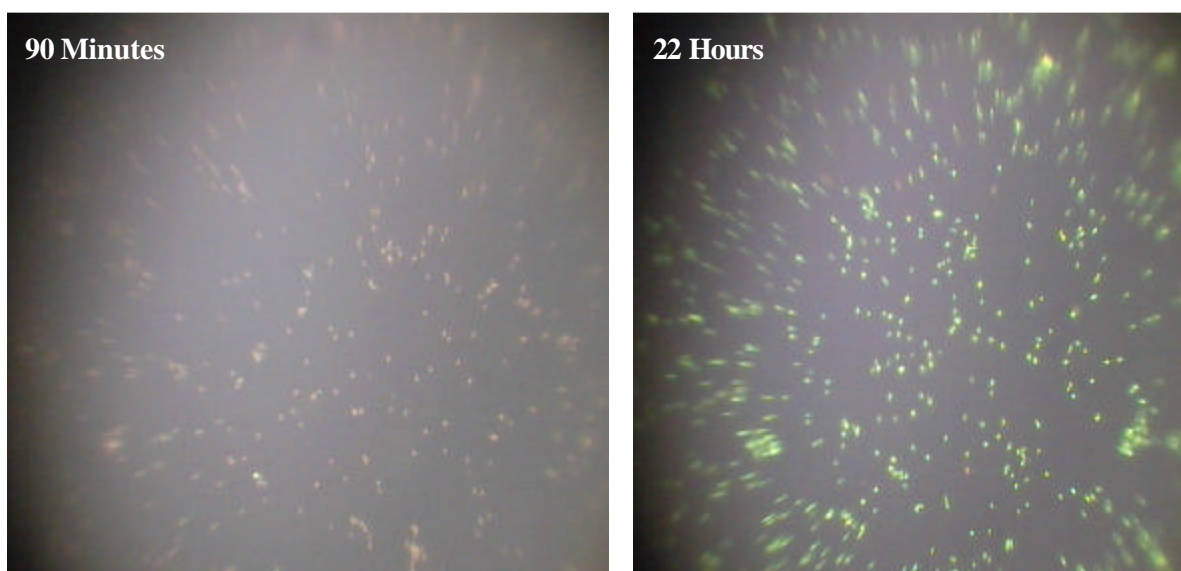


**Figure 11-3b:** Non-specific binding of microorganisms in the BBQ Briskets homogenate with PEO-Protein-A chips

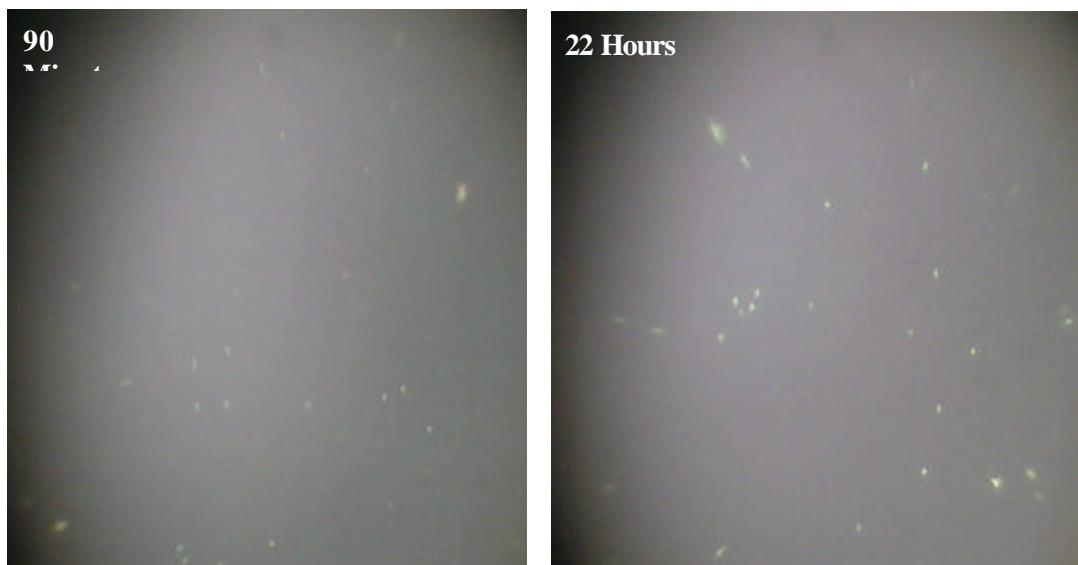


**Figure 11-3c:** Non-specific binding of microorganisms in the clam chowder homogenate with PEO-Protein-A chips

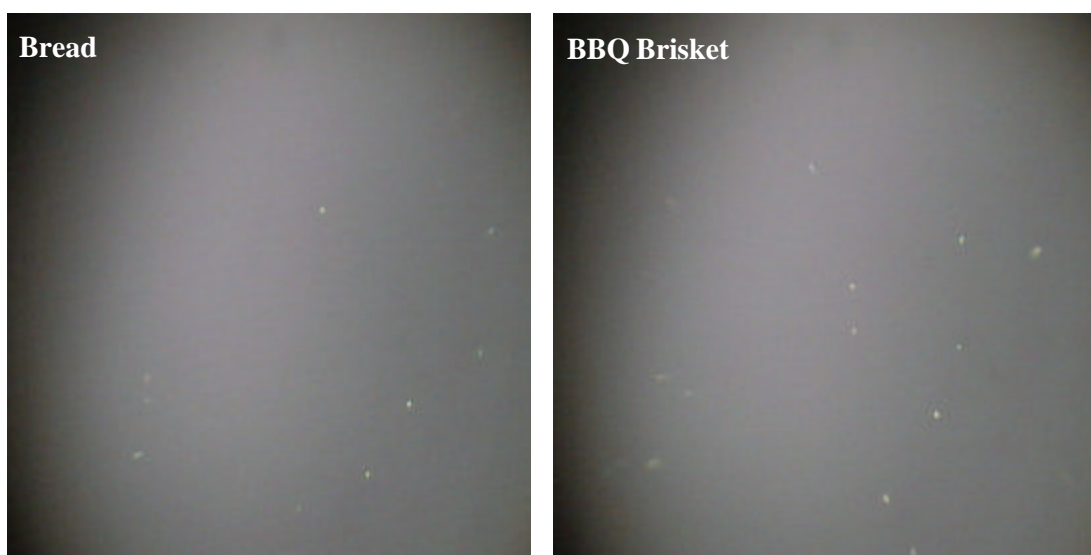


**Figure 11-3d:** Non-specific binding of microorganisms (90 minutes) in the bread (left) and BBQ briskets (right) homogenates with PEO-chips (without Protein-A).

**Summary.** The ultimate goal of this project was the application of the SatCon biosensor to the detection of foodborne pathogens. This work was planned in collaboration with SBCCOM Natick, MA. To this end, experiments for verifying *S. Aureus*, *E.coli* O157: H7, and SAE model systems, and the spiking of food systems (not yet chosen) were planned. All cell strains and corresponding antibodies were purchased. Non-specific binding studies were conducted at SatCon using food systems spiked with the avirulent *E. coli* O30 system. Significant binding was found and suspected to be the result of lipids binding to the surface. Verification of *E.coli* and *S. aureus* model systems was attempted but thwarted by the logistics of transporting Protein-

A coated chips without corrupting the sensitive chip surfaces. No other work was able to be carried out before all funding was exhausted.

## Chapter 12 : Summary and Conclusions

The development of a novel interferometric, evanescent-wave-based biosensor system for the detection of foodborne pathogens was undertaken over an 18-month period. A 'doubly differential' interferometer, capitalizing on the difference in evanescent response between modulating polarizations, was used as the transducer because of its promise for high sensitivity (at a level of fg/mm<sup>2</sup> surface mass) and unlabelled detection. The development of the interferometer was eventually hampered by the inability to fabricate working waveguides for grating-coupled double-differential testing. A first generation of grating-coupled waveguides was fabricated but was unusable due to poor throughput. The next generation waveguides, incorporating 1<sup>st</sup> order diffraction gratings, never reached fabrication due to design uncertainties, risk and resulting delays. SatCon resorted to singly-differential measurements using grating-coupled waveguides obtained from Dr. Daniel Campbell at the Georgia Tech Research Institute to establish interferometer performance limits and to perform preliminary integration and laboratory characterization efforts.

The development of the transducer was combined with several parallel developments. The waveguide surface was derivatized with a self-assembled monolayer (SAM) of polyethylene oxide (PEO) to which protein-A was covalently attached. This provided a 'Teflon' like surface for the suppression of non-specific binding and the carefully controlled positioning of receptors. Work was terminated before patterning and optimization could be carried out. The receptor system was based on a protein-A linker for the general attachment of IgG immuno-receptors. A model *E. coli* system was developed for testing and immuno-receptor attachment and regeneration was demonstrated through a series of benchtop binding experiments.

Non-specific binding (NSB) of proteins was addressed by the application of a PEO SAM mentioned above. A novel optical technique proposed by the Boston University group for the controlled desensitization of the waveguide surface and the microfluidic based filtering to diffuse small molecules from large cells as a means of mass extraction was also explored as an additional approach to NSB and for 'on-chip' sample preparation, respectively. No data were able to be produced from the former optical experiments. Stand-alone gravity driven disposable cartridges were designed by Micronics, Inc for SatCon and tested. Cell recovery was typically measured at 60-70% while removal of BSA protein was slightly higher. Although not optimized, these results suggest that this technique alone will not be adequate for 'on-chip' sample preparation.

A novel flow cell based on the dynamics of flow at low Reynolds number to spatially direct cells nearer to the receptors for enhanced capture efficiency was conceived. A device was designed and tested. The experimental data were in excellent agreement with theoretical predictions and eventually limited by the stability of the pump station.

Experiments were planned using prism coupled waveguides produced by the Boston University group to obtain intermediate data while the more time intensive development of the grating coupled waveguides was underway. No data was able to be produced due to fatal design flaws in the production of the waveguides. Eventually working grating coupled waveguide devices were obtained from Dr. Daniel Campbell at the Georgia Tech Research Institute and a preliminary integration and laboratory characterization was carried out. Refractive index data on bulk fluidics, non-specific protein adsorption,

and specific capture of proteins was collected. Preliminary experiments with bacterial cells were not able to be completed because of the unavailability of quality waveguides.

Finally, the application of the technology to the detection of Foodborne pathogens was undertaken. Experiments establishing model systems and their recovery from different food systems were planned but not executed before all resources were expended.

**Future Work.** Overall, the lack of availability of working grating coupled waveguides has impeded the progress in demonstrating the effectiveness of this approach and further work is required to access its value. A list of four major items to demonstrate the capability of this biosensor is:

- The completed fabrication of these waveguide devices is essential to prove the feasibility of this technique and make measurements of microbiological targets. A commercial fabrication facility capable of doing the work has been identified and contracted. The fabrication setup of these devices is complete, photolithographic masks have been purchased, wafers have been delivered, and the process is ready for thin film deposition and feature etching. Inconsistencies in modeling results which have confused the selection of the final design parameters must be worked out before proceeding to manufacture.
- The preliminary work for the immobilization of Protein-A onto a PEO SAM has been completed, however, this task has not been fully completed. To effectively utilize Protein-A, its density of surface binding sites must be controlled. Protein-A is capable of generating non-specific binding through its presence. Currently Protein-A surface density is estimated to be between 30 and 40 percent. The exact ratio of Protein-A to PEO is crucial and is a tradeoff between the amount of non-specific binding and the capture affinity of the surface. This ratio will be different depending on the target. For example, the binding of large objects such as cells that are orders of magnitude bigger than an immuno-receptor suggests only a fraction of a percent surface coverage is needed to capture an organism whereas the detection of small proteins will require coverage at the level of tens of percent.
- Differential detection techniques are powerful methods for effectively integrating a 'control experiment' into the instrument. In order to take full advantage of the common-mode rejection between the target and reference channels they must be in close proximity to each other. This can only be implemented if the Protein-A receptor patch can be positioned with millimeter accuracy. The development of surface patterning techniques must be continued to control of the positioning of receptor regions.
- An area more important than the sensitive transduction of the captured cells is the actual capturing of these targets. While hydrodynamic focusing is an important contribution for increasing the capture probability it comes at the price of a much longer processing time. Therefore, a key area for future work, more important than transducer development, is the concentration of the sample to expedite significantly the processing time. This is essential to address a problem common to all biosensors, namely the small detection volumes inherent to their design in contrast to the large sample volumes encountered with real world problems.